FEUP Universidade do Porto
Faculdade de Engenharia

IDENTIFICATION OF COHESIVE LAWS OF CORTICAL BONE UNDER MODE I, MODE II AND MIXED-MODE I+II

Fábio André Magalhães Pereira

2015

Thesis presented to the Faculty of Engineering of the University of Porto
for the Doctor Degree in Mechanical Engineering

Supervisors
Marcelo Francisco de Sousa Ferreira de Moura *Associate Professor*
José Joaquim Lopes Morais *Full Professor*
Nuno Miguel Magalhães Dourado *Assistant Professor*

GOVERNO DE PORTUGAL
FCT Fundação para a Ciência e a Tecnologia
MINISTÉRIO DA CIÊNCIA, TECNOLOGIA E ENSINO SUPERIOR
UNIÃO EUROPEIA Fundo Social Europeu
QREN QUADRO DE REFERÊNCIA ESTRATÉGICO NACIONAL PORTUGAL 2007.2013
POPH PROGRAMA OPERACIONAL POTENCIAL HUMANO

In memory of
Albano Pereira.

The author acknowledges financial support from Fundação para a Ciência e Tecnologia through grant no. SFRH/BD/80046/2011.

Agradecimentos

Desejo aqui, expressar a minha gratidão para com todos aqueles que tornaram possível a realização deste trabalho, nomeadamente aos meus orientadores, Prof. Marcelo Moura, Prof. José Morais e Prof. Nuno Dourado (co-orientador e amigo) pelo seu apoio incondicional, recetividade, por tudo terem feito no sentido de responder a todas as minhas dúvidas e a trabalheira dos últimos dias.

Gostaria igualmente de endereçar um enorme agradecimento ao Prof. José Xavier, por todo o acompanhamento, trabalho e total disponibilidade, à Prof. Maria Isabel Dias por todo o auxílio.

Aos meus amigos Cristóvão Santos, Luís Silva, João Pereira e Filipe Silva por todo o companheirismo, paciência, apoio, auxílio e toda a discussão desportiva.

O agradecimento mais importante dirige-se à Rosana, minha namorada por toda a compreensão, apoio, companheirismo e dedicação.

A toda a minha família em especial à minha mãe pela presença e suporte, agradeço também aos meus irmãos sobrinhas e cunhadas. Agradeço ainda à família da minha namorada, Zélia e Sara, o meu muito obrigado.

Às alunas de engenharia mecânica da UTAD, Ana Raquel, Andrea Olmos, Beatriz Pereira e Fátima Mouta.

Sem o apoio de todos este trabalho não seria possível.

Agradeço ainda às instituições Faculdade de Engenharia da Universidade do Porto, à Universidade de Trás-os-Montes e Alto-Douro e Instituto de Ciência e Inovação em Engenharia Mecânica e Engenharia Industrial o suporte à realização de todo o trabalho.

Agradeço À Fundação para a Ciência e Tecnologia, pelo suporte financeiro através da bolsa SFRH/BD/80046/2011.

Abstract

Fracture characterization of bovine cortical bone was performed in this work. Different test methods were proposed for fracture characterization under mode I, mode II and mixed-mode I+II loading. In modes I and II, miniaturized versions of the Double Cantilever Beam and End-Notched Flexure tests were used with success. For mixed-mode I+II the Single-Leg Bending and the Mixed-Mode Bending tests were utilized. The former is easy to perform but only propitiates one mixed-mode ratio. To overcome this difficulty a miniaturized version of the Mixed-Mode Bending apparatus was conceived and three mode ratios were tested.

An equivalent crack length based data reduction scheme was used for all tests to overcome the difficulties inherent to crack monitoring during propagation. The method propitiates the evolution of strain energy release rate as a function of equivalent crack length, i.e., the *Resistance*-curve. Despite the natural restrictions on bone specimen dimensions, small plateaus were identified in the *Resistance*-curves of all tests. This means that self-similar crack growth occurred for a given crack extent which is an essential statement for correct estimation of fracture energy. Numerical analysis including cohesive zone modelling were performed to validate all the procedure used to get the fracture energy. It was concluded that the proposed tests with the suggested specimen dimensions provide rigorous bone fracture characterization for the analysed loading modes.

Cohesive laws used to mimic bone fracture under different loading modes were obtained following two procedures. The direct one is based on the differentiation of the function fitted to the experimental relation between strain energy release rate and crack opening displacement measured by digital image correlation technique. The method proved to be reliable and simple in the case of pure modes loading. For the mixed-mode I+II case the uncoupled, Sørensen and Högberg methods were used. The Högberg method seems to be the most suitable for determination of the cohesive law components in mode I and mode II of the mixed-mode I+II loading. The inverse procedure combines numerical simulations with a developed optimization algorithm to determine the cohesive law minimizing the difference between numerical and experimental load-displacement

curves. The shape of the law is not imposed a priori, which can be considered an important advantage relative to classical inverse procedures.

As a final remark, it can be affirmed that the present work can be viewed as a valuable contribution to define suitable procedures to perform appropriate fracture characterization of cortical bone. Although in this study bovine bone has been used as testing material, the presented processes and procedures can easily be extended to humans', thus becoming relevant for human health purposes with obvious social-economic impact.

Resumo

Neste trabalho realizaram-se ensaios de caracterização à fratura do tecido ósseo cortical de bovino. Para tal, propuseram-se três métodos diferentes para a caracterização à fratura sob solicitações de modo I, de modo II e de modo misto I+II. Nos modos I e II foram concebidas e utilizadas com sucesso versões miniaturizadas dos ensaios *Double Cantilever Beam* e *End-Notched Flexure*. Para a caracterização à fratura sob solicitações de modo misto I+II utilizaram-se os ensaios *Single-Leg Bending* e *Mixed-Mode Bending*. O primeiro é de fácil execução, mas propicia um único rácio de modo misto. Para ultrapassar esta dificuldade foi projetada e construída uma versão miniaturizada do sistema de amarras usado no ensaio *Mixed-Mode Bending*, tendo sidos testados três rácios de modo misto.

Para ultrapassar as dificuldades inerentes à monitorização do comprimento de fenda durante os ensaios, usou-se um procedimento de tratamento de resultados experimentais baseado no conceito de fenda equivalente. O método permite a obtenção da curva de *Resistência*, ou seja da evolução da taxa de libertação de energia de deformação em função do comprimento de fenda equivalente. Apesar das restrições naturais no que concerne às dimensões dos provetes obtidos a partir do osso cortical, foi possível identificar pequenos patamares nas curvas de *Resistência*, o que é fundamental para se promover uma correta medição da energia de fratura. Foram feitas simulações numéricas incluindo modelos coesivos com o objetivo de validar todo o procedimento experimental usado para a determinação das energias de fratura. Os resultados obtidos permitiram concluir que os testes propostos e as dimensões sugeridas para os provetes propiciam uma rigorosa caracterização à fratura do osso para os modos de solicitação considerados.

As leis coesivas que permitem simular a fratura do osso sob os diversos modos de solicitação foram obtidas usando dois procedimentos. O método direto baseia-se na derivação da função ajustada à relação experimental entre a taxa de deformação de energia de deformação e o deslocamento de abertura da fenda, medido pela técnica de correlação digital de imagem. Este método provou ser eficaz e simples nos casos de solicitação sob modos puros de carregamento. Para a solicitação de modo misto I+II utilizaram-se os modelos *uncoupled*, Sørensen e Högberg. O modelo de Högberg aparenta ser o mais eficaz na determinação das componentes de modo I e de modo II da lei coesiva

de modo misto I+II. O método inverso desenvolvido neste trabalho combina simulações numéricas com um algoritmo de otimização para determinar a lei coesiva que minimiza a diferença entre as curvas força-deslocamento numérica e experimental. Neste método a forma da lei não é imposta previamente, o que se pode considerar uma vantagem importante relativamente aos métodos inversos clássicos.

Como conclusão final pode-se afirmar que o presente trabalho pode ser visto como uma importante contribuição para a definição de procedimentos adequados para uma correta caracterização à fratura do osso cortical. Apesar de se ter usado o osso de bovino como material de estudo, os processos e procedimentos desenvolvidos neste trabalho são extensíveis ao osso cortical humano, tornando-se assim relevantes no domínio da saúde pública com óbvio impacto socioeconómico.

Contents

Agradecimentos ……..…… ii
Abstract ……...…… iii
Resumo …… v
Contents ……..… vii
Lists of Figures …… x
Lists of Tables …….. xvii
Nomenclature …… xix

CHAPTER I – Introduction

1.1 - Introduction 1
1.2 - Structure and composition of cortical bone 2
1.3 - Fracture in bone 5
1.4 - Cohesive zone models 12
1.5 - Application of cohesive zone models to bone 17
1.6 - Cohesive mixed-mode I+II damage model 19

CHAPTER II – Fracture behaviour of cortical bone under pure mode I loading

2.1 - Introduction 22
2.2 - Material and specimens 22
2.3 - Double Cantilever Beam – Data reduction scheme 28
2.4 - Identification of cohesive law - direct method 35
2.5 - Identification of cohesive law - new inverse method 39
2.6 - Analysis and discussion of experimental mode I *Resistance*-curves 45
2.7 - Analysis and discussion: mode I cohesive law 49

2.8 - Conclusions 55

CHAPTER III – Fracture behaviour of cortical bone under pure mode II loading

3.1 - Introduction 56

3.2 - Experiments 56

3.3 - End Notched Flexure – Data reduction scheme 57

3.4 - Identification of cohesive laws - direct method 60

3.5 - Identification of cohesive law - new inverse method 63

3.6 - Analysis and discussion of experimental mode II *R*-curves 65

3.7 - Analysis and discussion: mode II cohesive law 67

3.8 - Conclusions 73

CHAPTER IV – Fracture behaviour of cortical bone under mixed-mode I+II – SLB test

4.1 - Introduction 74

4.2 - Experiments 75

4.3 - Single Leg Bending - data reduction scheme 76

4.4 - Numerical analysis of SLB test method 78

4.5 - Analysis and discussion of experimental mixed-mode I+II *R*-curves 82

4.6 - Identification of cohesive laws - direct method 87

4.7 - Conclusions 89

CHAPTER V – Fracture behaviour of cortical bone under mixed-mode I+II – MMB test

5.1 - Introduction 91

5.2 - Experiments 92

5.3 - Mixed-Mode Bending – Data reduction scheme 94

5.4 - Analysis of experimental mixed-mode I+II *R*-curves 97

5.5 - Numerical analysis of MMB test method..... 104

5.6 - Analysis of mixed-mode I+II cohesive law..... 106

5.7 - Conclusions 125

CHAPTER VI – Conclusions

Conclusions 127

References

References 130

Lists of Figures

CHAPTER I – Introduction

Fig. 1.1 – (a) Structure and composition of femur (Norris and Siegfried, 2011) and (b) micro-structure of cortical bone (Doblaré et al., 2004). 4
Fig. 1.2 – Microstructure of cortical bone of a longitudinal section obtained from optical microscopic (50 ×): (a) lamellar bone and (b) woven bone. 4
Fig. 1.3 – Hierarchical structure of cortical bone (Rho et al., 1998). 5
Fig. 1.4 – Cortical bone fracture tests performed under mode I loading: (a) Schematic representation of a long bone showing the axes of bone and the orientation of the specimens (L: longitudinal; R: radial; T: Tangential); (b) Compact Tension (CT); (c) Single-Layer Compact Sandwich (SLCS); (d) Double Cantilever Beam (DCB); (e) Single Edge Notched Beam (SENB); (f) Chevron-Notched Beam (CNB) (g) Chevron Notched Tension (CNT) (Higher specimen dimension correspond to longitudinal direction). 7
Fig. 1.5 – Cortical bone fracture tests performed in mode II: (a) Compact Shear (CS); (b) Single Edge Notched Asymmetric Four-Point Bending (SEN-AFPB); (c) End-Loaded Split (ELS) (d) End-Notched Flexure (ENF) (All the specimens are orientated in longitudinal direction of bone)..... 10
Fig. 1.6 – Cortical bone fracture tests performed in mode I: (a) Double Cleavage Drilled Compression (DCDC); (b) Single Leg Bending (SLB) (All the specimens are orientated in longitudinal direction of bone). 11
Fig. 1.7 – Dugdale model (Schwalbe et al. 2012)..... 12
Fig. 1.8 – Barenblatt model (Gross and Seelig, 2007). 13
Fig. 1.9 – Free-edge notched plate under shear and normal loading (Gross and Seelig, 2007). 13
Fig. 1.10 – Cohesive zones (schematic): a) metal-particle reinforced ceramics; b) fibre-matrix composite; c) heterogeneous ceramics, concrete; d) ductile material with void formation; e) brittle material with micro-cracks; f) cohesive zone model adapted from (Gross and Seelig, 2007). 15
Fig. 1.11 – Stress distributions and softening curves: (a) ductile-brittle metal, (b) quasi-brittle concrete (adapted from Bažant, 2002). 15

Fig. 1.12 – Typical traction–separation laws: (a) (Needleman, 1987), (b) Needleman, (1990), (c) Hillerborg et al., (1976), (d) Bažant, (2002),(e) Scheider and Brocks, (2003), (f) Tvergaard and Hutchinson, (1992). 16
Fig. 1.13 – (a) CT specimen for fracture toughness testing of human cortical bone. (b) Schematics of 2D, 4-noded cohesive element and its compatibility with solid elements. Note that the *n* and *s* axes denote the normal and tangential displacements of the cohesive element, respectively (Ural and Vashishth, 2006). 18
Fig. 1.14 – Bilinear cohesive law (Pereira et al., 2012). 18
Fig. 1.15 – Stepwise cohesive law. 20

CHAPTER II – Fracture behaviour of cortical bone under pure mode I loading

Fig. 2.1 - Aspect of bovine femur after harvesting of the diaphysis part to get specimens. 23
Fig. 2.2 – Machining operations: (a) Milling; (b) specimen for three point bending test; (c) pre-crack execution; (d) creating lateral grooves. 24
Fig. 2.3 – Geometry of the three point bending test specimen. 25
Fig. 2.4 – Determination of submerged weight. 27
Fig. 2.5 – (a) Optical microscope image of a longitudinal section of cortical bone (50x); (b) binary image; (c) lacuna; (d) vascular porosity (~4%). 28
Fig. 2.6 – Schematic representation of the DCB specimen used for mode I fracture characterization of bone. 29
Fig. 2.7 – Crack-tip detail in bone. 29
Fig. 2.8 – Introduction of the pre-crack with a sharp blade duly set in the test machine. 32
Fig. 2.9 – Example of a *speckle* pattern. 33
Fig. 2.10 – Image processing. 34
Fig. 2.11 – Photography of the DCB test. 34
Fig. 2.12 – Finite element mesh used in the DCB test: (a) undeformed configuration, (b) deformed configuration (diagonal crosses represent the cohesive elements). 36
Fig. 2.13 – Bilinear cohesive law ($G_{Ic} = G_{I\mu} + G_{Ib}$) (Pereira et al., 2012) 37
Fig. 2.14 – The $G_I = f(w_I)$ relationship obtained in finite element analysis and the adjusted one using a smoothing spline fitting. 38

Fig. 2.15 – Comparison between the cohesive law used as input (i.e., Numerical) in the model and the one obtained by the direct method. 38
Fig. 2.16 – Load-displacement curves: experimental and numerical. 39
Fig. 2.17 – Cohesive law used as input in the numerical model. 40
Fig. 2.18 – Load-displacement curve and the corresponding *R*-curve of a DCB test in bovine bone revealing a series of points used for adjustment in the proposed inverse method 40
Fig. 2.19 – Organogram of the developed *Bissection* algorithm (*i*=1, 2, 3, 4, and 5)..... 41
Fig. 2.20 – Nelder-Mead domain: **B** – best vertex; **N** – next to worst vertex; **W** – worst; E – expansion vertex; R – reflection vertex; C_R – contraction vertex on R side; C_W – contraction vertex on W side. Adapted from Walters (1991). 42
Fig. 2.21 – Organogram of the developed *Nelder-Mead* Algorithm (*i*=1,2,3,4 and 5)... 43
Fig. 2.22 – Numerical load-displacement curves: reference, *Bissection* and *Nelder Mead* algorithm. 44
Fig. 2.23 – Numerical *Resistance*-curves: reference, *Bissection* algorithm and *Nelder Mead* algorithm. 44
Fig. 2.24 – Comparison between the cohesive law used as input and the ones obtained by the inverse methods 45
Fig. 2.25 –*R*-curves under mode I loading of bovine cortical bone. 47
Fig. 2.26 – Crack evolution: (a) initial stage, (b) intermediate stage, (c) load peak - propagation onset, (d) significant propagation (specimen 7) 48
Fig. 2.27 – Crack opening displacements evolution as a function of applied displacement (*i* =I, II). 48
Fig. 2.28 – Typical G_I=f(w_I) experimental relationship and smoothing spline fitting.... 50
Fig. 2.29 – Comparison between the experimental and numerical curves identified by the developed inverse optimization method: (a) *P*-δ curves, (b) *R*-curves and (c) cohesive laws (specimen 5). 51
Fig. 2.30 – Cohesive laws obtained by the direct method. 52
Fig. 2.31 – Cohesive laws obtained by the developed inverse method. 52

Fig. 3.1 – Testing setup of the ENF test. 57
Fig. 3.2 – Schematic representation of the ENF test specimen. 58
Fig. 3.3 – Crack-tip detail in bone. 59
Fig. 3.4 – Crack propagation in mode II at the peak load: the white squares identify the DIC points. 60
Fig. 3.5 – Finite element mesh used in the ENF test: (a) undeformed configuration, (b) deformed configuration (diagonal crosses represent the cohesive elements). 61
Fig. 3.6 – Trapezoidal cohesive law used for mode II fracture characterization of bovine cortical bone. 62
Fig. 3.7 – Comparison between the mode II cohesive law used as input in the model and the one obtained by the direct method. 62
Fig. 3.8 – Experimental and numerical load-displacement curves of the ENF test. 63
Fig. 3.9 – Comparison between determined and reference load-displacement curves. 64
Fig. 3.10 – Comparison between determined and reference *R*-curves. 64
Fig. 3.11 – Comparison between determined and cohesive law used as input. 65
Fig. 3.12 – Mode II fracture *R*-curves of bovine cortical bone 65
Fig. 3.13 – Load-displacement curve of an ENF test (specimen 17) - plotted letters correspond to stages presented in Fig. 3.14. 68
Fig. 3.14 – Crack evolution: (a) initial stage, (b) intermediate stage, (c) load peak - propagation onset and (d) significant propagation (specimen 17). 68
Fig. 3.15 – Evolution of crack opening displacements with the applied displacement. 69
Fig. 3.16 – Comparison between the experimental (direct method) and numerical curve identified by the inverse optimization method: (a) P-δ curves, (b) *R*-curves, (c) Cohesive laws (specimen 14). 70
Fig. 3.17 – Mode II cohesive laws obtained by the direct method. 71
Fig. 3.18– Mode II cohesive laws obtained by the inverse method. 71

CHAPTER IV – Fracture behaviour of cortical bone under mixed-mode I+II – SLB test

Fig. 4.1– Photography of the SLB experimental test applied to cortical bone. 75
Fig. 4.2– Schematic representation of the SLB test. 76
Fig. 4.3 – Finite element mesh used for the SLB test (a) undeformed configuration, (b) deformed configuration at peak load (diagonal crosses represent the cohesive elements).. 79
Fig. 4.4 – Numerical load-displacement curve of the SLB test. 80
Fig. 4.5 – Evolution of fracture process zone. 80
Fig. 4.6 – Numerical load-displacement curve for adjusted SLB specimen dimensions. .81
Fig. 4.7 – Numerical *R*-curves for adjusted SLB specimen dimensions. 82
Fig. 4.8 – Experimental load–displacement curves of the SLB test in bovine cortical bone. 83
Fig. 4.9 – Opening and shear displacements at the notch tip (Detail A) and undefined crack tip position (Detail B). 83
Fig. 4.10 – Mode I *R*-curves issuing from the mixed-mode I+II SLB test. 85
Fig. 4.11 – Mode II *R*-curves issuing from the mixed-mode I+II SLB test. 85
Fig. 4.12 – Fracture envelop for cortical bone in G_I *versus* G_{II} space. 86
Fig. 4.13 – Fracture envelop in G_I-G_{II} space and numerical results obtained with the CBBM and Szekrényes and Uj (2004) methods. 87
Fig. 4.14 – Numerical components in mode I and mode II of the mixed-mode cohesive laws (i = I, II). 88
Fig. 4.15 – Crack opening displacements relation. 89

CHAPTER V – Fracture behaviour of cortical bone under mixed-mode I+II – MMB test

Fig. 5.1 – Schematic representation of the miniaturized version of the MMB text fixture constructed for bone fracture characterization under mixed-mode I+II loading. 92
Fig. 5.2 – Schematic representation of the MMB test. 93
Fig. 5.3 – MMB experimental test. 94
Fig. 5.4 – Superposition loading analysis of the MMB specimen. 95

Fig. 5.5 – Experimental load-displacement curves of the MMB test: (a) G_I/G_{II}=0.33, (b) G_I/G_{II}=1.24, (c) G_I/G_{II}=2.53. 98
Fig. 5.6 – Mixed-mode *R*-curves (G_I/G_{II}=0.33): (a) Mode I, (b) Mode II. 99
Fig. 5.7 – Mixed-mode *R*-curves (G_I/G_{II}=1.24): (a) Mode I, (b) Mode II. 100
Fig. 5.8 – Mixed-mode *R*-curves (G_I/G_{II}=2.53): (a) Mode I, (b) Mode II. 101
Fig. 5.9 – Fracture envelope for cortical bone in G_I versus G_{II} space (**bold** marks correspond to average results). 102
Fig. 5.10 – Finite element mesh used for the MMB test: (a) undeformed configuration, (b) deformed configuration at peak load (ratio G_I/G_{II}=2.53). 105
Fig. 5.11 – Examples of w_{II} versus w_I local displacements for each MMB ratio. 107
Fig. 5.12 – Normalized $\bar{G}(\overline{w}_I,\overline{w}_{II})$ curves of all fracture tests and the fitted surface. ... 108
Fig. 5.13 – Normalized cohesive laws components obtained by the application of Sørensen and Kirkegaard, (2006) method: (a) mode I, (b) mode II. 109
Fig. 5.14 – Cohesive laws components obtained by the application of Sørensen and Kirkegaard, (2006) method. 110
Fig. 5.15 – Graphical presentation of the mixed-mode cohesive law, adapted from Högberg (2006). 112
Fig. 5.16 – Mode I components of the cohesive laws for G_I/G_{II}=0.33: (a) uncoupled method; (b) Högberg. 113
Fig. 5.17 – Mode II components of the cohesive laws for G_I/G_{II}=0.33: (a) uncoupled method; (b) Högberg. 114
Fig. 5.18 – Mode I components of the cohesive laws for G_I/G_{II}=1.24: (a) uncoupled method; (b) Högberg. 115
Fig. 5.19 – Mode II components of the cohesive laws for G_I/G_{II}=1.24: (a) uncoupled method; (b) Högberg. 116
Fig. 5.20 – Mode I components of the cohesive laws for G_I/G_{II}=2.53: (a) uncoupled method; (b) Högberg. 117
Fig. 5.21 – Mode II components of the cohesive laws for G_I/G_{II}=2.53: (a) uncoupled method; (b) Högberg. 118
Fig. 5.22 – Normal stress variation as a function of mode mixity, θ: (a) uncoupled; (b) Högberg 121

Fig. 5.23 – Shear stress variation as a function of mode mixity, θ: (a) uncoupled; (b) Högberg..... 122
Fig. 5.24 – Critical equivalent crack opening displacements as a function of mode mixity, θ. 123
Fig. 5.25 – Total energy release rate variation as a function of mode mixity, θ (■ mean series values). 124
Fig. 5.26 – Critical opening displacement variation as a function mode mixity, θ (■ mean series values). 124

Lists of Tables

CHAPTER I – Introduction

Table 1.1 – Cortical bone fracture properties for pure mode I loading found in the literature for the TL fracture propagation system. 8

CHAPTER II – Fracture behaviour of cortical bone under pure mode I loading

Table 2.1 – Components of the optical system and DIC measuring parameters 33
Table 2.2 – Elastic properties of cortical bone. 35
Table 2.3 – Parameters of the cohesive law. 36
Table 2.4 – Rules for Nelder-Mead moves. 42
Table 2.5 – Experimental results. G_{Ic} fracture energy; E_L Longitudinal flexure modulus; d_h apparent density; m_w water mass fraction; m_o organic mass fraction; m_m mineral mass fraction; *Por* porosity. 46
Table 2.6 – Range of fracture energy in several works. 47
Table 2.7 – Cohesive laws. $\sigma_{I,u}$, ultimate strength, w_{Ic} ultimate relative displacement, $G_{law,I}$ circumscribed cohesive law area (non-valid test: -). 54

CHAPTER III – Fracture behaviour of cortical bone under pure mode II loading

Table 3.1 – Dimensions used in the numerical model. 61
Table 3.2 – Parameters of the cohesive law for mode II loading for bovine cortical bone. 61
Table 3.3 – Experimental results. G_{IIc}, fracture energy; d_h, apparent density; m_w, water mass fraction; m_o, organic mass fraction; m_m, mineral mass fraction; *Por* porosity. 66
Table 3.4 – Values of fracture energy found in other works. 67
Table 3.5 – Experimental results. $\sigma_{II,u}$, ultimate cohesive shear strength; $w_{II,c}$, maximum mode II opening displacement; $G_{law,II}$, fracture energy evaluated form de cohesive law. 72
Table 3.6 – Shear strengths values found in other works. 72

CHAPTER IV – Fracture behaviour of cortical bone under mixed-mode I+II – SLB test

Table 4.1 – Parameters of the cohesive law for mode I and mode II (Dourado et al., 2013; Pereira et al., 2012). 79
Table 4.2 – Experimental total fracture energy G_T and its components G_I and G_{II}. 84

CHAPTER V – Fracture behaviour of cortical bone under mixed-mode I+II – MMB test

Table 5.1 – Experimental results (G_I/G_{II}=0.33). G_I, G_{II}, fracture energy components, E_L longitudinal flexure modulus, d_h apparent density, m_w water mass fraction, m_o organic mass fraction, m_m mineral mass fraction, *Por* porosity. 103
Table 5.2 – Experimental results (G_I/G_{II}=1.24). G_I, G_{II}, fracture energy components, E_L longitudinal flexure modulus, d_h apparent density, m_w water mass fraction, m_o organic mass fraction, m_m mineral mass fraction, *Por* porosity. 103
Table 5.3 – Experimental results (G_I/G_{II}=2.53). G_I, G_{II}, fracture energy components, E_L longitudinal flexure modulus, d_h apparent density, m_w water mass fraction, m_o organic mass fraction, m_m mineral mass fraction, *Por* porosity. 104
Table 5.4 – Dimensions used in the numerical model. 105
Table 5.5 – Elastic properties of cortical bone. 105
Table 5.6 – Parameters of the cohesive law for mode I and mode II. 105
Table 5.7 – Experimental components of cohesive laws for G_I/G_{II}=0.33. 119
Table 5.8 – Experimental components of cohesive laws for G_I/G_{II}=1.24 (– non valid test). 119
Table 5.9 – Experimental components of cohesive laws for G_I/G_{II}=2.53 (– non valid test). 120

Nomenclature

Latin

a	Crack length
a_0	Initial crack length
a_e	Equivalent crack length
a_{ei}	Equivalent crack length for mode i loading (i = I, II)
A	Section area
B	Specimen thickness
b	Specimen thickness at half-height
c	Lever length (MMB test)
C	Compliance
C_0	Initial compliance
C_{0i}	Mode i initial compliance (i = I, II)
C_i	Mode i compliance (i = I, II)
$C_{0IIcorr}$	Corrected initial compliance under mode II loading
C_{IIcorr}	Corrected compliance under mode II loading
d	Damage parameter
d^{coh}	Cohesive zone length
d_h	Apparent density
Dif_i	Difference between the numerical and experimental load at point i
d_m	Total damage parameter
E_f	Flexural modulus
E_{fi}	Mode i flexural modulus (i = I, II)
E_L	Longitudinal elastic modulus
E_T	Transverse elastic modulus

G	Strain energy release rate
$G_{c,t}$	Högberg fracture energy
G_{ic}	Fracture energy under mode *i* loading (*i* = I, II)
G_i	Strain energy release rate under mode *i* loading (*i* = I, II)
G_{ib}	Fracture energy under mode *i* loading due to "fibre-bridging"
$G_{i\mu}$	Fracture energy under mode *i* loading due "micro-cracking"
G_i^{WW}	Williams (1989) mode *i* strain energy release rate
$G_{law,i}$	Area circumscribed by cohesive laws under mode *i* loading
G_{LT}	Shear modulus in the LT plane
G_T	Total energy release rate
G_{Tc}	Total fracture energy
h	Specimen half-height
I	Second moment of area
j	Inflection point
J	*J* integral
k	Interfacial stiffness (*j* = 2, 3, …, *n*)
K_i	Stress intensity factor under mode *i* loading (*i* = I, II, III)
K_{ic}	Critical stress intensity factor under mode *i* loading
K_I^{coh}	Stress intensity factor owing to cohesive stresses under mode I
L	Loading span
M_f	Bending moment
m_m	Mineral mass fraction
m_o	Organic mass fraction
m_w	Water mass fraction
P	Load
P_i	Mode *i* loading component (MMB test)
P_i^{exp}	Experimental load value at point *i*

P_i^{num}	Numerical load value at point *i*
Por	Porosity percentage
Q	Tangential load
R	Stiffness
S_θ	Normalized mixed-mode cohesive law
T	Cohesive modulus
t	Half-thickness of the beam
T_c	Critical cohesive modulus
U	Elastic strain energy
V	Transverse load
V_w	Specimen volume
w	Crack opening displacement
W_a	Ash weight
w_c	Critical crack opening displacement
W_d	Dehydrated weight
W_h	Hydrated weight
w_i	Crack opening displacement for mode *i* loading (*i* = I, II)
$\overline{w}_i$	Normalized crack opening displacement for mode i loading (i = I, II)
w_{ic}	Critical crack opening displacement for mode *i* loading
$\overline{w}_{i,Hög}$	Normalized crack opening displacement proposed by Högberg for mode i loading (i = I, II)
w_m	Equivalent crack opening displacement
w_{mc}	Critical equivalent crack opening displacement
W_S	Submerged weight

Greek

α	Power law parameter
β	Mode ratio
δ	Displacement
δ_i	Mode *i* displacement (MMB test)
ρ_w	Density of the distilled water
δ^{bot}	Bottom beam displacement
δ^{sup}	Superior beam displacement
Δ	Crack length correction
Δa_{ei}	Mode *i* equivalent crack length variation (*i* = I, II)
Δa_{FPZ}	Equivalent crack length variation due to FPZ
λ	Högberg dimensionless displacement parameter
λ_{corr}	Corrected Högberg dimensionless displacement parameter
ψ	Phase angle
θ	Mode mixity
σ_i	Mode *i* stress (*i* = I, II)
$\bar{\sigma}_i$	Normalized mode *i* stress (*i* = I, II)
$\sigma_{i,u}$	Mode *i* ultimate strength (*i* = I, II)
σ_m	Stress under mixed-mode loading
σ_u	Ultimate strength
$\sigma_{j,i}$	Mode *i* stress component for the *j* inflection point of the mixed-mode loading (*i* = I, II)
$\sigma_{um,i}$	Mode *i* component of the ultimate strength of the mixed-mode loading (*i* = I, II)
$\sigma_{i,um}$	Ultimate strength of mode *i* component under mixed-mode
σ^{coh}	cohesive stresses
ν_{LT}	Poisson's ratio in the LT plane

Φ	Potential energy

ACRONYMS

AFPB	Asymmetric four-point bending
CBBM	Compliance based beam method
CCD	Charge coupled device
CN	Chevron notched
CNB	Chevron notched beam
CNT	CHEVRON notched tension
COD_I	Crack opening displacement in mode I loading
COD_{II}	Crack opening displacement in mode II loading
CS	Compact shear
CT	Compact tension test
CZM	Cohesive zone models
DCB	Double cantilever beam
DCDC	Double cleavage drilled compression
DIC	Digital Image Correlation
ELS	End loaded split
ENF	End-notched flexure
FPZ	Fracture process zone
K-factor	Stress intensity factor
L	Longitudinal
LEFM	Linear elastic fracture mechanics
MMB	Mixed-Mode Bending
R	Radial
SEN	Single edge notched
SENB	Single edge notched beam
SLB	Single leg bending
SLCS	Single-layer compact sandwich
T	Tangential

CHAPTER I

Introduction

1.1 - Introduction

Bone is a living tissue whose structure and shape assures the necessary conditions for mobility of vertebrate animals. This structure continuously evolves throughout life, resulting from removal of old bone and replacement with newly formed one, in a process known as bone remodelling. The changes in the composition and structure of bone tissue are influenced by the mechanical and physiological environmental conditions (Doblaré et al., 2004). Morphologically, bone is classified in two principal types: cortical (or compact) and cancellous (trabecular or porous), whose differences are related to their functions. The former is found in the surface of long bones (e.g., femur, tibiae, fibula), while the latter is found in the epiphyses of long bones and particularly in the core of flat and short bones. Cancellous tissue plays an important role in the enhancement of resistance and distribution of loads in the epiphyses of long bones and in short and flat bones. Though being porous, and therefore potentially weak, cancellous bone is shaped and organized in such a way that strength is provided only where it is necessary. On the other hand, cortical bone provides the main support for body loads in the diaphysis of long bones. Hence, it can be viewed as a crucial structural material of skeleton and its mechanical characterization is an important research topic.

Despite its inherent remodelling capacity, fracture in cortical bone is very likely to occur, due to accidental causes, fatigue and disease (Doblaré et al., 2004). Predicting cortical bone fracture risks is a relevant topic of research with a significant socio-economic impact motivated by the progressive ageing of the population. In this context, Fracture Mechanics arises as an essential tool to evaluate cortical bone quality (Wang and Puram, 2004). Damage initiation and propagation in cortical bone tissue is characterized by the existence of a so-called Fracture Process Zone (FPZ) that develops in the vicinity of the crack tip. An

effective way to deal with the complex phenomena that occur in this non-linear domain consists in applying cohesive models by means of interface finite elements (Yang et al., 2006; Pereira et al., 2012). In this case the FPZ is considered lumped into cohesive surfaces, being the material fracture behaviour described by the cohesive law that relates stresses with relative displacements of adjacent surfaces. This approach presents some advantages relatively to classical methods based on Fracture Mechanics. One of them lies in the fact that it does not require the existence of an initial crack. Additionally, its application to fracture of materials and structures is not limited by any constraint due to FPZ dimensions. The major limitation arises from the unawareness of some fundamental aspects of cohesive models, namely the correct identification of cohesive laws with physical meaning.

The developed work presented in this thesis is focused on the fracture characterization of the cortical bone tissue involving femurs of young bovines with approximately eight months of age. This material exhibits a plexiform structure which is different from the human's osteonal structure. As with human bone, cortical bovine bone tissue is an orthotropic material. In this work, a special attention has been given to the identification of cohesive laws under pure mode I, mode II and mixed-mode I+II loading of bovine cortical bone. Though confined to bovine bone, both the testing procedure and identification methodologies are valid to human bone tissue, at least for the considered fracture propagation system. All the procedure can be used in systematic studies involving the assessment of the influence of several factors (e.g., age, drugs, environmental and others) on bone toughness. Also, some expected outcomes are of general nature, being envisaged its application to other quasi-brittle materials.

1.2 - Structure and composition of cortical bone

Bones can be divided into different subgroups (Clifford et al., 2013; Sikavitsas et al., 2001): long bones (femur and tibia), short bones (wrist and ankle) and flat bones (skull vault and irregular bones) (Salgado et al., 2004). These skeletal organs comprise mainly two types of tissues: cancellous and cortical tissues. Cancellous bone amounts around 20% of the total skeleton and cortical around 80% of the total skeleton. The proportions of these tissues differ at various locations in the skeleton (Salgado et al., 2004).

Cortical bone is a composite material with heterogeneous, anisotropic and hierarchical microstructure (Rho et al., 1998). It is almost solid, being only 10% porous, and is essentially constituted by a mineral phase (mainly hydroxyapatite), an organic phase

(mainly collagen) and water. The mineral phase is essentially responsible for stiffness and strength while the organic phase and water play an essential role on viscoelasticity and toughness (Norman et al., 1995). Bones can be divided into different subgroups (Clifford et al., 2013; Sikavitsas et al., 2001): long bones (femur and tibia), short bones (wrist and ankle) and flat bones (skull vault and irregular bones) (Salgado et al., 2004).

At the macroscopic level long bones are divided by two main zones (Fig. 1.1a): epiphyses and diaphysis. Epiphyses correspond to the top and bottom of long bones and are composed mostly by cancellous bone surrounded by a thin layer of cortical bone (Dias et al., 2005). The diaphysis is located in the middle region of long bones and contains the medullary cavity in the centre surrounded by a thin membrane called endosteum (Fig. 1.1b). A membrane called periosteum covers the outer bone (Fig. 1.1b) and provides nutrients and oxygen, removes unused materials and connects with ligaments and tendons (Norris and Siegfried, 2011). The cortical bone is located between the endosteum and periosteum.

Throughout life, two different tissues are present the in composition of cortical bone at the microscale: woven and lamellar bone (Fig. 1.2). In the embryo phase cortical bone is constituted by woven bone being later replaced by lamellar bone. Normally, woven bone is not found in the skeleton after four or five years reappearing only if a healing process occurs after bone fracture. The two types of bone present many differences in composition, organization, growth and mechanical properties. Woven bone is quickly formed and poorly organized with a more or less random arrangement of collagen fibres and mineral crystals. Lamellar bone is slowly formed, in a highly organized and oriented layers of collagen fibres and mineral crystals (lamellae), assembled in concentric microstructures called Haversian systems or osteons (Fig. 1.1b), that make it more resistant than woven bone (Doblaré et al., 2004). Each osteon has a central microscopic Haversian canal (Fig. 1.1b). A perpendicular system of canals, called Volkmann's canals, penetrate and cross between the Haversian systems. This network ensures circulation into even the hardest bone structure (Norris and Siegfried, 2011).

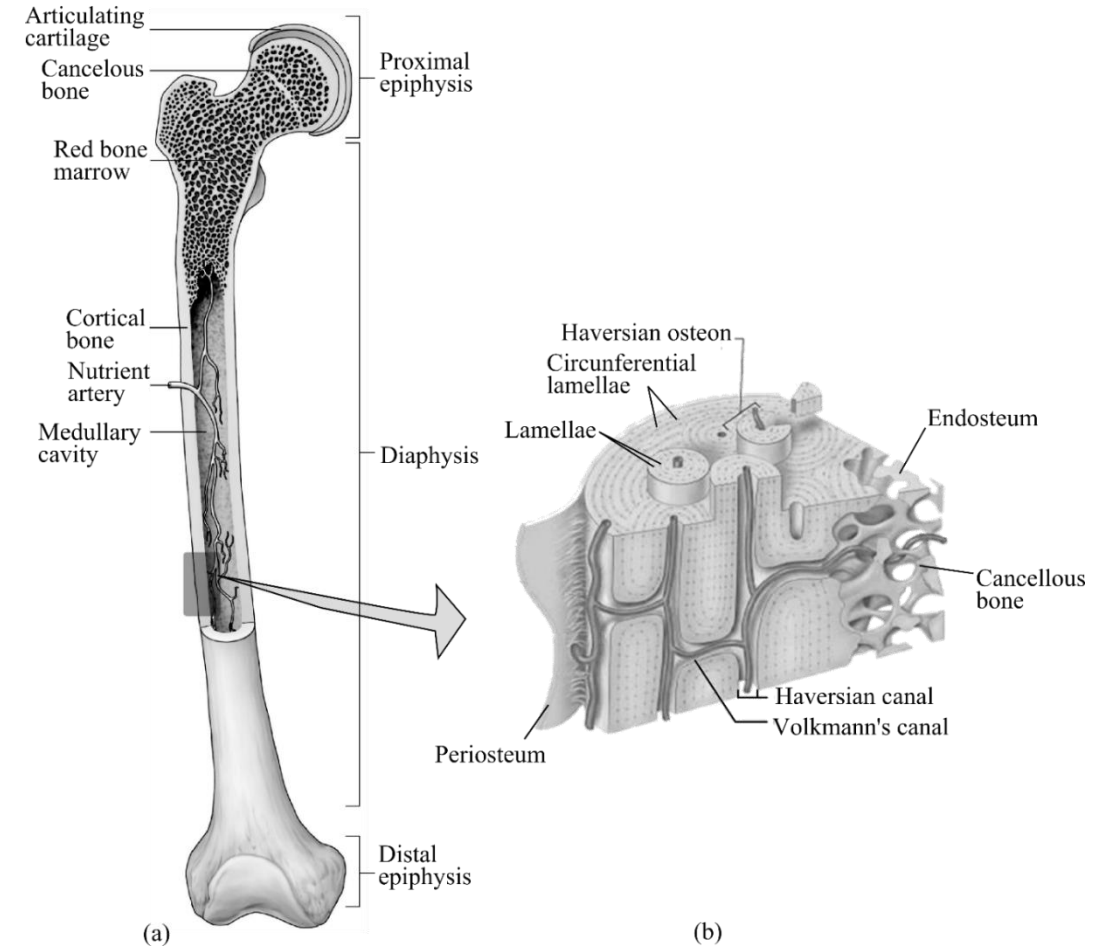

Fig. 1.1 – (a) Structure and composition of femur (Norris and Siegfried, 2011) and (b) micro-structure of cortical bone (Doblaré et al., 2004).

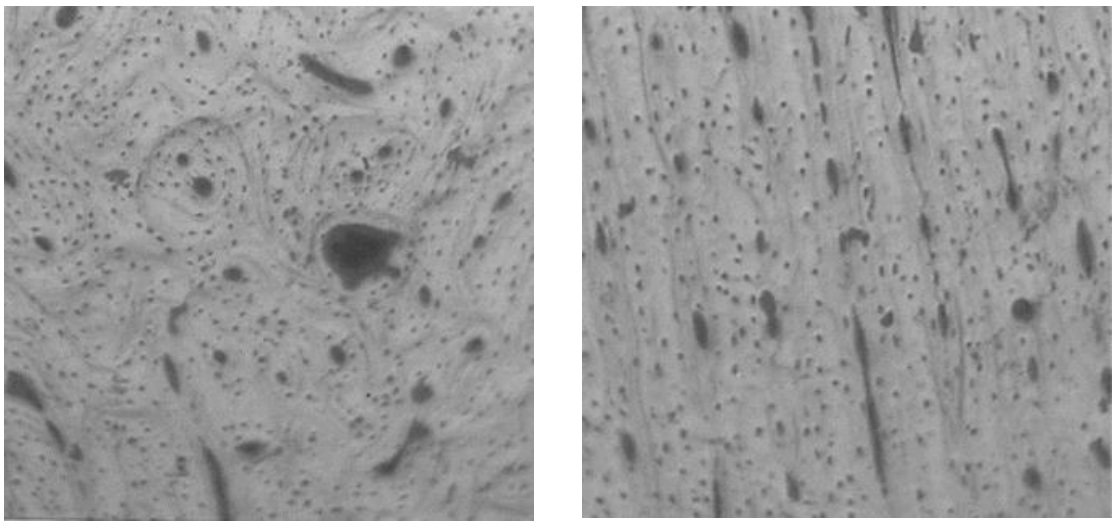

(a) (b)

Fig. 1.2 – Microstructure of cortical bone of a longitudinal section obtained from optical microscopic (50 ×) (Pereira, 2009): (a) lamellar bone and (b) woven bone.

At sub-microstructural level the Haversian osteon (Fig. 1.3) is composed by mineralized collagen fibres formed into planar arrangements called lamellae (3–7mm wide). In some cases (osteons) these layers (lamellae) of mineralized collagen fibres wrap in concentric layers (3–8 lamellae) around the Harvesian canal (Rho et al., 1998). The lower levels of bone hierarchy reveal a composite of collagen fibres and mineral nanoparticles of carbonated hydroxyapatite. The organic phase of bone matrix consists of collagen and a series of non-collagenous proteins and lipids. A large part (85-90%) of the total bone protein consists of collagen fibrils (Termine and Robey, 1996). The mineralized collagen fibril of about 100 nm in diameter is the basic building block of the bone material. Fibrils consist of an assembly of 300 nm long and 1.5 nm thick collagen molecules, which are deposited by the osteoblasts (bone forming cells) into the extracellular space and then self-assembled into fibrils (Fratzl and Weinkamer, 2007).

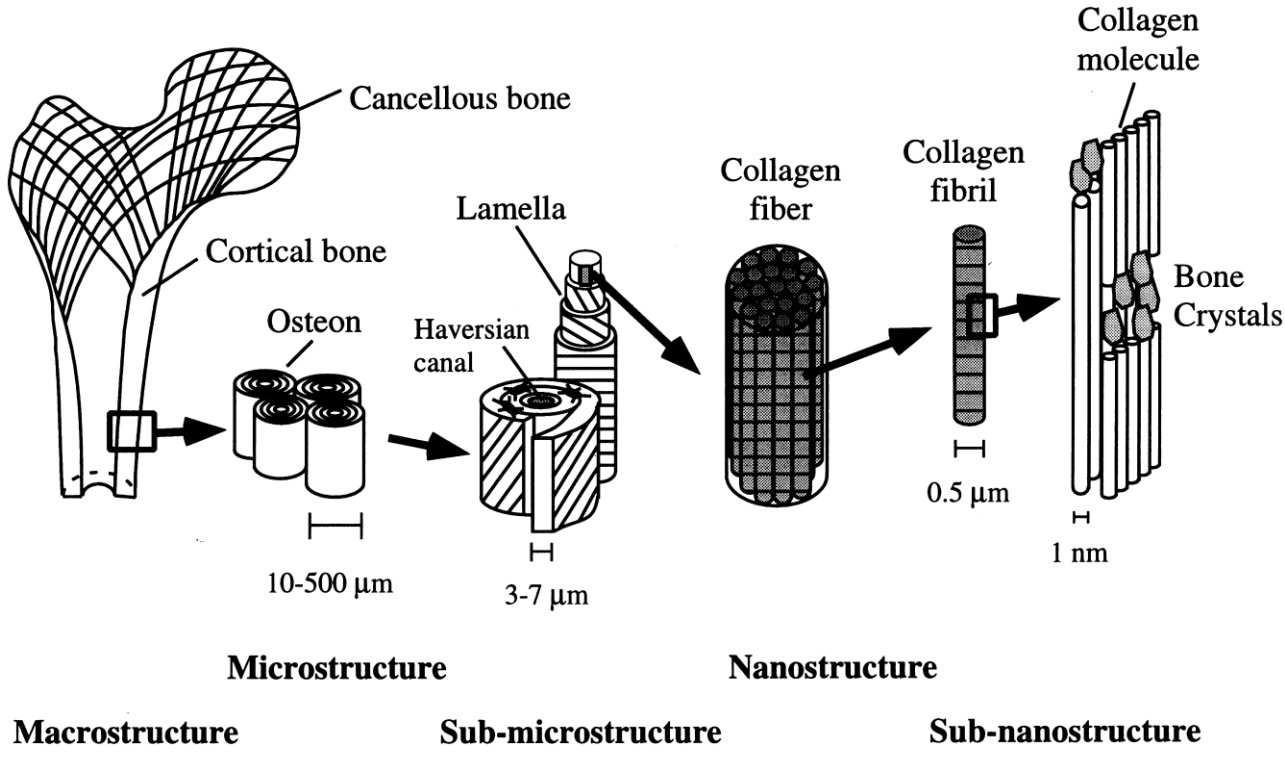

Fig. 1.3 – Hierarchical structure of cortical bone (Rho et al., 1998).

1.3 - Fracture in bone

Cortical bovine bone tissue is an orthotropic material presenting three material directions (Fig. 1.4a): longitudinal (L), radial (R) and tangential (T). In this thesis, a special attention has been given to the TL fracture propagation system (the first letter identifies the normal

direction to the crack plane, while the second specifies the direction of crack propagation) of bovine cortical bone.

The first works dedicated to fracture characterization of bone were based on Linear Elastic Fracture Mechanics (LEFM) approaches and were focused on the evaluation of the critical stress intensity factor or the critical energy release rate (Norman et al., 1995, 1996). The majority of the works have been dedicated to determination of the resistance to pre-crack starting advance under tension (Mode I loading), both in the longitudinal (Norman et al., 1995, 1996) and transverse (Phelps et al., 2000) axes of long bones. For the fracture characterization of bone under mode I loading many experimental tests have been applied (Fig. 1.4). Melvin and Evans, (1973) were the first researchers who performed fracture tests in cortical bone using the Compact Tension test (CT) which, in fact, is the most commonly used test (Fig. 1.4b) (Akkus et al., 2000; Brown et al., 2000; Koester et al., 2011; Nalla et al., 2003, 2004; Norman et al., 1995, 1996; Vashishth et al., 1997; Zioupos and Currey, 1998; Feng et al.. 2000). However, other tests have been applied in the context of mode I fracture characterization of cortical bone, as is the case of the Single-Layer Compact Sandwich (SLCS) (Fig. 1.4c) (Wang and Agrawal, 1996; Wang et al., 1998; Phelps et al., 2000), the Double Cantilever Beam (DCB) (Fig. 1.4d) (Morais et al., 2010; Pereira et al., 2012), the Single Edge Notched Beam (SENB) (Fig. 1.4e) (Phelps et al., 2000; Lucksanasombool et al., 2001; Yan et al., 2007; Li et al., 2013), the Chevron Notched Beam (CNB) (Fig. 1.4f) (Yan et al., 2006, 2008; Zioupos and Currey, 1998), the Chevron Notched Tension (CNT) (Fig. 1.4g) (De Santis et al., 2000).

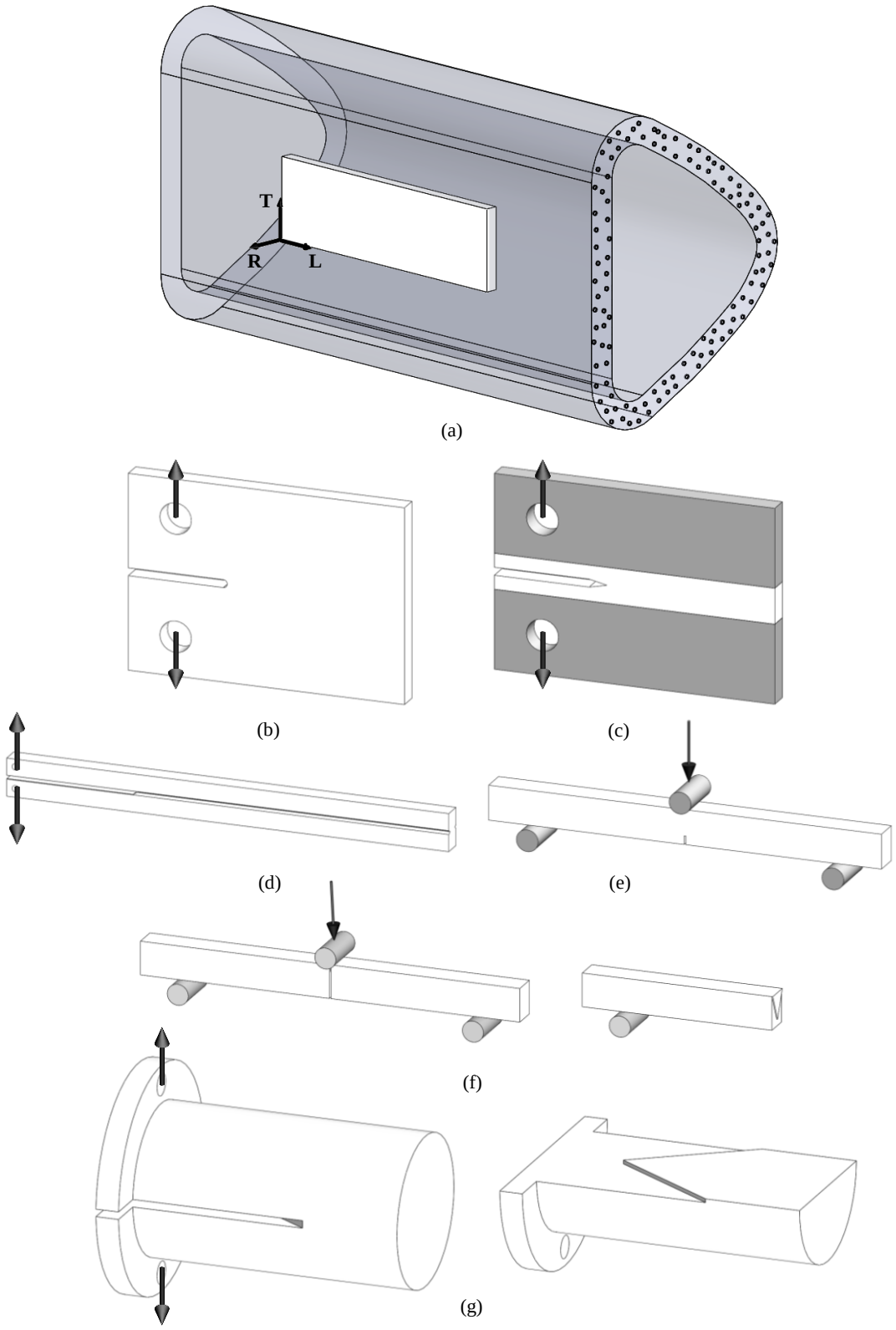

Fig. 1.4 – Cortical bone fracture tests performed under mode I loading: (a) Schematic representation of a long bone showing the axes of bone and the orientation of the specimens (L: longitudinal; R: radial; T: Tangential); (b) Compact Tension (CT); (c) Single-Layer Compact Sandwich (SLCS); (d) Double Cantilever Beam (DCB); (e) Single Edge Notched Beam (SENB); (f) Chevron-Notched Beam (CNB) (g) Chevron Notched Tension (CNT) (Higher specimen dimension correspond to longitudinal direction).

A wide range of critical stress intensity factors or critical energy release rates for cortical bone has been reported in the literature, for the very reason that they vary depending on the source, type and location of tested bone, as well as the experimental method (Brown et al., 2000; Yan et al., 2006). Table 1.1 shows some results obtained for cortical bone.

Table 1.1 – Cortical bone fracture properties for pure mode I loading found in the literature for the TL fracture propagation system.

Authors	Test	Bone	K_{Ic} (MN m$^{-3/2}$)	G_{Ic} (N/mm)
(Melvin and Evans, 1973)	SENB	Bovine femur	3.21± 0.43	1.39 – 2.56
(Wright and Hayes, 1977)	CT	Bovine femur	3.0-3.95	0.82 – 1.52
(Behiri and Bonfield, 1984)	CT	Bovine tibia	2.8 – 6.3	0.63 – 2.88
(Norman et al., 1992)	CT	Human femur	2.2 – 5.7	0.35 – 0.90
(Norman et al., 1995)	CT	Bovine tibia	6.29 – 6.73	0.90 – 0.99
		Human tibia	4.05 – 4.32	0.60 – 0.83
(Brown et al., 2000)	CT	Human femur	*	0.71 ± 0.29
		Human tibia	*	0.82 ± 0.33
(Phelps et al., 2000)	SCS	Baboon femur	1.76 ± 0.48	*
(Feng et al., 2000)	CT	Bovine femur	3.0 ± 0.24	0.64 ± 0.10
(De Santis et al., 2000)	CNT	Bovine femur	4.87± 0.5	*
(Lucksanasombool et al., 2001)	SENB	Bovine femur	2.30 ± 0.27	0.40 ± 0.71
(Yan et al., 2007)	SENB	Bovine femur	3.0 – 2.4/ 2.6±0.3	*
(Morais et al., 2010)	DCB	Bovine femur	*	1.91 ± 0.30
(Pereira et al., 2012)	DCB	Bovine femur	*	1.77 ± 0.35

Most of the results presented in Table 1.1 were obtained using LEFM concepts to characterize the fracture behaviour of cortical bone, although it is clear that this approach provides a limited insight into fracture behaviour of cortical bone. In fact, as a consequence of its composition and microstructure, several toughening mechanisms have been observed in the fracture of cortical bone, such as diffuse micro cracking, crack deflection and fibre bridging (Nalla et al., 2003; Vashishth et al., 2000; Yang et al., 2006; Yeni and Norman, 2000). These toughening mechanisms are responsible for the development of the so-called *Resistance* curve (*R*-curve) behaviour observed by several researchers (Malik et al., 2003; Nalla et al., 2004; Vashishth, 2004). This fact, allied to the size scale phenomena involved in fracture testing of cortical bone renders the pure LEFM theory inexact when applied to this material (Lucksanasombool et al., 2001; Ural and Vashishth, 2006). In this context, the

use of nonlinear fracture mechanics based methods, as is the case of cohesive zone models, becomes essential for a valid fracture characterization.

Much less attention has been dedicated to mode II fracture in bone relative to mode I. The fundamental reasons are related to experimental difficulties namely the definition of an appropriate test method. However, fracture characterization under mode II acquires special relevance for different reasons. Effectively, fractures can occur under pure shear loading as is the case of twisting or torsion efforts during normal activities (Turner et al., 2001). Additionally, mixed-mode fracture involving mode I and mode II will prevail under general loading conditions. The first work characterizing the fracture process under pure mode II loading in cortical bone was presented by Norman et al. (1996), who have used the Compact Shear (CS) test (Fig. 1.5a), which consists on loading in shear an adapted version of the well-known Compact Tension test (CT). However, some difficulties were pointed to this test. One of them is the nearly insensitivity observed in the compliance as a function of crack length, which renders difficult the establishment of compliance calibration commonly used to estimate the material toughness. Additionally, both unstable crack propagation and a quite short ligament length hinder a correct evaluation of fracture energy under pure mode II loading (Pereira et al., 2011). Alternatively, Zimmermann et al. (2009, 2010) utilized the Asymmetric Four-Point Bending Test using Single Edge Notched specimens (SEN-AFPB) (Fig. 1.5b) to perform fracture characterization of bone under mixed-mode I+II loading. These authors observed that mode II loading is a particular case only achieved when the pre-crack is oriented along the centreline of the testing rig. In fact, in this situation the bending moment cancels out and a shear force is present. However, posterior numerical analyses of this test (Pereira et al., 2011) have shown that fracture process zone ahead of the crack tip is under mixed-mode I+II instead of the intended pure mode II, which leads to a monotonic increase of the *R*-curve as the crack grows. Recently, de Moura et al. (2011) performed a numerical analysis on the application of the End-Loaded Split (ELS) and End-Notched Flexure (ENF) (Fig.1.5(c-d)) tests to pure mode II fracture characterization of bone. The main concerns were related to specimen dimensions available in bone versus extensive fracture process zone that develops under pure mode II loading. Effectively, it must be guaranteed that self-similar crack growth occurs for a given crack extent in order to provide a valuable measurement of fracture energy. The authors have concluded that with a careful choice of specimen dimensions, both tests (i.e., ELS and ENF) can be used to measure pure mode II toughness in bone. More recently, the same authors (Pereira et al., 2011) carried out experimental ELS tests using bovine cortical bone and

confirmed the test adequacy for this purpose, although some negative aspects may be pointed. One of them is the variability of the clamping conditions which influences the measured toughness. Instead, the ENF test (Dourado et al. 2013) is very easy to perform and does not present the referred limitations, although it provides a smaller region for self-similar crack growth. In fact, the available distance is located between the crack tip and the compressive zone in the vicinity of the applied load, which can be insufficient in small specimens as is the case of the ones obtained in bone.

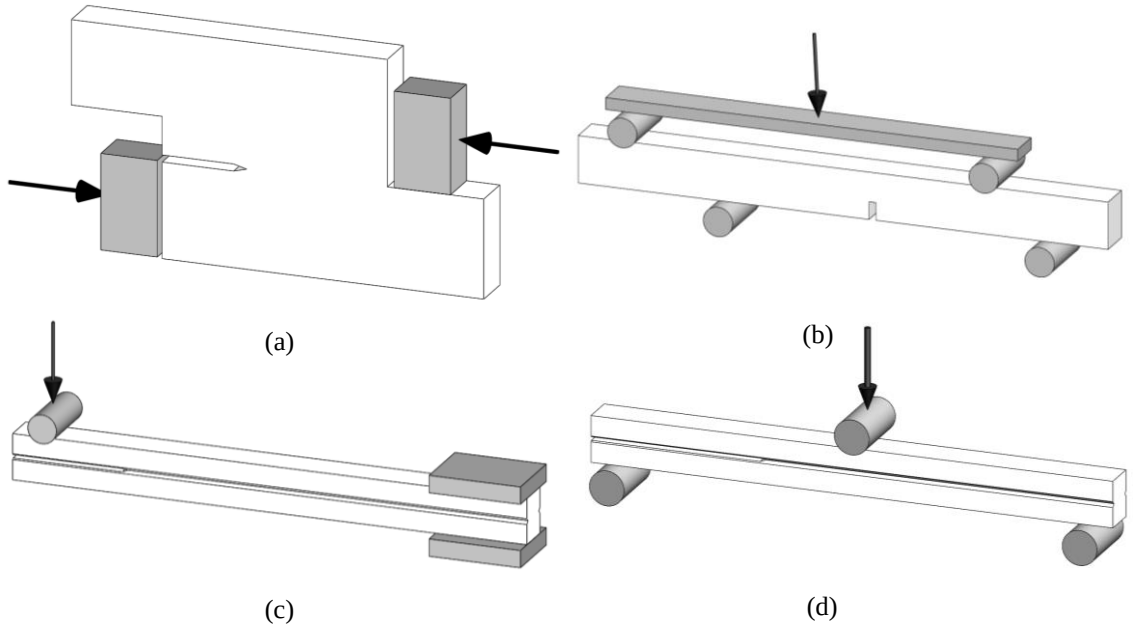

Fig. 1.5 – Cortical bone fracture tests performed in mode II: (a) Compact Shear (CS); (b) Single Edge Notched Asymmetric Four-Point Bending (SEN-AFPB); (c) End-Loaded Split (ELS) (d) End-Notched Flexure (ENF) (All the specimens are orientated in longitudinal direction of bone).

It is well know that fracture in bone rarely occurs under pure mode loading (I, II or III) conditions, being instead submitted to a complex stress state that corresponds to mixed-mode loading. In light of this, the knowledge of cortical bone fracture behaviour under these circumstances is very important. Only few works have addressed this issue so far. George and Vashishth (2006) have studied the combined effect of axial-torsion fatigue loading on fracture of human bone from donors of different ages. The authors concluded that uniaxial testing of materials subjected to multiaxial stresses provides a non-conservative estimate of fatigue life by a factor of twenty, since multiaxial loading forwards mixed-mode failure. The authors observed that micro-cracks form in mode I and propagate in mode II or mode III. Zimmermann et al. (2010) attempted to measure the *R*-curve of

human cortical bone under physiologically relevant mixed-mode I+II loading conditions based on stress intensity factors or, shorter, *K*-factor (i.e., K_I, K_{II} and K_{III}) generated at the crack tip. These authors used the Single Edge Notched Asymmetric Four-Point Bending (SEN-AFPB) test, but some difficulties related to crack deflection and continuous rise of *R*-curve were pointed. This later phenomenon is probably due to spurious effect related to confinement of non-negligible FPZ by means of compressive stresses developed ahead of crack tip induced by bending. In fact, the useful dimension for the development of a fracture process zone is defined by the crack tip and half-length of the specimen which could be insufficient. Olvera et al. (2012) used a Double Cleavage Drilled Compression (DCDC) (Fig. 1.6a) test geometry, which axially loads a sample containing a longitudinal crack in applied far-field compression (in the vicinity of the hole). The mixed-mode ratio variation is achieved by the modification of the position of the hole. Based on the success of the ENF test, Pereira et al. (2014) have used a similar test but for mixed mode I+II, called the Single Leg Bending (SLB) test (Fig.1.6b). This test presents an inconvenient related to difficult variation of the mode ratio. Effectively, using specimen arms of equal height the SLB test only provides fracture characterization for a given constant mode ratio. However, in cortical bone the consideration of different specimen arms is unfeasible since premature failure of the thinner specimen arm takes place. Anyway, this test is very easy to perform and propitiates a very good initial approach to the fracture characterization under mixed-mode I+II conditions. Using a partition mode methodology, Pereira et al. (2014) obtained the *R*-curves for both components of strain energy release rate (i.e., mode I and mode II).

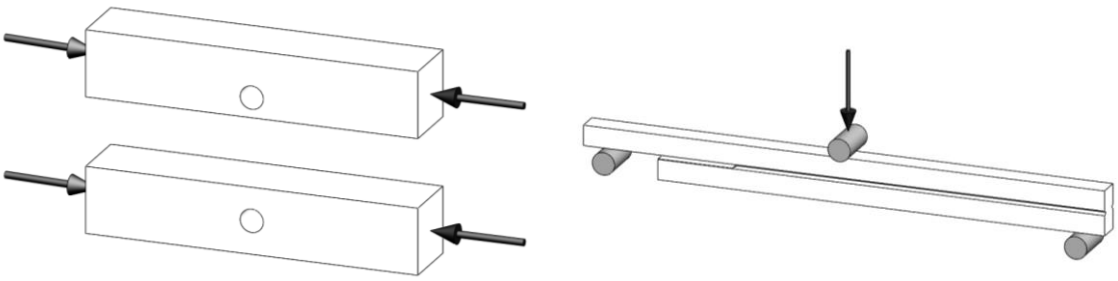

(a) (b)

Fig. 1.6 – Cortical bone fracture tests performed in mode I: (a) Double Cleavage Drilled Compression (DCDC); (b) Single Leg Bending (SLB) (All the specimens are orientated in longitudinal direction of bone).

1.4 - Cohesive zone models

In this section a brief overview of cohesive zone models (CZM) is given. These models are based on the simple idea of a softening relationship between stresses (σ_I in Fig. 1.7) and crack opening displacements. Cohesive zone models can be applied to fracture processes where debonding is localized in a narrow band leading to a strip-shaped process zone. Examples of their fields of application are metals, polymers, ceramics, concrete, fibre reinforced materials, wood, rock, glass, bonded joints and others. The first cohesive zone model was proposed by Barenblatt (1959) for the description of perfect brittle fracture of a linear elastic body. The same author published later a more complete work on this issue (Barenblatt, 1962). However, the history puts on the same level of importance the work of Dugdale (1960), who introduced a strip yield model with the idea of a cohesive strength preventing a crack from extending. The magnitude of this cohesive strength is equal to the yield strength of the material. The strain hardening is not considered since the material is supposed to behave in an elastic-ideally plastic manner. As the local stress is limited by the yield strength of the material, the occurrence of a physically unrealistic singularity at the crack tip is avoided (Fig. 1.7).

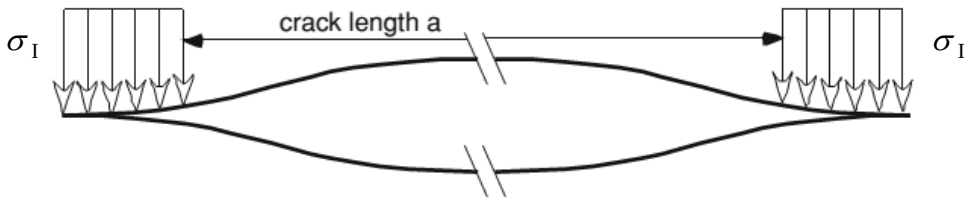

Fig. 1.7 – Dugdale model (Schwalbe et al. 2012).

Cohesive models in their present form date back to the work of Barenblatt (1962), who replaced the yield strength by a cohesive law to model the de-cohesion of atomic lattices. This author considered a zone ahead of the crack tip (cohesive zone) with length d^{coh}, in a contour where the separation of the crack faces takes place (Fig. 1.8a). Along the distance d^{coh} intermolecular cohesive stresses σ^{coh} are present. The relation between the stresses, σ^{coh}, and the crack opening displacement, w, define the so-called cohesive law (Fig. 1.8b).

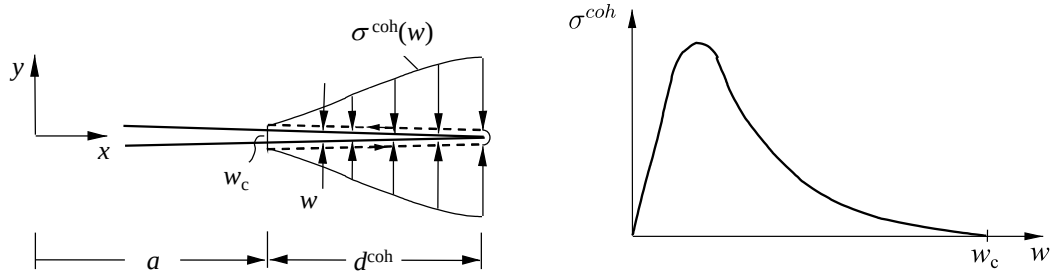

(a) (b)

Fig. 1.8 – Barenblatt model (Gross and Seelig, 2007).

The Barenblatt model is based on three assumptions:

1. The cohesive zone is small compared with all other dimensions, i.e., $d^{\text{coh}} << a$;
2. The distribution of the crack opening displacement, w, and cohesive stress, σ^{coh}, in the cohesive zone is, for a given material, always the same and independent of the external load;
3. The opposite crack faces smoothly join each other at the end of the cohesive zone.

The last condition is equivalent to the requirement of a vanishing stress intensity factor at the fictitious crack tip, i.e., the stresses remain finite everywhere. This can be expressed as $K_{\text{I}} + K_I^{coh} = 0$, where K_{I} and K_I^{coh} are the K-factors due to the external load and due to the cohesive stresses, respectively. Considering a plate with a notch at the free-edge submitted to the loading conditions represented in Fig. 1.9 (P and Q stand for normal and tangential loads, respectively), the respective K-factors (Gross and Seelig, 2007), K_I^{coh} can be written as,

$$\begin{Bmatrix} K_{\text{I}} \\ K_{\text{II}} \end{Bmatrix} = \begin{Bmatrix} P \\ Q \end{Bmatrix} \frac{2}{\sqrt{2\pi a}} \tag{1.1}$$

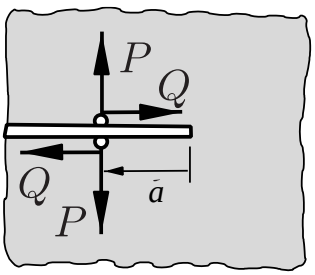

Fig. 1.9 – Free-edge notched plate under shear and normal loading (Gross and Seelig, 2007).

$$K_{\mathrm{I}}^{coh} = -\frac{\sqrt{2}}{\sqrt{\pi}} T \text{ , with } T = \int_{a}^{a+d} \frac{\sigma^{coh}(x)}{\sqrt{x}} dx \tag{1.2}$$

where T is the cohesive modulus introduced by Barenblatt, which can be regarded as a measure of the state of the process zone. Since $d^{\mathrm{coh}} << a$, as stated by Barenblatt, the K-factors $K_{\mathrm{I}}(a)$ and $K_{\mathrm{I}}(a+ d^{\mathrm{coh}})$ due to the external load are equal, which leads $K_{\mathrm{I}} + K_I^{coh} = 0$, to the simple relation

$$T = \frac{\sqrt{\pi}}{\sqrt{2}} K_{\mathrm{I}} \tag{1.3}$$

Therefore, the failure concept based on Barenblatt's cohesive modulus ($T = T_{\mathrm{c}}$) and the K-concept ($K_{\mathrm{I}} = K_{\mathrm{Ic}}$) are equivalent. The equivalence to Griffith's energy release rate can be established using the J-integral approach where, as in Dugdale model, the contour C is chosen along the crack faces of the cohesive zone. This leads to

$$J = -\int_{a}^{a+d} \sigma^{coh}(x) \frac{d}{dx} \left| \delta^{\mathrm{sup}} - \delta^{bot} \right| dx = -\int_{a}^{a+d} \sigma^{coh}(x) \frac{dw}{dx} dx = \int_{o}^{w} \sigma^{coh}(w^*) dw^* \tag{1.4}$$

where w is the crack opening displacement and δ^{sup}, δ^{bot} refer to displacements of the superior and bottom crack faces. Since a small cohesive zone is assumed, $J=G$ and the energy release rate is uniquely given by the area below $\sigma^{\mathrm{coh}}(w)$ curve. The critical energy release rate is calculated substituting w by w_{c} (Fig.1.8b) in the last integral.

In contrast to Barenblatt model for brittle fracture the length of the cohesive zone is not small in many other fracture processes. For materials with an elastic-plastic or viscoelastic behaviour the first assumption made by Barenblatt is not valid. In fact, as schematically represented in Fig. 1.10 the fracture process zone for different materials may be quite significant. This region is generally characterized by development of bridges between the crack faces which transfer the cohesive forces. Their dependence on the crack opening displacement w is expressed by a material specific cohesive law, $\sigma(w)$. The cohesive law describes the local constitutive behaviour inside the cohesive zone in terms of a traction-separation relation. Taking into account the microscopic fracture processes, this constitutive law differs considerably from that of the surrounding material (Gross and Seelig, 2007).

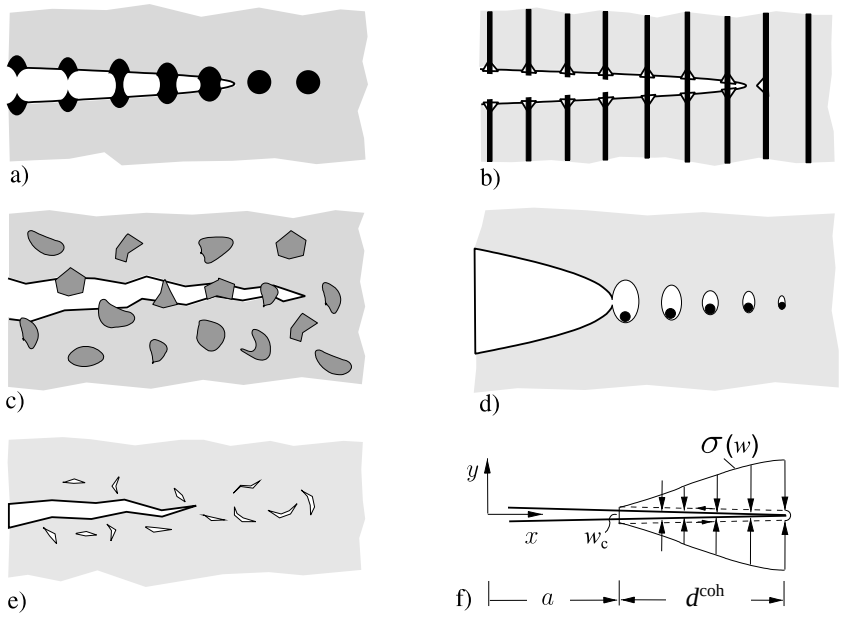

Fig. 1.10 – Cohesive zones (schematic): a) metal-particle reinforced ceramics; b) fibre-matrix composite; c) heterogeneous ceramics, concrete; d) ductile material with void formation; e) brittle material with micro-cracks; f) cohesive zone model adapted from (Gross and Seelig, 2007).

Since the cohesive law describes the stress crack opening displacement relation, an alteration on this relation allows the reproduction of different fracture behaviour (Fig. 1.11).

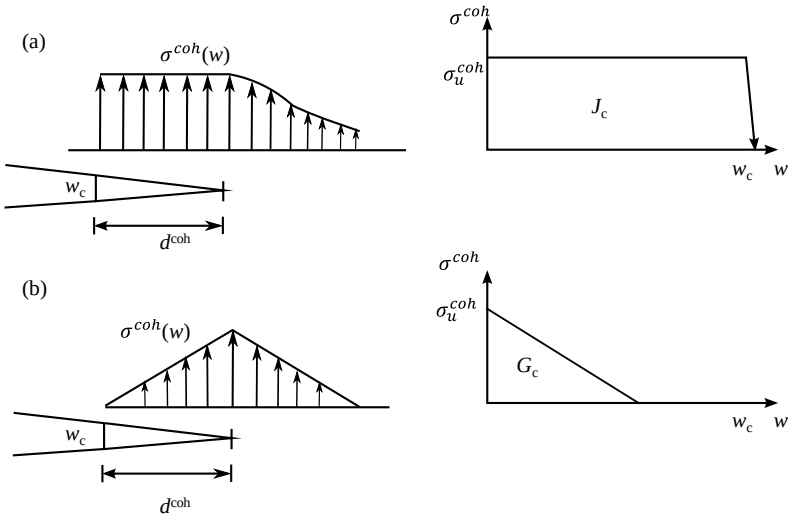

Fig. 1.11 – Stress distributions and softening curves: (a) ductile-brittle metal, (b) quasi-brittle concrete (adapted from Bažant, 2002).

This capacity of adaptation of cohesive models extended their application to a large number of materials. The first work applying cohesive models to the fracture behaviour of materials was performed by Hillerborg et al. (1976). This author used cohesive models in a finite element analysis to describe the damage behaviour of concrete.

Other pioneer works were realized by Needleman (1987) and Tvergaard and Hutchinson (1992). Needleman (1987) is responsible for the first analysis of micro-damage in ductile materials (particle debonding from a ductile matrix) and Tvergaard and Hutchinson (1992) made the first macroscopic crack extension analysis in ductile materials. Figure 1.12 illustrates different cohesive laws that have been used by several authors.

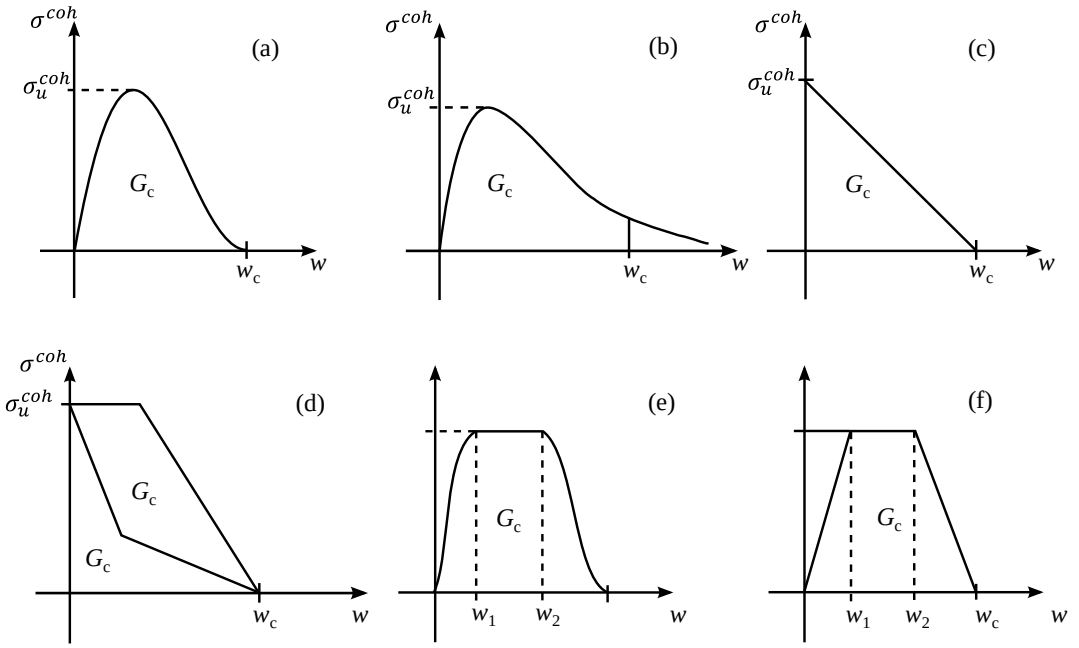

Fig. 1.12 – Typical traction–separation laws: (a) (Needleman, 1987), (b) Needleman, (1990), (c) Hillerborg et al., (1976), (d) Bažant, (2002),(e) Scheider and Brocks, (2003), (f) Tvergaard and Hutchinson, (1992).

The concepts described above were initially developed considering pure loading modes (I or II). However, these models can also be used in the context of mixed-mode loading conditions, being the mixed-mode I+II the most frequent case. The mixed-mode models are usually an extension of the pure mode ones referred above considering different ways to combine the loading modes. Two approaches can be used for the definition of cohesive laws under mixed-mode (e.g., I+II) fracture loading: uncoupled and coupled models. The uncoupled method (Kafkalidis and Thouless 2002) is based on the assumption that the stress-crack opening relation in mode I is independent of the crack opening in mode II and vice-versa,

$$\sigma_i = \sigma_i(w_i) \quad (i\text{=I, II}) \tag{1.5}$$

Alternatively, the coupled approach (Sørensen and Kirkegaard, 2006) assumes that the cohesive stresses depend both on the normal (w_{I}) and tangential crack opening displacement (w_{II}).

$$\sigma_i = \sigma_i(w_{\mathrm{I}}, w_{\mathrm{II}}) \quad (i=\mathrm{I},\ \mathrm{II}) \tag{1.6}$$

Both methods will be applied in this work, thus being detailed later in Chapters 4 and 5.

1.5 - Application of cohesive zone models to bone

In this thesis the concept of cohesive law allied to finite element analysis has been applied in the context to cortical bone fracture. Cohesive elements can be used for the simulation of damage development and crack propagation in bone being essential for the sake of validation of some proposed procedures. These analyses can be useful in the framework of systematic studies involving the influence of several parameters (e.g., age, drugs, diseases and others) on the resistance of bone to fracture. With this aim, the definition of the cohesive law, i.e., the constitutive relationship between stresses and the crack opening displacements characterizing bone fracture under different loading modes becomes a fundamental issue.

The first work using cohesive models to describe the fracture behaviour of cortical bone was presented by Ural and Vashishth (2006). The authors performed a finite element analysis of the CT specimens (Fig. 1.13) considering cohesive elements disposed along the crack path. The simplest linear cohesive law defined by the ultimate strength σ_{u} and the fracture energy G_{c} was used. The authors concluded that the numerical simulations can predict the experimental *R*-curve behaviour, which was managed in order to relate it with age.

Yang et al. (2006) and Cox and Yang (2007) analysed the validity of the LEFM to deal with the fracture process in cortical bone. The authors also proposed a model based on cohesive elements to reproduce the non-linear behaviour observed in bone data. A bilinear softening cohesive law (Fig. 1.14) was assumed to distinguish different damage mechanisms: the first descending branch of this law intends to describe damage development at the crack tip (micro-cracking), although the second one depicts the fracture phenomenon in the further crack wake (fibre-bridging). The numerical load-displacement curves were manually fitted to the experimental results from other works in order to determine the parameters of the cohesive law. It was inferred that LEFM is not appropriate for cortical bone fracture characterization.

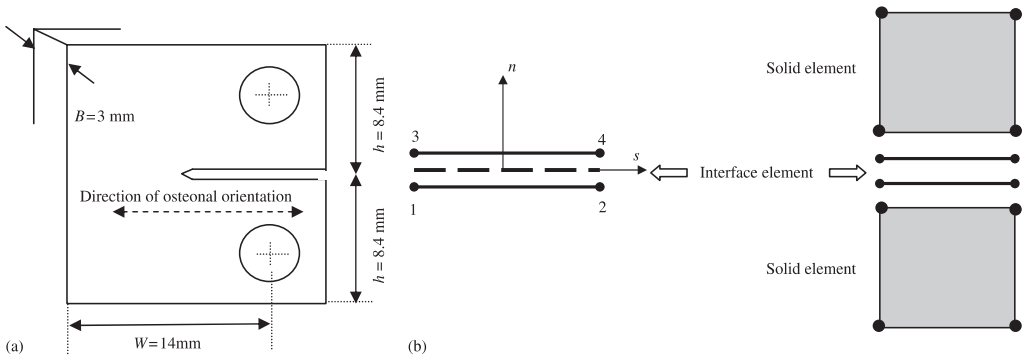

Fig. 1.13 – (a) CT specimen for fracture toughness testing of human cortical bone. (b) Schematics of 2D, 4-noded cohesive element and its compatibility with solid elements. Note that the *n* and *s* axes denote the normal and tangential displacements of the cohesive element, respectively (Ural and Vashishth, 2006).

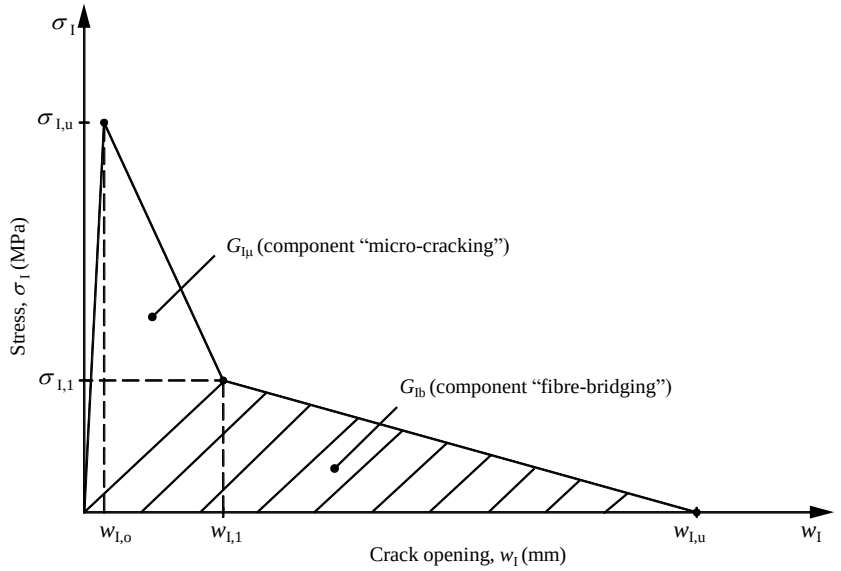

Fig. 1.14 – Softening bilinear cohesive law (Pereira et al., 2012).

Morais et al. (2010) identified the cohesive law parameters on a trial and error basis fitting the numerical load-displacement curve to each experimental one (objective function) obtained from DCB tests. They use the mode I fracture energy, G_{Ic}, determined experimentally and the fitting procedure was achieved changing the ultimate stress value. Another work applying the DCB test was performed by Pereira et al. (2012) considering the same objective function and using a developed genetic algorithm integrated in an inverse strategy. This procedure was able to identify the four parameters used to define the bilinear cohesive law. The algorithm was able to distinguish two different types of laws for the hydrated and dehydrated young bovine bone. However, the large number of iterations required by the algorithm to identify the global optimum solution suggests that a more efficient optimization method should be developed.

The capability of the cohesive elements to reproduce the behaviour of cortical bone under pure mode II was evaluated by Pereira et al. (2011) and Dourado et al. (2013). In the first work, the linear cohesive law was used to validate the proposed data reduction scheme based on equivalent crack concept. In the second, Dourado et al. (2013) identified the parameters of a trapezoidal cohesive law that provide a better agreement between the numerical and experimental load-displacement curves. However, the inverse method based procedure presents two drawbacks: the identification process requires a previous definition of the cohesive law shape and the non-unicity of the solution can be pointed in many cases. In light of this, the development of direct methods apt to identify the cohesive law is an important topic. These methods are based on the local measurement of the crack opening displacement during the test by different processes. Some works have already identified experimentally the relation between the stresses and the crack opening displacements. Sørensen (2002) determined experimentally the cohesive law by differentiation of a second order polynomial that was fitted to the experimental *J*-integral versus crack opening displacement relation. Many other methodologies have been proposed by several authors (Andersson and Biel, 2006; de Moura et al., 2012; Silva et al., 2013). However, the fitting operation required to establish the relationship between the strain energy release rate and the crack opening displacement (COD) can mask the natural scatter of the material and in some cases imposes a shape for the cohesive law.

1.6 - Cohesive mixed-mode I+II damage model

The proposed mixed-mode I+II cohesive zone model used in this work combines the two mode loading modes (I and II) through equivalent crack opening displacement values $w_m = \sqrt{w_I^2 + w_{II}^2}$ and mode ratio $\beta = w_{II} / w_I$. The cohesive law is based on stepwise softening relationship between stresses (σ_m) and equivalent crack opening displacements (w_m). Before damage onset $\sigma_m = k w_m$ where k is the interfacial stiffness. After damage onset the softening relationship is described by $\sigma_m = (1-d_m) k w_m$, being d_m the damage parameter ranging between zero and one. A stepwise softening law with several branches was used to replicate with accuracy the fracture behaviour of cortical bone. The crack opening displacements and stresses at the inflection points (j=2, 3,…n) (Fig. 1.15) are obtained considering the following stress criterion

$$\left(\frac{\sigma_{\mathrm{I}}}{\sigma_{j,\mathrm{I}}}\right)^{2\alpha}+\left(\frac{\sigma_{\mathrm{II}}}{\sigma_{j,\mathrm{II}}}\right)^{2\alpha}=1 \quad \text{if} \quad \sigma_{\mathrm{I}}>0$$
$$\sigma_{j\mathrm{m,II}}=\sigma_{j,\mathrm{II}} \quad \text{if} \quad \sigma_{\mathrm{I}}\le 0 \tag{1.7}$$

where $\sigma_{j\mathrm{m},i}$ and $\sigma_{j,i}$ with $(i=\mathrm{I,\ II})$ are the stress components of the mixed-mode I+II loading and the corresponding stress limit value in pure mode, respectively, at the inflection point *j*. For the relative displacements a similar relation is used

$$\left(\frac{w_{\mathrm{I}}}{w_{j,\mathrm{I}}}\right)^{2\alpha}+\left(\frac{w_{\mathrm{II}}}{w_{j,\mathrm{II}}}\right)^{2\alpha}=1 \tag{1.8}$$

which leads to

$$\sigma_{j\mathrm{m}}=\frac{\sigma_{j,\mathrm{I}}\sigma_{j,\mathrm{II}}\sqrt{1+\beta^2}}{\sqrt[\alpha]{\sigma_{j,\mathrm{II}}^{2\alpha}+\beta^{2\alpha}\sigma_{j,\mathrm{I}}^{2\alpha}}} \quad \text{and} \quad \delta_{j\mathrm{m}}=\frac{\delta_{j,\mathrm{I}}\delta_{j,\mathrm{II}}\sqrt{1+\beta^2}}{\sqrt[\alpha]{\delta_{j,\mathrm{II}}^{2\alpha}+\beta^{2}\delta_{j,\mathrm{I}}^{2\alpha}}} \tag{1.9}$$

For damage onset (point 1 in Fig. 1.15) the same equations can be used considering α=1 thus leading to the well-known quadratic stress criterion.

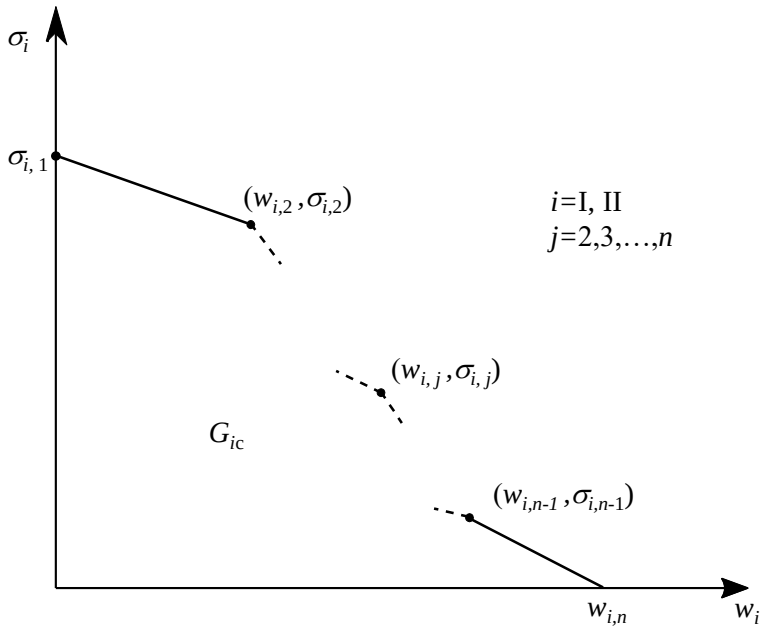

Fig. 1.15 – Stepwise cohesive law.

The power law energetic criterion

$$\left(\frac{G_{\mathrm{I}}}{G_{\mathrm{Ic}}}\right)^{\alpha}+\left(\frac{G_{\mathrm{II}}}{G_{\mathrm{IIc}}}\right)^{\alpha}=1 \tag{1.10}$$

was used in this numerical analysis to deal with damage propagation. Taking into consideration the relation between relative displacements and stresses, the strain energy release rates mode ratio becomes $G_{\mathrm{II}}/G_{\mathrm{I}}=\beta^2$, thus leading to

$$G_{\mathrm{T}}=G_{\mathrm{I}}+G_{\mathrm{II}}=G_{\mathrm{I}}\left(1+\beta^2\right)=\frac{G_{\mathrm{Ic}}G_{\mathrm{IIc}}\left(1+\beta^2\right)}{\sqrt[\alpha]{G_{\mathrm{IIc}}^{\alpha}+\beta^{2\alpha}G_{\mathrm{Ic}}^{\alpha}}} \tag{1.11}$$

Equating the total energy (G_{T}) to the area of the mixed-mode I+II stepwise softening law (Fig. 1.15) allows the determination of the ultimate relative displacement for $j=n$ in the following equation

$$G_{\mathrm{T}}=\sum_{j=2}^{n}\frac{(\sigma_{j\mathrm{m}}+\sigma_{(j-1)\mathrm{m}})(w_{j\mathrm{m}}-w_{(j-1)\mathrm{m}})}{2} \tag{1.12}$$

The expression of the damage parameter on the several branches can now be easily obtained equating the corresponding softening relation to $(1-d_{\mathrm{m}})k\delta_{\mathrm{m}}$ and solving each equation in order to d_{m}. This leads to the following relationship

$$d_{\mathrm{m}}=1-\frac{1}{kw_{\mathrm{m}}}\left[\frac{\sigma_{j\mathrm{m}}\left(w_{\mathrm{m}}-w_{(j-1)\mathrm{m}}\right)+\sigma_{(j-1)\mathrm{m}}\left(w_{j\mathrm{m}}-w_{\mathrm{m}}\right)}{w_{j\mathrm{m}}-w_{(j-1)\mathrm{m}}}\right] \text{ for } w_{(j-1)\mathrm{m}}\le w_{\mathrm{m}}\le w_{j\mathrm{m}} \tag{1.13}$$

Depending on the position of a given integration point in the cohesive law, damage progression is simulated differently according to different stages of damage evolution. This model is of general application and will be used in the several steps of this thesis assuming simplifications according to the laws considered in each loading case.

CHAPTER II

CHAPTER 2

Fracture behaviour of cortical bone under pure mode I loading

2.1 - Introduction

This Chapter presents the experimental and numerical work performed for fracture characterization of young bovine cortical bone under mode I loading conditions. The Double Cantilever Beam (DCB) test was used to identify the mode I fracture energy of bovine cortical bone. Additionally, the internal microstructure of each specimen was assessed by means of gravimetric analysis and porosity evaluation.

Cohesive laws characterizing the material fracture behaviour under mode I loading conditions were identified by two different methods. The direct method is obtained by the differentiation of the relation between the mode I strain energy release rate (G_I) and the mode I crack opening displacement (COD_I). On the other hand, the inverse method allies a finite element model with an optimization algorithm to estimate the corresponding cohesive law. In this case, the cohesive law is identified by a trial and error procedure based on varying the stress values of the inflection points of a totally unconstraint cohesive law composed by four branches. The advantages and drawbacks of each method are thoroughly discussed. It was verified that cohesive laws provided by both methods are in agreement revealing the consistency of the procedures.

2.2 - Material and specimens

Ten fresh bovine femora of young animals were acquired from a local slaughterhouse, within a one day post-mortem period. The sex of the animals was not known and the ages were about 8 months. A longitudinal-transverse section was dissected from the interior medial region of the mid-diaphysis of each femur (Fig. 2.1) and immediately cleaned and

wrapped in gauze containing a saline solution and frozen at -20 °C. Before any machining operation the section has been unfrozen at room temperature for a period not less than 2 hours. Due to bone orthotropy, three different material directions can be defined: the longitudinal (L) direction aligned with osteons, the radial (R) direction along thickness and the tangential (T) direction. As illustrated in Fig. 2.1, a diaphysis portion were cut from each femur in order to perform fracture characterization in the TL system, where the first letter identifies the direction perpendicular to the crack plane and the second one the crack propagation direction.

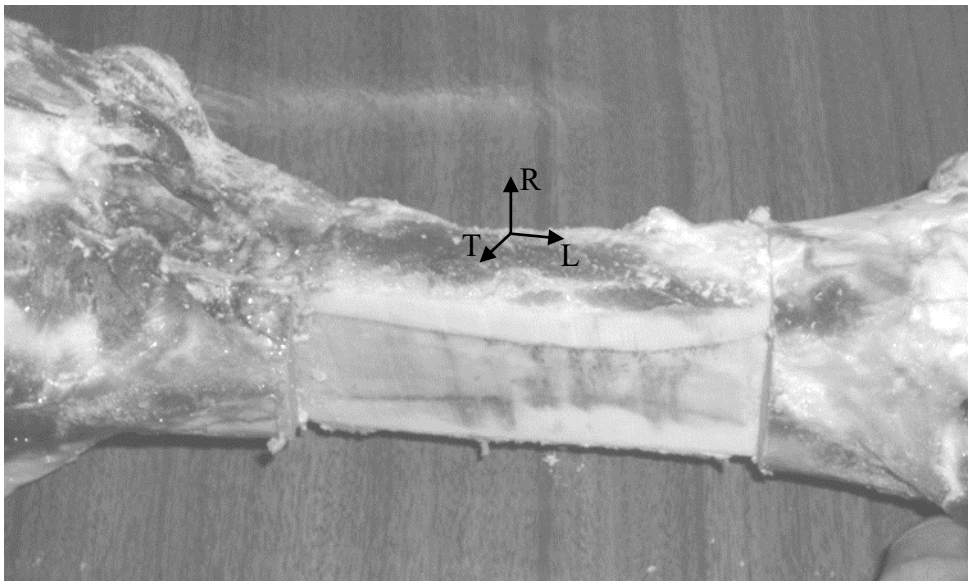

Fig. 2.1 - Aspect of bovine femur after harvesting of the diaphysis part to get specimens.

From these pieces a total of twenty DCB specimens (more or less 2 specimens from each part), with a length of approximately 60 mm and a thickness close to 2.5 mm, were cut using a milling machine (Fig. 2.2a). During this process, specimens were kept moist using a physiological saline solution and the endosteal and periosteal tissues were removed. Afterwards, a circular saw was used to cut the specimen to reach a width of about 6 mm (Fig. 2.2b).

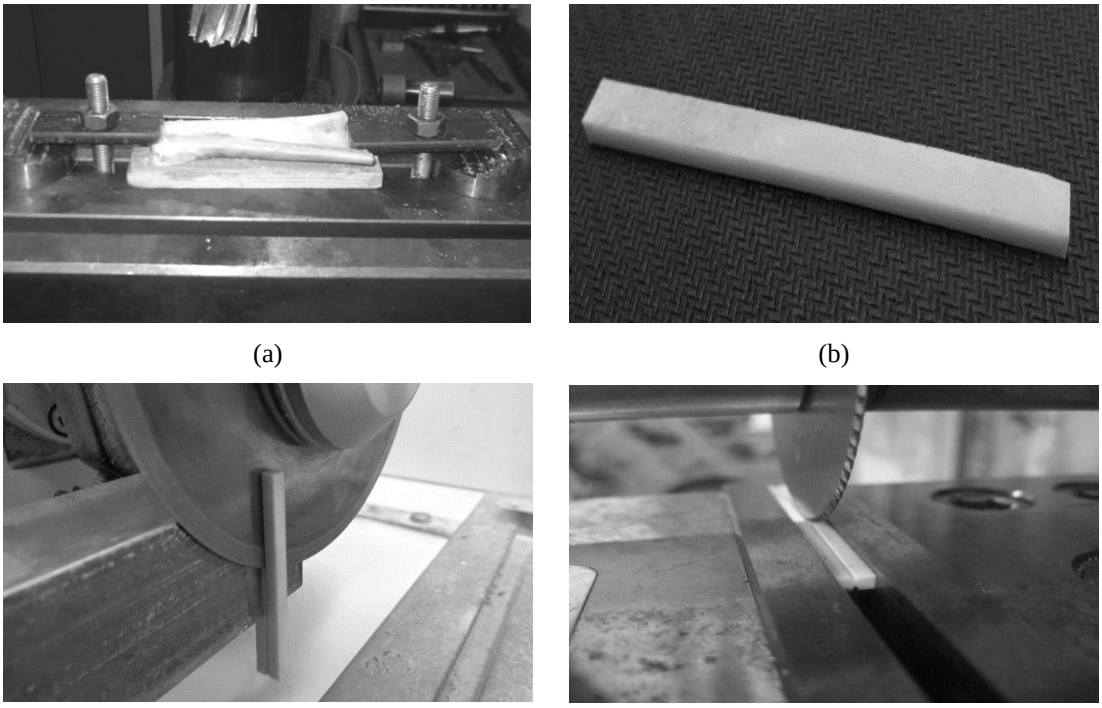

(a) (b)

(c) (d)

Fig. 2.2 – Machining operations: (a) milling; (b) specimen for three point bending test; (c) pre-crack execution; (d) creating lateral grooves.

The specimen was hydrated before performing three point bending tests (Fig. 2.3) to determine the longitudinal elastic modulus (E_L). The hydration process consists of immersing the specimens in physiological saline at 37°C during 24 hours till the mass equilibrium is reached. This process was executed more than one time during the experimental work. It will be repeated on gravimetric analysis and before any fracture tests, since the hydration level influences the fracture properties (Pereira et al., 2012).

Three point bending tests were performed in the same specimens used for fracture characterization using the DCB test, just before the execution of the pre-crack. They were executed in a servo-electrical testing system (Micro-Tester INSTRON® 5848) and the maximum displacement of the actuator was within the linear range of material response, thus preventing any damage of specimens. The longitudinal elastic modulus was determined considering the simple beam theory,

$$E_L = \frac{RL^3}{8hB^3} \tag{2.1}$$

being R the specimen stiffness, obtained from the initial slope of the load-displacement curve, and L, B and h geometrical variables (Fig. 2.3) that are compatible with notation

used in fracture tests. The average apparent longitudinal elastic modulus was E_L=18.01 GPa, whose value is within the normal range obtained for this property: 18.40 GPa (Currey et al., 1995); 19.94 GPa (Morais et al., 2010); 18.3 GPa (Pereira et al., 2011).

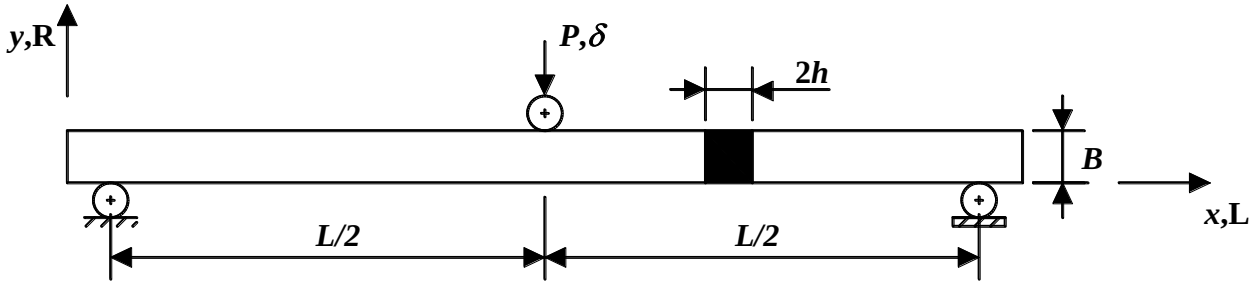

Fig. 2.3 – Geometry of the three point bending test specimen.

The next step was the execution of the pre-crack, a_0. Hence, an initial notch was introduced using a circular diamond saw with a thickness of 0.3 mm (Fig. 2.2c). In order to assure the crack propagation along the specimen mid-plane two longitudinal grooves with 0.5 mm depth were manufactured using a cutting blade with a V-tip (30°) configuration (Fig. 2.2d). This procedure avoids premature deviation of crack from its initial mid-plane, which precludes a pure mode I fracture characterization.

Immediately after the fracture mechanical tests, two samples were cut from each specimen for gravimetric and microstructural analyses of the tissue. Samples were then cleaned using an ultrasonic machine (Transsonic 660/H from Elma) during 15 minutes. These analyses were performed with two main objectives: the first one aims to find a relation between the fracture properties and any microstructural characteristic and the second one is to provide a comparison between the groups of specimens of each fracture tests. Afterwards, the samples used for gravimetric analysis were submitted to a rehydration process in order to determine the hydrated weight (W_h). Subsequently, a dehydration process was also performed to obtain the dehydrated weight (W_d). The dehydrating procedure consisted of placing the specimens in a vacuum oven containing desiccant during 24 hours at 37°C. A furnace was then used to burn the bone at 600 °C for 4 hours to evaluate the mineral content of bone which corresponds to the ash weight (W_a). The mass fractions of the mineral, organic, and aqueous phases were then calculated in a wet basis, using the following equations,

$$m_{\mathrm{w}} = \frac{W_{\mathrm{h}} - W_{\mathrm{d}}}{W_{\mathrm{h}}} \times 100 \text{, water mass fraction} \tag{2.2}$$

$$m_{\mathrm{o}} = \frac{W_{\mathrm{d}} - W_{\mathrm{a}}}{W_{\mathrm{a}}} \times 100 \text{, organic mass fraction} \tag{2.3}$$

$$m_{m} = \frac{W_{a}}{W_{h}} \times 100 \text{, mineral mass fraction} \tag{2.4}$$

The average mass fraction results (m_{m} =63.6%, m_{o} =24.1% and m_{w} =12.3%) are listed in Table 2.5. Morais et al. (2010) have obtained the mineral, organic and water mass fractions equal to 62.0%, 28.1% and 9.9%, respectively, for this very material. On the other hand, Pereira et al. (2012) have gotten 70.2%, 18.7% and 11.6%. The differences between the values determined in the cited works are associated to the applied technique. Morais et al. (2010) applied a gravimetric method similar to the one used in this work, although Pereira et al. (2012) have used a thermogravimetric analysis. It can be concluded that the present results are within the range of values of previous works. Comparing directly the actual results with the ones obtained by Morais et al. (2010), a slight difference between the organic and water mass fractions can be observed, probably due to a more effective dehydration process in this work.

The apparent density of the hydrated samples was also evaluated in this work. The volume of the samples was determined by using the Archimedes principle (Eq. 2.5), by immersing the samples in distilled water (Fig. 2.4). Hence,

$$V_{\mathrm{w}} = \frac{W_{\mathrm{S}}}{\rho_{\mathrm{w}}} \tag{2.5}$$

where W_{S}, stands for the submerged weight of the displaced water and ρ_{w} the density of the distilled water. The apparent density of the samples was then calculated as follows,

$$d_{\mathrm{h}} = \frac{W_{\mathrm{h}}}{V_{\mathrm{w}}} \tag{2.6}$$

The average apparent density (d_{h}=1.86 g/cm^3) is in agreement with the results found in literature: 2.05 g/cm^3 (Yan et al. 2008); 1.92-1.97 g/cm^3 (Sobelman et al. 2004); and 1.98 g/cm^3 Pereira, 2009). The values for the whole samples can be found in Table 2.5.

Fig. 2.4 – Determination of submerged weight.

The porosity of the specimens was measured by means of image processing analysis. The second sample extracted from the fracture test was used for that purpose. An optical microscope coupled with an 8 bit CCD Dolphin camera (Allied Vision Technologies) has been used to capture the images. In order to assure a good image quality, the samples were ground using progressively finer grades of SiC paper and lastly polished with 1 μm diamond suspension embedded in soft polishing cloth. For the image processing a MatLab® routine has been created. According to this routine the image $f(x,y)$ (Fig. 2.4a) is initially loaded by the software and then filtered using *thresholding* technique. The achieved binary image (Fig. 2.4b), $g(x,y)$ is created according to the following expression

$$g(x,y)=\begin{cases}1 \text{ if } f(x,y)\geq T\\ 0 \text{ if } f(x,y)<T\end{cases} \tag{2.7}$$

where T represents the grey level that has been chosen, for image segmentation. Then, a criterion of minimum area was used in order to ignore the canaliculi and lacuna visible in the resulting images (Fig. 2.4c), to get porosity measurements. The vascular porosity (i.e., the volume fraction of Harvesian canals and resorption cavities) was then estimated from the percentage of white area on the processed binary images (Fig. 2.4d). The results can be consulted in Table 2.5. The average value of vascular porosity (around 4.2%) is in

agreement with typical values found in literature (Morais et al., 2010; Phelps et al., 2000; Wang et al., 1998).

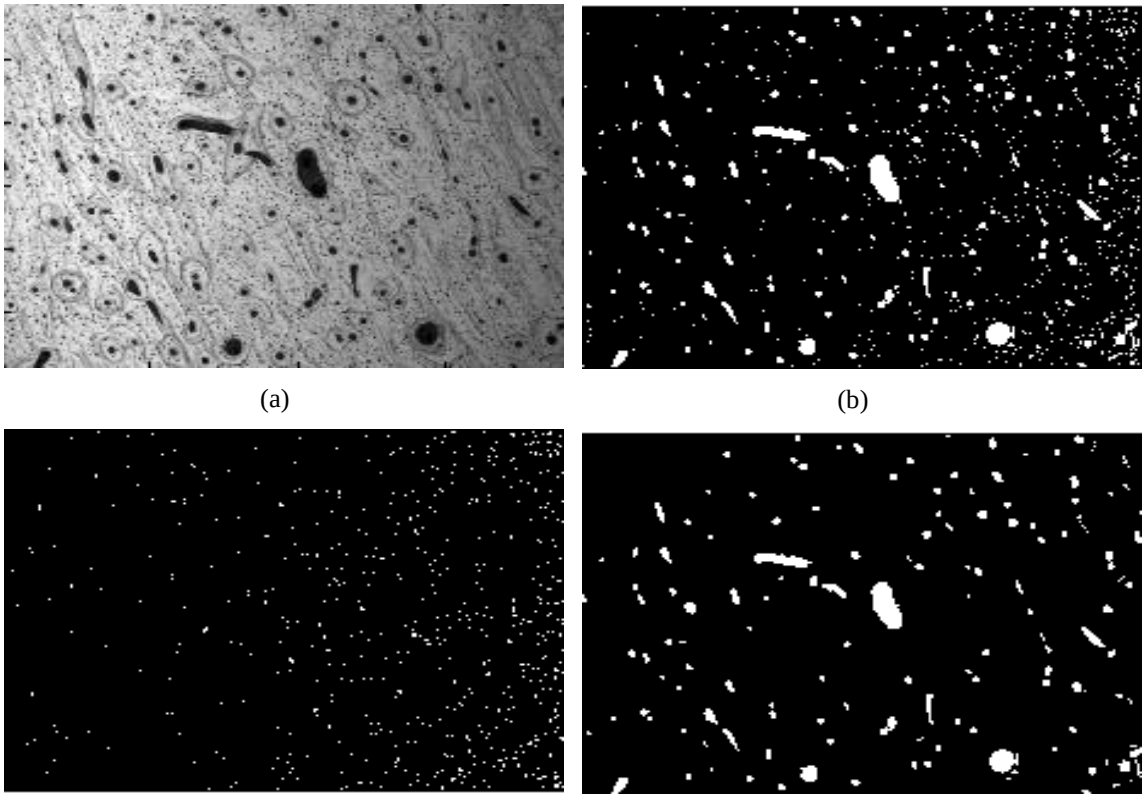

(a) (b)

(c) (d)

Fig. 2.5 – (a) Optical microscope image of a longitudinal section of cortical bone (50x); (b) binary image; (c) lacuna; (d) vascular porosity (~4%).

2.3 - Double Cantilever Beam – Data reduction scheme

Figure 2.6 presents the double cantilever beam (DCB) specimen configuration. Two symmetrical loads P are applied at the extremities of the specimen arms to compel the crack growth a-a_0 (a_0, represents the initial crack length) under pure mode I loading. Usually, the quantities measured during the test are the load P, the corresponding displacement value δ and the actual crack length a. Using this data it is possible to determine the strain energy release rate.

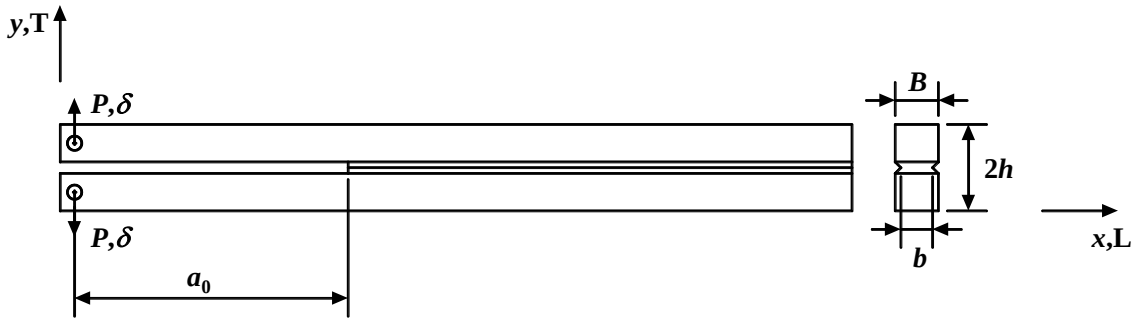

Fig. 2.6 – Schematic representation of the DCB specimen used for mode I fracture characterization of bone.

Classical data reduction schemes (Compliance Calibration Method and Modified Beam Theory) are based on the crack length monitoring during the test. However, this procedure is not easy to perform in bone owing to fracture mechanisms developing at the crack tip, as is the case of micro-cracking and fibre bridging (Fig. 2.7).

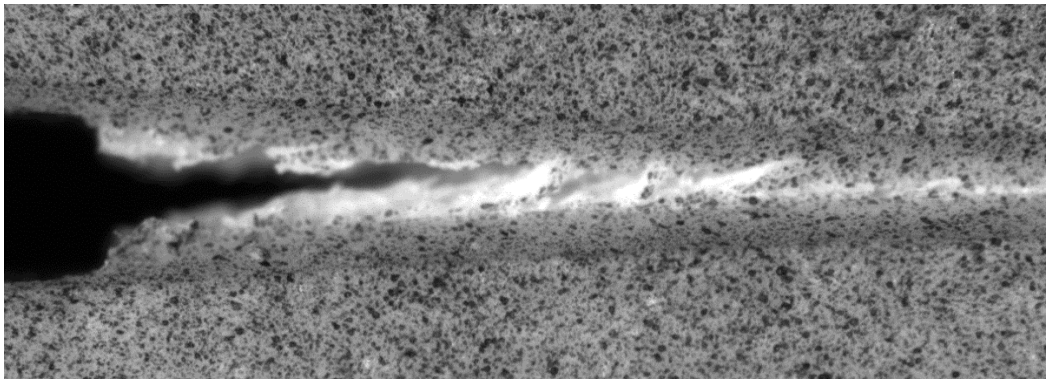

Fig. 2.7 – Crack-tip detail in bone.

In this work the Compliance Based Beam Method (CBBM) (de Moura et al., 2008) is adopted. This method does not require crack length monitoring during the test which was observed to be very difficult to perform with accuracy in bone. Instead, the CBBM uses the Timoshenko beam theory and the current specimen compliance to estimate an equivalent crack length. With this aim, the strain energy of the specimen due to bending and including shear effects (Timoshenko beam theory) writes,

$$U = 2\left[\int_0^a \frac{M_f^2}{2E_L I}dx + \int_0^a \int_{-h/2}^{h/2} \frac{\tau^2}{2G_{LT}} B dy dx\right] \tag{2.8}$$

where M_f is the bending moment and I represents the second moment of area, E_L and G_{LT} the elastic properties of bone (Fig. 2.6). The shear stress can be determined by,

$$\tau = \frac{3}{2}\frac{V}{A}\left(1-\frac{y^2}{t^2}\right) \tag{2.9}$$

where A, represents the section area of each arm ($0 \le x \le a$) and is equal to Bh. The parameters t and V represent, respectively, half-thickness of the beam and the transverse load of each arm. From Castigliano theorem ($\delta = \mathrm{d}U/\mathrm{d}P$) the specimen compliance C can be written as (de Moura et al., 2008),

$$C = \frac{8a^3}{E_{\mathrm{L}}Bh^3} + \frac{12a}{5BhG_{\mathrm{LT}}} \tag{2.10}$$

This equation was obtained assuming a perfect clamping condition at the crack tip (de Moura et al., 2008), which does not comply with the physical reality. Therefore, in order to include the effect of root rotation at the crack tip, a correction to the crack length should be incorporated (Hashemi et al., 1990),

$$\Delta = h\sqrt{\frac{E_{\mathrm{L}}}{11G_{\mathrm{LT}}}\left[3-2\left(\frac{\Gamma}{1+\Gamma}\right)^2\right]} \tag{2.11}$$

where

$$\Gamma = 11.8\sqrt{\frac{E_{\mathrm{L}}E_{\mathrm{L}}}{G_{\mathrm{LT}}}} \tag{2.12}$$

On the other hand, bone is a natural material presenting some variability of its elastic properties which means that the longitudinal modulus E_{L} can vary from specimen to specimen. In this context, an effective elastic modulus (E_{f}) can be evaluated from Eq. (2.10) considering the initial values of compliance (C_0) and crack length (a_0), as follows

$$E_{\mathrm{f}} = \left(C_0 - \frac{12\left(a_0+|\Delta|\right)}{5BhG_{\mathrm{LT}}}\right)^{-1}\frac{8\left(a_0+|\Delta|\right)^3}{Bh^3} \tag{2.13}$$

and used in Eqs. (2.11-2.12) instead of E_{L}. An iterative procedure involving Eqs. (2.11-2.13) should be used till a converged value of E_{f} is reached. During crack propagation, Eq. (2.10) can be rewritten as

$$C = \frac{8a_{\mathrm{e}}^3}{E_{\mathrm{f}}Bh^3} + \frac{12a_{\mathrm{e}}}{5BhG_{\mathrm{LT}}} \tag{2.14}$$

where a_{e} is the equivalent crack length accounting for the presence of a non-negligible fracture process zone (FPZ) which reflects on the registered specimen compliance. In fact, the energy dissipated in this region should be considered which does not occur if the real

crack length is used. In this circumstance, Eq. (2.14) can be solved to yield a_e as a function of the current compliance during the test (i.e., a_e=f(C)). Eq. (2.14) can be written as,

$$\alpha a_e^3 + \beta a_e + \gamma = 0 \tag{2.15}$$

where the coefficients α, β and γ are, respectively

$$\alpha = \frac{8}{Bh^3 E_f}; \beta = \frac{12}{5BhG_{LT}}; \gamma = -C \tag{2.16}$$

Using Matlab® software and only keeping the real solution it gives,

$$a_e = \frac{1}{6\alpha} A - \frac{2\beta}{A} \tag{2.17}$$

with

$$A = \left(\left(-108\gamma + 12\sqrt{3\left(\frac{4\beta^3 + 27\gamma^2\alpha}{\alpha} \right)} \right) \alpha^2 \right)^{\frac{1}{3}} \tag{2.18}$$

The R-curve (i.e., G_I = f(a_e)) can be obtained combining the Irwin-Kies equation

$$G = \frac{P^2}{2b} \frac{dC}{da} \tag{2.19}$$

where b is the width of the resistant section, with Eq. (2.14), thus leading to

$$G_I = \frac{6P^2}{Bbh} \left(\frac{2a_e^2}{h^2 E_f} + \frac{1}{5G_{LT}} \right) \tag{2.20}$$

This method presents several advantages. In fact, the crack length monitoring during its growth is not necessary, since the equivalent crack is a calculated parameter as a function of the current specimen compliance (data captured from the load-displacement curve). This is a very important aspect because crack length monitoring in bone fracture is not easy to perform. In addition, the real crack length does not include the effect of energy dissipation occurring ahead of the crack tip due to the developed non-negligible FPZ. Furthermore, this method accounts for scattering of elastic properties, because the elastic modulus is a computed parameter defined as a function of the initial values of a_0 and C_0. From Eq. (2.12) it can be observed that the shear modulus G_{LT} has a small influence on the results and therefore a typical value can be used instead (de Moura et al., 2008).

One of the crucial aspects of this test is the necessity to consider a pre-existing crack. In light of this condition, a small pre-crack was produced (Fig. 2.8) prior to the mechanical tests using a sharp blade attached to a servo-electrical testing machine (Micro-Tester

INSTRON® 5848). The blade was thus forced to move 0.15 mm against the notch root at a displacement rate of 100 mm/min. This procedure was executed twice for each specimen.

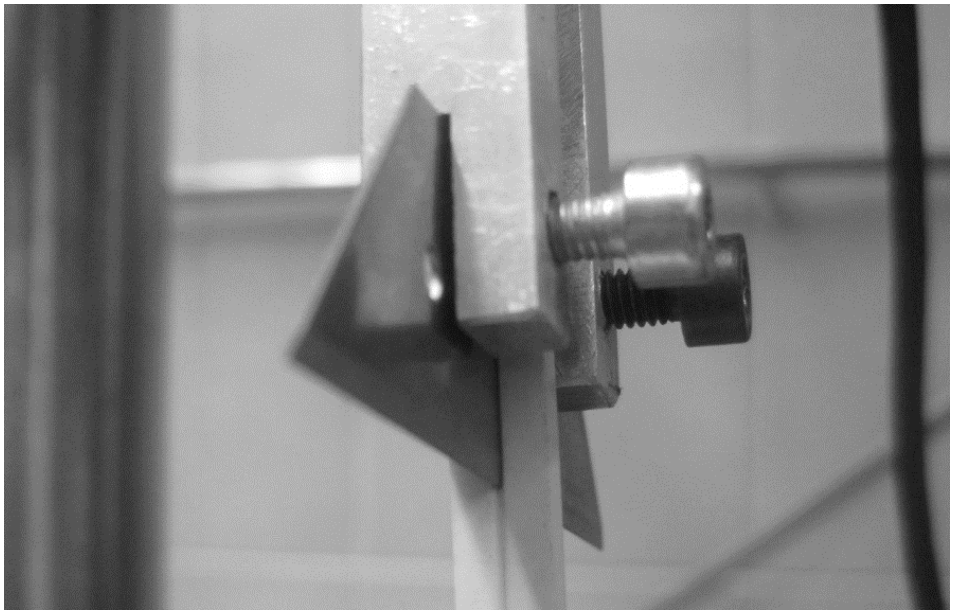

Fig. 2.8 – Introduction of the pre-crack with a sharp blade duly set in the test machine.

Another relevant aspect is the measurement of the crack opening displacement (*w*) by means of the Digital Image Correlation (DIC) technique using the ARAMIS DIC-2D system (GOM mbH, 2007; Xavier et al., 2012). For this purpose, the surface of the bone specimen was previously painted using an airbrush with matte black ink thus allowing a suitable speckle pattern for DIC measurements (Fig. 2.9). The components of the optical system together with DIC measuring parameters used in the post-processing are summarised in Table 2.1. An 8-bit charge coupled device (CCD) camera coupled with a telecentric lens covering a region of 7.1×5.4 mm^2 was used perpendicular to the specimen face. The focus of the image was guaranteed by setting the working distance to 63.3 mm, yielding a conversion factor of 4.0 μm/pixel. The shutter time and lighting system were set to enhance contrast and avoid over and under exposition. For DIC analyses, a subset size of 15×15 $pixel^2$ (0.060×0.060 mm^2) and a subset step of 13×13 $pixel^2$ (0.052×0.0524 mm^2) were selected for enhancing spatial resolution. Rigid-body translation tests were systematically carried out before testing to check image quality and accuracy by comparing the measurements with reference theoretical rigid-body movements (Sousa et al., 2011a, 2011b). The displacement resolution was set in the range of $1–2\times10^{-2}$ pixel (0.04-0.08 μm) (Table 2.1), depending on the final quality of the speckled pattern.

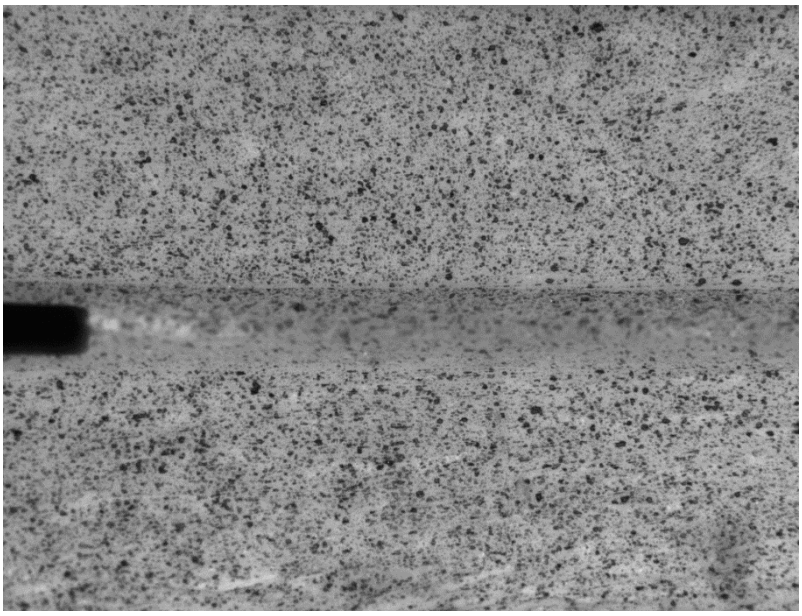

Fig. 2.9 – Example of a *speckle* pattern.

Table 2.1 – Components of the optical system and DIC measuring parameters

CCD camera	
Model	Baumer Optronic FWX20 (8 bits, 1624×1236 pixels, 4.4 μm/pixel)
Shutter time	1.0 ms
Acquisition frequency	1 Hz
Lens	
Model	Opto Engineering Telecentric lens TC 23 09
Magnification	1.0±3%
Field Of View (1/1.8")	7.1 mm×5.4 mm
Working Distance	63.3±2 mm.
Working F-number	11
Field Depth	0.9 mm
Conversion factor	4.0 μm/pixel
Lighting	Raylux 25 white-light LED
DIC measurements	
Subset size	15×15 pixel^2 (0.060×0.060 mm^2)
Subset step	13×13 pixel^2 (0.052×0.052 mm^2)
Resolution	1-2×10^{-2} pixel (0.04-0.08 μm)

The region affected by the lateral grooves was excluded for displacements measurements (Fig. 2.10), due to image quality problems on that region. The crack opening displacement has been measured using the nearest points of crack tip outside this critical region.

The DCB tests (Fig. 2.11) were performed on a servo-electrical testing machine (Micro-Tester INSTRON® 5848 – Dynamic Laboratory – ECT-UTAD) imposing displacement

control with an actuator velocity of 0.5 mm/min. Load–displacement (P–δ) curves were registered with an acquisition rate of 5 Hz, while the images for DIC measurements were acquired using a frequency of 1 Hz. The average specimen dimensions were $2h$=6.0 mm, b=2.0 mm, B=3.1 mm and a_0=23.2 mm in Fig. 2.6.

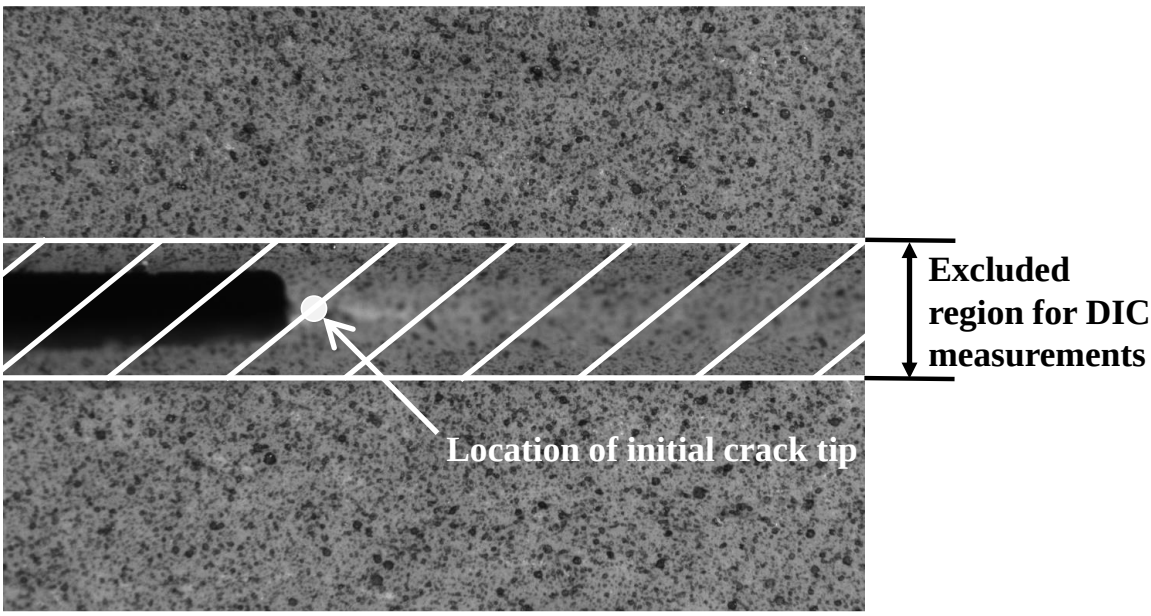

Fig. 2.10 – Image processing.

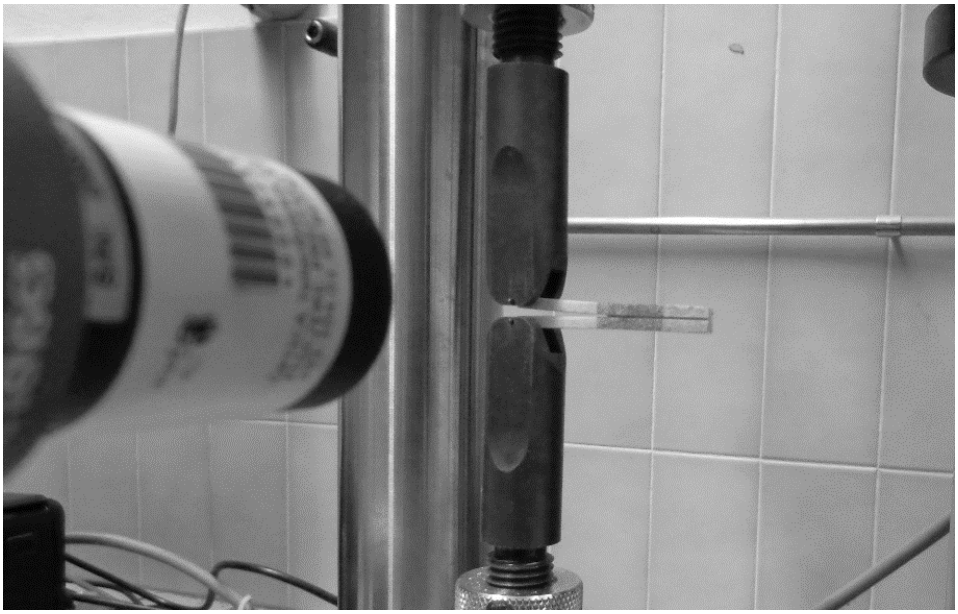

Fig. 2.11 – Photography of the DCB test.

2.4 - Identification of cohesive law - direct method

The procedure described above provides the establishment of the relationship $G_I = f(w_I)$ in the course of the DCB test, which can be used to identify the cohesive law representative of the material fracture behaviour under pure mode I loading. In fact, this law is the basis of the cohesive zone models (CZM) establishing a softening relationship between stresses and relative displacements between homologous points belonging to the cohesive surface. The cohesive law can be obtained through the following relation (Rice, 1968),

$$G_I = \int_0^{w_I} \sigma(w)\mathrm{d}w \tag{2.21}$$

which leads to

$$\sigma_I(w_I) = \frac{\mathrm{d}G_I}{\mathrm{d}w_I} \tag{2.22}$$

It should be noted that the differentiation of the $G_I = f(w_I)$ relation was performed after adjusting a smoothing spline fitting using the MatLab® software. In order to validate the direct identification method a numeric simulation was previously performed. This numerical procedure is advantageous since the cohesive law is known a priori, thus allowing the assessment of the efficacy of the identification method. In light of this, a finite element analysis including cohesive zone model was used to simulate damage initiation and propagation in the DCB average specimen dimensions of bone. Figure 2.12 illustrates the finite element mesh used in this procedure containing 1080 two-dimensional plane stress solid elements and 120 interface finite elements positioned in the crack path (i.e., ligament section). Small increments (0.01 of the applied displacement) were used to ensure smooth damage propagation in the course of the loading process using the elastic properties presented in Table 2.2.

Table 2.2 – Elastic properties of cortical bone.

E_L (GPa)	E_T (GPa)	G_{LT} (GPa)	ν_{LT}
18.01[+]	9.55*	4.74*	0.37*

[+] Experimental result
* Morais et al. (2010)

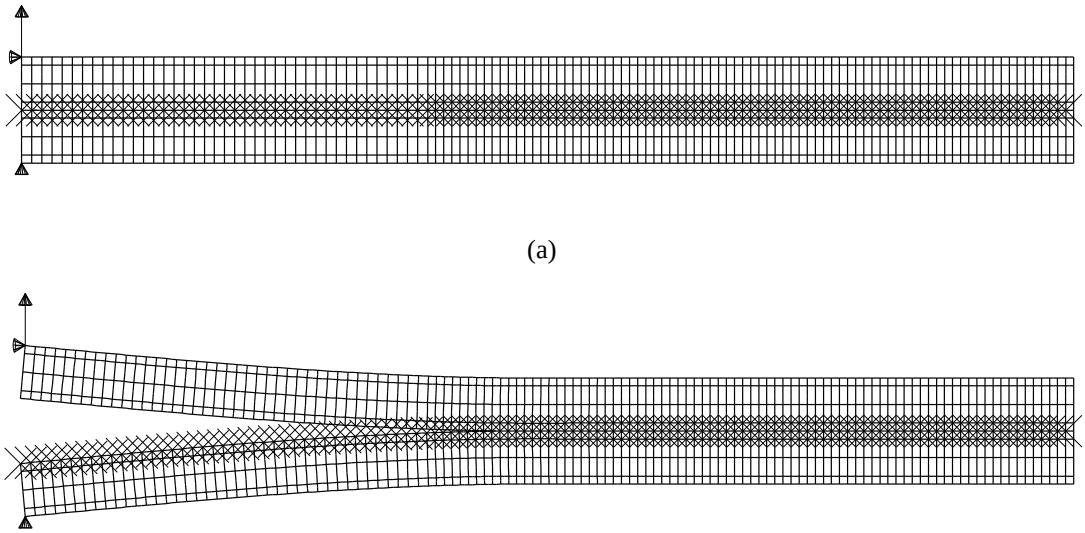

(a)

(b)

Fig. 2.12 – Finite element mesh used in the DCB test: (a) undeformed configuration, (b) deformed configuration (diagonal crosses represent the cohesive elements).

The bilinear damage cohesive law (Fig. 2.13) has been introduced as input in the numerical model. The area circumscribed by the cohesive law corresponds to the mode I fracture energy G_{Ic}. Table 2.3 presents the cohesive parameters used in the numerical model. The coordinates of the inflection point ($\sigma_{I,1}$, $w_{I,1}$) were defined using information obtained in a previous work (Pereira et al., 2012). Since the existent bone set revealed to have higher fracture energies, the values obtained in referred previous work could not be directly used. Consequently, the same ratio of areas corresponding to the two different damage mechanisms (G_{Iu}/G_{Ib}) and the ratio between the stress and the crack opening displacement ($\sigma_{I,1}/w_{I,1}$) of the inflection point were assumed.

Table 2.3 – Parameters of the cohesive law.

G_{IC} (N/mm)	$\sigma_{I,u}$ (MPa)	$\sigma_{I,1}$ (MPa)	$w_{I,1}$ (mm)
2.610 [+]	36.0 *	6.0 [#]	0.1 [#]

[+] Experimental result
* From Pereira et al. (2012)
[#] Established from Pereira et al. (2012)

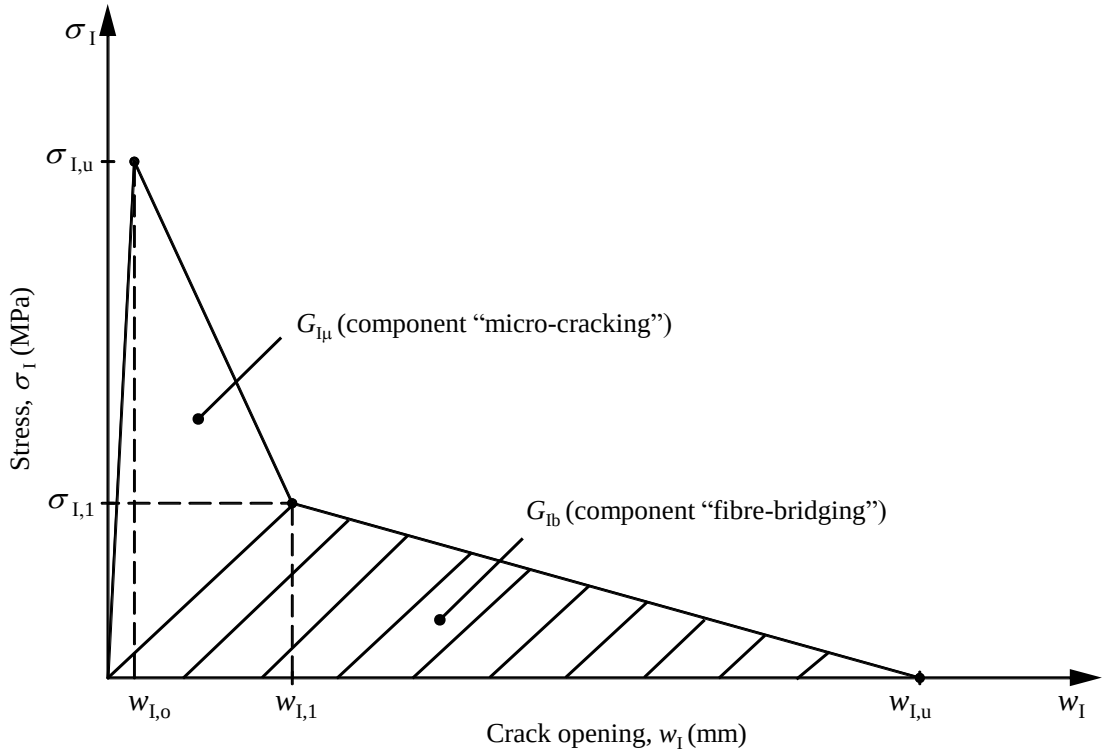

Fig. 2.13 – Bilinear cohesive law ($G_{Ic} = G_{I\mu} + G_{Ib}$) (Pereira et al., 2012).

Applying the CBBM method to the *P*-δ numerical curve provides the evolution of strain energy release rate during the test. This parameter can be combined with the relative displacements between crack faces to obtain the relationship $G_I = f(w_I)$. Subsequently, the curve fitting tool available in Matlab® software is used to fit (adjustment parameter, $p \approx 1$) a smoothing spline (Fig. 2.14), which is later utilized for differentiation aiming to determine the cohesive law. The cohesive law used as input in the finite element analysis and the one determined by this method are compared in Fig. 2.15. Overall excellent agreement can be observed. The slight difference observed in the vicinity of the local strength (peak stress point) between the two plotted curves is a result of the high initial stiffness used in the cohesive zone modelling. Taking into account these results the proposed procedure to obtain the cohesive law under mode I loading has been considered effective.

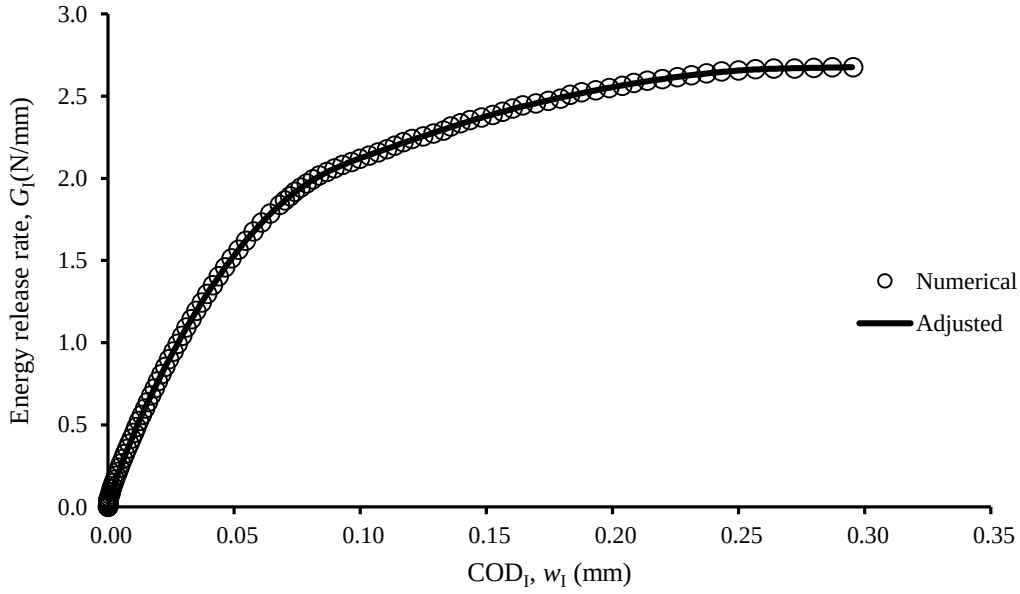

Fig. 2.14 – The $G_I = f(w_I)$ relationship obtained in finite element analysis and the adjusted one using a smoothing spline fitting.

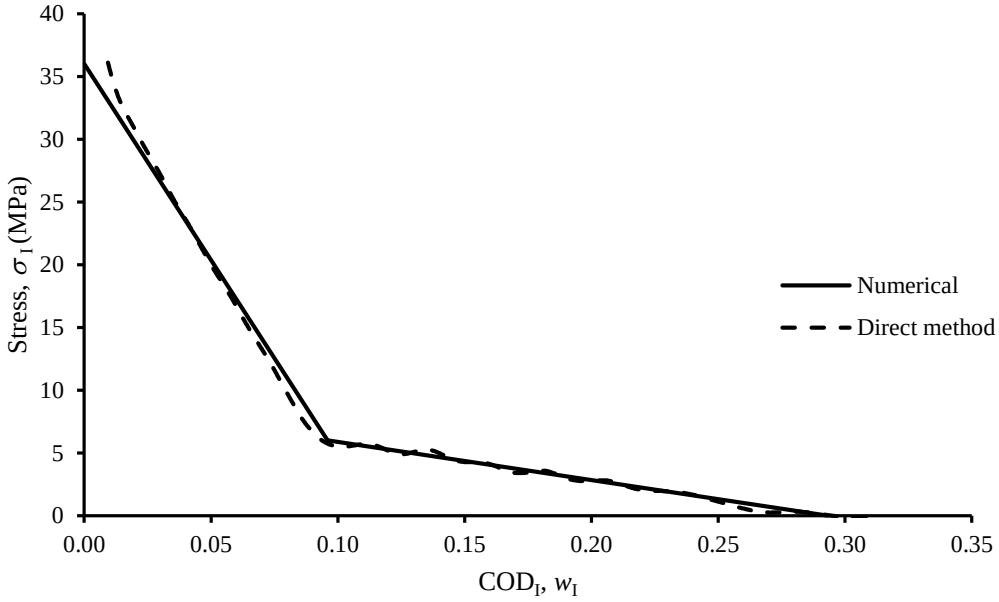

Fig. 2.15 – Comparison between the cohesive law used as input (i.e., Numerical) in the model and the one obtained by the direct method.

Since the experimental fracture energy (G_{Ic}=2.61 N/mm) was used in the previous numerical validation a comparison of the numerical P-δ curve with the ensemble of experimental ones was performed (Fig. 2.16). Overall, the numerical curve replicates in a

satisfactory way the global response of bone under mode I loading, which means that the proposed procedure is appropriate.

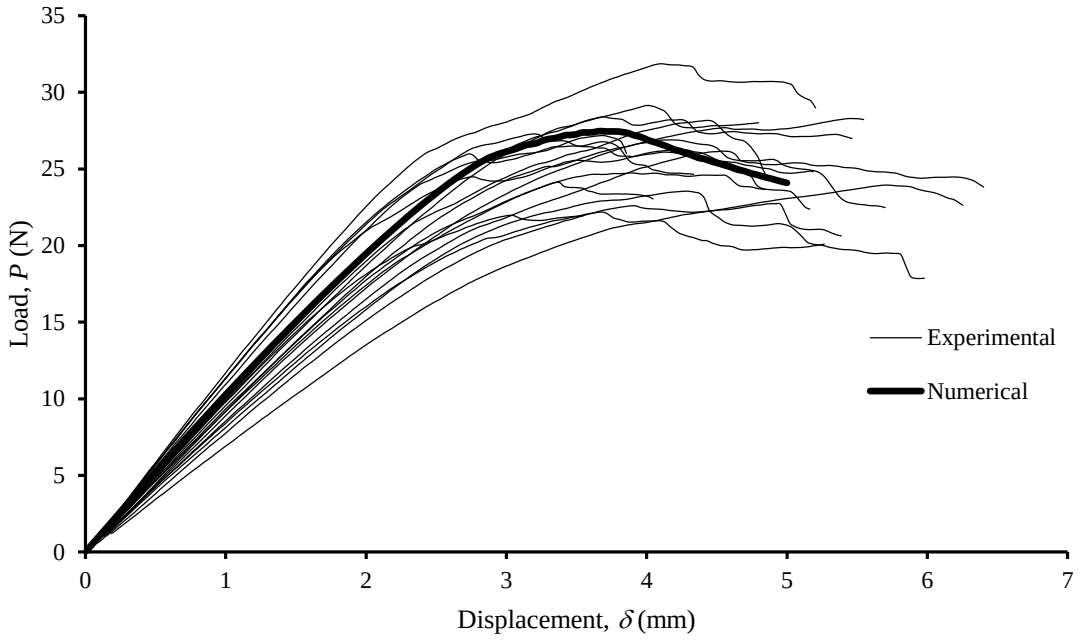

Fig. 2.16 – Load-displacement curves: experimental and numerical.

2.5 - Identification of cohesive law - new inverse method

The inverse method consists of identification of the cohesive law minimizing an objective function. In the present work an algorithm using a trial and error procedure is followed aiming to fit the numerical and experimental load-displacement curves. Two optimization methods based on inverse procedure were developed in order to identify the cohesive law representative of the fracture behaviour of bone. In both methods, a finite element analysis was performed considering a totally shape free cohesive law. The law has four linear sections (Fig. 2.17) and was implemented as a user-subroutine in the finite element code. The methods use as input the data issuing from the load-displacement curve and from the *R*-curve. The first step, common to both methods, is to select some points to perform the adjustment in the load-displacement and *R*-curves (Fig. 2.18). The first point was fixed at the nonlinearity onset of the P-δ curve, while the remaining ones were disposed along the non-linear region before the peak load.

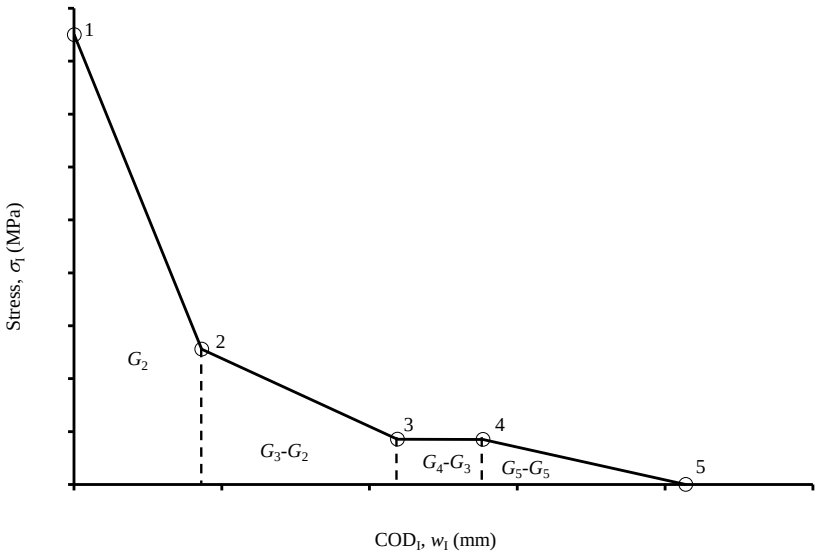

Fig. 2.17 – Cohesive law used as input in the numerical model.

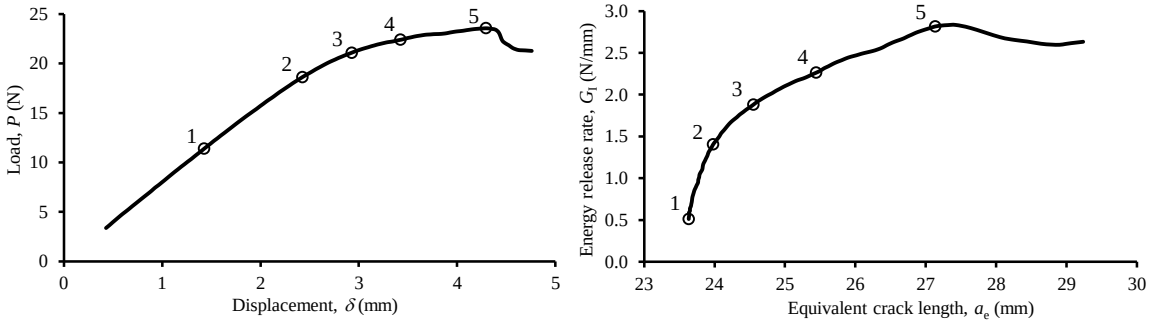

Fig. 2.18 – Load-displacement curve and the corresponding *R*-curve of a DCB test in bovine bone revealing a series of points used for adjustment in the proposed inverse method.

For each point of adjustment the traction value (σ_I) was arbitrarily chosen and the corresponding relative displacement (w_I) is determined from the strain energy release rate measured in the *R*-curve. This value of energy is equated to the area below the cohesive law in Fig. 2.17, thus allowing defining the corresponding relative displacement. The objective function used in this optimization problem is given by,

$$Dif_i = P_i^{num} - P_i^{exp} \; ; \quad i=1,2,3,4,5 \text{ of the } P\text{-}\delta \text{ curve} \tag{2.23}$$

with P_i^{exp} and P_i^{num} standing for the experimental and the numerical load. The goal is to minimize the absolute values issued from the previous function. However, the traction value for the first point, which corresponds to the local strength, was determined following a different procedure. In fact, the range of traction values that provides a good agreement between the numerical and experimental load-displacement curves is large. Consequently,

the global response, i.e., the comparison of the whole numerical and experimental *P*-δ curves, should also be considered in addition to the local difference analysis. This iterative process relies on the definition of new stress values aiming the minimization of Eq. (2.23). Two optimization methods were used to comply with this objective. The difference between them is related to the way they seek the solution. The first one (Fig. 2.19), called *Bissection*, is based on the typical behaviour of a "user". Hence, if the numerical curve underestimates the experimental one at a point then the traction value is increased and vice-versa. The *Bissection* method (Chapra and Canale, 1985) is only used in the case of consecutive differences with contrary signals. Then, the new stress value will be the midpoint of the two previous stress points.

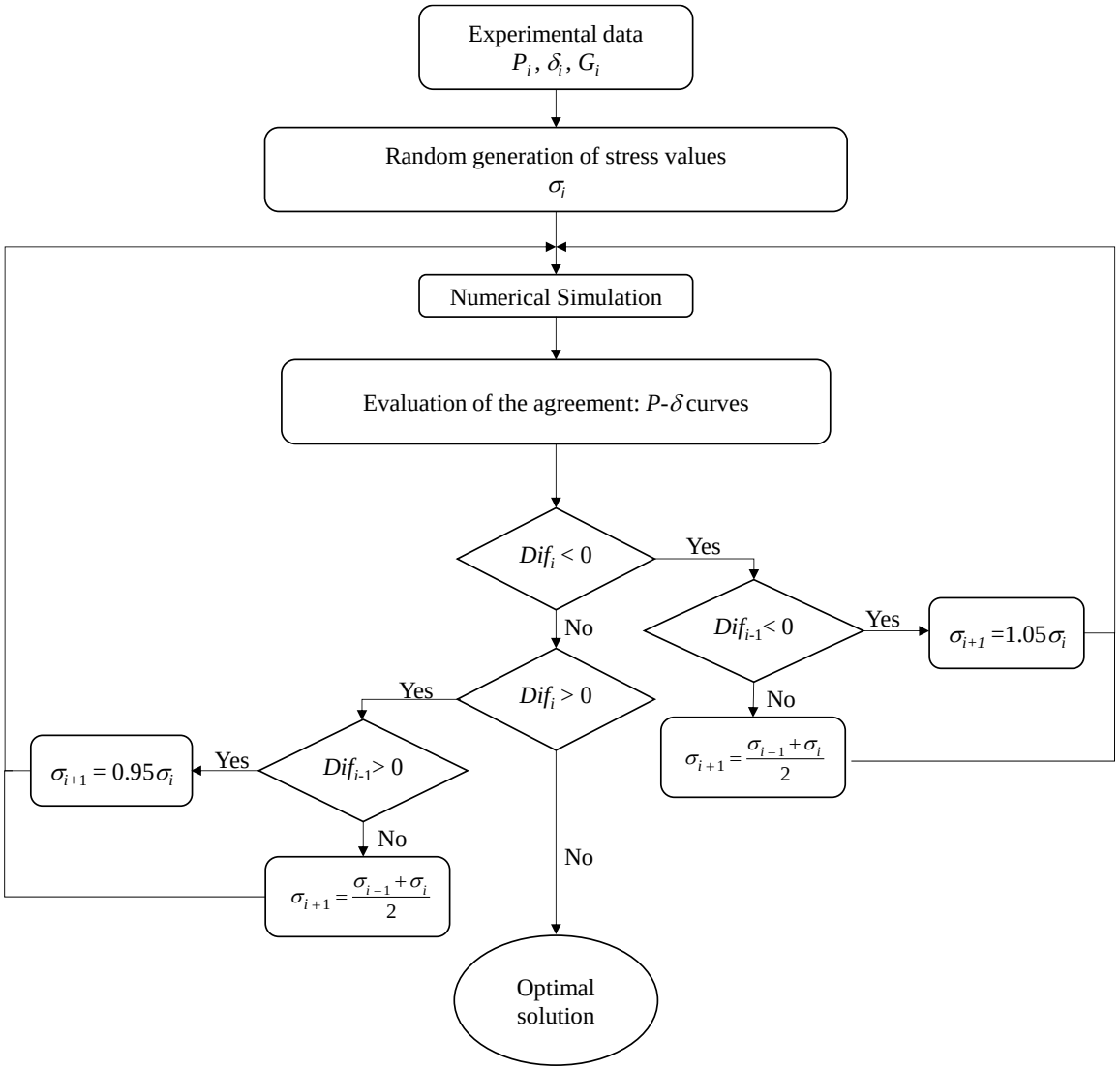

Fig. 2.19 – Organogram of the developed *Bissection* algorithm (*i*=1, 2, 3, 4, and 5).

The second method uses the *Nelder-Mead* algorithm. This is an unconstrained and derivative-free optimization method which creates a *simplex* considering the outcome from the user-defined objective function. A *simplex* is a diagram defined by a set of vertexes whose number is obtained as a function of the quantity of variables used in the optimization problem (n). Hence, for an objective function with one variable (n=1) the number of vertexes of the referred diagram is set to n+1 (i.e., a line segment). The first step of this method consists of ordering the vertexes of the diagram in a decreasing order of the response given by the objective function (from the best to the worst). The vertexes referred by the letters **B**, **N** and **W** in Fig. 2.20 designate the best, the next one and the worst, respectively. Vertex R is initially calculated using the equation presented in Fig. 2.20.

The response issued by this updating is quantified to define the next stage of the algorithm represented in Table 2.4. Hence, if the response of the optimization problem has fallen in the interval $\mathbf{N} \leq R \leq \mathbf{B}$, then the line segment is forced to assume the set of points **B**, **N**, and R (i.e., BNR), followed by the reordering of those points according to the evaluation of the objective function. In a like manner, if R > **B**, then vertex E has to be evaluated (equations in Fig. 2.20). The comparison to vertex **B** is made and a redefinition of the line segment performed (BNE or BNR). The remaining segment configurations are defined by comparison to the position of vertex **W**, giving rise to sequences BNC_R or BNC_W. The organogram of the developed *Nelder-Mead* algorithm can be visualized in Fig. 2.21.

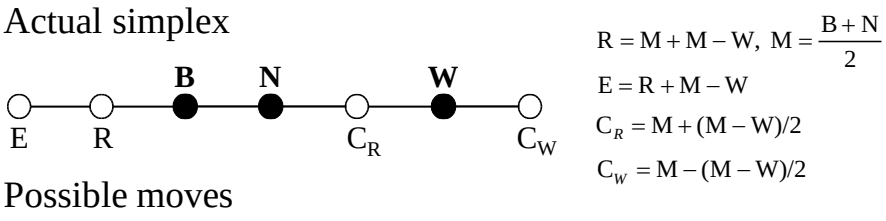

Fig. 2.20 – *Nelder-Mead* domain: **B** – best vertex; **N** – next to worst vertex; **W** – worst; E – expansion vertex; R – reflection vertex; C_R – contraction vertex on R side; C_W – contraction vertex on W side. Adapted from Walters (1991).

Table 2.4 – Rules for Nelder-Mead moves.

Rules		Next simplex
$N \leq R \leq B$		BNR
$R > B$	$E \geq B$	BNE
	$E < B$	BNR
$R < N$	$R \geq W$	BNC_R
	$R < W$	BNC_W

The numerical model presented in the previous section has been used to validate the optimization methods. Figures 2.22-2.24 illustrate comparisons between the numerical curves used as reference and numerical curves identified by each optimization algorithm. From Fig. 2.24 it can be concluded that both algorithms lead to good identifications of the cohesive law used as input.

The only important difference between the two algorithms lies in the computational costs. In this context, the *Bissection* algorithm found a good approximation after a total of seven simulations, while the *Nelder-Mead* algorithm used twenty five. As the computing time consumption is an important parameter, it can be concluded that the first algorithm is preferable. Consequently, the *Bissection* algorithm was chosen to deal with the experimental results.

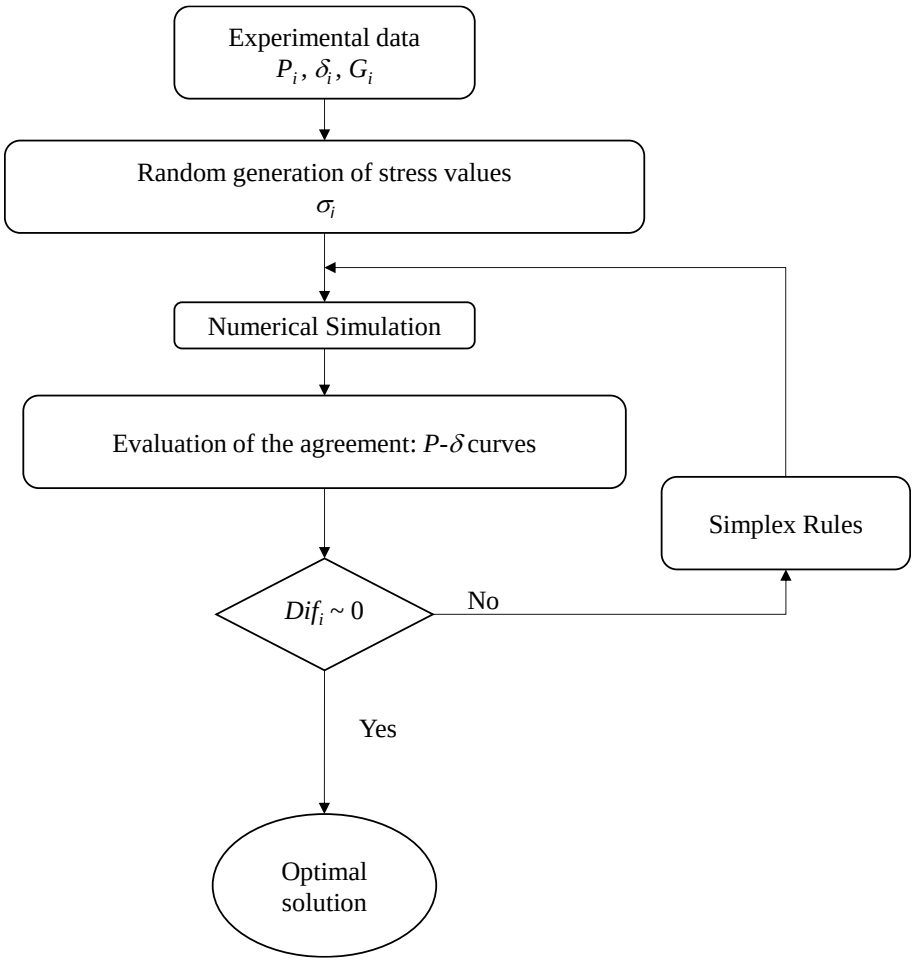

Fig. 2.21 – Organogram of the developed *Nelder-Mead* Algorithm (*i*=1,2,3,4 and 5).

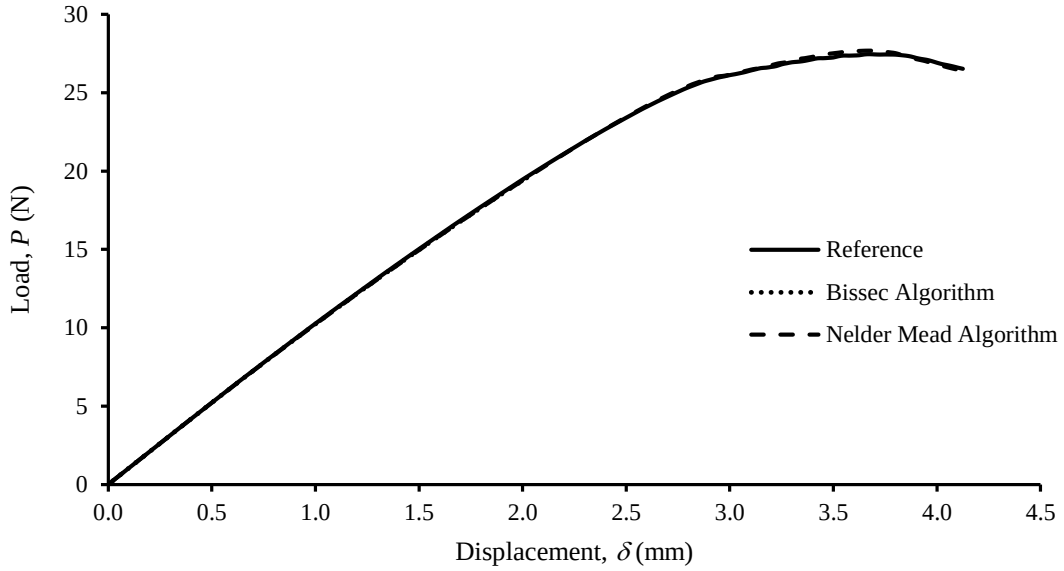

Fig. 2.22 – Numerical load-displacement curves: reference, *Bissection* and *Nelder Mead* algorithm.

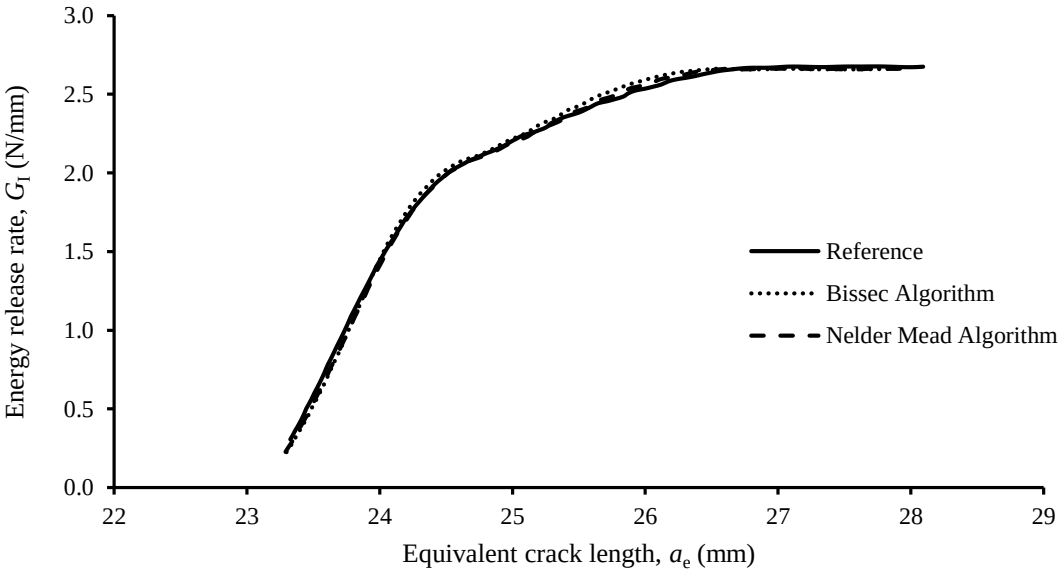

Fig. 2.23 – Numerical *Resistance*-curves: reference, *Bissection* algorithm and *Nelder Mead* algorithm.

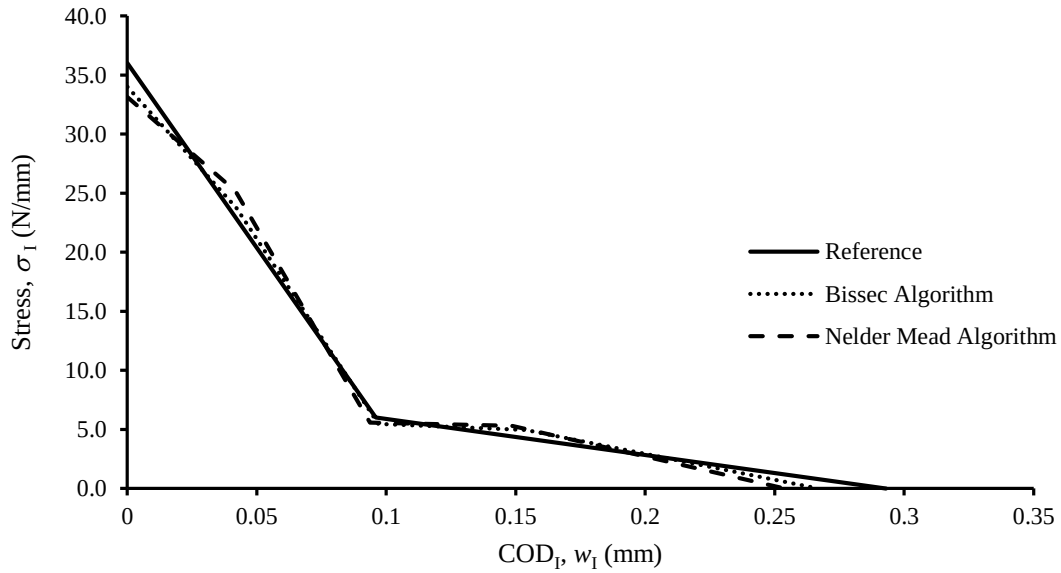

Fig. 2.24 – Comparison between the cohesive law used as input and the ones obtained by the inverse methods.

2.6 - Analysis and discussion of experimental mode I *Resistance*-curves

In this section the experimental results of fracture energy are presented and discussed. Generally, the *R*-curves shown in Fig. 2.25 reveal the existence of a plateau meaning that the FPZ has developed completely allowing a clear measurement of the fracture energy. These results can be viewed as a symptom of a meticulous preparation of the experimental work. Table 2.5 groups all experimental results considered valid after the application of a statistical method that allows the identification of spurious results. In other words, this statistical analysis permits identifying whether a given result corresponds to natural material variation or is a consequence of another fortuity event (Chauvenet criterion). Pearson product-moment correlation coefficients were calculated to identify any relationship between the mechanical properties (G_{Ic} and E_L) and the other material parameters (d_h, m_w, m_o, m_m and *Por*). Specifically, fracture energy (G_{Ic}) has non-significant correlations with the referred material parameters at the required significance level (p>0.05) (Sheskin, 2003). The absence of significant correlations have already been found by Phelps et al. (2000) and Pereira (2009). However, Yeni et al. (1998) has found significant correlations, though it is important to refer the low apparent density range in their work. Another important aspect is the nature of bone used in the experiments. Phelps et al. (2000) used bone from baboons femora, Yeni et al. (1998) used human femur and tibia, and Pereira (2009) worked with bovine femur, the same material used in this work.

Finally, it can be concluded that the fracture energy achieved in this work compares well with values found in other works (Table 2.6).

Table 2.5 – Experimental results. G_{Ic} fracture energy; E_L Longitudinal flexure modulus; d_h apparent density; m_w water mass fraction; m_o organic mass fraction; m_m mineral mass fraction; *Por* porosity.

Specimen Number	G_{Ic} (N/mm)	E_L (GPa)	d_h (g/cm^3)	m_w (%)	m_o (%)	m_m (%)	*Por* (%)
1	2.91	16.28	2.02	12.58	24.18	63.24	3.75
2	1.99	17.56	1.74	13.79	24.54	61.68	-
3	2.95	18.75	1.94	12.58	22.98	64.44	4.38
4	2.89	18.08	2.00	12.10	22.44	65.46	3.39
5	1.91	17.07	2.00	12.02	23.27	64.70	4.55
6	2.27	17.86	2.02	12.47	25.96	61.56	4.78
7	3.12	17.83	1.93	12.65	32.96	54.38	4.71
8	2.58	15.48	1.87	12.64	27.17	60.19	5.35
9	2.50	18.13	1.93	12.28	34.74	52.98	4.10
10	2.49	17.84	1.97	12.06	21.78	66.16	3.73
11	1.70	21.25	1.91	11.66	21.82	66.51	4.24
12	2.41	18.83	1.94	12.06	22.62	65.32	3.27
13	2.81	19.39	1.96	12.34	22.52	65.14	4.58
14	2.44	18.03	1.83	11.98	21.54	66.48	4.71
15	2.38	16.78	1.93	12.37	21.94	65.69	4.60
16	3.02	17.88	2.05	11.50	21.64	66.87	4.02
17	2.62	19.58	1.98	12.58	24.18	63.24	3.75
Average	2.53	18.04	1.94	12.33	24.49	63.18	4.24
CoV (%)	16.0	7.4	3.9	4.1	15.8	6.4	13.3

Table 2.6 – Range of fracture energy in several works.

Work	Bone Type	Experimental Test	G_{Ic} (N/mm)
(Bonfield et al., 1978)	Bovine femur	CT	0.92-2.78
(Morais et al., 2010)	Bovine femur	DCB	1.91 ± 0.30
(Pereira et al., 2012)	Bovine femur	DCB	1.76 ± 0.39

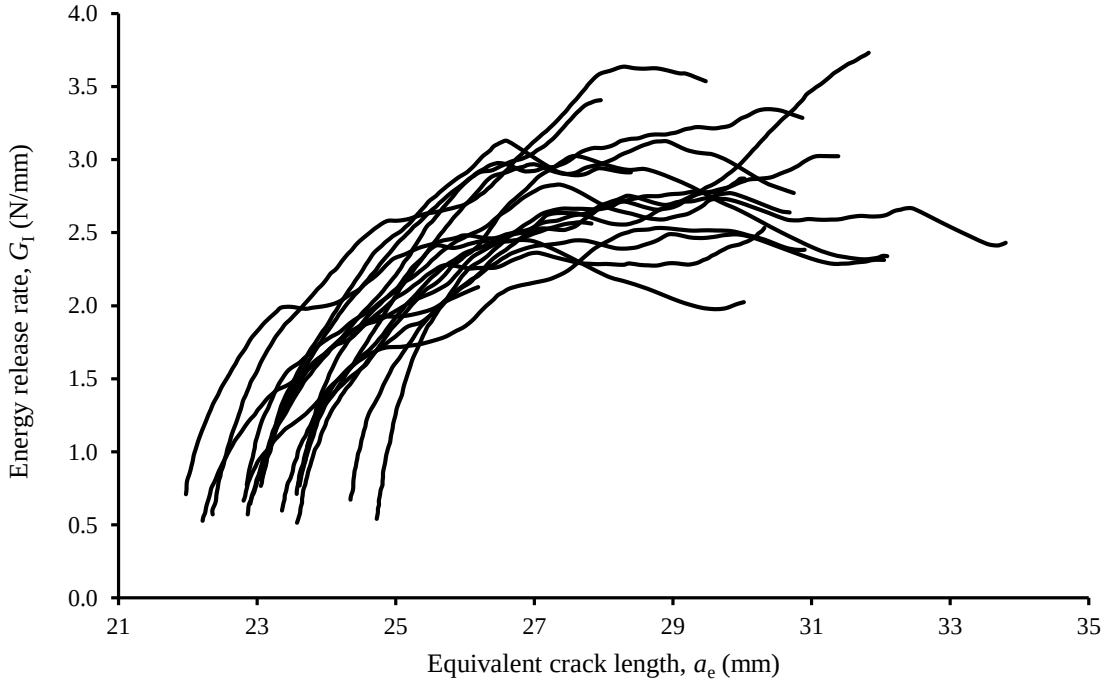

Fig. 2.25 –*R*-curves under mode I loading of bovine cortical bone.

Figure 2.26 shows the crack evolution during the fracture test in different stages. The presented sequence of pictures shows a clear self-similar propagation along the crack path compelled by the lateral grooves, revealing that the propagation occurs as a result of vertical displacement. In fact, the nearly perfect alignment between the top and bottom notch corners in the vicinity of the crack reveals that shear loading is at least negligible in this test. Fig. 2.27 plots the evolution of crack opening displacements in mode I and mode II with the applied displacement. Clearly, the results show the predominance of mode I, because the mode II displacements can be considered insignificant at the peak load.

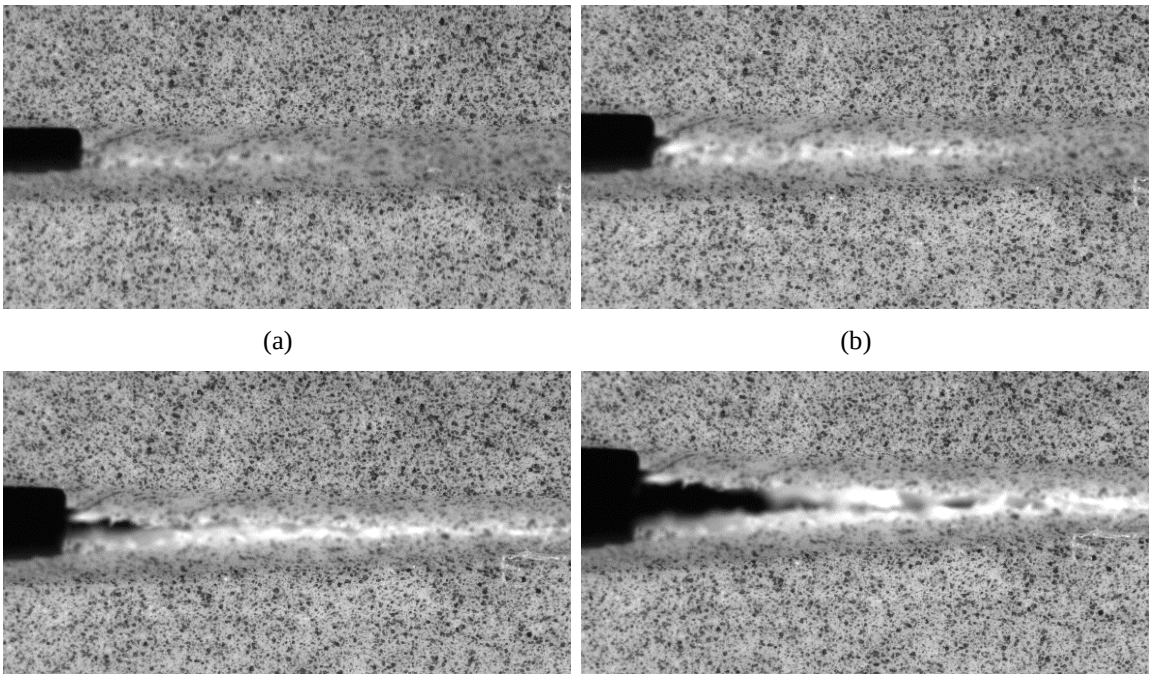

(a) (b)

(c) (d)

Fig. 2.26 – Crack evolution: (a) initial stage, (b) intermediate stage, (c) load peak - propagation onset, (d) significant propagation (specimen 7).

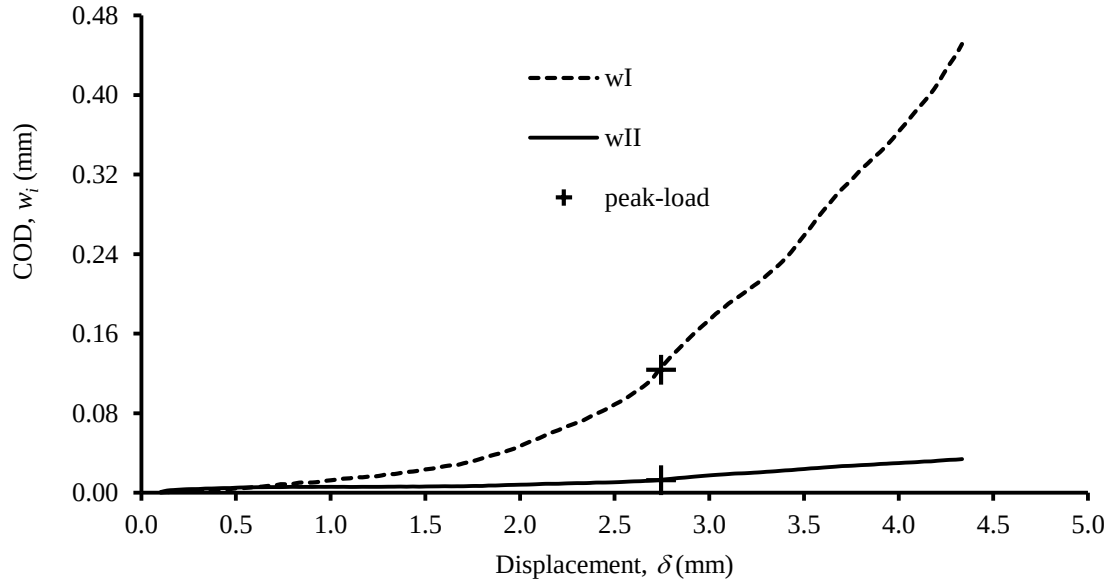

Fig. 2.27 – Crack opening displacements evolution as a function of applied displacement (i =I, II).

2.7 - Analysis and discussion: mode I cohesive law

The methods described in Sections 2.4 and 2.5 were applied to the experimental results in order to identify the cohesive laws mimicking the fracture behaviour of bovine cortical bone under pure mode I loading. The fitting operation obtained by smoothing spline adjustment to the experimental data can be seen in Fig. 2.28. This procedure provides a good representation of the experimental data and simultaneously eliminates the data noise. An important task of the direct identification method is the correct tracking of the ultimate strength which corresponds to the inflection point located at the initial rising trend of the $G_I = f(w_I)$ curve. Observing the plot it is possible to identify a nearly linear region where this point is located which highlights the difficulty of its identification. To deal with this problem the quality of the fitting is very important. This aspect emphasizes the relevance of a rigorous experimental work and the importance of testing a large number of samples, conditions that were satisfied in this work.

Figure 2.29 plots the comparison between the experimental curves and the curves resulting from the optimization strategy issuing from the application of the inverse method. The load–displacement curves reveal excellent agreement which indicates the good performance of the developed inverse method. These results suggest that the objective function linked with a cohesive law with four linear branches is able to reproduce the fracture behaviour of cortical bone under mode I loading. The spurious stress increase (non-physical behaviour consequence of material heterogeneity) in the third branch of the numerical cohesive law indicates that this method can deal with imperfections, which are very common in biological materials.

Figures 2.30 and 2.31 show the aspect of the cohesive laws determined by the direct and inverse methods, respectively (cohesive parameters presented in Table 2.7). It is possible to observe that the cohesive laws obtained by the direct method do not assume the nil value at the beginning due to the difficulty of the DIC method to provide accurate measurements at the early stages of the test.

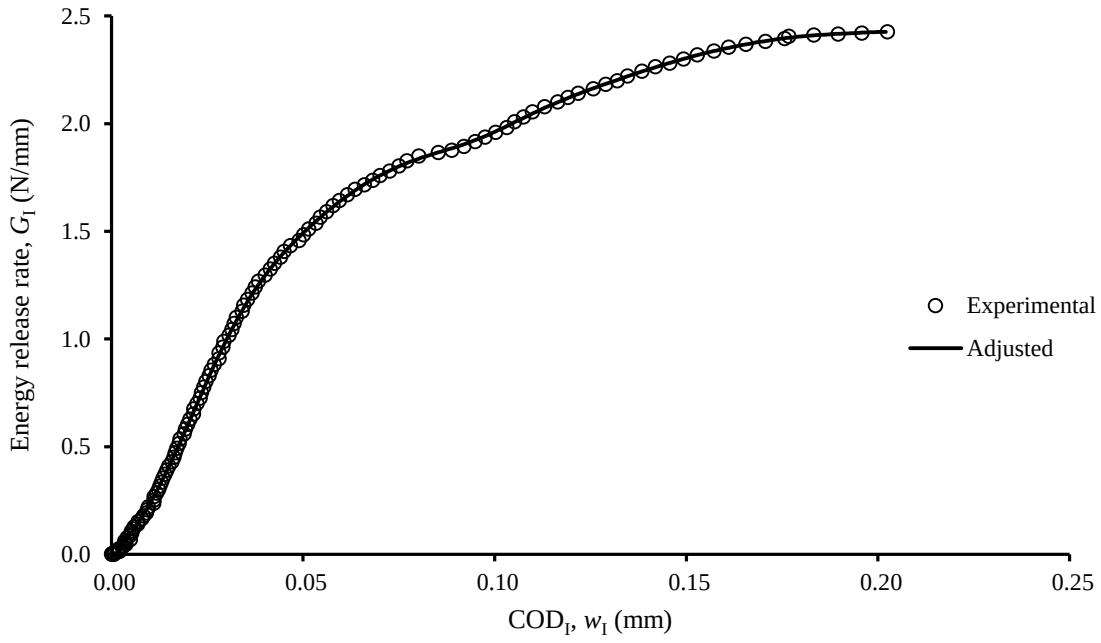

Fig. 2.28 – Typical G_I=f(w_I) experimental relationship and smoothing spline fitting.

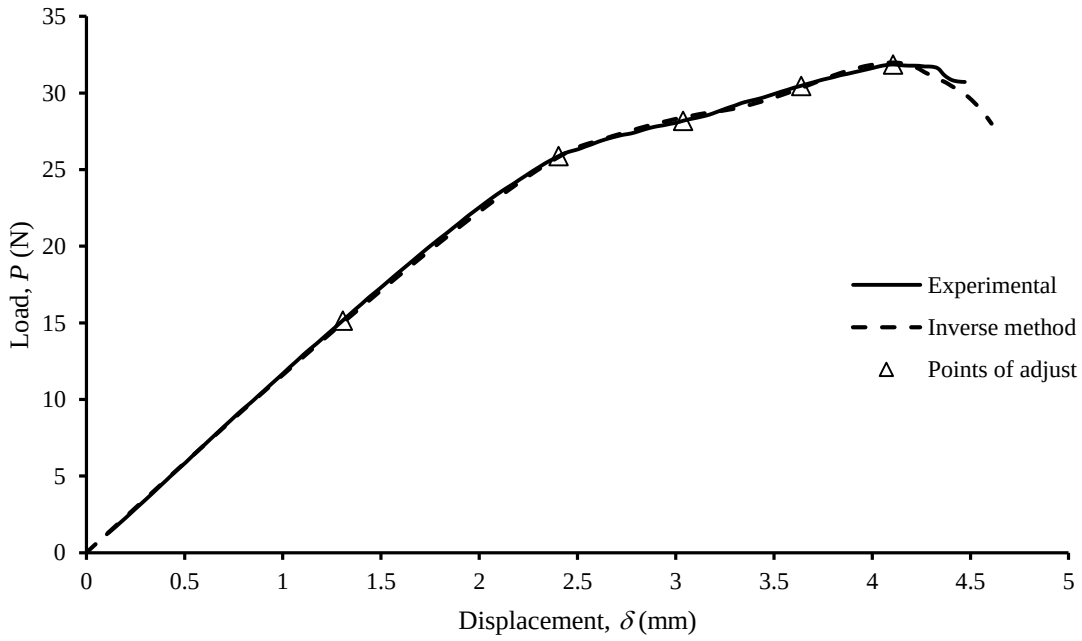

(a)

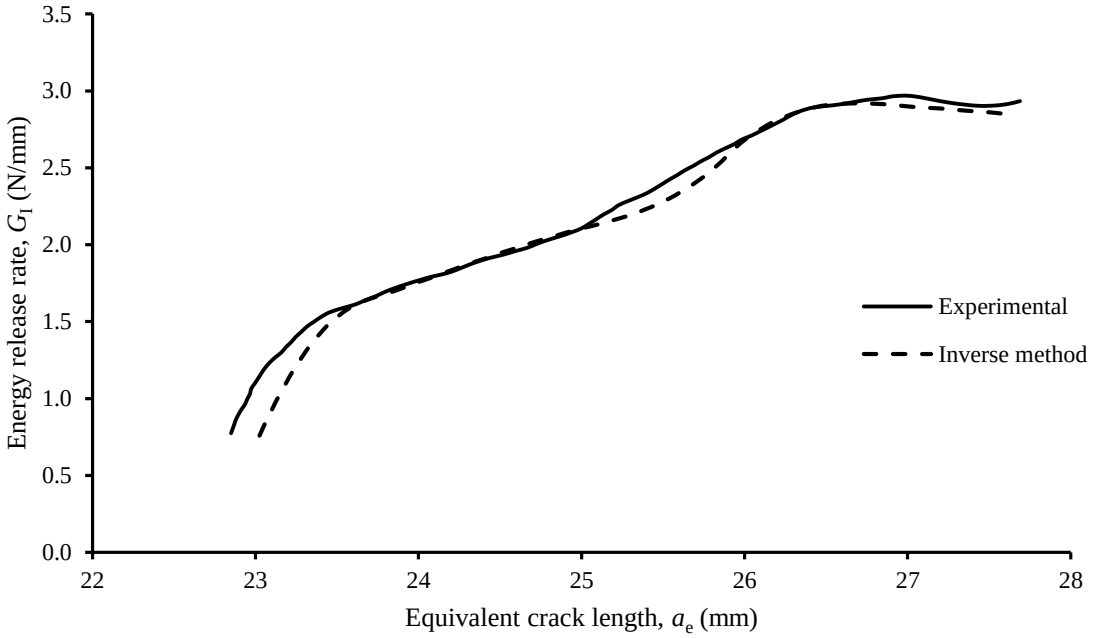

(b)

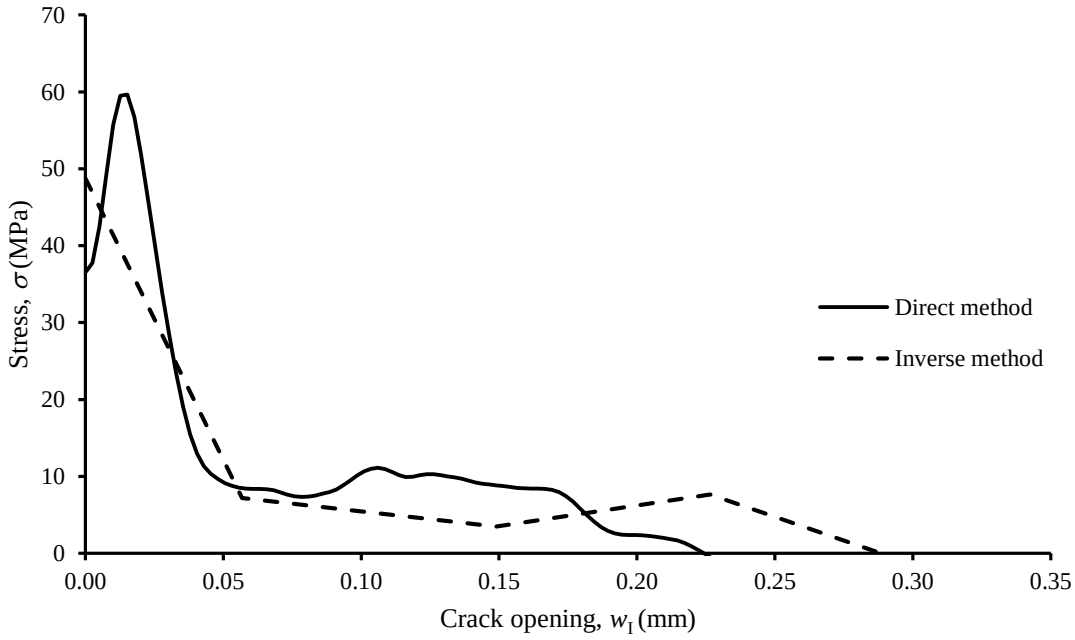

(c)

Fig. 2.29 – Comparison between the experimental and numerical curves identified by the developed inverse optimization method: (a) P-δ curves, (b) R-curves and (c) cohesive laws (specimen 5).

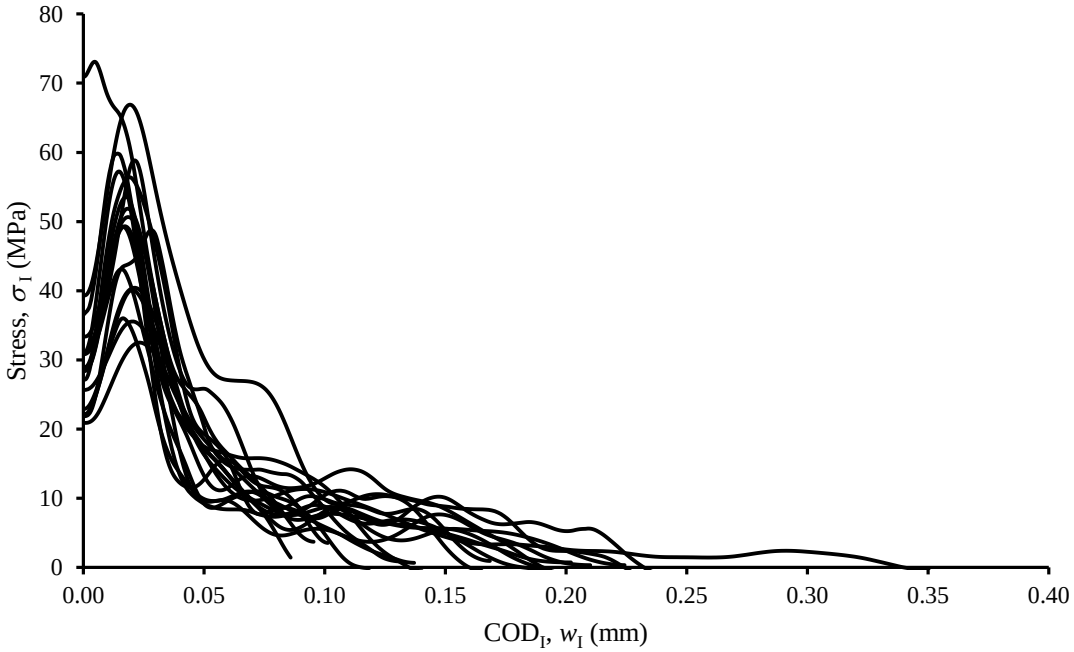

Fig. 2.30 – Cohesive laws obtained by the direct method.

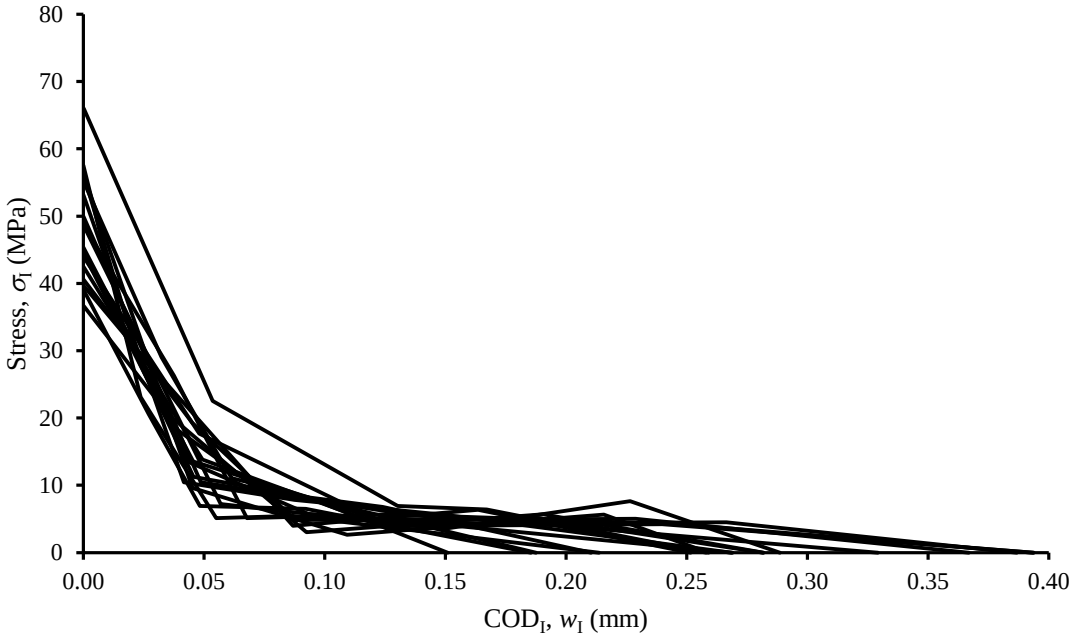

Fig. 2.31 – Cohesive laws obtained by the developed inverse method.

Although a significant number of variables influence the fracture properties in cortical bone, such as the age, mass fraction, location, used method, material origin, among others, a comparison between the present results and the ones obtained by other authors was performed to assess the performance of the procedures used in this work. Nevertheless, only a few works detailing the identification of the ultimate strength of cortical bone for the transverse direction can be found in the literature. Burstein et al. (1972) obtained a value of 52 MPa using cortical bone from bovine femur. On the other hand, Ural and Vashishth, (2006) achieved 43.5 MPa for human cortical bone from a donor with 50 years old. Pereira et al., (2012) determined a value of 36.0 MPa in cortical bone from bovine femur. This result was obtained using a developed inverse method based on genetic algorithms on a sample with fracture energy significantly lower than the value achieved in this work. Analysing the average values identified for ultimate strength by the direct and developed inverse methods (Table 2.7), it can be settled that these results correspond to a typical value for this material. In addition, it should be emphasized that both methods (i.e., direct and inverse) have propitiated the same result based on the test-*t* student (p>0.05). In general, inverse problems may not lead to a unique solution. This means that there may exist several combinations of stress values that lead to the minimization of the defined objective function. Therefore, the physical meaning of the solution is a good way to evaluate the issued result. Consequently, it can be concluded that this method provides an acceptable identification of the referred parameters of the cohesive laws.

The area circumscribed by the experimental cohesive laws ($G_{law,I}$ in Table 2.7) was achieved by numerical integration process. It is important to refer that the average fracture energy issuing from the *R*-curves (G_{Ic}=2.53 N/mm) is in agreement with the average one resulting from this process ($G_{law,I}$=2.58 N/mm). This statement means that all the procedure used to get the cohesive laws is working properly.

Table 2.7 – Cohesive laws. $\sigma_{I,u}$, ultimate strength, w_{Ic} ultimate relative displacement, $G_{law,I}$ circumscribed cohesive law area (non-valid test: -).

	Direct method			Inverse method	
Specimen	$\sigma_{I,u}$ (MPa)	w_{Ic} (mm)	$G_{law,I}$ (N/mm)	$\sigma_{I,u}$ (MPa)	w_{Ic} (mm)
1	73.09	0.10	2.94	45.00	0.37
2	49.24	0.09	2.01	56.25	0.12
3	49.31	0.19	2.99	42.50	0.39
4	59.63	0.19	2.99	48.72	0.29
5	43.10	0.12	1.92	57.53	0.21
6	32.50	0.19	2.29	44.53	0.27
7	58.83	0.17	3.15	44.00	0.39
8	48.75	0.13	2.59	39.71	0.25
9	35.50	0.34	2.78	53.18	0.27
10	56.40	0.14	2.52	55.21	0.15
11	36.01	0.14	1.73	39.07	0.19
12	40.07	0.14	2.42	45.36	0.21
13	50.64	0.22	2.85	48.75	0.33
14	51.84	0.21	2.48	56.21	0.26
15	40.42	0.20	2.45	36.72	0.28
16	57.20	0.23	3.04	49.98	0.39
17	53.53	0.18	2.65	40.61	0.28
Average	49.18	0.18	2.58	47.25	0.27
CoV(%)	21.3	33.9	16.1	14.0	30.1

2.8 - Conclusions

This section summarizes the main conclusions of the DCB test applied to bone fracture characterization under mode I loading. It can be settled that:

- the method used to access the mass fractions and porosity content seems to be adequate considering the low coefficient of variation;
- no significant correlation was found between the fracture energy and other evaluated material parameter;
- the DIC technique is able to measure the COD_I, since the average critical opening displacement (170 μm) is much larger than the displacement resolution (0.04-0.08 μm);
- the direct method provides an entire identification of cohesive law based only on experimental information and without imposing any constraint in the shape of the law;
- the two algorithms developed in the context of inverse method are able to identify the cohesive law typical of cortical bone; *Bissection* method proved to be more efficient;
- *Bissection* method linked to a finite element model with a shape free cohesive law with four linear branches and based only on adjustment between the P-δ curves, revealed to be efficient on the identification of the cohesive law; it was then concluded that the four branches considered for the cohesive law seem to be enough to identify an unconstrained shape;
- comparing the direct and the inverse laws it can be concluded that they provide solutions statistically equivalents, i.e., the cohesive laws obtained by both methods are consistent each other.

CHAPTER III

Fracture behaviour of cortical bone under pure mode II loading

3.1 - Introduction

This Chapter presents the work related to fracture characterization of cortical bone under pure mode II loading conditions. End-Notched Flexure (ENF) tests were carried out to identify the *Resistance*-curve. Specimens' production and microstructure analysis were performed following procedures described in previous chapter. Careful choice of specimen dimensions was performed in order to guarantee self-similar crack growth for a given crack extent. This condition is fundamental to be fulfilled in order to provide valid measurement of fracture energy.

The identification of the cohesive laws under mode II loading was performed by means of the direct and inverse methods. The direct method requires the measurement of mode II crack opening displacements (COD_{II}) in the course of the experimental tests. As in the mode I fracture characterization, the DIC technique was successfully applied. The inverse method combines numerical simulation with an optimization algorithm. Both methods were validated by numerical analysis. The cohesive laws obtained by the two methods are statistically in agreement which confirms the validity of the followed procedure.

3.2 - Experiments

Cortical bone used to fabricate the specimens was harvested from the mid-diaphysis of ten young bovine femurs. The procedure followed to produce the samples is similar to the one described in Section 2.2. The specimen configuration, dimensions and orientation are similar to the ones of the DCB specimen. The only difference relies on the absence nonexistence of holes in the specimen arms. Before the execution of experimental tests,

two samples from each specimen were harvested for gravimetric and microstructural analysis of the bone tissue. The applied method was detailed in Section 2.2.

Figure 3.1 illustrates the testing setup of the performed ENF tests. In order to minimize spurious friction effects during the mechanical test, two Teflon® films with a pellicle of lubricant between them were introduced in the pre-crack region (Fig. 3.1). Load–displacement (P–δ) curves were obtained using a servo-electrical testing system (MicroTester INSTRON® 5848 – Dynamic Laboratory – ECT-UTAD), with constant displacement rate of 0.5 mm/min. A 2 kN load-cell was used and the data acquisition frequency set to 5 Hz.

For measurement of the COD_{II} a speckled pattern was created on the surface of each specimen prior to the mechanical test. The COD_{II} was then obtained by post-processing the displacement field at the initial crack tip using the digital image correlation technique (DIC). A more detailed description of this experimental method can be found in Section 2.3.

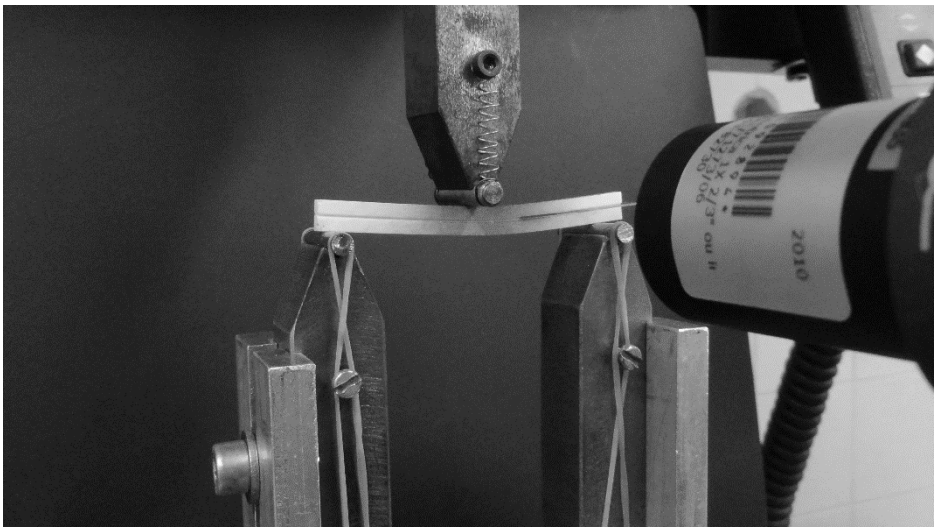

Fig. 3.1 – Testing setup of the ENF test.

3.3 - End Notched Flexure – Data reduction scheme

The ENF test consists of a three point bending test with a pre-cracked specimen (Fig. 3.2). As a result of the applied loading, sliding between the two arms occur leading to shear loading at the crack tip thus providing fracture characterization under mode II loading. In order to determine the energy release rate the CBBM method adapted for mode II loading was applied. In fact, the classical data reduction schemes based on crack length monitoring during the test are particularly difficult to apply in mode II tests since crack

grows with their faces in contact (Fig. 3.3), which makes its rigorous monitoring an almost impossible task. As described for mode I fracture characterization, the CBBM is based on an equivalent crack length estimated from the specimen compliance and using the Timoshenko beam theory.

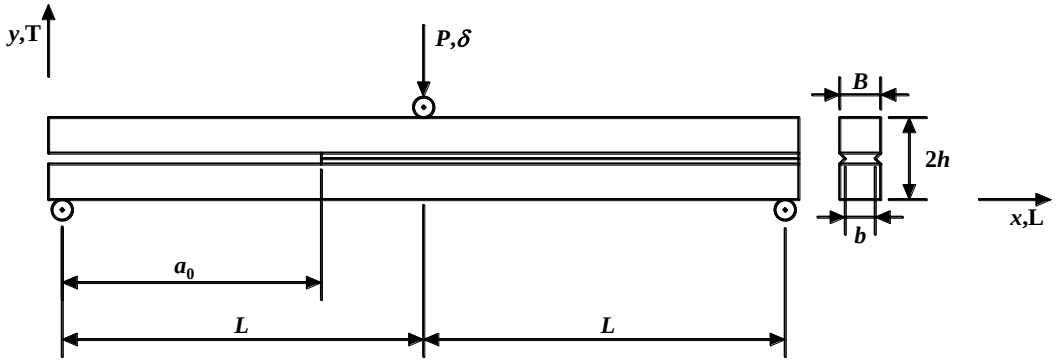

Fig. 3.2 – Schematic representation of the ENF test specimen.

The strain energy of the ENF specimen due to bending and shear effects is given by

$$U = \int_0^{2L} \frac{M_{\mathrm{f}}^2}{2E_{\mathrm{L}}I} dx + \int_0^{2L} \int_{-h}^{h} \frac{\tau^2}{2G_{\mathrm{LT}}} B\, dy\, dx \tag{3.1}$$

where M_{f} is the bending moment, E_{L} the elastic modulus in the longitudinal direction, I the second moment of area of the specimen section, B the specimen width and G_{LT} the shear modulus of the LT plane. It should be noted that the integration domain in x direction is divided in three segments (i.e., $0 \le x < a$, $a \le x < L$, $L \le x < 2L$). The shear stress is given by Eq. (2.9). Considering the Castigliano theorem ($\delta = \mathrm{d}U/\mathrm{d}P$) the specimen compliance becomes (de Moura et al., 2006),

$$C = \frac{3a^3 + 2L^3}{8Bh^3E_{\mathrm{L}}} + \frac{3L}{10BhG_{\mathrm{LT}}} \tag{3.2}$$

There are some aspects that can affect the accuracy of Eq. (3.2) when applied to the present case. Effectively, crack tip root rotation and stress concentration is not accounted for when beam theory is considered. Additionally, bone is a natural material presenting pronounced scatter in its elastic properties. These aspects can be indirectly taken into account by means of a corrected elastic modulus E_{f} obtained from Eq. (3.2) using the initial values of crack length (a_0) and compliance (C_0), as follows

$$E_{\mathrm{f}} = \frac{3a_0^3 + 2L^3}{8Bh^3} \left(C_0 - \frac{3L}{10BhG_{\mathrm{LT}}} \right)^{-1} \tag{3.3}$$

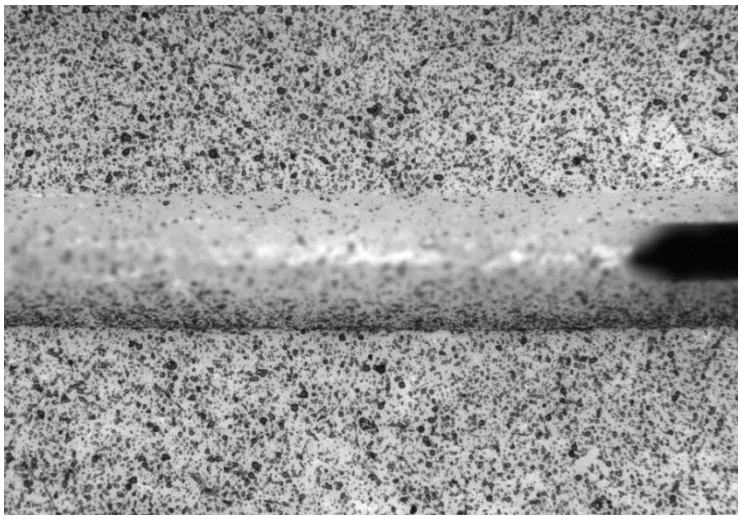

Fig. 3.3 – Crack-tip detail in bone.

Therefore, during crack growth the current compliance C is used to estimate an equivalent crack length a_e through Eqs. (3.2-3.3),

$$a_e = \left[\frac{C_c}{C_{0c}} a_0^3 + \frac{2}{3}\left(\frac{C_c}{C_{0c}} - 1 \right) L^3 \right]^{1/3} \tag{3.4}$$

where

$$C_c = C - \frac{3L}{10BhG_{LT}} \quad ; \quad C_{0c} = C_0 - \frac{3L}{10BhG_{LT}} \tag{3.5}$$

Using Eqs. (3.2,3.4) and Irwin-Kies relation (Eq. 2.19), $G_{II}=f(a_e)$ can be obtained as follows,

$$G_{II} = \frac{9P^2 a_e^2}{16bBh^3 E_f} \tag{3.6}$$

It should be referred that the width of the ligament section is affected by the presence of the longitudinal grooves. Consequently, the dimension b in Fig. 3.2 is used instead of the specimen width B. This procedure provides an easy achievement of the R-curve (i.e., $G_{II}=f(a_e)$) since it only depends on data issuing from the load-displacement curve, thus avoiding the problematic and probably inaccurate crack length measurement in the course of the test. In addition, the influence of the energy dissipated in a non-negligible fracture process zone is indirectly taken into account, since the current specimen compliance is used to get the a_e.

3.4 - Identification of cohesive laws - direct method

As already done for mode I loading the cohesive law characterizing mode II fracture of cortical bone was determined by means of the so-called direct method. In this case, the direct method consists of establishing the relation between the strain energy under mode II loading (G_{II}) and the crack opening displacement in mode II (w_{II}), i.e. $G_{II}=f(w_{II})$, which was fitted by spline function method. The differentiation of this fitted relation relative to crack tip shear displacement leads to the cohesive law under mode II loading.

Figure 3.4 shows the relative shear displacement at the notch tip proving the existence of sliding, characteristic of mode II loading. It should be emphasized that propagation follows the path defined by the lateral grooves at the specimen half-height, which is crucial to avoid unwanted mixed-mode loading. The COD_{II} corresponds to the absolute difference between the points localized above and below the lateral grooves (plotted squares in Fig. 3.4).

The direct method was validated by means of a numerical simulation using a pre-established cohesive law. Hence, a FE mesh (Fig. 3.5) was created using a finite element code with 1080 two-dimensional plane stress solid elements and 106 interface finite elements positioned along the crack path (i.e., ligament section). Dimensions used in the simulation are listed in Table 3.1 and correspond to mean values registered experimentally. In order to simulate the effect of the lateral grooves, the width of cohesive elements was considered equal to *b* instead of *B* used for the width of the arms. Elastic properties introduced in the model can be consulted in Table 2.2. Boundary conditions were simulated assuming null vertical displacements at the supports (Fig. 3.5) and restricting the horizontal movement on top central node to avoid rigid body movements. Load was applied imposing a vertical displacement at the central upper node, thus reproducing the effect of the actuator.

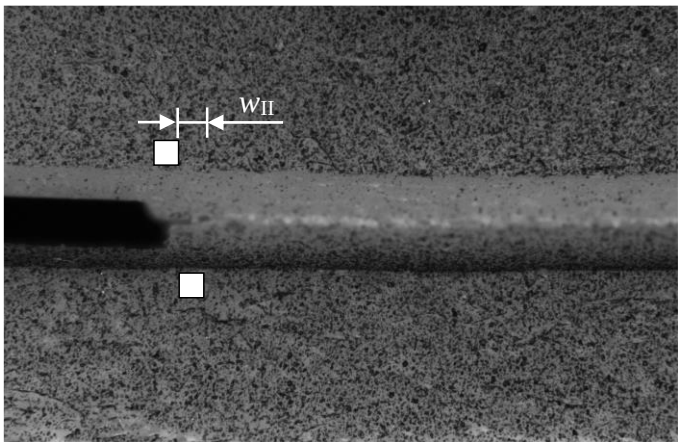

Fig. 3.4 – Crack propagation in mode II at the peak load: the white squares identify the DIC points.

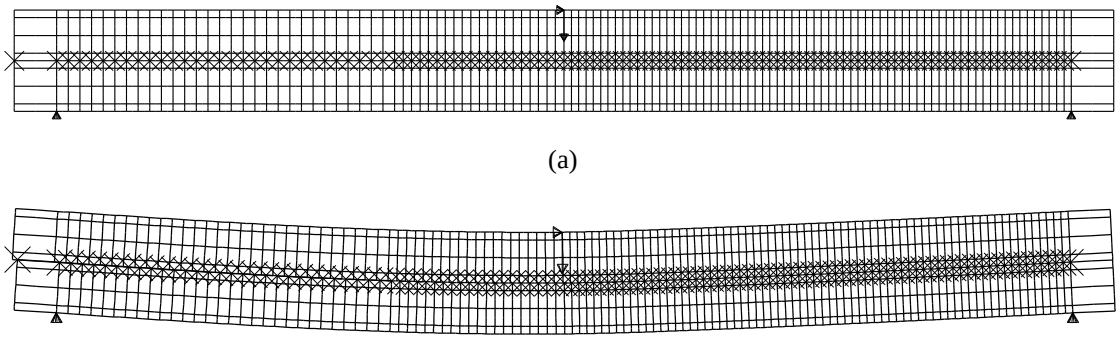

(a)

(b)

Fig. 3.5 – Finite element mesh used in the ENF test: (a) undeformed configuration, (b) deformed configuration (diagonal crosses represent the cohesive elements).

Some preliminary mode II fracture tests in bone have shown high values of mode II toughness. Anyway, the *R*-curves revealed a plateau which means that self-similar crack growth has occurred. As a consequence, it was decided to use a trapezoidal cohesive zone model in the numerical analysis to simulate damage onset and growth (Fig. 3.6). This law permits to consider higher area (i.e., fracture energy) than the simpler bilinear cohesive law without increasing markedly the ultimate relative shear displacement, which would preclude self-similar crack growth owing to restrictions on specimen dimensions. Table 3.2 presents the cohesive parameters used in the numerical model.

Table 3.1 – Dimensions used in the numerical model.

$2L$ (mm)	a_0 (mm)	B (mm)	b (mm)	$2h$ (mm)
60	19.55	2.91	1.53	6.0

Table 3.2 – Parameters of the cohesive law for mode II loading for bovine cortical bone.

G_{IIC} (N/mm)	$\sigma_{II,u}$ (MPa)	$w_{II,1}$ (MPa)
3.11 [+]	59.5*	0.018*

[+] Experimental result
* From (Dourado et al., 2013).

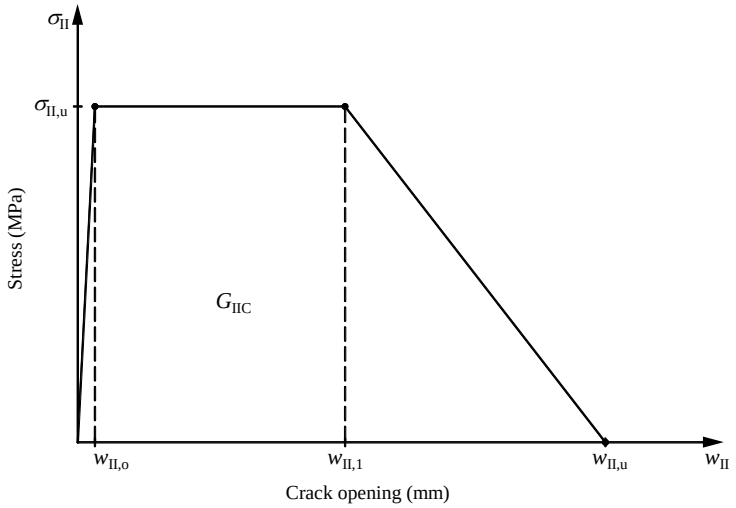

Fig. 3.6 – Trapezoidal cohesive law used for mode II fracture characterization of bovine cortical bone.

Figure 3.7 shows the agreement between the cohesive law determined by the direct method and the one that was introduced in the numerical simulation. Globally, a good agreement was obtained. The only significant difference is on the early stages of COD_{II}, which is attributed to the high initial stiffness used in the cohesive zone modelling $\left(\text{i.e.}, 1\times10^{6}\ \text{N}/\text{mm}^{3}\right)$, which causes difficulties in the fitting procedure applied to the G_{II}=f(w_{II}) relation.

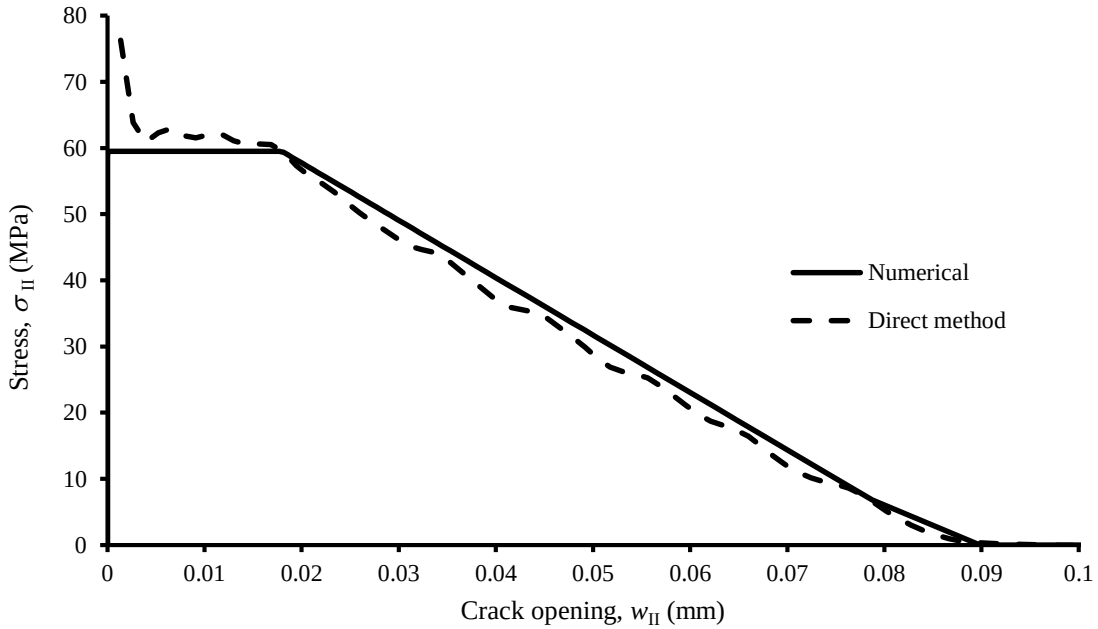

Fig. 3.7 – Comparison between the mode II cohesive law used as input in the model and the one obtained by the direct method.

A comparison between numerical and experimental load-displacement curves was also performed (Fig. 3.8), since the fracture energy used as input in the numerical model was the mean experimental value. In spite of the large scatter typical of a natural material it is possible to state that the numerical curve reflects the global behaviour revealed by the experimental ones.

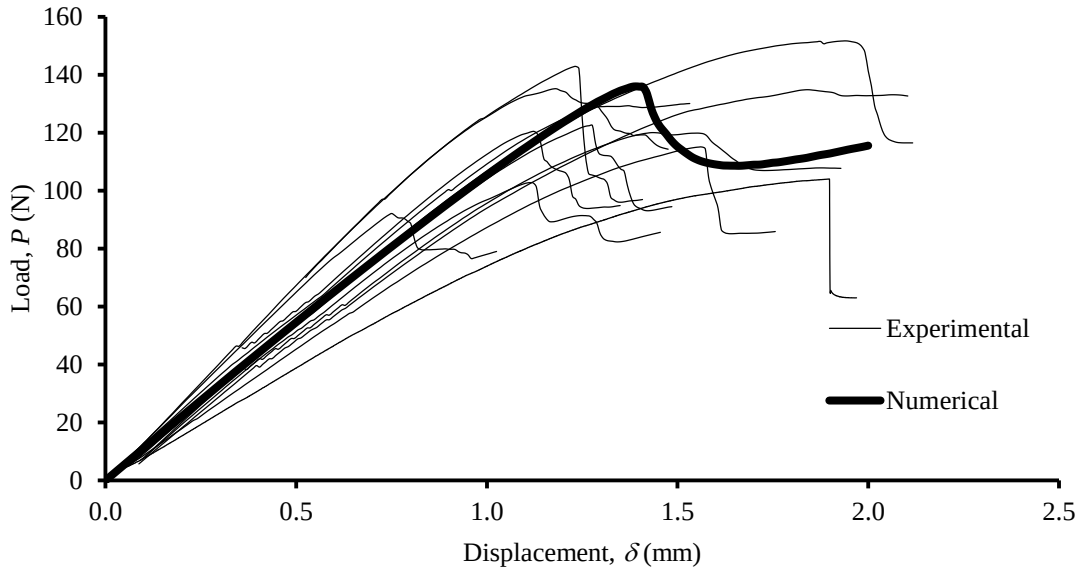

Fig. 3.8 – Experimental and numerical load-displacement curves of the ENF test.

3.5 - Identification of cohesive law - new inverse method

For the identification of the cohesive law under mode II loading the optimization algorithm called *Bissection* (detailed in Section 2.5) was also applied. The developed algorithm using the *Nelder Mead* method was not applied because this method is computationally more expensive. For the sake of validation, the numerical model presented in Section 3.4 was used considering a shape free cohesive law with four descending linear branches, similarly to the procedure followed for mode I in Section 2.5.

The comparison between the load-displacement curve obtained from the cohesive law used as input in the numerical simulation (Fig. 3.7) and the one achieved through an optimization procedure is visible in Fig. 3.9 (designated as Reference and Bissection Algorithm, respectively). A similar comparison is presented in Fig. 3.10 for the *R*-curves. It can be concluded that the defined objective function has led to an excellent agreement between the two curves. Globally, it can be stated that the cohesive law issuing from the *Bissection*

method follows with good approximation the one used as input in the numerical simulation (Fig. 3.11).

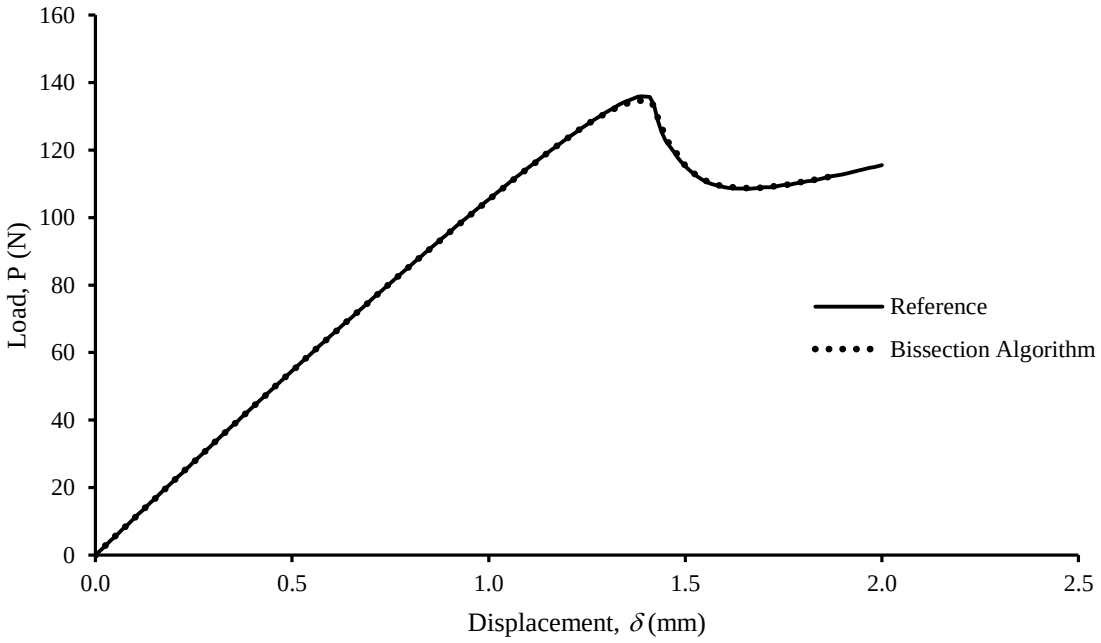

Fig. 3.9 – Comparison between determined and reference load-displacement curves.

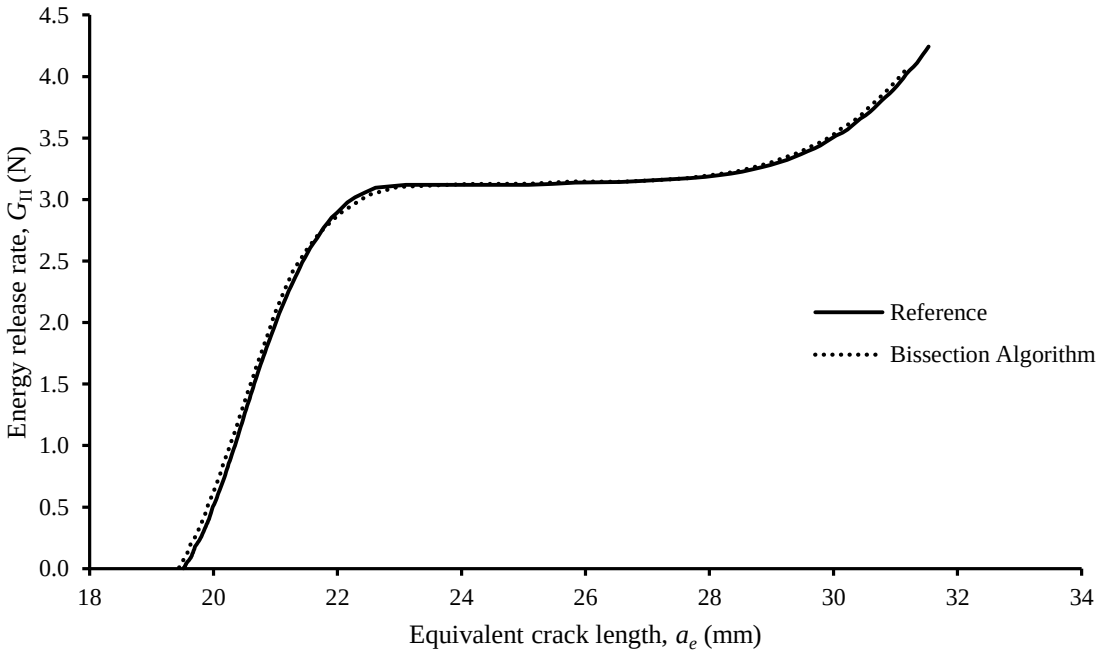

Fig. 3.10 – Comparison between determined and reference *R*-curves.

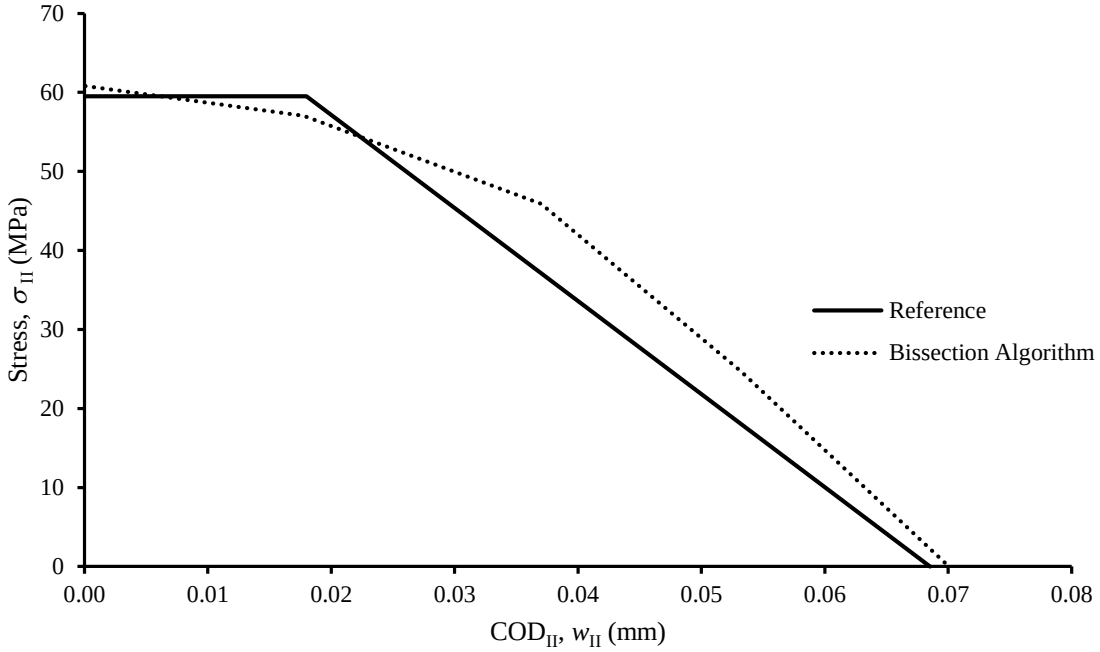

Fig. 3.11 – Comparison between determined and cohesive law used as input.

3.6 - Analysis and discussion of experimental mode II *R*-curves

The mode II *R*-curves were obtained following the CBBM method described in Section 3.3. In this context, data issuing from the load-displacement curves (Fig. 3.8) were used to get the mode II *R*-curves presented in Fig. 3.12.

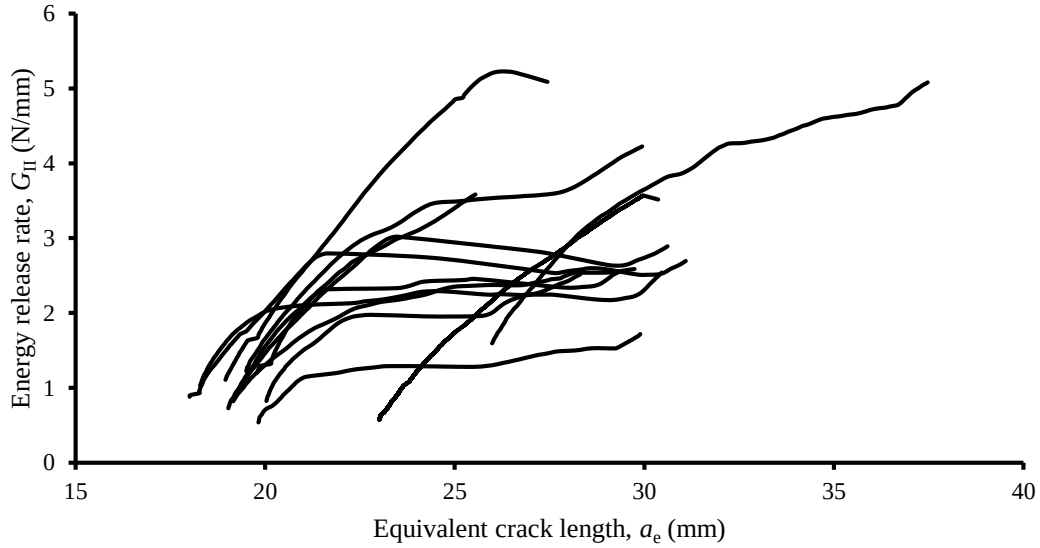

Fig. 3.12 – Mode II fracture *R*-curves of bovine cortical bone.

Two statements should be pointed from the observation of these curves: the large scatter, exceeding the one observed for mode I, can be viewed as the negative aspect; the positive perspective is related to the attainment of a plateau in practically all the tests revealing that self-similar crack growth under constant fracture energy took place for a given crack extent. This is a relevant aspect since in the ENF test it is common the existence of confinement of the FPZ in the vicinity of the central loading point and bone does not provide quite long specimens. The existence of plateaus in the generality of the *R*-curves validates the utilization of the ENF test with the proposed dimensions as an adequate fracture test for fracture characterization of cortical bone under mode II loading.

All experimental results are grouped in Table 3.3 and were considered valid by the Chauvenet criterion.

Table 3.3 – Experimental results. G_{IIc}, fracture energy; d_h, apparent density; m_w, water mass fraction; m_o, organic mass fraction; m_m, mineral mass fraction; *Por* porosity.

Specimen Number	G_{IIc} (N/mm)	d_h (g/cm^3)	m_w (%)	m_o (%)	m_m (%)	*Por* (%)
1	3.84	2.06	11.45	24.03	64.53	4.67
2	2.99	1.95	12.38	22.79	64.83	4.25
3	2.80	2.02	11.77	24.25	63.98	4.13
4	2.13	2.00	11.78	23.07	65.16	3.23
5	1.29	1.99	11.52	23.40	65.08	3.39
6	2.32	2.04	12.30	23.00	64.71	4.30
7	5.21	2.04	11.75	22.66	65.59	4.31
8	2.37	2.03	12.02	22.75	65.24	4.35
9	3.02	2.03	11.62	23.09	65.30	3.59
10	1.97	2.02	11.63	22.73	65.64	3.68
11	3.48	2.01	11.72	22.21	66.07	4.33
12	4.54	2.05	11.87	21.73	66.40	5.21
Average	3.00	2.02	11.82	22.98	65.21	4.12
CoV(%)	37.4	1.5	2.4	3.0	1.0	13.6

Pearson product-moment correlation coefficients were calculated to identify any relationship between the mechanical properties (G_{IIc} and E_f) and the material composition parameters (d_h, m_w, m_o and m_m). Examining the correlation coefficients, no significant ($p > 0.05$) correlations with the fracture energy have been found. The gravimetric analysis revealed results similar to the mode I samples, which means that they can be considered typical results pointing to the same nature of the material and allowing to combine the fracture energy values for the two modes. The average energy release rate obtained to pure mode II, (i.e., G_{IIc}=3.0 N/mm) is of the same order of the values found in other works (Table 3.4). The differences are probably associated to the used experimental test method and the natural variability of the material issued from different sources.

Table 3.4 – Values of fracture energy found in other works.

Reference	Bone Type	Experimental Test	G_{IIc} (N/mm)
(Norman et al., 1996b)	Human Tibia	CS	4.2 ± 2.52
(Pereira et al., 2011)	Bovine femur	ELS	2.65 ± 0.21
(Dourado et al., 2013)	Bovine femur	ENF	2.25 ± 0.36

3.7 - Analysis and discussion: mode II cohesive law

The direct method detailed in Section 3.4 combines the data given by load-displacement curve and the digital image correlation (Figs. 3.13-3.14) to obtain the evolution of the energy release rate (G_{II}) as a function of crack tip shear displacement (w_{II}).

The displacements were directly measured by DIC technique. Figure 3.15 presents the evolution of the mode I and mode II crack opening displacements as functions of the applied displacement. The mode I component is much smaller comparatively to the mode II component, excluding the vicinity of start crack advance (near the peak load) and the crack propagation phase. This finding could be explained by the asymmetry of damage distribution relative to the initial neutral plane of ENF specimen, prompted by the crack propagation. However, this phenomenon does not hinder the proper identification of mode II cohesive law, which is determined by the experimental data recorded up to the peak load (i.e. during the development of FPZ).

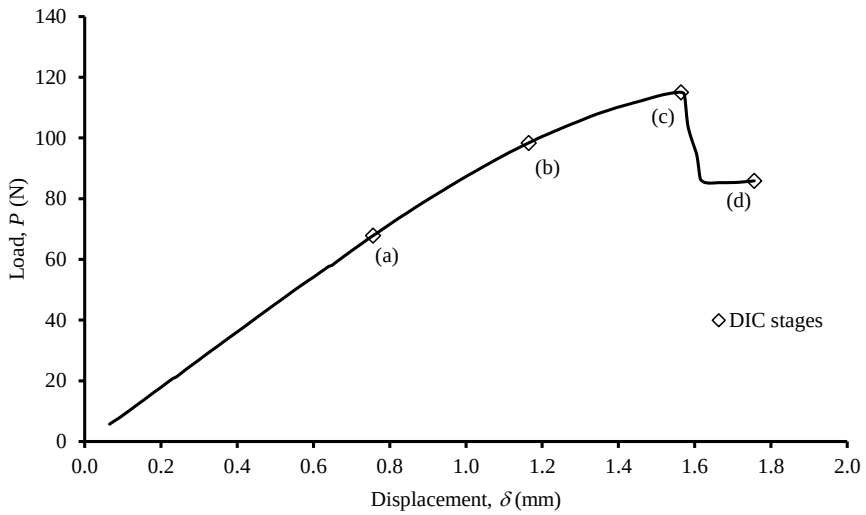

Fig. 3.13 – Load-displacement curve of an ENF test (specimen 17) - plotted letters correspond to stages presented in Fig. 3.14.

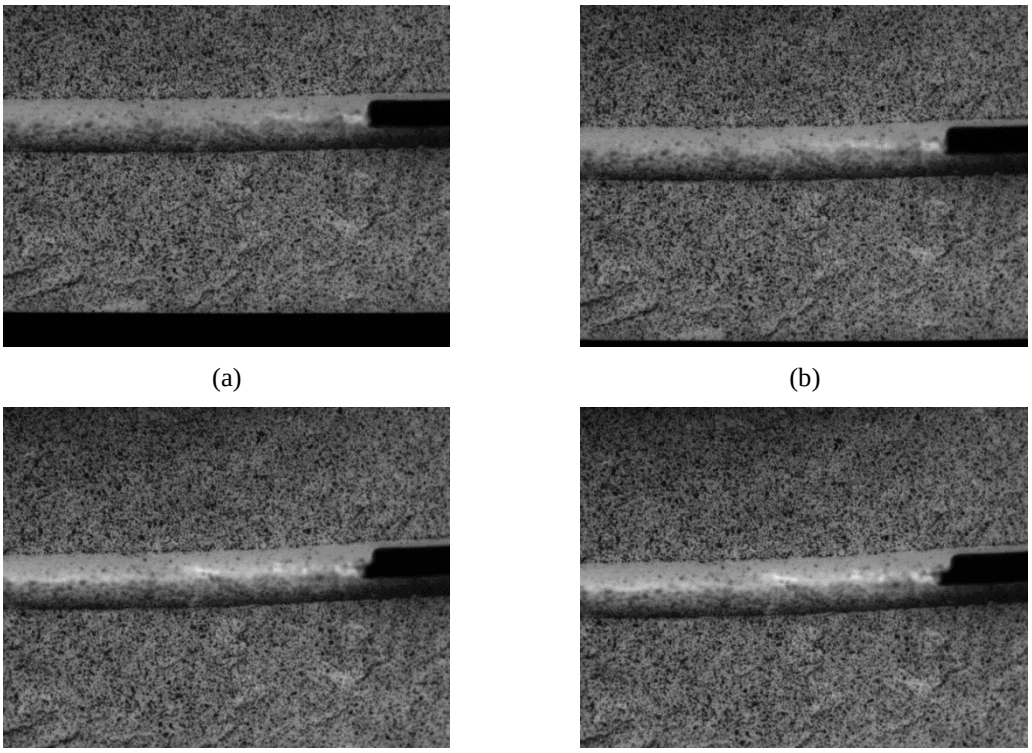

Fig. 3.14 – Crack evolution: (a) initial stage, (b) intermediate stage, (c) load peak - propagation onset and (d) significant propagation (specimen 17).

The mode II cohesive laws of cortical bone identified by means of the direct method are presented later (Fig. 3.17) and they will be discussed along with the cohesive laws determined by the inverse method presented above (section 3.5).

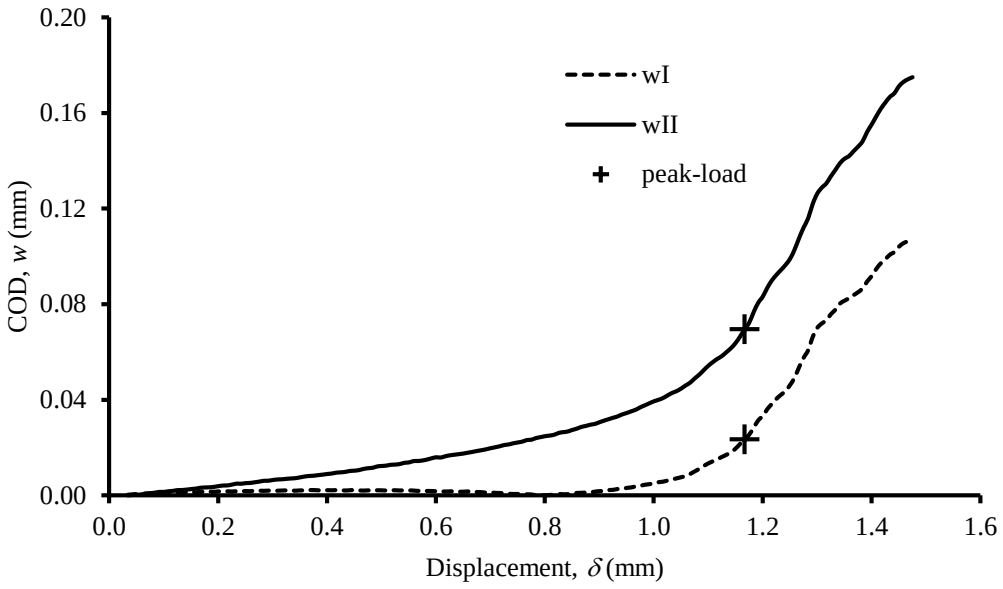

Fig. 3.15 – Evolution of crack opening displacements with the applied displacement.

Figure 3.16 shows an example of the agreement achieved between the numerical curve obtained by the inverse method and the experimental one. Figures 3.16a and 3.16b reveal that good agreement was obtained for the load-displacement and *R*-curves. The observed difference between the cohesive laws (Fig. 3.16c) identified by the direct (denoted as Experimental) and the inverse methods (denoted as Numerical) is due to the method differences. Anyway, it should be emphasized that the global trend is in agreement. These results highlight the capability of the cohesive numerical model to reproduce the mode II fracture phenomenon in cortical bone.

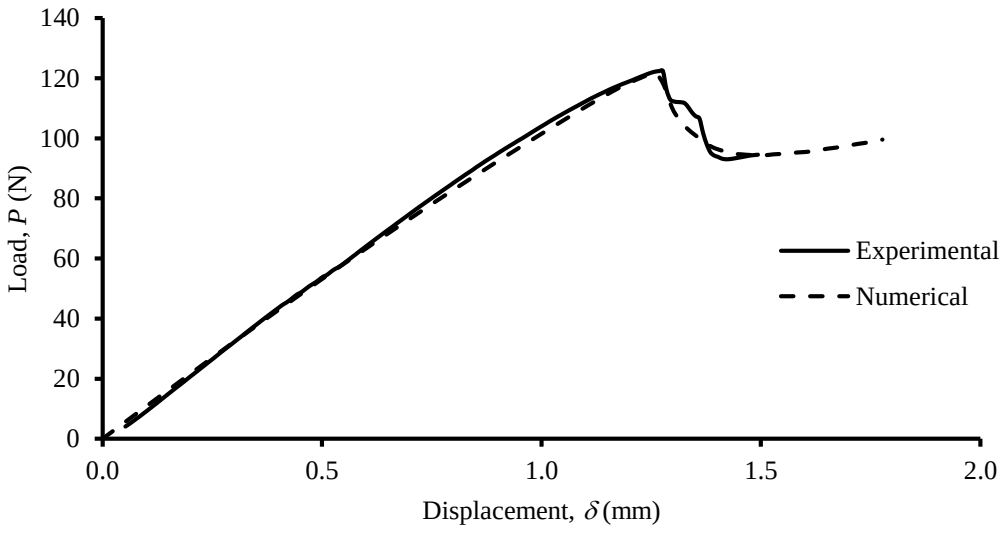

(a)

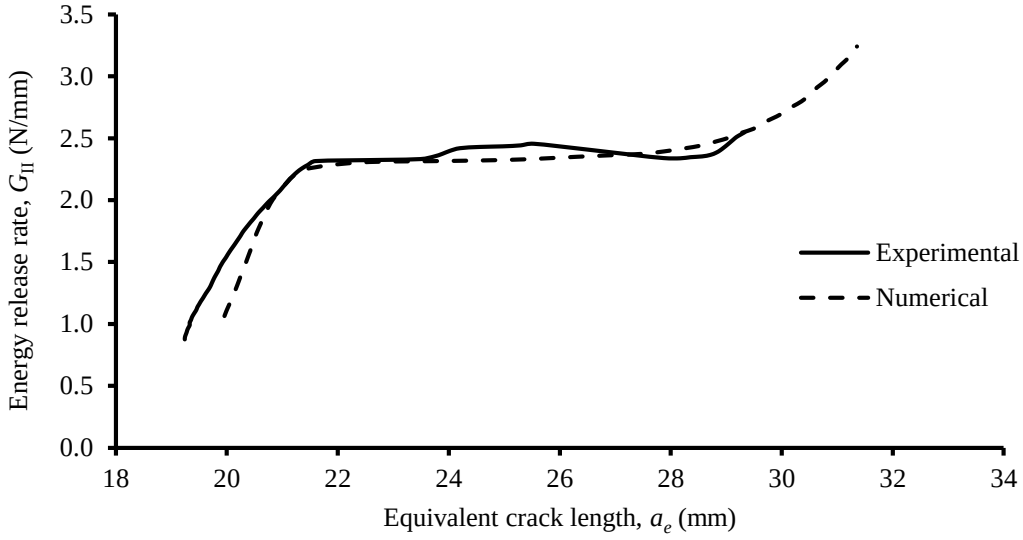

(b)

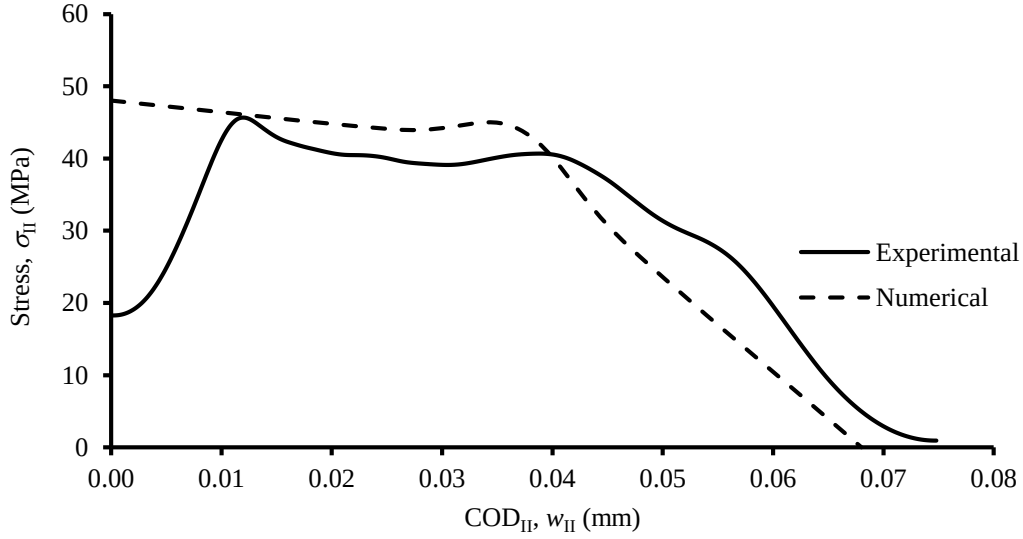

(c)

Fig. 3.16 – Comparison between the experimental (direct method) and numerical curve identified by the inverse optimization method: (a) *P*-δ curves, (b) *R*-curves, (c) Cohesive laws (specimen 14).

Figures 3.17 and 3.18 present the cohesive laws determined respectively by the direct and inverse methods. The detailed results can be consulted in Table 3.5. A comparison between the average values obtained for the shear strength show an acceptable difference between the results issued from the two methods. In fact, the average shear strength identified by the inverse method is 16% higher than the one obtained with the direct method. This result can be explained by the existence of a small mode I component that was revealed in the experimental work which is indirectly accounted for in the direct method, although the

inverse method works in pure mode II. Nevertheless, the results obtained by the two methods were compared using the test-*t*. In light of this, the two results were considered statistically equivalent.

Shear strength in bone has been measured by several authors (Table 3.6), although most of them refer to human cortical bone. Anyway, it can be concluded that they are similar to the ones obtained in this work.

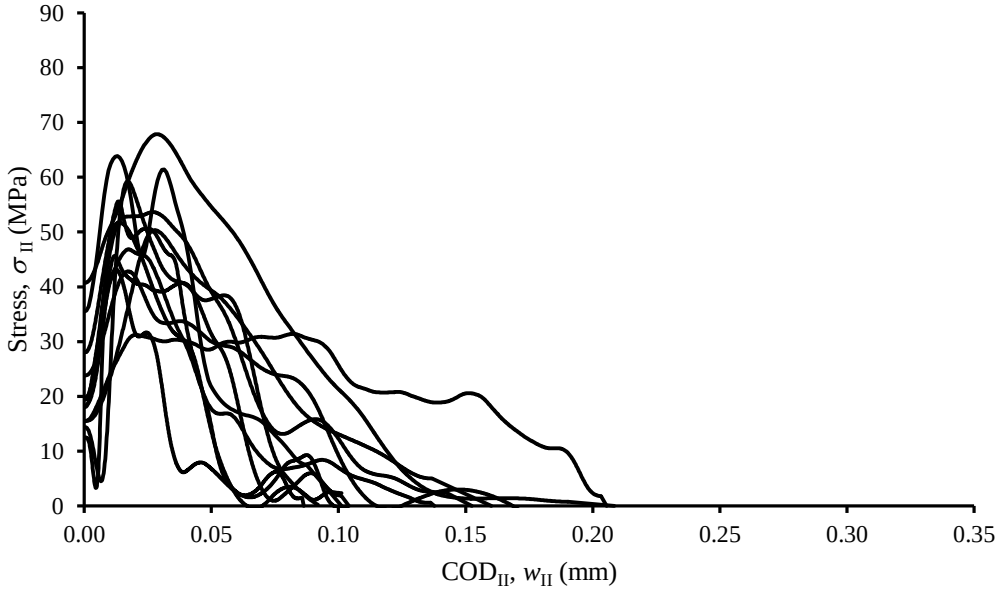

Fig. 3.17 – Mode II cohesive laws obtained by the direct method.

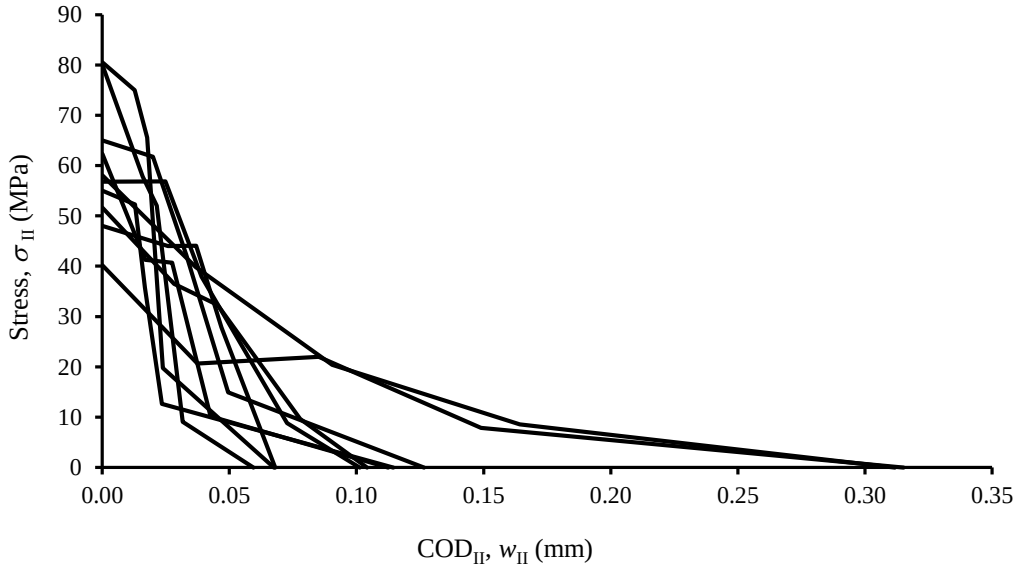

Fig. 3.18– Mode II cohesive laws obtained by the inverse method.

Table 3.5 – Experimental results. $\sigma_{II,u}$, ultimate cohesive shear strength; $w_{II,c}$, maximum mode II opening displacement; $G_{law,II}$, fracture energy evaluated form de cohesive law.

	Experimental			Numerical	
Specimen Number	$\sigma_{II,u}$ (MPa)	w_{IIc} (mm)	$G_{law,II}$ (N/mm)	$\sigma_{II,u}$ (MPa)	w_{IIc} (mm)
1	50.32	0.16	3.49	40.16	0.32
2	63.90	0.10	3.05	65.00	0.13
3	59.24	0.09	2.69	50.00	0.10
4	55.61	0.10	2.13	80.53	0.07
5	43.13	0.09	1.30	55.00	0.02
6	45.65	0.10	2.34	48.00	0.07
7	67.88	0.21	5.25	58.09	0.31
8	46.85	0.14	2.39	62.35	0.11
9	42.81	0.12	2.93	51.62	0.10
10	51.70	0.06	1.92	80.00	0.06
11	53.65	0.15	3.54	56.81	0.10
12	31.41	0.21	4.55	48.00	0.28
Average	51.01	0.13	2.97	57.96	0.14
CoV(%)	19.7	37.4	37.6	21.4	74.2

Table 3.6 – Shear strengths values found in other works.

Work	Bone Type	Experimental Test	σ_{II} (MPa)
(Turner et al., 2001)	Human femur	Iosipescu	51.6 ± 1.90
(Dong et al., 2013)	Human tibia	Inclined double notch shear	61.4 ± 6.30
(Dourado et al., 2013)	Bovine femur	Inverse method	59.5 ± 6.30
(Tang et al., 2015)	Human femur	Iosipescu	49.9 ± 6.20

3.8 - Conclusions

The main conclusions obtained during the fracture characterization of young bovine cortical bone under mode II loading conditions are:

- the correlation between fracture properties and the other measured quantities does not appear to be significant;
- the *R*-curves revealed a plateau which indicates that this test configuration allows the entire development of FPZ and satisfies the conditions of self-similar crack growth for a given crack extent; this result is very important owing to a valid fracture characterization under mode II;
- optimization *Bissection* method allied to a finite element analysis with cohesive elements following an unconstraint cohesive law are able to accurately identify the law for this material in an inverse procedure;
- the direct and inverse methods to get the cohesive laws were both validated numerically;
- comparing the local shear strengths obtained by the direct and the inverse methods, it can be concluded that they provide solutions statistically equivalents, i.e., the cohesive laws obtained by both methods are consistent each other; this fact allows concluding that the solution obtained by the inverse method points to a result with physical meaning.

CHAPTER IV

Fracture behaviour of cortical bone under mixed-mode I+II – SLB test

4.1 - Introduction

A first approach to the fracture characterization of cortical bone under mixed mode I+II is described. The Single Leg Bending (SLB) test was chosen due to its simplicity, because it basically consists in a three-point-bending test. As in pure mode loading cases, a data reduction scheme based on the equivalent crack length concept was used to overcome the difficulties inherent to crack length monitoring in the course of the test. The method was applied to the experimental load-displacement curves in order to obtain *Resistance*-curves (or *R*-curves) in each mode. The resulting values of the strain energy release rate components were plotted in the $G_I - G_{II}$ space and three energetic power laws were determined to simulate mixed-mode I+II damage numerically.

A direct method for the identification of the cohesive laws in each mode was applied numerically. In this context, the strain energy release rate components (G_I and G_{II}) as a function of the crack opening displacements in mode I (COD_I designated by w_I) and in mode II (COD_{II} designated by w_{II}), obtained in the numerical analysis using cohesive zone modelling, allowed identifying the components of the cohesive laws under mixed-mode I+II.

4.2 - Experiments

The SLB tests were performed using femurs from the same package utilized for an initial testing campaign of pure modes fracture characterization of bovine cortical bone detailed in Dourado et al. (2013) and Pereira et al. (2012). Consequently, the pure mode fracture values obtained in the referred works will be combined with the mixed-mode I+II results issuing from the SLB tests.

The specimens were harvested from fresh femurs (one day post-mortem) of young bovine, being immediately preserved in gauzes soaked in physiological saline at −20°C. The procedure to obtain the specimen configuration can be consulted in section 2.2. In the SLB test specimen it is necessary to cut the bottom arm of the specimen, which was performed using a precision cutting machine (Isomet® 5000) with a saw blade at 3000 rpm. Indeed, the SLB consists in a three-point-bending test which is performed in a specimen with a smaller bottom arm, leading to a direct contact between one support and the top arm (Fig. 4.1). The experimental tests were executed in a servo-electrical testing system (MicroTester INSTRON 5848 – Dynamic Laboratory – ECT-UTAD), using a constant displacement rate of 0.5 mm/min. The load–displacement curves ($P-\delta$ curves) were registered during the test and used in the developed data reduction scheme to evaluate the *R*-curves.

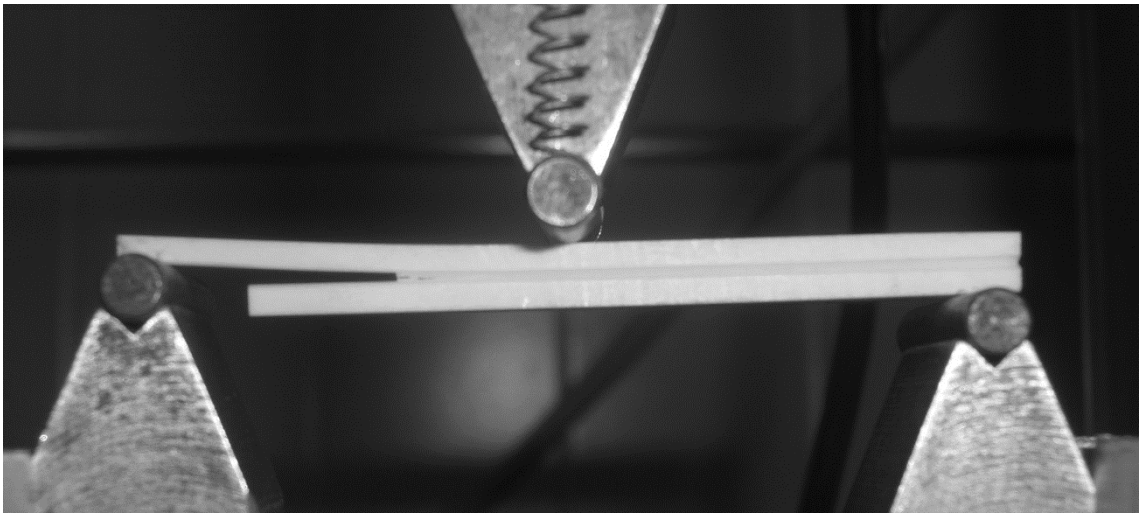

Fig. 4.1– Photography of the SLB experimental test applied to cortical bone.

4.3 - Single Leg Bending - data reduction scheme

Two methodologies were used to determine the *R*-curves. One was proposed by Szekrényes and Uj (2004), consisting in overlapping the Winkler elastic foundation model to the Timoshenko beam theory. This procedure allows determining the specimen compliance according to the crack length. Considering the specimen orientation shown in Fig. 4.2 the specimen compliance becomes Szekrényes and Uj (2004),

$$C = \frac{7a^3 + 2L^3}{8Bh^3E_{\mathrm{L}}} + \frac{a+L}{8BhkG_{\mathrm{LT}}} + \frac{a^3}{8Bh^3E_{\mathrm{L}}} \times \\ \times \left[2.71\left(\frac{h}{a}\right)\left(\frac{E_{\mathrm{L}}}{E_{\mathrm{T}}}\right)^{1/4} + 2.45\left(\frac{h}{a}\right)^2\left(\frac{E_{\mathrm{L}}}{E_{\mathrm{T}}}\right)^{1/2} + 1.11\left(\frac{h}{a}\right)^3\left(\frac{E_{\mathrm{L}}}{E_{\mathrm{T}}}\right)^{3/4} \right] \tag{4.1}$$

where k=5/6 is the shear correction factor. Using the Irwin-Keys equation (Eq.2.19), the energy release rate assumes this expression,

$$G_{\mathrm{T}} = \frac{21P^2a^2}{16Bbh^3E_{\mathrm{L}}} + \frac{P}{16BbhkG_{\mathrm{LT}}} + \frac{P^2a^2}{16Bbh^3E_{\mathrm{L}}} \times \\ \times \left[5.42\left(\frac{h}{a}\right)\left(\frac{E_{\mathrm{L}}}{E_{\mathrm{T}}}\right)^{1/4} + 2.45\left(\frac{h}{a}\right)^2\left(\frac{E_{\mathrm{L}}}{E_{\mathrm{T}}}\right)^{1/2} \right] \tag{4.2}$$

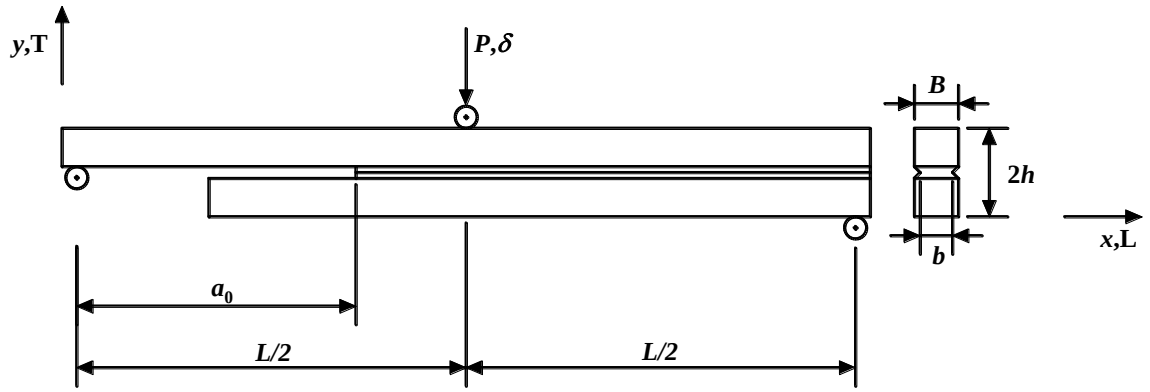

Fig. 4.2– Schematic representation of the SLB test.

Additionally, these authors adjusted the Williams (1988) method to perform the partition modes, obtaining the following expressions

$$G_{\mathrm{I}} = \frac{12P^2a^2}{16Bbh^3E_{\mathrm{L}}} + \frac{P^2}{16BbhkG_{\mathrm{LT}}} + \frac{P^2a^2}{16Bbh^3E_{\mathrm{L}}} \times \\ \times \left[5.42\left(\frac{h}{a}\right)\left(\frac{E_{\mathrm{L}}}{E_{\mathrm{T}}}\right)^{1/4} + 2.45\left(\frac{h}{a}\right)^2\left(\frac{E_{\mathrm{L}}}{E_{\mathrm{T}}}\right)^{1/2} \right] \tag{4.3}$$

$$G_{\mathrm{II}} = \frac{9P^2a^2}{16Bbh^3E_{\mathrm{L}}} \tag{4.4}$$

However, this method presents some drawbacks. The first one is the necessity to know a priori the elastic properties (particularly the E_{L}), which is not an easy task for natural materials characterized by non-negligible scatter in its elastic properties. On the other hand, this method implies the direct measurement of the crack length during the test. Alternatively, the determination of an equivalent crack length determined through the relation between compliance and crack length achieved in previous mechanical tests (compliance calibration method), can be followed. Both of these procedures present difficulties. As referred previously crack length monitoring during fracture tests is not easy. On the other hand, compliance calibration performed in different specimens is clearly affected by the scatter properties between specimens. In light of this, the compliance-based beam method (CBBM), already used for pure modes, was developed and applied for SLB test (Oliveira et al., 2009). This method is based on Timoshenko beam theory and specimen compliance to assess the equivalent crack length, thus overcoming evident limitations in crack monitoring during propagation. Following the same procedure described in previous Chapters for pure mode tests, the specimen compliance is determined as follows (Oliveira et al., 2009),

$$C = \frac{28a^3 + L^3}{32Bh^3E_{\mathrm{L}}} + \frac{3(a+L)}{20BhG_{\mathrm{LT}}} \tag{4.5}$$

where E_{L} and G_{LT} represent the elastic longitudinal and shear moduli, respectively. Due to scatter in the elastic properties of bone tissue, an effective flexural modulus E_{f} was used instead of E_{L}. This is accomplished considering in Eq. (4.5) the initial values of crack length a_0 and compliance C_0, leading to

$$E_{\mathrm{f}} = \left(C_0 - \frac{3(a_0+L)}{20BhG_{\mathrm{LT}}} \right)^{-1} \frac{28a_0^3 + L^3}{32Bh^3} \tag{4.6}$$

This procedure allows accounting for material variability, thus eliminating the influence of scatter in elastic properties on the measured fracture energy. In addition, a previous test to

evaluate the elastic modulus of each specimen is unnecessary. It should be noted that G_{LT} has a minor influence on the results (Dourado et al., 2013), which means that a typical value can be used.

During propagation, Eq. (4.5) can be used to evaluate an equivalent crack length (a_e) as a function of the current compliance (i.e., $C = \delta/P$). This crack length takes into account the rotation effect between the top and bottom arms at crack tip and the development of fracture process zone. Total fracture energy under mixed-mode (G_T) can be computed using the Irwin-Kies expression (Eq. 2.19),

$$G_T = \frac{21P^2a_e^2}{16Bbh^3E_f} + \frac{3P^2}{40BbhG_{LT}} \tag{4.7}$$

Considering the partition modes method proposed by Szekrényes and Uj (2004), mode I and mode II strain energy release rate components yield

$$G_I = \frac{12P^2a_e^2}{16Bbh^3E_f} + \frac{3P^2}{40BbhG_{LT}} \tag{4.8}$$

$$G_{II} = \frac{9P^2a_e^2}{16Bbh^3E_f} \tag{4.9}$$

This methodology allows identifying the *R*-curves without performing crack length monitoring. In addition, the energy consumed by the development of the fracture process zone influencing the load–displacement curve is taken into account, because the current compliance is used to compute the equivalent crack length.

It should be noted that for the case that the thickness of the specimen arms is the same (as used in this work), the ratio between Eq. (4.8), neglecting the shear term, and Eq. (4.9) provides a constant energetic mixed-mode ratio of G_I/G_{II} =1.33 throughout the test. The modification of this value is possible to accomplish in a certain range using specimens presenting arms with different arms. However, this task was not performed in this work owing to difficulties on specimen's fabrication.

4.4 - Numerical analysis of SLB test method

A two-dimensional numerical model using cohesive elements was developed to verify the ability of the SLB test on fracture characterization of cortical bone under mixed-mode I+II loading conditions. The finite element mesh (Fig. 4.3) was composed by 1010 two-

dimensional plane stress solid elements (width *B*, according to Fig. 4.2), with 106 interface finite elements disposed along the specimen half-height (width *b*, according to Fig. 4.2).

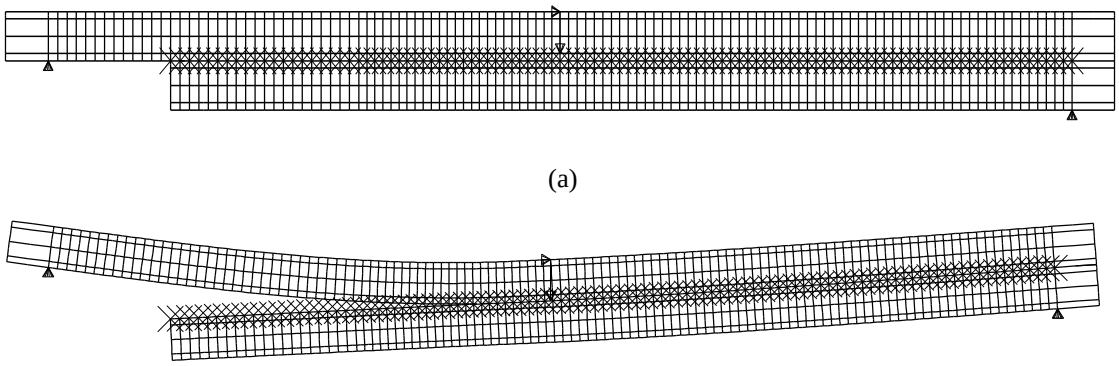

(a)

(b)

Fig. 4.3 – Finite element mesh used for the SLB test (a) undeformed configuration, (b) deformed configuration at peak load (diagonal crosses represent the cohesive elements).

Taking into account that this simulation was performed as a first attempt to characterize mixed-mode I+II fracture in cortical bone, all the model inputs (i.e., elastic and fracture properties) were taken from other works. In light of this, the used elastic properties correspond to the ones presented in Chapter 2 (Table 2.2) and dimensions (a_0 = 21.0 mm; B = 3.3 mm; b = 2.3 mm; h = 3.0 mm; L = 60 mm) which correspond to dimensions employed in a previous ENF test (Dourado et al., 2013) owing to similarity between the two tests (i.e., ENF and the SLB). The cohesive parameters introduced in the model can be consulted in Table 4.1.

Table 4.1 – Parameters of the cohesive law for mode I and mode II (Dourado et al., 2013; Pereira et al., 2012).

	$\sigma_{i,u}$ (MPa)	$w_{i,1}$ (mm)	$\sigma_{i,1}$ (MPa)	G_{ic} (N/mm)
Mode I (i = I)	36	0.07	4.9	1.77
Mode II (i = II)	59.5	0.018	59.5	2.25

Nodal boundary conditions were considered to simulate both the action of the loading cylinder and supports. A linear energetic criterion (α = 1 in Eq.1.10) was initially considered to simulate damage growth under mixed-mode I+II loading.

The numerical load-displacement curve shown in Fig. 4.4 reveals a pronounced non-linear behaviour with a continuous increase in load. Figure 4.5 shows that propagation occurs with a slight decreasing of the fracture process zone, which is an indication of some influence of the compressive zone created by the actuator. This problem is related to limitations on the specimen size or could be a result of inadequacy of the linear energetic criterion (Eq. 1.10 with $\alpha = 1$) assumed for crack propagation.

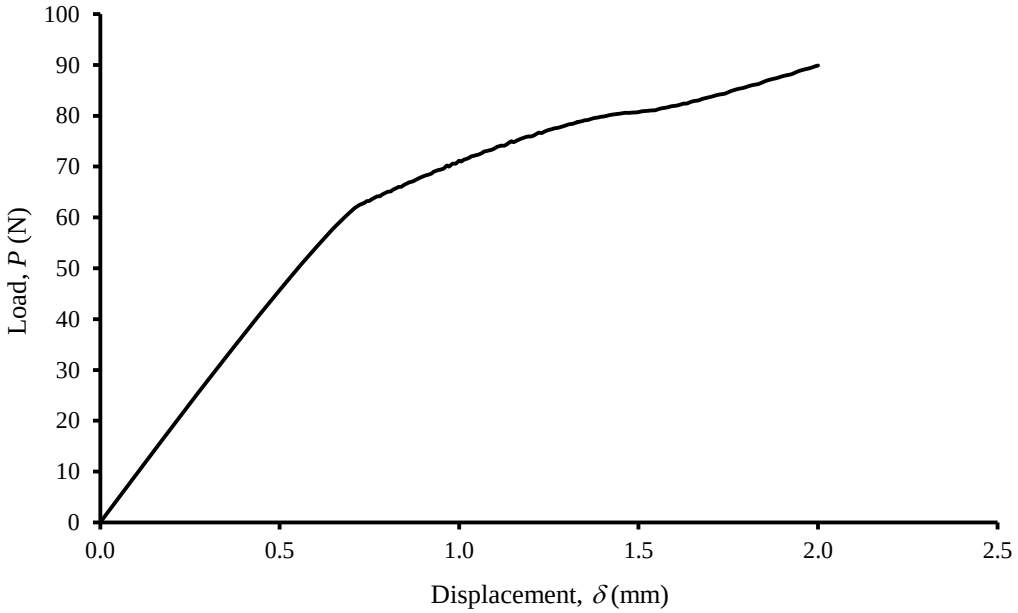

Fig. 4.4 – Numerical load-displacement curve of the SLB test.

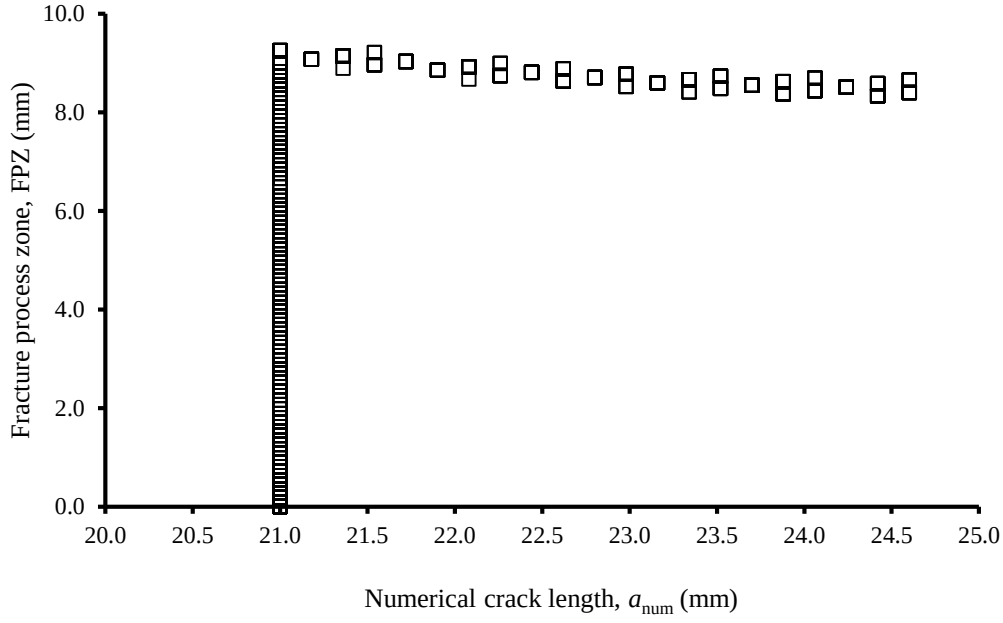

Fig. 4.5 – Evolution of fracture process zone.

Due to these unwanted results, additional numerical simulations were performed in order to evaluate the influence of the specimen dimensions on the attainment of an acceptable *R*-curve. With this goal, the specimen dimensions were adjusted in order to minimize the influence of the compressive load close to the actuator. Therefore, the crack length was decreased as well as the specimen height to maintain the beam conditions as close as possible, taking into account bone natural size restrictions. A satisfactory result was obtained with the following dimensions: a_0 = 17.5 mm; B = 3.0 mm; b = 1.6 mm; h = 2.5 mm; L = 60 mm. The P-δ curve issuing from this simulation is shown in Fig. 4.6. In this case, a typical curve is observed, with a well-defined peak load followed by a decrease promoted by crack growth, and with a subsequent increase by its end resulting from the compressive effects referred above. This load displacement relation led to *R*-curves with plateau (Fig. 4.7) in both methods (Szekrényes and CBBM). However, a clear difference between the *R*-curves determined from each method is also detected which will be thoroughly analysed later in the analysis of experimental results.

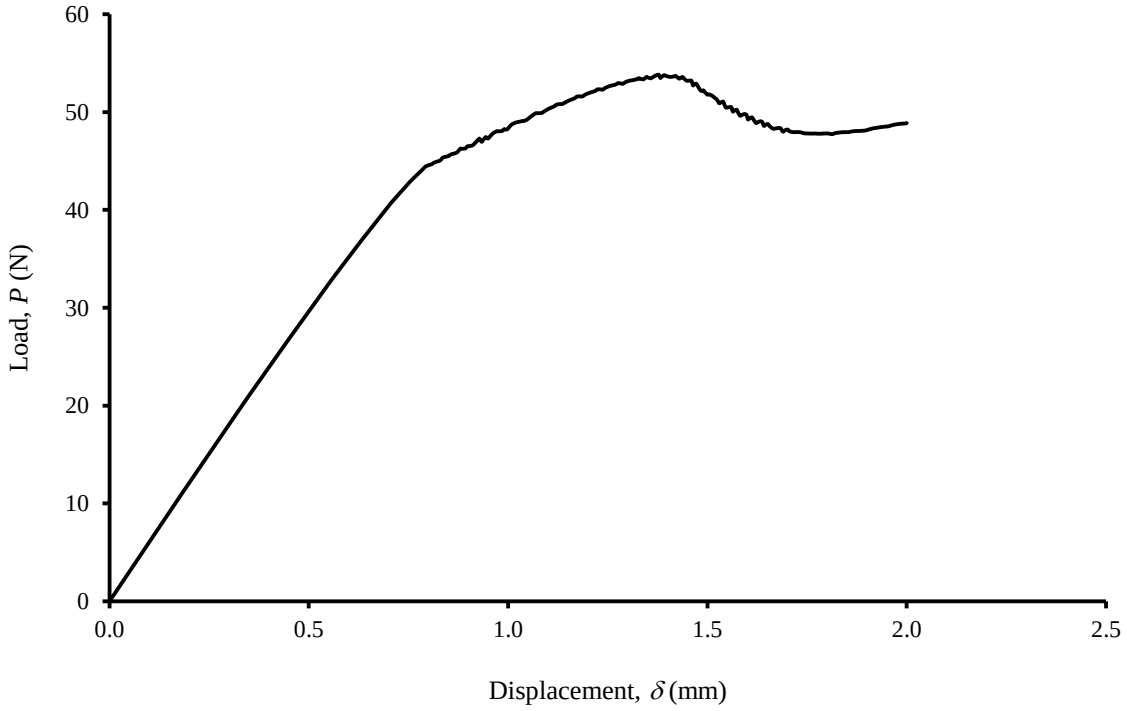

Fig. 4.6 – Numerical load-displacement curve for adjusted SLB specimen dimensions.

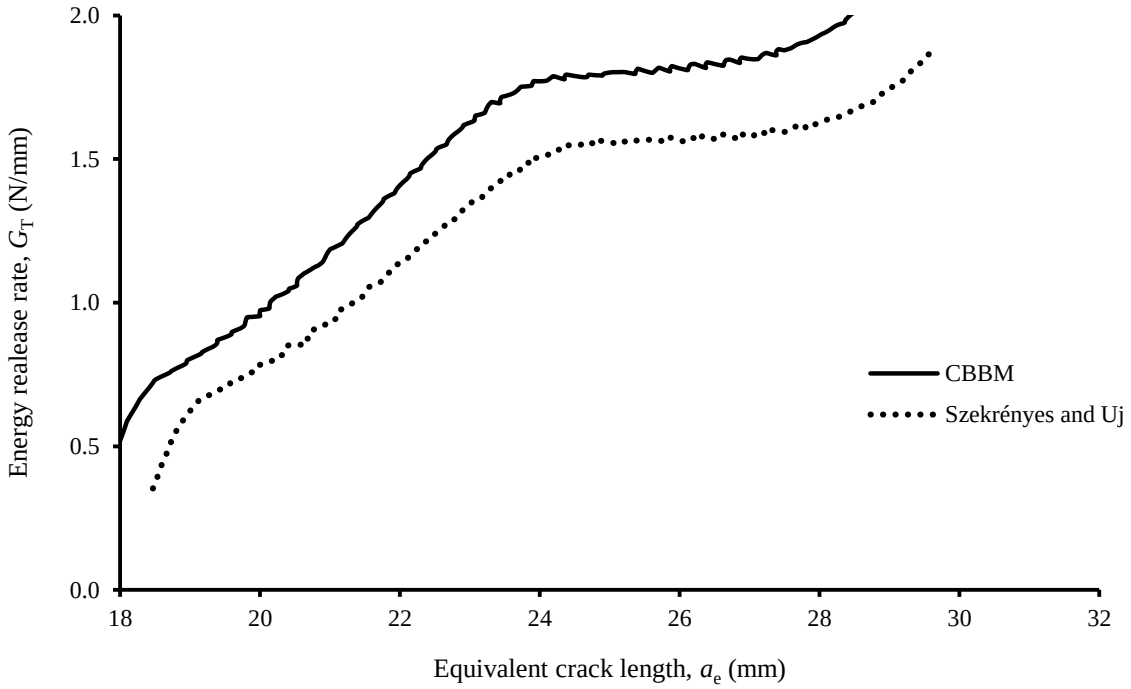

Fig. 4.7 – Numerical *R*-curves for adjusted SLB specimen dimensions.

4.5 - Analysis and discussion of experimental mixed-mode I+II *R*-curves

The specimens were produced taking into account the numerical work guidelines in order to minimize the influence of the compressive load close to the actuator. The resulting average specimen dimensions were a_0 = 18.2 mm; B = 2.9 mm; b = 1.7 mm; h = 2.5 mm; L = 60 mm. Figure 4.8 presents all the experimental load-displacement curves and the numerical curve issued from the finite element model presented at the end of this section. Some scatter is visible in the initial stiffness and peak load, which is a result of a natural material composition like bone and also due to some unavoidable specimen size variability. In general, the load-displacement curves present a decrease after the peak load which is an indication of the attainment of self-similar crack growth conditions with a fully developed fracture process zone.

A detail of the fractured region revealing the presence of relative shear and opening displacements characteristic of mixed-mode I+II loading is presented in Fig. 4.9 (detail A). Detail B puts into evidence the difficulty to identify the crack-tip position with the required accuracy for a truthful evaluation of its length, which is necessary to evaluate toughness in classical data reduction methods.

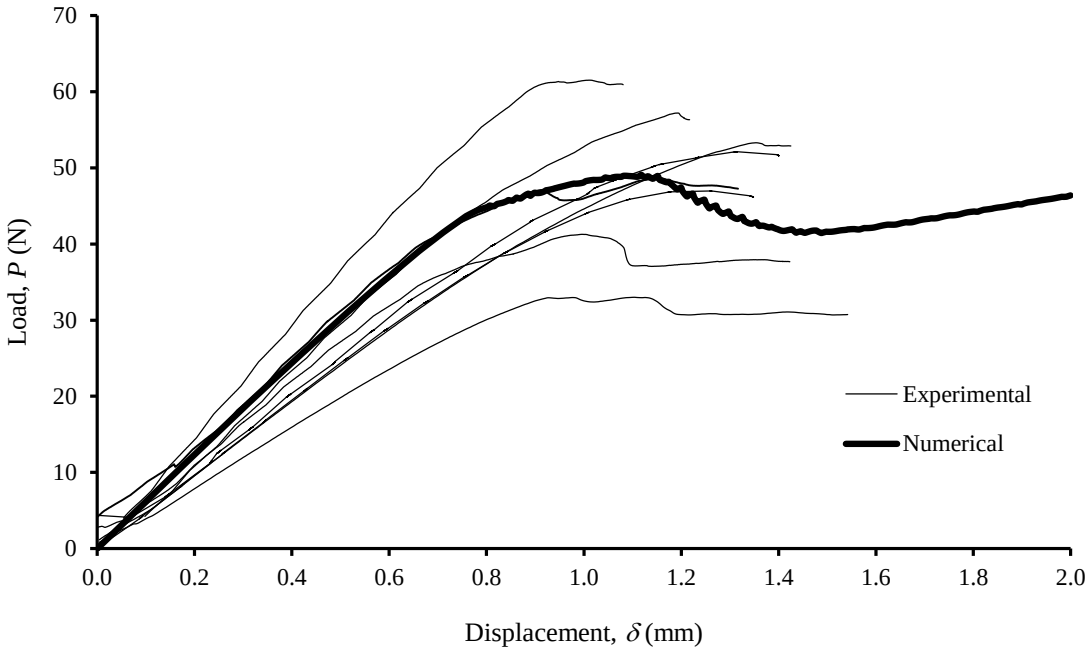

Fig. 4.8 – Experimental load–displacement curves of the SLB test in bovine cortical bone.

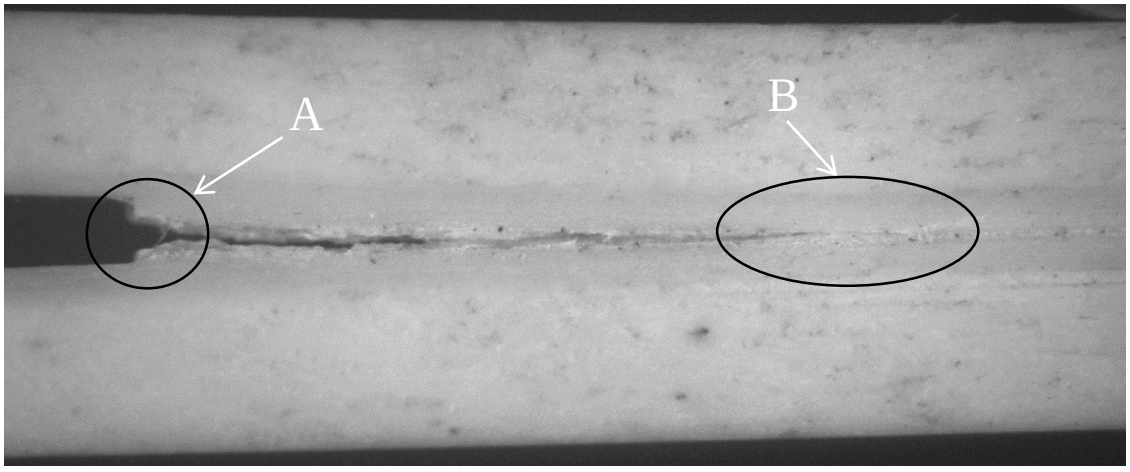

Fig. 4.9 – Opening and shear displacements at the notch tip (Detail A) and undefined crack tip position (Detail B).

The experimental *R*-curves were determined using only the CBBM (Figs 4.10 and 4.11). In fact, the Szekrényes and Uj (2004) method requires experimental compliance calibration (i.e., $C=f(a)$), which is difficult to perform accurately in specimens with significant restrictions on their dimensions. It can be observed that the energy release rate tends to a plateau after a certain crack extent, which means that crack advance occurs under self-similar way with a completely developed fracture process. These conditions allow accurate evaluation of total fracture energy as well as its mode I and mode II components. Another important aspect is the increase of the energy release rate after the plateau meaning that

crack propagation is being influenced by the compressive region. The values in this region are then affected by this spurious phenomenon and should not be considered valid for fracture characterization of bone. Table 4.2 summarizes the set of results corresponding to eight valid tests. A scatter of approximately 15 % was obtained, which can be viewed as quite acceptable result for a natural material like bone. The global mixed-mode ratio (G_I/G_{II}) using the issued average energy component values is equal to 1.34, which is in agreement with the values obtained in other materials using the SLB test (Szekrényes and Uj 2004; Oliveira et al. 2007). A comparison between the experimental and numerical *R*-curves from CBBM and Szekrényes and Uj (2004) method can be visualized on Figs. 4.10-4.11. The plots show that the simulation can capture the global aspect of experimental curves satisfactorily. The numerical model will be described later this section.

Table 4.2 – Experimental total fracture energy G_T and its components G_I and G_{II}.

Specimen	G_I (N/mm)	G_{II} (N/mm)	G_T (N/mm)
1	0.88	0.64	1.52
2	0.59	0.43	1.02
3	0.71	0.53	1.24
4	0.85	0.64	1.49
5	0.78	0.58	1.37
6	0.61	0.45	1.06
7	0.74	0.55	1.28
8	0.86	0.64	1.49
Average	0.75	0.56	1.31
CoV(%)	14.9	15.2	15.0

As referred in section 4.2, the SLB tests were executed using the same bone sample that have been used by Pereira et al. (2012) and Dourado et al. (2013). Consequently, the experimental values of fracture energy in pure modes determined previously (Pereira et al. 2012; Dourado et al. 2013) are included in the abscissas and ordinate axes of Fig. 4.12, and the corresponding average values (G_{Ic} = 1.77N/mm and G_{IIc} = 2.25N/mm). The SLB results were also plotted in order to define the fracture envelops in the G_I-G_{II} space. Figure 4.12

includes three power laws (Eq. 1.10) with different exponents (α): $\alpha = 0.62$ captures the average trend, while the other ones ($\alpha = 0.52$ and $\alpha = 0.72$) delimit the found range.

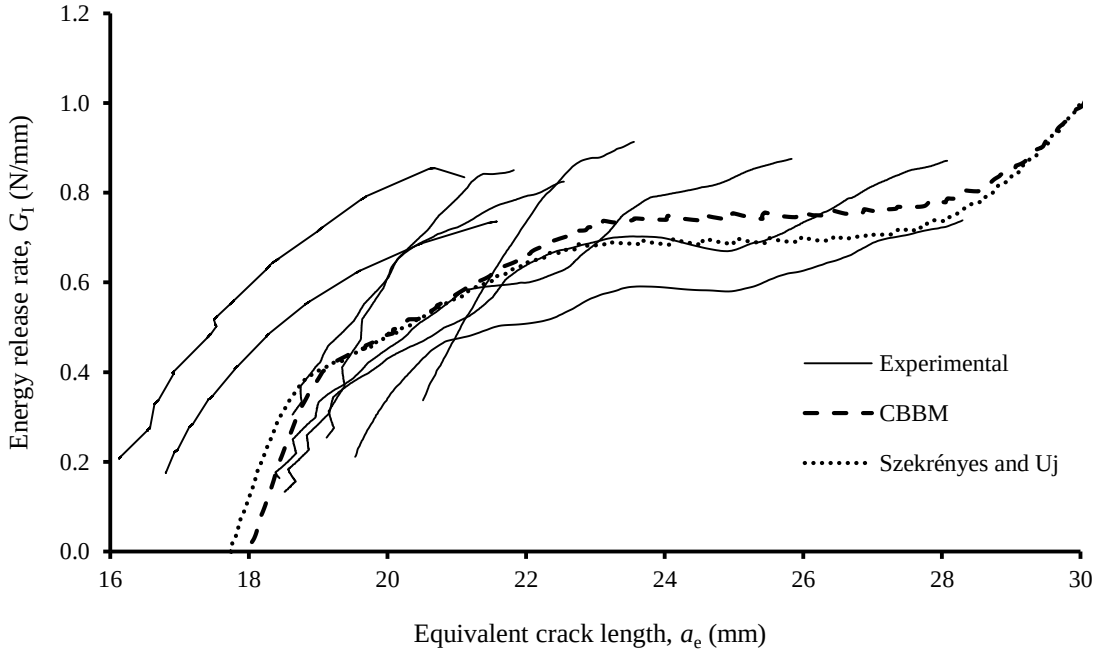

Fig. 4.10 – Mode I *R*-curves issuing from the mixed-mode I+II SLB test.

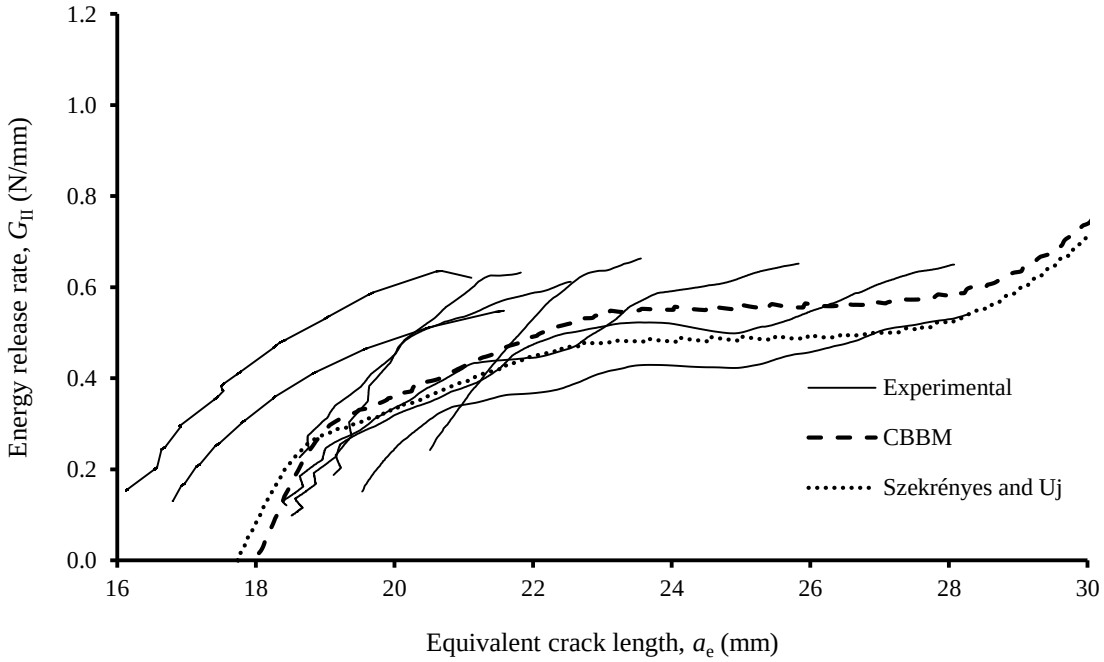

Fig. 4.11 – Mode II *R*-curves issuing from the mixed-mode I+II SLB test.

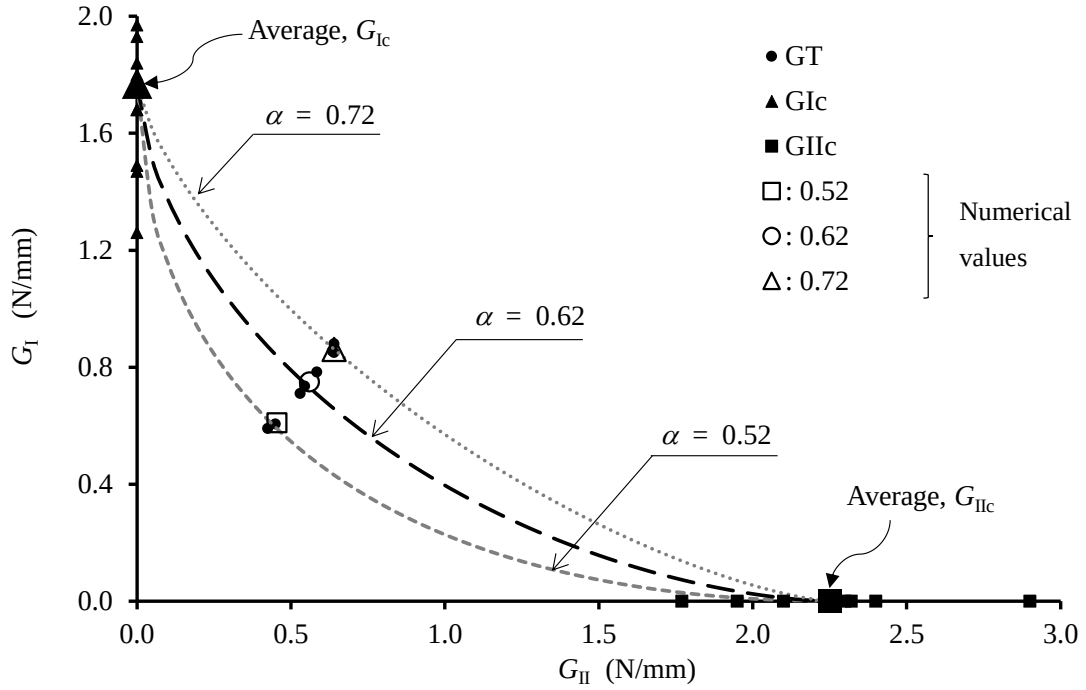

Fig. 4.12 – Fracture envelop for cortical bone in G_I *versus* G_{II} space.

Numerical simulations were performed considering the nominal dimensions of tested specimens and the average fracture energetic criterion (α = 0.62) aiming to verify the suitability of the two data reduction schemes and the ability of the SLB test for mixed-mode I+II fracture characterization of bone. Figures 4.8, 4.10 and 4.11 show respectively the *P*-δ curve, the mode I *R*-curve and the mode II *R*-curve issuing from this simulation, and a comparison between them and the experimental curves. It can be concluded that the numerical curves mimic the global behaviour observed in experiments, satisfactorily. The trend exhibited by the *R*-curves puts into evidence that the fracture process zone has fully developed ahead of the crack tip, emphasizing that the necessary conditions have been attained to permit the freely growth of the FPZ for a given crack extent. This is confirmed by the existence of a plateau on the *R*-curve. Following the plateau, an increase in the energy release rate is visible, which results from the compressive stress field that is induced by the actuator. It is clear that the CBBM and the data reduction scheme proposed by Szekrényes and Uj (2004) provide different results. In order to evaluate the adequacy of each method on the appropriate identification of the fracture energy, the mode I and mode II values were plotted (Fig. 4.13) into G_I-G_{II} space and compared with the inputted criterion. It turns clear from this figure that the CBBM provides better agreement. This difference

could be associated to the strain energy released on the development of the fracture process zone, which is not contemplated on the method proposed by Szekrényes and Uj (2004).

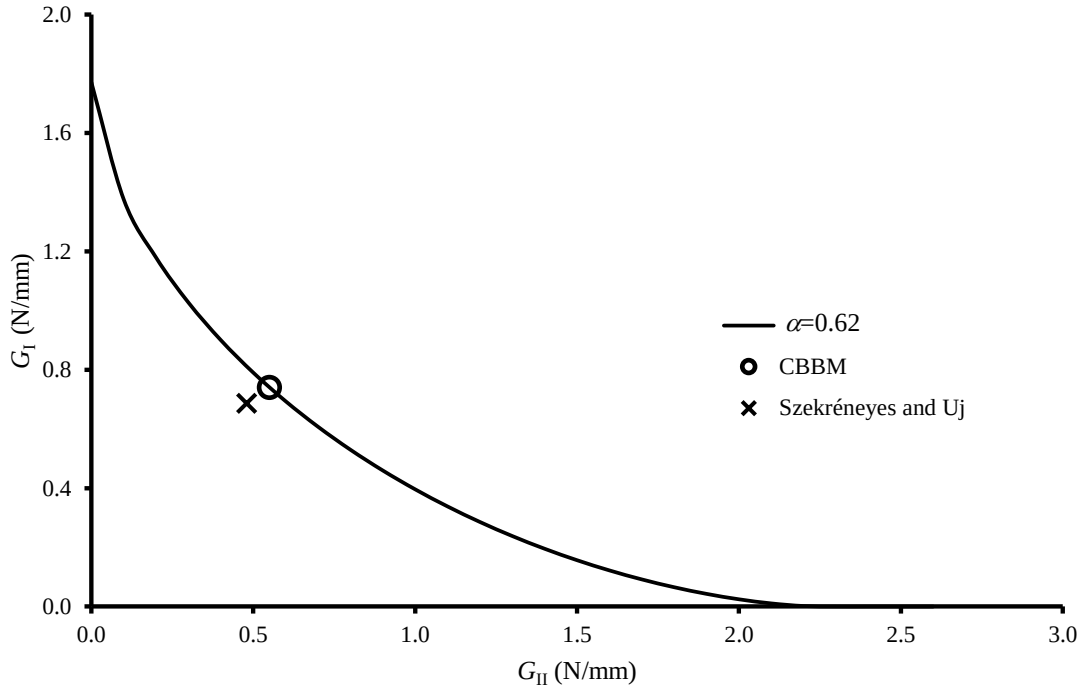

Fig. 4.13 – Fracture envelop in G_I-G_{II} space and numerical results obtained with the CBBM and Szekrényes and Uj (2004) methods.

4.6 - Identification of cohesive laws - direct method

A common assumption under mixed-mode I+II loading conditions is that the normal stresses are almost independent of the mode II crack opening displacement and vice-versa, i.e., the shear stresses depends weakly on the mode I crack opening displacement. As a result the cohesive laws can be decoupled (Mohammed and Liechti, 2000; Yang and Thouless, 2001), i.e., the total fracture energy, G_T, can be separated into the mode I (G_I) and mode II components (G_{II}),

$$G_T = G_I + G_{II} \tag{4.10}$$

where,

$$G_I = \int_0^{w_I} \sigma_I(w)\, dw; \qquad G_{II} = \int_0^{w_{II}} \sigma_{II}(w)\, dw \tag{4.11}$$

Consequently, the cohesive law for each mode can be obtained from the differentiation of G_I and G_{II} in order to the corresponding crack opening displacements. The method for the determination of cohesive laws under mixed-mode I+II is similar to the one applied for

pure modes. Thus, a spline function was fitted to the strain energy *versus* crack opening relations ($G_i(w_i)$, i=I, II) to eliminate scatter and provide a suitable differentiation of the function. A more detailed description of this process can be found in section 2.4.

Figure 4.14 shows the components of both modes of the mixed-mode cohesive law. In comparison with the pure mode loading, the validation of this result (mixed-mode) is not straightforward. In fact, the cohesive laws used as input in the mixed-mode model refer to pure modes and the resulting mixed-mode cohesive law is a combination between the two modes, thus making problematic the identification process.

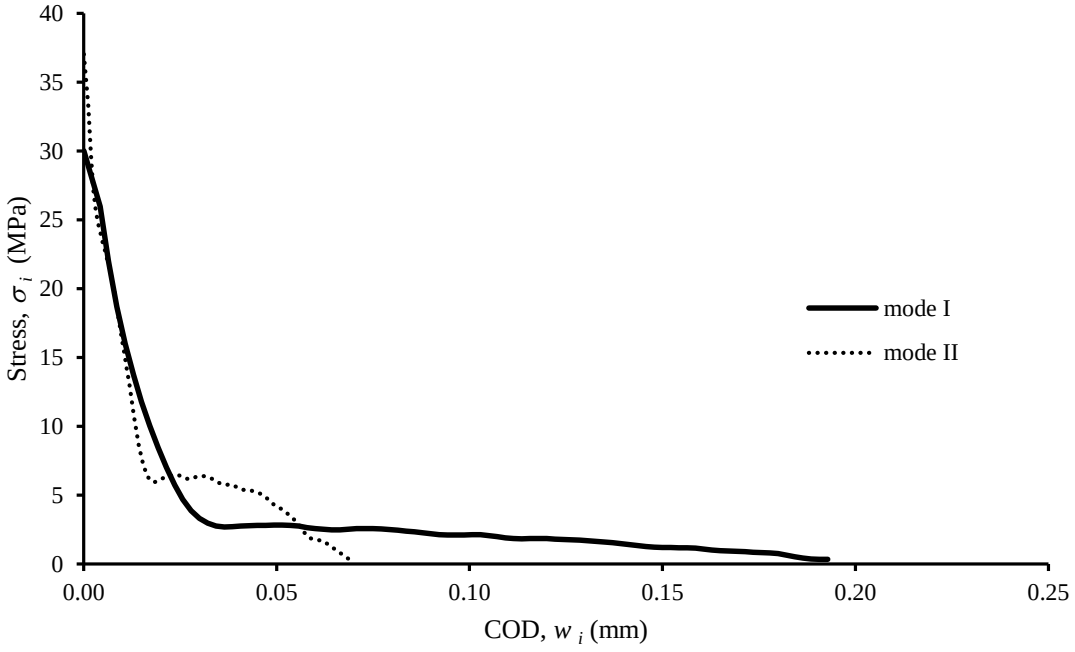

Fig. 4.14 – Numerical components in mode I and mode II of the mixed-mode cohesive laws (i = I, II).

Another relevant aspect comprises the phase angle (ψ), which is defined as follows,

$$\psi = \arctan\left(\frac{w_{II}}{w_I}\right) \tag{4.12}$$

Effectively, the plotting of w_{II} *versus* w_I shown in Fig. 4.15 allows concluding that the phase angle ψ is not constant.

One way to overcome the cited difficulties and evaluate the suitability of the identified cohesive law components (Fig. 4.14) is to verify whether the stress criterion (Eq. 1.7) used as input in the model to simulate damage onset (i.e., α=1), is accurately reproduced. Hence, substituting in Eq. (1.7) the ultimate stress values obtained in Fig. 4.14 and the critical pure

mode values introduced in the model (Table 4.1) a value of 1.04 is obtained, which can be considered a good approximation. In light of this, it can be concluded that this method is appropriate for identification of cohesive law components under mixed-mode I+II loading of cortical bovine bone.

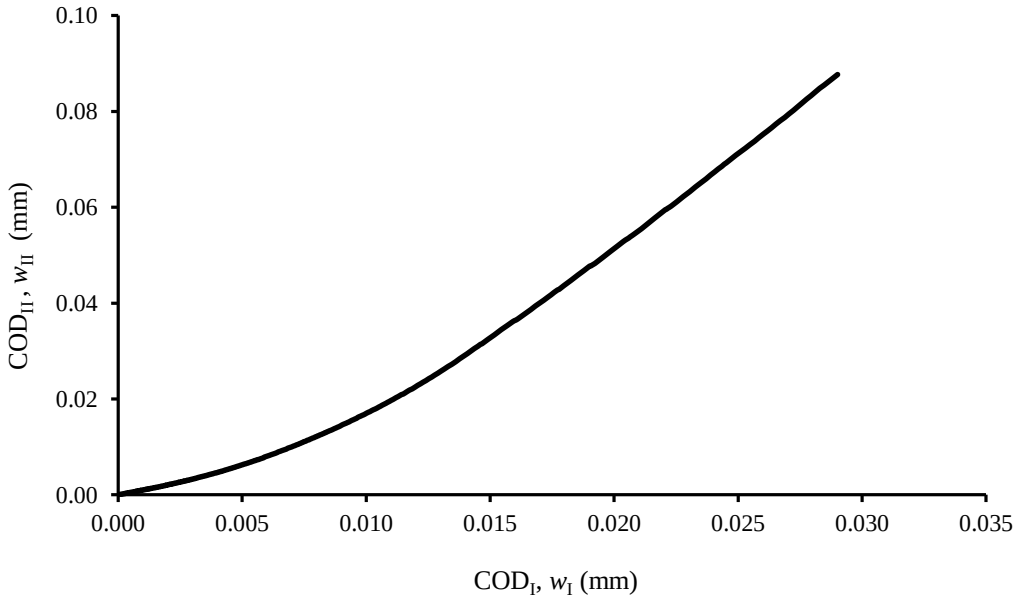

Fig. 4.15 – Crack opening displacements relation.

4.7 - Conclusions

The fundamental aspects resulting from the fracture characterization of bovine cortical bone under mixed-mode I+II loading can be summarized as follows:

- the proposed SLB test is adequate for fracture characterization of cortical bone under mixed- mode I+II loading conditions; however, this test presents a limitation relative to the variation of mixed-mode ratio;
- the CBBM is adequate for the identification of *R*-curves for total energy and corresponding mode I and mode II components, without requiring the complex and innacurate crack length monitoring during the test;
- the strain energy release rate appears to follow an energetic power law evolution with the parameter α ranging between 0.52 and 0.72;
- cohesive zone models prove to be effective on the reproduction of the cortical bone under mixed-mode I+II fracture process;

- a method based only on the relation between the strain energy release rate components and the corresponding crack opening displacements appears to be adequate for the identification of the cohesive law components.

CHAPTER V

Fracture behaviour of cortical bone under mixed-mode I+II loading – MMB test

5.1 - Introduction

The mechanical behaviour of cortical bone under mixed-mode I+II loading conditions is analysed in this Chapter. With this aim, a miniaturized version of the Mixed-Mode Bending (MMB) test apparatus was conceived in order to provide fracture characterization under a wide range of mixed-mode ratios. Therefore, three different mixed-mode ratios were considered thus giving rise to a broad representability of bone fracture behaviour in the mode I versus mode II space.

The *R*-curve for each mode component was accurately evaluated. The MMB tests can be viewed as a combination of the DCB and ENF tests used for pure modes fracture characterization. Consequently, the CBBM previously developed for such tests was applied to MMB test to avoid crack measurements during the mechanical test. Bone microstructure and elastic longitudinal modulus were identified in order to typify each sample and to relate them with the obtained fracture properties.

Mode I and mode II components of cohesive laws under mixed-mode I+II were obtained experimentally considering an uncoupled and coupled mixed-mode approaches. It was concluded that the method proposed by Högberg is the best suited for the purpose of getting the components of the cohesive laws.

5.2 - Experiments

A miniaturized version of the MMB test apparatus was constructed for the fracture characterization of cortical bone under mixed-mode I+II loading (Fig. 5.1). The developed system is based on the device developed by de Moura et al. (2010) for wood fracture characterization. The MMB test is a combination of the DCB and the ENF tests using a unique lever to apply mixed-mode I+II loadings. The load on the top dowel tends to pull the upper specimen arm resulting on an opening load in mode I similar to that of the DCB test. At the same time, the load at the fulcrum bends the specimen creating a mode II loading similar to the one of ENF test. The mixed-mode loading ratio is controlled by altering the yoke position. In fact, this changing reflects on the variation of the relative magnitude of the two resulting loads acting on the specimen. A saddle mechanism is used to hold the bearings aligned with the specimen mid-plane and assure the connection between the yoke and the loading lever.

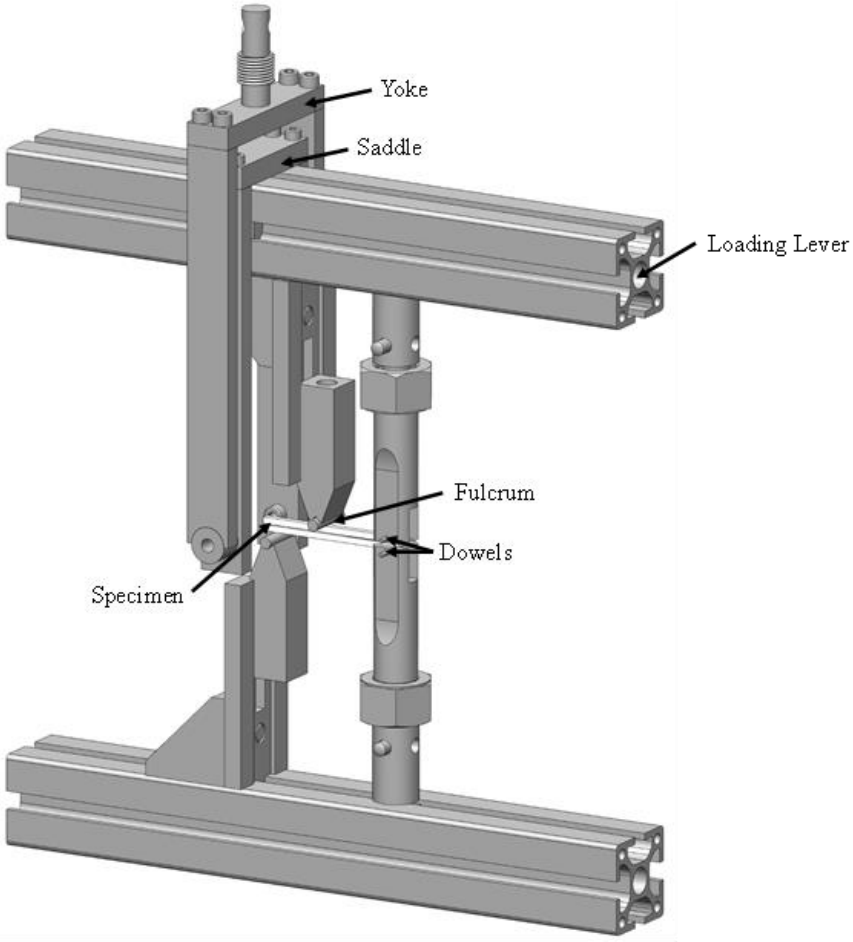

Fig. 5.1 – Schematic representation of the miniaturized version of the MMB text fixture constructed for bone fracture characterization under mixed-mode I+II loading.

For the experimental work thirty fresh bovine femora of young animals were used to produce the MMB specimens. The storage conditions and the machining process were similar to the ones utilized in DCB tests and is detailed in previous section 2.2. Specimen dimensions (L=30 mm, $2h$=5.9 mm, b=1.6 mm, B=2.7 mm and a_0=20.5 mm in Fig. 5.2) were similar for all the mode-mixities tested.

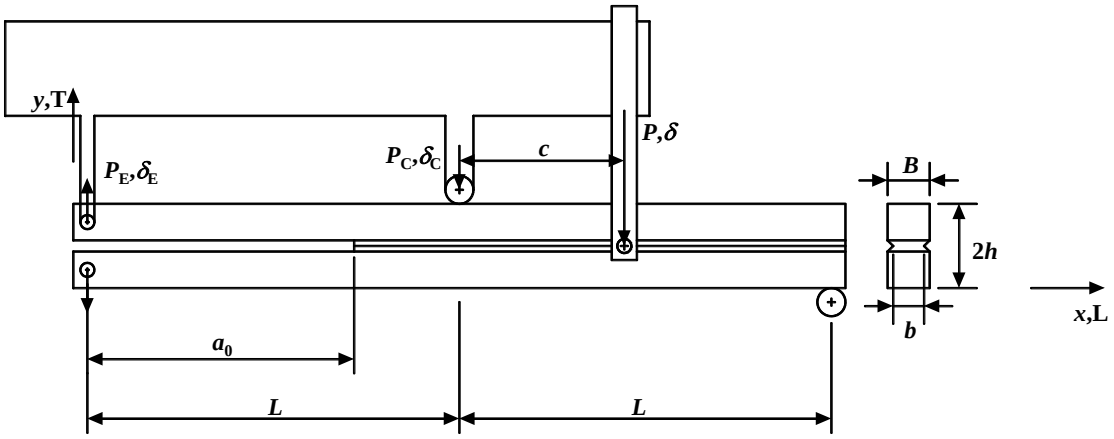

Fig. 5.2 – Schematic representation of the MMB test.

Three different mode ratios G_I/G_{II} were considered to have a broad representability of bone fracture behaviour in the G_I-G_{II} space. The alteration of the mode-mixity is easily performed in the MMB test by changing the lever length of the apparatus (parameter c in Fig. 5.2). Actually, it can be seen from Eq. (5.1) that G_I/G_{II} ratio is only function of the distance c,

$$\frac{G_I}{G_{II}} = \frac{4}{3}\left(\frac{3c-L}{c+L}\right)^2, \; c \geq \frac{L}{3} \tag{5.1}$$

According to Reeder (1989) this relation is only valid for c higher than $L/3$ to assure that the mode I loading is strong enough to open the crack. The c distances considered (29, 18, and 44 mm) lead to three different mode ratios: eighteen specimens for predominant mode I (G_I/G_{II}=2.53), twenty for equitable loading modes (G_I/G_{II}=1.24) and eighteen for predominant mode II (G_I/G_{II}=0.33).

The mechanical tests (Fig. 5.3) were realized using a servo-electrical testing system (MicroTester INSTRON® 5848 – Dynamic Laboratory – ECT-UTAD) with constant displacement rate of 0.5 mm/min. A 2 kN load-cell was used and the data acquisition frequency was set equal to 5 Hz. As in previous DCB and ENF tests, DIC analysis was performed to get the evolution of the crack opening displacements during the test. The DIC acquisition frequency (1 Hz) was the same for all tests.

The longitudinal elastic modulus, the mass fraction of bone constituents (water, mineral and organic constituents) and the porosities were evaluated for all the specimens that were considered valid during the experimental fracture tests following procedures described in previous chapters.

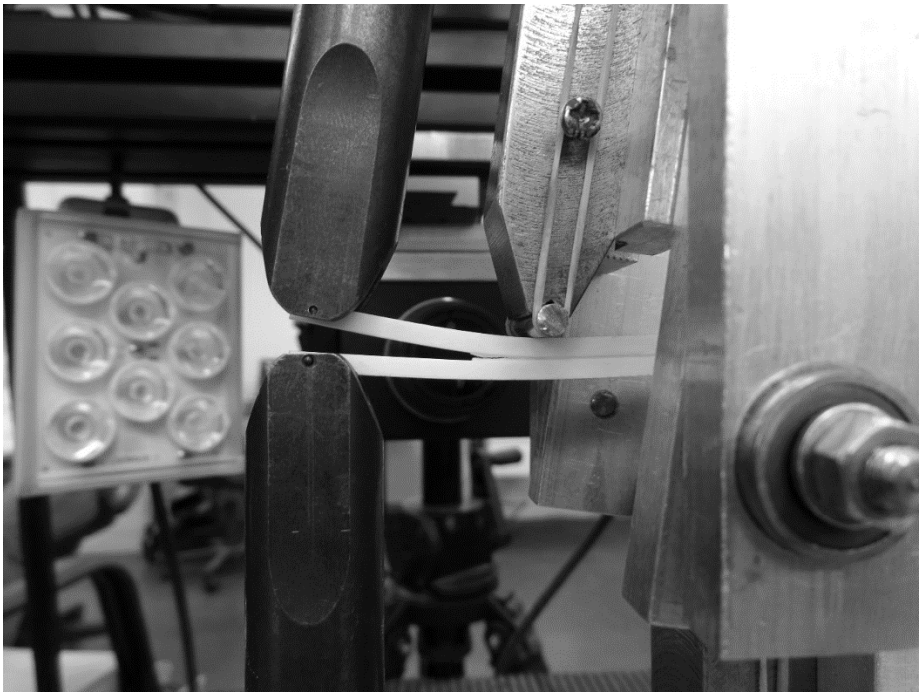

Fig. 5.3 – MMB experimental test.

5.3 - Mixed-Mode Bending – Data reduction scheme

The MMB test (Fig. 5.2) is a combination of the DCB and ENF tests used for fracture characterization under mode I and II, respectively. Consequently, the MMB loading can be represented by a superposition of a mode I and mode II loadings equivalent to those used in DCB and ENF tests, respectively. As a consequence, the strain energy release rate equations obtained for DCB and ENF tests using beam theory can be used to obtain the equations for MMB tests. The mode I and II loading components can be expressed as (Fig. 5.4)

$$P_{\mathrm{I}} = \left(\frac{3c - L}{4L} \right) P \tag{5.2}$$

$$P_{\mathrm{II}} = \left(\frac{c + L}{L} \right) P \tag{5.3}$$

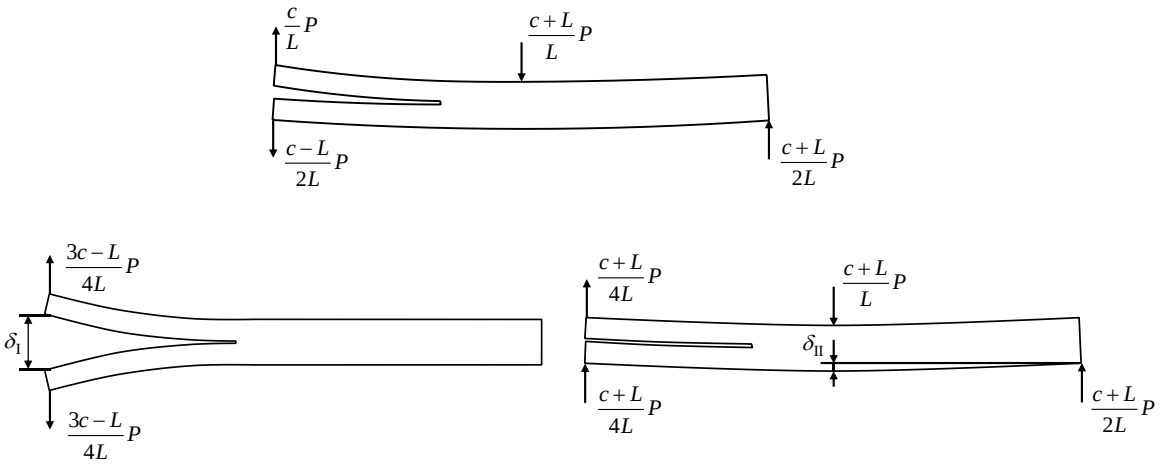

Fig. 5.4 – Superposition loading analysis of the MMB specimen.

Using simple beam theory analysis the expressions for mode I and mode II energy release rates in the MMB test are as follows (Reeder, 1989)

$$G_{\mathrm{I}} = \frac{12a^2P_{\mathrm{I}}^2}{B^2h^3E_{\mathrm{L}}} \tag{5.4}$$

$$G_{\mathrm{II}} = \frac{9a^2P_{\mathrm{II}}^2}{16B^2h^3E_{\mathrm{L}}} \tag{5.5}$$

Following this procedure the beam root rotation at the crack tip, which is pronounced in mode I, and the shear deformation, in the two modes, are not accounted for. To overcome these difficulties crack length corrections are recommended for DCB and ENF tests. For the DCB test Williams (1989) proposed,

$$G_{\mathrm{I}}^{\mathrm{WW}} = \frac{12(a+h|\Delta_{\mathrm{I}}|)^2P_{\mathrm{I}}^2}{B^2h^3E_{\mathrm{L}}} \tag{5.6}$$

where the correction term Δ_{I} is given by

$$\Delta_{\mathrm{I}} = \sqrt{\frac{E_{\mathrm{L}}}{11G_{\mathrm{LT}}}\left[3-2\left(\frac{\Gamma}{1+\Gamma}\right)\right]^2}\ \text{, with}\ \Gamma = 1.18\frac{\sqrt{E_{\mathrm{L}}E_{\mathrm{T}}}}{G_{\mathrm{LT}}} \tag{5.7}$$

For the ENF test Wang and Williams (1992) proposed the following expression,

$$G_{\mathrm{II}}^{\mathrm{WW}} = \frac{9(a+|\Delta_{\mathrm{II}}|h)^2P_{\mathrm{II}}^2}{16B^2h^3E_{\mathrm{L}}} \tag{5.8}$$

being Δ_{II}

$$\Delta_{\mathrm{II}} = 0.42\Delta_{\mathrm{I}} \tag{5.9}$$

The displacement for mode I and mode II components can be obtained from the so-called corrected beam theory (Reeder, 2003),

$$\delta_{\mathrm{I}} = \frac{8(a+\Delta_{\mathrm{I}})^3 P_{\mathrm{I}}}{Bh^3 E_{\mathrm{L}}} \quad \text{and} \quad \delta_{\mathrm{II}} = \frac{\left[2L^3 + 3(a+\Delta_{\mathrm{II}})^3\right] P_{\mathrm{II}}}{8Bh^3 E_{\mathrm{L}}} \tag{5.10}$$

The relationship between these displacements and the one applied to the loading lever is (Juntti et al., 1999),

$$\delta = \left(\frac{3c-L}{4L}\right)\delta_{\mathrm{I}} + \left(\frac{c+L}{L}\right)\delta_{\mathrm{II}} \tag{5.11}$$

Using Eqs. (5.6, 5.8) the mode ratio as a function of distance *c* becomes

$$\frac{G_{\mathrm{I}}^{\mathrm{WW}}}{G_{\mathrm{II}}^{\mathrm{WW}}} = \frac{4}{3}\left(\frac{3c-L}{c+L}\right)^2 \left(\frac{a+h\Delta_{\mathrm{I}}}{a+0.42\Delta_{\mathrm{I}}h}\right)^2 \tag{5.12}$$

The relationship between specimen compliance ($C=\delta/P$) and crack length (a) can be established by means of Timoshenko beam theory (de Moura et al., 2006),

$$C_{\mathrm{I}} = \frac{\delta_{\mathrm{I}}}{P_{\mathrm{I}}} = \frac{8a^3}{E_{\mathrm{L}}Bh^3} + \frac{12a}{5BhG_{\mathrm{LT}}} \tag{5.13}$$

The presented equation is based on Timoshenko beam theory and does not consider some crucial aspects like stress concentrations at the crack tip or material variability between specimens. To include these effects, the elastic modulus E_{L} is replaced by a corrected flexural modulus E_{fI} which can be obtained from Eq. (5.13) using the measured initial compliance ($C_{0\mathrm{I}}$), and considering the root rotation correction for the initial crack length proposed by Wang and Williams (1992) (Eqs. 5.6-5.8),

$$E_{\mathrm{fI}} = \left(C_0 - \frac{12\left(a_0 + h\left|\Delta_{\mathrm{I}}\right|\right)}{5BhG_{\mathrm{LT}}}\right)^{-1} \frac{8\left(a_0 + h\left|\Delta_{\mathrm{I}}\right|\right)^3}{Bh^3} \tag{5.14}$$

On the other hand, an equivalent crack length (a_{eI}) should be considered during propagation to account for the FPZ effect at the crack tip. The equivalent crack length can be calculated from Eq. (5.13) and considering a_{eI} instead of a. The solution of the cubic equation can be consulted on section 2.2. The strain energy component in mode I can now be obtained from

$$G_{\mathrm{I}} = \frac{12a_{\mathrm{eI}}^2 P_{\mathrm{I}}^2}{Bbh^3 E_{\mathrm{fI}}} \tag{5.15}$$

A similar procedure can be used for mode II. In this case the equation of the compliance $C_{II}=\delta_{II}/P_{II}$, can be written as (de Moura et al., 2006),

$$C_{II} = \frac{\delta_{II}}{P_{II}} = \frac{3a^3 + 2L^3}{12E_L I} + \frac{3L}{10G_{LT}Bh} \tag{5.16}$$

The flexural modulus in this case can be obtained using the initial compliance and crack length i.e., C_{0II} and a_0

$$E_{fII} = \frac{3a_0^3 + 2L^3}{12I}\left(C_{0II} - \frac{3L}{10G_{LT}Bh}\right)^{-1} \tag{5.17}$$

The effect of the FPZ is indirectly included considering the equivalent crack concept based on specimen compliance and Timoshenko beam theory during propagation. Combining Eqs. (5.16-5.17) it can be written,

$$a_{e_{II}} = a + \Delta a_{FPZ} = \left[\frac{C_{IIcorr}}{C_{0II\,corr}}a_0^3 + \frac{2}{3}\left(\frac{C_{IIcorr}}{C_{0IIcorr}} - 1\right)L^3\right]^{1/3} \tag{5.18}$$

where C_{IIcorr} is given by

$$C_{IIcorr} = C_{II} - \frac{3L}{10G_{LT}Bh} \tag{5.19}$$

G_{II} can now be obtained from

$$G_{II} = \frac{9P_{II}^2 a_{eII}^2}{16BbE_{fII}h^3} \tag{5.20}$$

The presented methodology allows obtaining the strain energies G_I and G_{II} using only the P–δ data and can be considered the CBBM version for the MMB test. Using this method it is not necessary to measure the crack length during propagation because the calculated equivalent crack length is used instead of the real one. Another advantage is related to the fact that a_e includes the effect of the FPZ, which is not taken into account when the real crack length is considered.

5.4 - Analysis of experimental mixed-mode I+II *R*-curves

The results of fracture energy and its mode components are presented in this section. The P-δ curves (Fig. 5.5) were used to get the *R*-curves for all specimens considering the described CBBM method (Figs 5.6-5.8). Generally, it is possible to identify a small horizontal asymptote (*plateau*), which corresponds to a stable crack propagation under self-

similar conditions. The energy release rate is plotted as a function of the equivalent crack length variation (Δa_{eI} and Δa_{eII}), owing to the differences between the estimated mode I and mode II equivalent crack length.

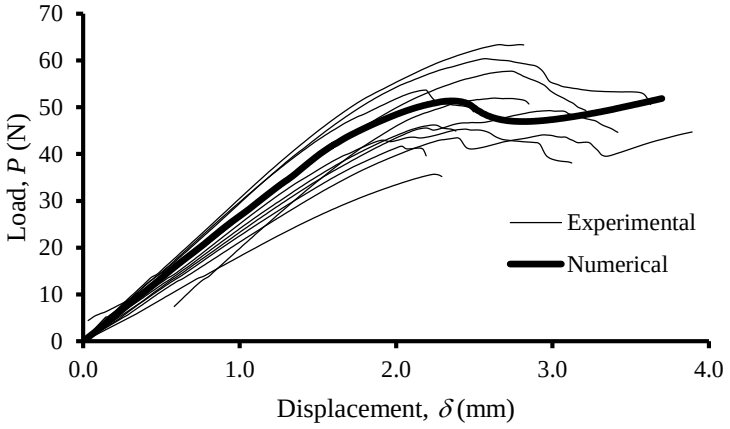

(a)

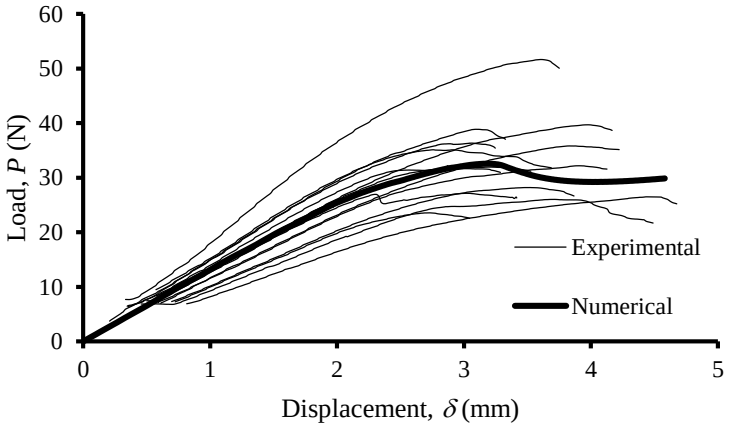

(b)

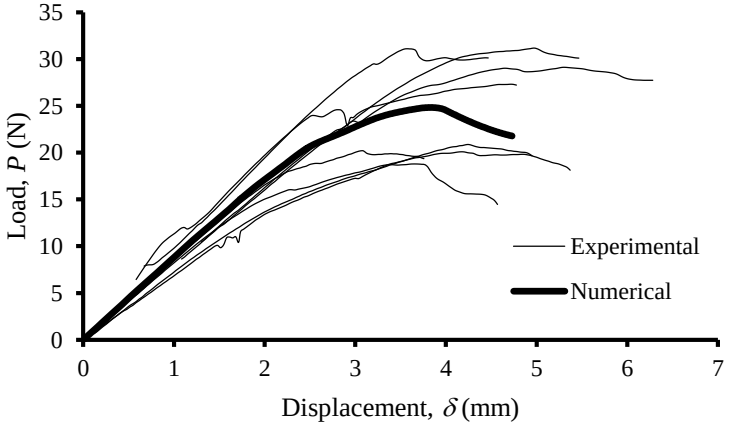

(c)

Fig. 5.5 – Experimental load-displacement curves of the MMB test: (a) G_I/G_{II}=0.33, (b) G_I/G_{II}=1.24, (c) G_I/G_{II}=2.53.

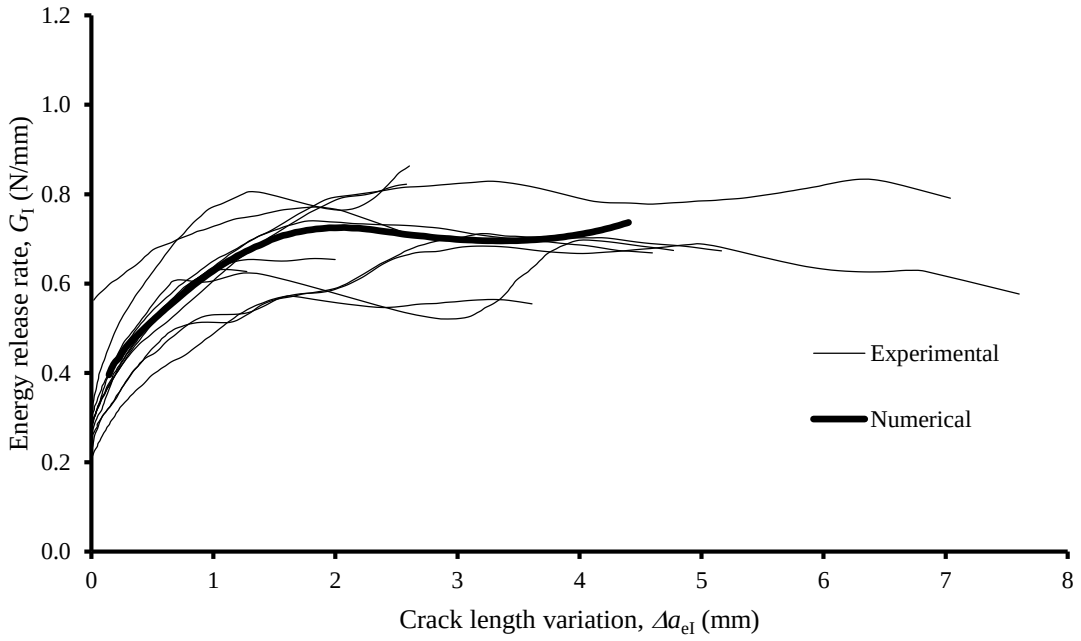

(a)

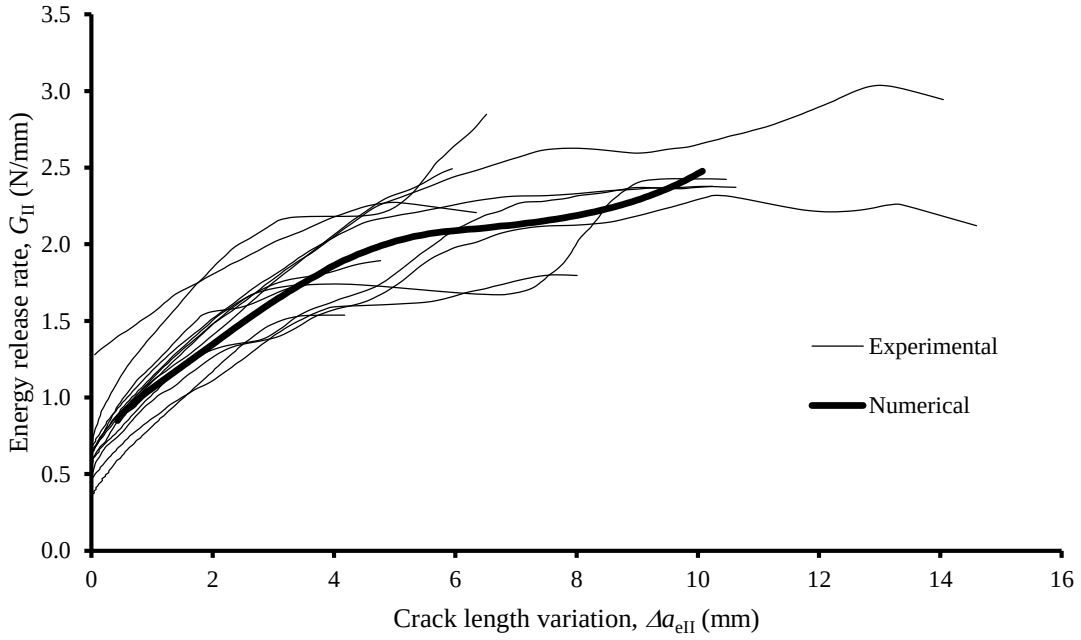

(b)

Fig. 5.6 – Mixed-mode *R*-curves (G_I/G_{II}=0.33): (a) Mode I, (b) Mode II.

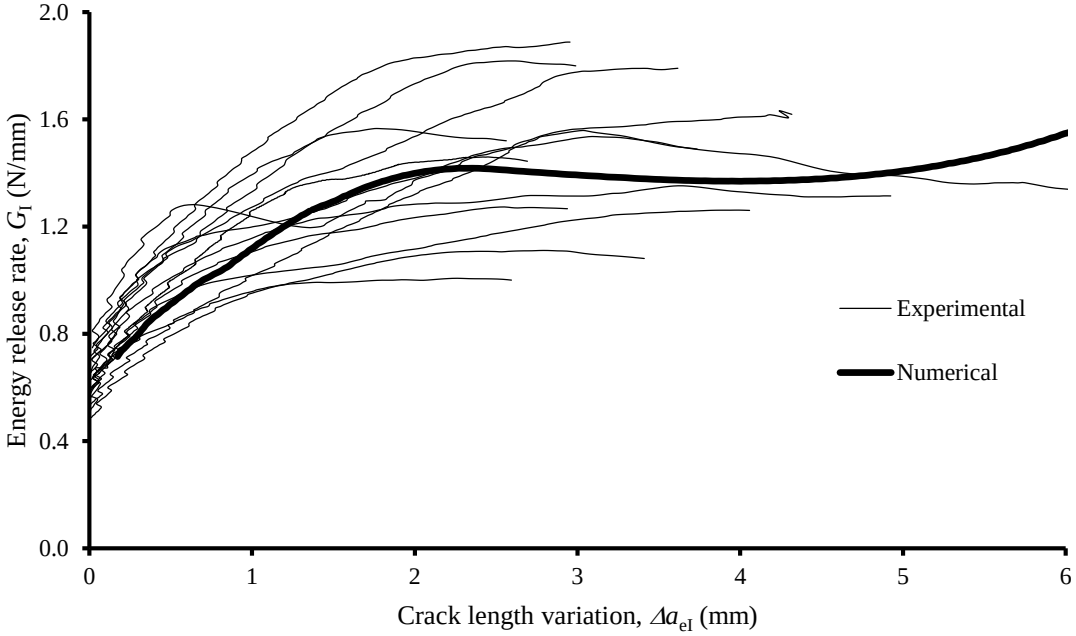

(a)

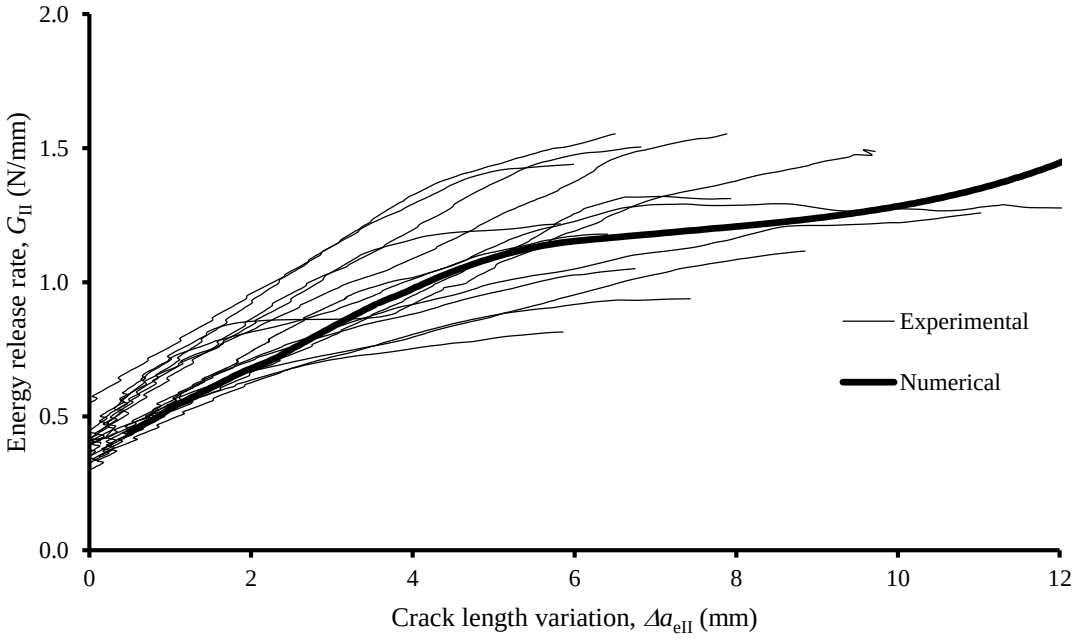

(b)

Fig. 5.7 – Mixed-mode *R*-curves (G_I/G_{II}=1.24): (a) Mode I, (b) Mode II.

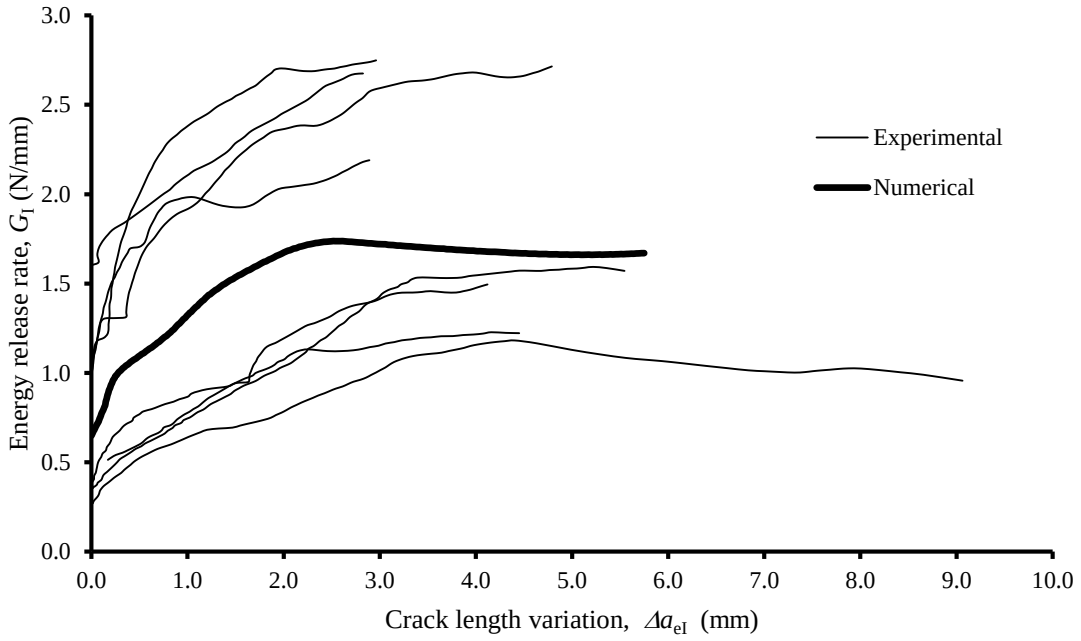

(a)

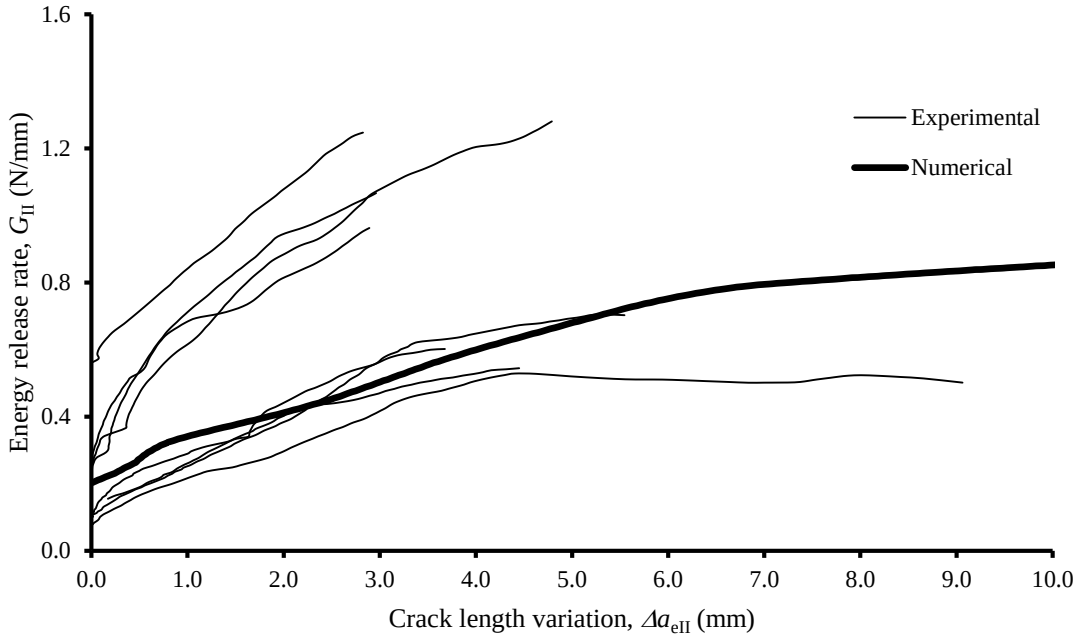

(b)

Fig. 5.8 – Mixed-mode *R*-curves (G_I/G_{II}=2.53): (a) Mode I, (b) Mode II.

Figure 5.9 presents all the results and the average values for each mode ratio. In order to find a fracture energetic criterion mimicking bone fracture behaviour under mixed-mode I+II loading, a power law fitting (Eq. 1.10) was used considering three different values for the exponent α (0.6, 0.85 and 1.4). The limiting values attributed to the parameter α capture the global range with few exceptions. The power law with exponent equal to 0.85 captures

the average trend. Although specimens from different donors were used with inherent material variability, this result compares well with previous ones using the SLB test (see previous Chapter).

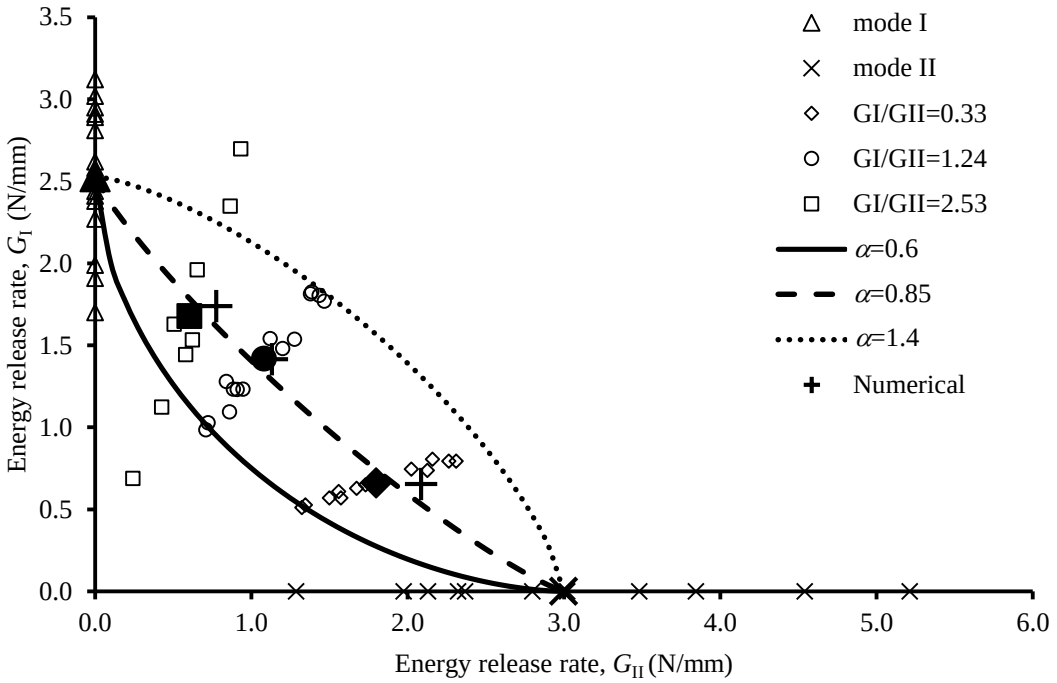

Fig. 5.9 – Fracture envelope for cortical bone in G_I versus G_{II} space (**bold** marks correspond to average results).

The individual results for each specimen can be visualized on Tables 5.1-5.3. All the results were considered valid by the Chauvenet criterion. It is important to refer that once again no significant correlation was found between the fracture energy components and the other evaluated variables. The difference observed between the foreseen mixed-mode ratio and the one really obtained can be explained by material orthotropy, some specimen dimensions imprecisions and by the fact that the estimated mixed-mode ratios have been calculated through Eq. 5.1 which is based only on simple beam theory.

Table 5.1 – Experimental results (G_I/G_{II}=0.33). G_I, G_{II}, fracture energy components, E_L longitudinal flexure modulus, d_h apparent density, m_w water mass fraction, m_o organic mass fraction, m_m mineral mass fraction, *Por* porosity.

Specimen	G_I (N/mm)	G_{II} (N/mm)	Ratio G_I/G_{II}	E_L (GPa)	d_h (g/cm^3)	m_w (%)	m_o (%)	m_m (%)	*Por* (%)
1	0.74	2.13	0.35	14.89	1.99	13.86	23.41	62.73	3.84
2	0.53	1.35	0.39	16.26	2.04	11.71	23.13	65.16	4.29
3	0.61	1.56	0.39	18.65	2.04	11.58	22.53	65.88	3.97
4	0.65	1.73	0.38	17.25	2.05	11.50	22.62	65.88	4.14
5	0.75	2.02	0.37	17.12	2.01	11.76	23.94	64.30	4.81
6	0.57	1.57	0.36	15.96	2.03	11.50	22.92	65.58	2.91
7	0.63	1.67	0.38	16.18	2.04	11.60	22.72	65.67	4.00
8	0.81	2.16	0.37	14.63	2.04	11.87	23.46	64.67	3.49
9	0.51	1.32	0.39	19.01	2.07	11.91	22.88	65.20	5.05
10	0.79	2.31	0.34	16.72	2.03	11.82	22.69	65.49	4.63
11	0.79	2.26	0.35	19.42	2.03	11.94	22.64	65.42	4.49
Average	0.67	1.83	0.37	16.83	2.03	11.91	22.99	65.09	4.15
CoV(%)	16.4	19.9	4.8	9.1	1.0	5.6	1.9	1.4	14.7

Table 5.2 – Experimental results (G_I/G_{II}=1.24). G_I, G_{II}, fracture energy components, E_L longitudinal flexure modulus, d_h apparent density, m_w water mass fraction, m_o organic mass fraction, m_m mineral mass fraction, *Por* porosity.

Specimen	G_I (N/mm)	G_{II} (N/mm)	Ratio G_I/G_{II}	E_L (GPa)	d_h (g/cm^3)	m_w (%)	m_o (%)	m_m (%)	*Por* (%)
1	1.23	0.95	1.30	15.71	2.09	11.18	24.86	63.96	3.83
2	1.54	1.28	1.20	14.76	2.09	11.17	22.46	66.37	3.74
3	1.83	1.39	1.32	18.88	2.04	11.50	24.14	64.36	3.90
4	1.28	0.84	1.52	17.77	2.04	12.07	24.75	63.18	5.25
5	1.77	1.47	1.21	15.96	2.14	13.45	24.43	62.12	4.06
6	1.03	0.72	1.42	17.62	2.11	11.50	23.31	65.19	4.65
7	1.09	0.86	1.27	16.55	2.13	11.79	23.46	64.75	3.67
8	1.54	1.12	1.38	19.57	2.08	11.34	22.6	66.06	3.73
9	1.23	0.91	1.35	17.10	1.94	12.73	23.14	64.13	6.51
10	1.48	1.20	1.23	16.46	2.08	10.90	22.79	66.31	4.54
11	1.81	1.38	1.31	17.37	2.03	11.79	23.76	64.45	3.84
12	1.80	1.44	1.26	16.77	1.96	11.86	22.91	65.23	3.78
13	1.23	0.89	1.39	17.03	2.08	12.27	23.22	64.51	4.23
14	0.99	0.71	1.39	17.62	2.10	11.83	22.42	65.75	3.43
Average	1.42	1.08	1.33	17.08	2.06	11.81	23.45	64.74	4.23
CoV(%)	21.4	25.3	6.8	7.2	2.8	5.7	3.5	1.9	19.3

Table 5.3 – Experimental results (G_I/G_{II}=2.53). G_I, G_{II}, fracture energy components, E_L longitudinal flexure modulus, d_h apparent density, m_w water mass fraction, m_o organic mass fraction, m_m mineral mass fraction, *Por* porosity.

Specimen	G_I (N/mm)	G_{II} (N/mm)	Ratio G_{Ic}/G_{IIc}	E_L (GPa)	d_h (g/cm^3)	m_w (%)	m_o (%)	m_m (%)	*Por* (%)
1	2.70	0.93	2.89	14.98	2.03	12.00	21.80	66.20	4.20
2	1.63	0.51	3.21	17.05	2.01	11.43	22.30	66.27	4.80
3	2.35	0.87	2.71	20.44	2.05	12.19	22.29	65.52	3.68
4	1.96	0.65	3.00	18.11	2.06	11.58	22.03	66.39	3.76
5	1.12	0.43	2.63	17.89	1.96	12.21	25.12	62.67	4.31
6	0.69	0.24	2.84	19.44	2.05	11.38	22.69	65.93	3.00
7	1.53	0.62	2.46	18.13	1.99	11.82	23.35	64.83	3.45
8	1.44	0.58	2.49	17.01	2.06	11.79	24.06	64.15	3.62
Average	1.68	0.60	2.78	17.88	2.03	11.80	22.96	65.25	3.85
CoV(%)	38.7	37.1	9.3	9.2	1.8	2.7	5.0	2.0	14.6

5.5 - Numerical analysis of MMB test method

A two-dimensional numerical analysis including cohesive zone modelling of the MMB test was performed. The three experimental mixed-mode ratios and their average dimensions from each specimens group (Table 5.4) were considered. The numerical model was constructed within a commercial code software using 2426 two-dimensional plane stress solid elements (width *B*, according to Fig. 5.2), with 218 cohesive elements (width *b*, according to Fig. 5.2). The loading apparatus was simulated considering spherical rigid bodies and a loading beam tied to the specimen by means of triangular rigid bodies. Contact surfaces were assumed between the spherical rigid bodies and the specimen. Boundary conditions can be seen in Fig. 5.10, and consist of clamping the bottom supports and imposing a vertical displacement to the right beam extremity. The elastic and fracture properties introduced in numerical model can be consulted on Tables 5.5-5.6. Elastic modulus was obtained adjusting the numerical curve to the range of experimental P-δ curves. Fracture properties were extracted from the DCB (Chapter II) and ENF (Chapter III) results and adapted to a bi-linear cohesive law for the sake of simplification. The inflection point was determined adjusting its coordinates to the range of the cohesive law curves identified by the inverse method (Figs. 2.31 and 3.18).

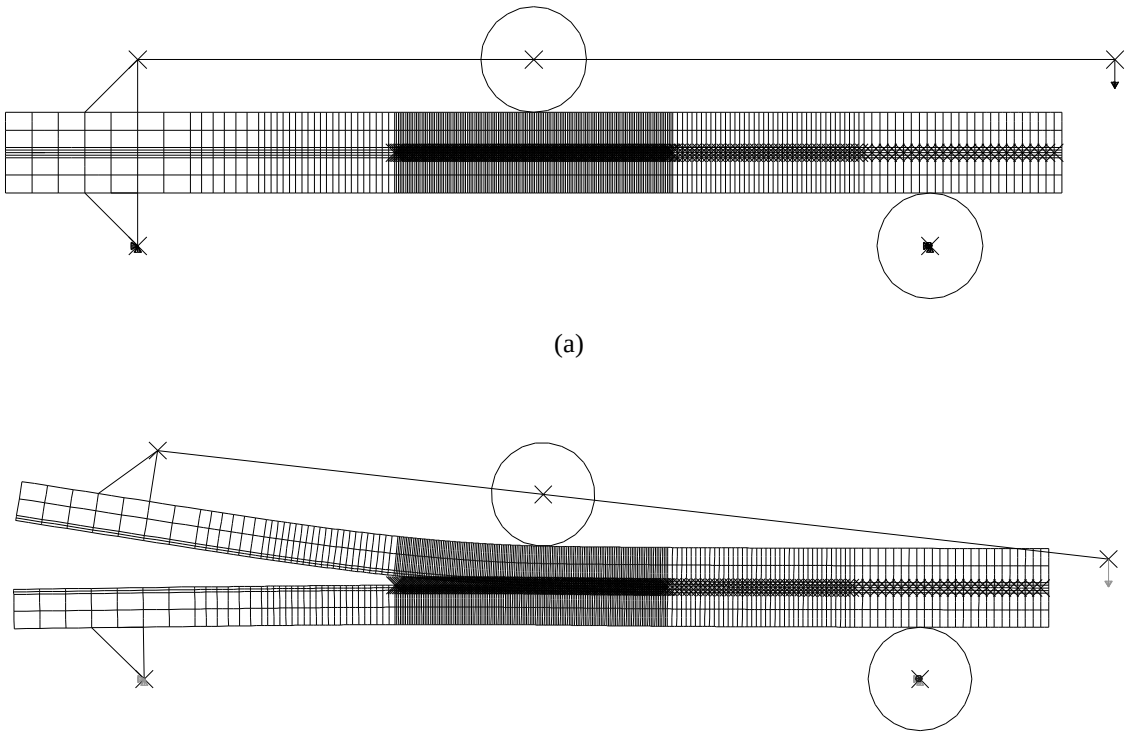

(a)

(b)

Fig. 5.10 – Finite element mesh used for the MMB test: (a) undeformed configuration, (b) deformed configuration at peak load (ratio G_I/G_{II}=2.53).

Table 5.4 – Dimensions used in the numerical model.

Ratio G_I/G_{II}	L (mm)	a_0 (mm)	B (mm)	b (mm)	$2h$ (mm)
0.33	60	20.64	2.55	1.42	6.00
1.24	60	20.98	2.65	1.61	5.94
2.53	60	19.47	2.80	1.72	6.09

Table 5.5 – Elastic properties of cortical bone.

E_L (GPa)	E_T (GPa)	G_{LT} (GPa)	ν_{LT}
12-13.5[+]	9.55[*]	4.74[*]	0.37[*]

[+]- adjusted to experimental P-δ curves.
[*]- Morais et al. (2010).

Table 5.6 – Parameters of the cohesive law for mode I and mode II.

	$\sigma_{i,u}$ (MPa)	$w_{i,1}$ (mm)	$\sigma_{i,1}$ (MPa)	G_{ic} (N/mm)
Mode I (i = I)	47.3*	0.05[+]	9.99[+]	2.53*
Mode II (i = II)	58.0*	0.05[+]	22.16[+]	3.00*

[+]- adjusted to inverse method cohesive law curves.
[*]- pure mode tests performed in this work.

A comparaision between numerical and experimental curves can be seen on Figs. 5.5-5.8. It can be concluded that the numerical results fits well in the experimental curves. Moreover, Fig. 5.9 shows that the numerical values of fracture energy (identified by crosses) follow the introduced mixed-mode criterion (α=0.85) with a sligh overestimation, thus proving the appropriateness of the MMB test in the context of bone fracture characterization under mixed-mode I+II loading.

5.6 - Analysis of mixed-mode I+II cohesive law

For the experimental identification of cohesive law under mixed-mode I+II loading conditions, three methods were considered: the uncoupled method (Mohammed and Liechti, 2000; Yang and Thouless, 2001) detailed on section 4.6, the method proposed by Sørensen and Kirkegaard (2006) and the one developed by Högberg (2006). The application of the last two methods is based on the fact that the influence of COD_I on shear stresses and COD_{II} on normal stresses needs to be evaluated. The Sørensen and Kirkegaard (2006) method provides a surface function describing all the mixed-mode ratios, although the other approaches only identify cohesive law components associated to the local mixed-mode ratio. The approach proposed by Sørensen and Kirkegaard (2006) for the identification of cohesive laws under mixed-mode I+II is thus based on the assumption that the stresses are derived from an energy potential function,

$$G_T = \Phi\left(w_I, w_{II}\right) \tag{5.21}$$

where w_I and w_{II} are the crack opening displacements in mode I and mode II, respectively. According to their assumption the components of the cohesive laws in each mode are derived from the previous energy potential,

$$\sigma_I\left(w_I, w_{II}\right) = \frac{\partial \Phi}{\partial w_I} \quad \text{and} \quad \sigma_{II}\left(w_I, w_{II}\right) = \frac{\partial \Phi}{\partial w_{II}} \tag{5.22}$$

The cohesive stresses (Eq. 5.22) are independent of the trajectory of the local displacements being only dependent on the current displacement values. This hypothesis is mostly valid when the phase angle, ψ, (Eq.4.12) remains constant during crack growth. Fig. 5.11 plots an example for each mode ratio proving that the linear evolution of COD_{II} (w_{II}) versus COD_I (w_I) (i.e., ψ constant) up to the peak load is an acceptable assumption making valid the application of the method.

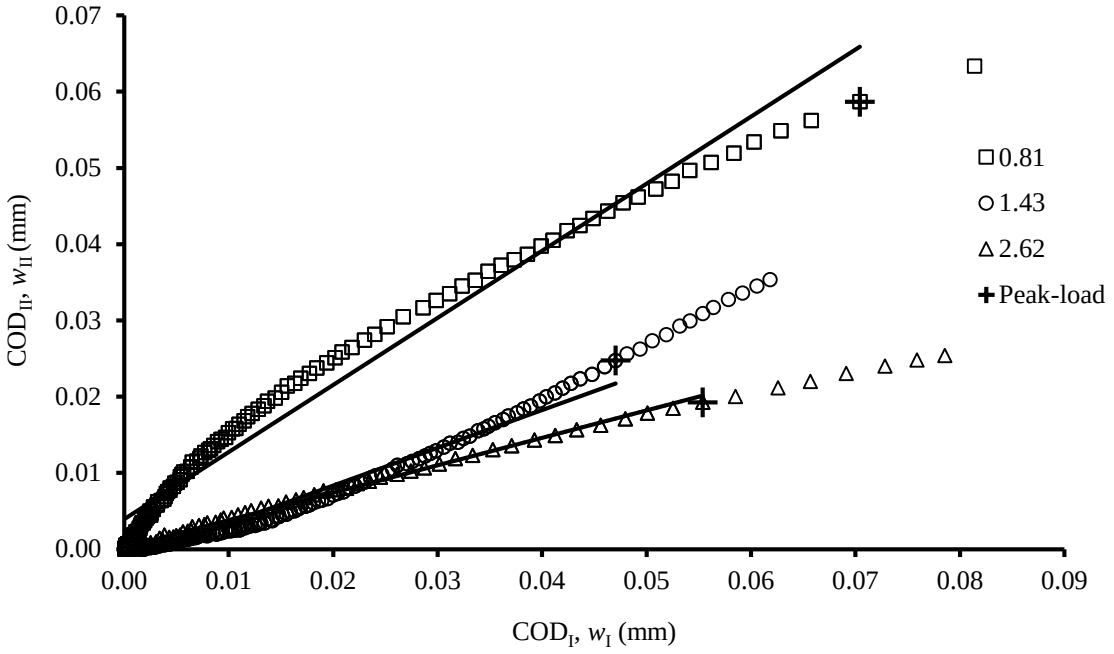

Fig. 5.11 – Examples of w_{II} versus w_I local displacements for each MMB ratio.

From Eqs. (5.21-5.22) the components of the cohesive laws can be obtained generating a series of G_T-w_I-w_{II} datasets for various phase angle values ψ. Sørensen and Kirkegaard (2006) normalized the crack opening displacements using the end crack opening displacement where the cohesive stresses vanish (i.e., beginning of plateau). In this context, the displacements were normalized using the following expression,

$$\overline{w}_i = \frac{w_i}{w_{mc}} \quad (i=\text{I,II}) \tag{5.23}$$

with w_{mc} representing the critical equivalent crack opening displacement for each specimen. The results given by the pure modes DCB and ENF tests and MMB tests were normalized by the total fracture energy ($\bar{G}=G_T/G_{Tc}$) and plotted in Fig. 5.12 as function of the $\overline{w}_I$ and $\overline{w}_{II}$. They were fitted by a polynomial function of fourth degree (Eq. 5.24: a_{00}= -0.0008473; a_{10} = 2.477; a_{01} = 1.035; a_{20} = -1.609; a_{11} = -8.488; a_{02} = 4.214; a_{30} = -0.7086; a_{21} = 11.17; a_{12} = 3.796; a_{03}=-7.8; a_{40} = 0.8408; a_{31} = -4.049; a_{22} = -4.923; a_{13} = 1.161; a_{04} = 3.626).

$$\begin{aligned}\overline{G} = {} & a_{00} + a_{10}\overline{w}_I + a_{01}\overline{w}_{II} + a_{20}\overline{w}_I + a_{11}\overline{w}_I\overline{w}_{II} + a_{02}\overline{w}_{II}^2 + a_{30}\overline{w}_I^3 + a_{21}\overline{w}_I^2\overline{w}_{II} + \\ & + a_{12}\overline{w}_I\overline{w}_{II}^2 + a_{03}\overline{w}_{II}^3 + a_{40}\overline{w}_I^4 + a_{31}\overline{w}_I\overline{w}_{II} + a_{22}\overline{w}_I\overline{w}_{II} + a_{13}\overline{w}_I\overline{w}_{II}^3 + a_{04}\overline{w}_{II}^4\end{aligned} \tag{5.24}$$

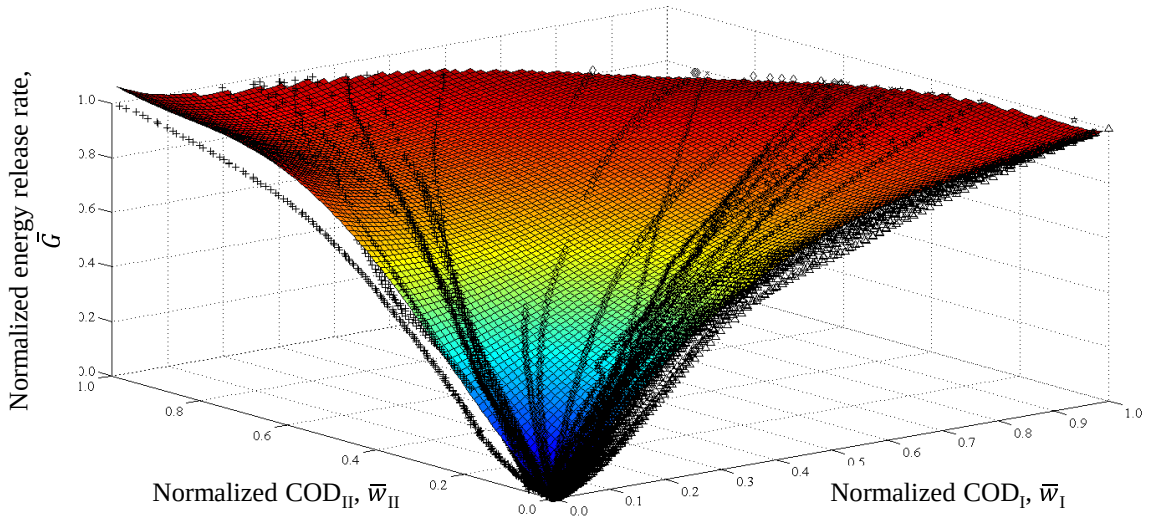

Fig. 5.12 – Normalized $\bar{G}(\bar{w}_{I},\bar{w}_{II})$ curves of all fracture tests and the fitted surface.

The differentiation of the previous polynomial provides the evolution of the cohesive laws as function of the phase angle (Fig. 5.13). Mode I components of the cohesive laws represented in Fig. 5.13a reveal that pure mode I law is well captured. In addition, a coherent evolution of these mode I components of cohesive laws with the increase of phase angle is also observed. However, in the region correspondent to pure mode II a spurious outline resulted, owing to inadequate fitting process probably induced by natural experimental variations and/or insufficient datasets used in fitting procedure. Similar conclusions can be drawn for mode II (Fig. 5.13b). In fact, a pure mode II representation was obtained and a logical evolution as a function of the phase angle was observed. Once again the plotting on the pure mode I plane resulted in a spurious profile probably due to the same reasons pointed above. Figure 5.14 illustrates the pure mode laws issuing from Fig. 5.13 after conversion. Logical representations were obtained with two exceptions. The final branches of the two laws do not point to zero stresses as should be, which can be explained by polynomial adjustment inaccuracies. Additionally, the early ascending branch of the pure mode II law (in the pre-peak region) should not reveal the initial elastic behaviour with quite low stiffness; effectively, the expected behaviour in mode II should be similar to the one observed in mode I, i.e., high initial stiffness up to the peak value. The local strength values ($\sigma_{I,u}$ = 36.0 and $\sigma_{II,u}$ = 44.1 MPa) are inferior, although of the same order of the ones found in pure mode fracture tests by direct and inverse methods (DCB pointed to $\sigma_{I,u}$ =49.18; 47.25 MPa and ENF to $\sigma_{II,u}$ =51.01; 57.96 MPa). Moreover, the areas circumscribed by both curves up to the critical crack opening displacement (around 0.14-0.15 mm) lead to pure mode fracture energies (G_{Ic}=2.38 and G_{IIc}=2.83 N/mm) that are in

agreement with the ones obtained in pure mode fracture tests (G_{Ic}=2.53 and G_{IIc}=3.0 N/mm). These results validate the procedure followed to get the envelope of the cohesive laws under general mixed-mode I+II loading. In fact, the found differences can be attributed to the natural dispersion of experimental results typical of a natural material like bone.

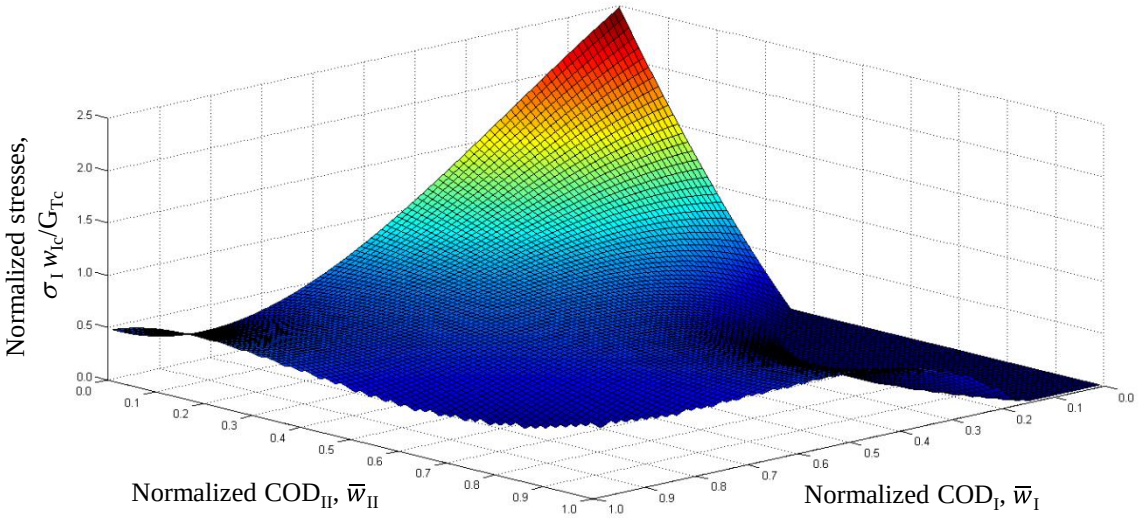

(a)

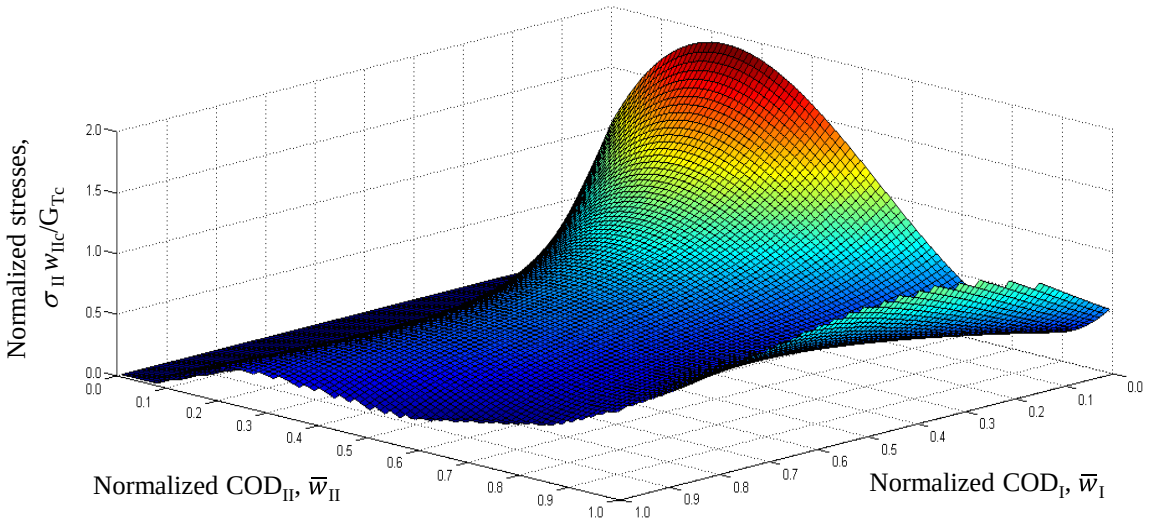

(b)

Fig. 5.13 – Normalized cohesive laws components obtained by the application of Sørensen and Kirkegaard, (2006) method: (a) mode I, (b) mode II.

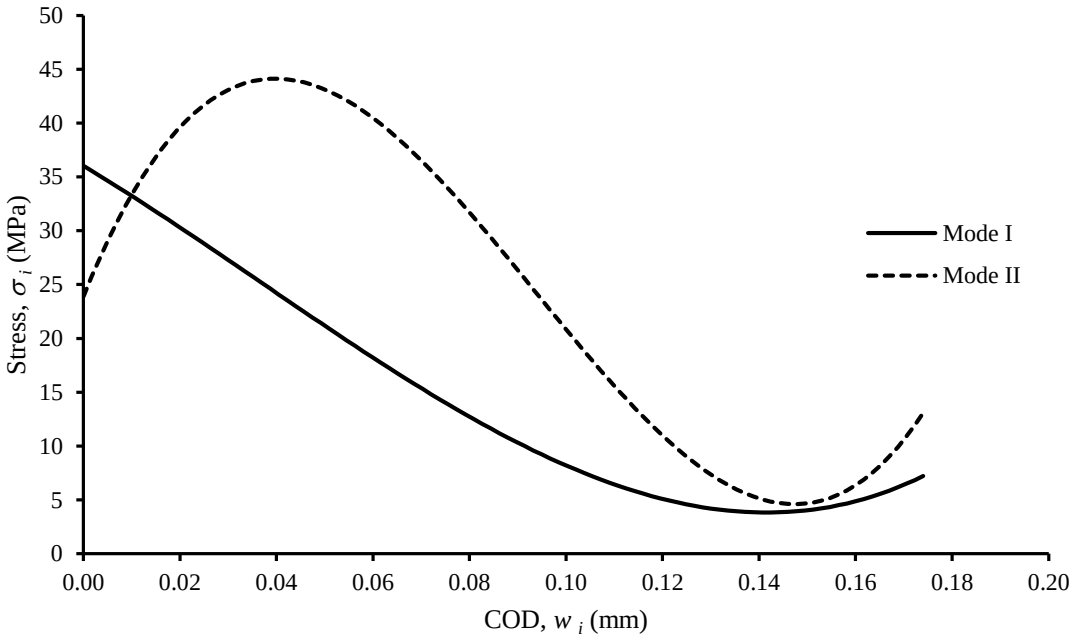

Fig. 5.14 – Cohesive laws components obtained by the application of Sørensen and Kirkegaard, (2006) method.

The uncoupled method proposed by Yang and Thouless (2001) was also applied to estimate the components of the cohesive laws under mixed-mode I+II loading. This method required a special treatment of the w_{II} values measured by DIC analysis in the early stages of the experimental tests. In fact, the very small values of this parameter at the beginning of the tests were not well captured due to resolution problems of DIC technique. To overcome this drawback, a linear relationship was assumed for the w_{II} versus w_I evolution during test to correct these initial values of w_{II} (Fig. 5.11). The cohesive laws resulting from the application of this method will be presented later with the ones issuing from the Högberg method in order to perform a pertinent comparison.

The method developed by Högberg (2006) was also used to get the components of the cohesive laws under mixed-mode I+II loading. This method implies the introduction of dimensionless parameters. Therefore, the crack opening displacements and strengths were normalized using the critical values obtained in pure modes (Eqs. 5.25-5.26),

$$\overline{\sigma}_{\mathrm{I}} = \frac{\sigma_{\mathrm{I}}}{\sigma_{\mathrm{I,u}}} \quad \text{and} \quad \overline{\sigma}_{\mathrm{II}} = \frac{\sigma_{\mathrm{II}}}{\sigma_{\mathrm{II,u}}} \tag{5.25}$$

$$\overline{w}_{\mathrm{I,Hög}} = \frac{w_{\mathrm{I}}}{w_{\mathrm{Ic}}} \quad \text{and} \quad \overline{w}_{\mathrm{II,Hög}} = \frac{w_{\mathrm{II}}}{w_{\mathrm{IIc}}} \tag{5.26}$$

In light of this, all the displacements and stresses will vary in the range of [0, 1]. Högberg (2006) considered a linear cohesive law whose fracture energies in pure modes are given by,

$$G_{\mathrm{Ic}} = \frac{1}{2}\sigma_{\mathrm{I,u}} w_{\mathrm{Ic}} \quad \text{and} \quad G_{\mathrm{IIc}} = \frac{1}{2}\sigma_{\mathrm{II,u}} w_{\mathrm{IIc}} \tag{5.27}$$

Substituting the displacements and the stresses by their normalized parameters, the normalized fracture energies become equal in mode I and mode II, i.e. $\overline{G}_{\mathrm{Ic}} = \overline{G}_{\mathrm{IIc}} = 1/2$. The displacements in mode I and mode II are coupled via a dimensionless displacement parameter, λ, which is defined by

$$\lambda^2 = \overline{w}^2_{\mathrm{I,Hög}} + \overline{w}^2_{\mathrm{II,Hög}} \tag{5.28}$$

However, this parameter uses the normalized crack opening displacements (Eq. 5.26) determined using the average critical values obtained under pure mode loading which in a material like bone is a problematic procedure due to markedly material variability. In this context, a redefinition of parameter λ (named λ_{corr}) is required. Thus, the critical value of the equivalent $\mathrm{COD}_{\mathrm{I+II}}$ (designated by w_{mc}) was used to normalize the equivalent crack opening displacement w_{m} of each specimen,

$$\lambda_{\mathrm{corr}} = \frac{w_{\mathrm{m}}}{w_{\mathrm{mc}}} \tag{5.29}$$

Another fundamental parameter of Högberg method is the mode mixity, θ, (Eq. 5.30) which is defined by the ratio of the dimensionless normal and tangential displacements being the pure mode I given by $\theta = \pi/2$ and the pure mode II by $\theta = 0$. These considerations are graphically presented in Fig. 5.15.

$$\theta = \arctan\left(\frac{\overline{w}_{\mathrm{I,Hög}}}{\overline{w}_{\mathrm{II,Hög}}}\right) \tag{5.30}$$

The mixed-mode cohesive relation $S(\lambda)$ can be derived from a potential defined by,

$$\overline{G}(\lambda,\theta) = \int_0^{\lambda} S(\lambda^*)\mathrm{d}\lambda^* \tag{5.31}$$

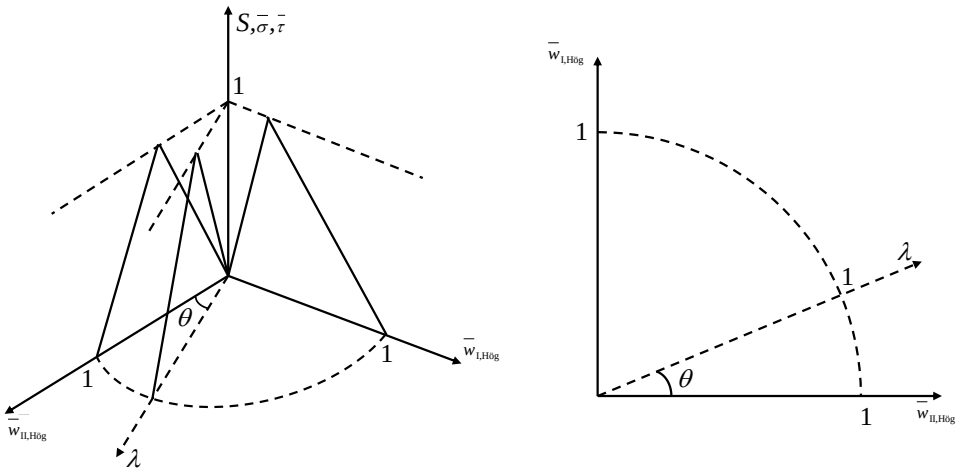

Fig. 5.15 – Graphical presentation of the mixed-mode cohesive law, adapted from Högberg (2006).

According to the method proposed by Högberg (2006) there is a potential function $\overline{G}(\lambda)$ for each mode mixity, i.e. the normalized mixed-mode cohesive law can be obtained using the following expression,

$$S_\theta(\lambda) = \frac{d\overline{G}(\lambda)}{d\lambda} \tag{5.32}$$

where,

$$\overline{G}(\lambda) = \frac{G(\lambda)}{2G_{\mathrm{Tc}}} \tag{5.33}$$

The last stage of this method consists of modes partitioning (Högberg, 2006),

$$\sigma_{\mathrm{I}}(w_{\mathrm{I}}, w_{\mathrm{II}}) = \sigma_{\mathrm{I,u}}\,\overline{w}_{\mathrm{I}}\,\frac{S_\theta}{\lambda} \tag{5.34}$$

$$\sigma_{\mathrm{II}}(w_{\mathrm{I}}, w_{\mathrm{II}}) = \sigma_{\mathrm{II,u}}\,\overline{w}_{\mathrm{II}}\,\frac{S_\theta}{\lambda} \tag{5.35}$$

According to Eq. (5.29), the Eq. (5.32) assumes the following form,

$$S_\theta(\lambda_{\mathrm{corr}}) = \frac{d\overline{G}(\lambda_{\mathrm{corr}})}{d\lambda_{\mathrm{corr}}} \tag{5.36}$$

The aspect of all the obtained components of the cohesive laws can be observed in Figs 5.16-5.21. Comparing the cohesive laws between both methods it can be concluded that the Högberg laws generally present higher scatter and noise. A plausible justification is the use of the critical strengths and ultimate displacements obtained from pure mode fracture tests. As already referred, in a natural material with high variability like cortical bone, the expected variation of properties leads to dispersion amplification. Tables 5.7-5.9

summarize all these results, i.e., it contains the maximum stresses ($\sigma_{um,I}$, $\sigma_{um,II}$), the critical COD_{I+II} (w_{mc}), the fracture energy components (area circumscribed by the curves) of the cohesive law and θ values for each specimen, thus propitiating a better comprehension of the observed trends.

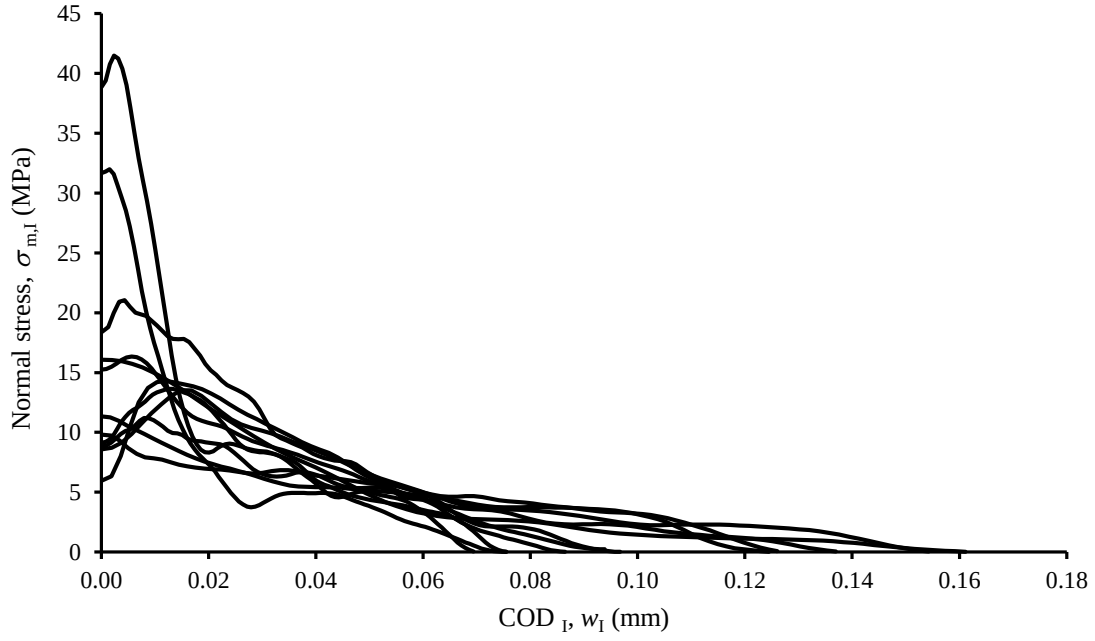

(a)

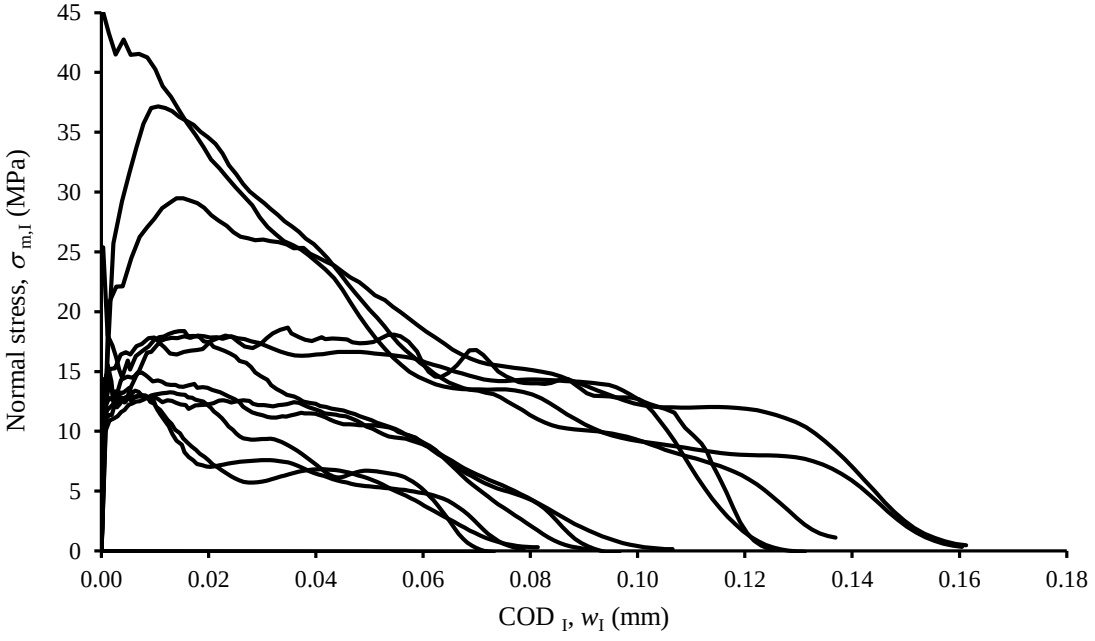

(b)

Fig. 5.16 – Mode I components of the cohesive laws for G_I/G_{II}=0.33: (a) uncoupled method; (b) Högberg.

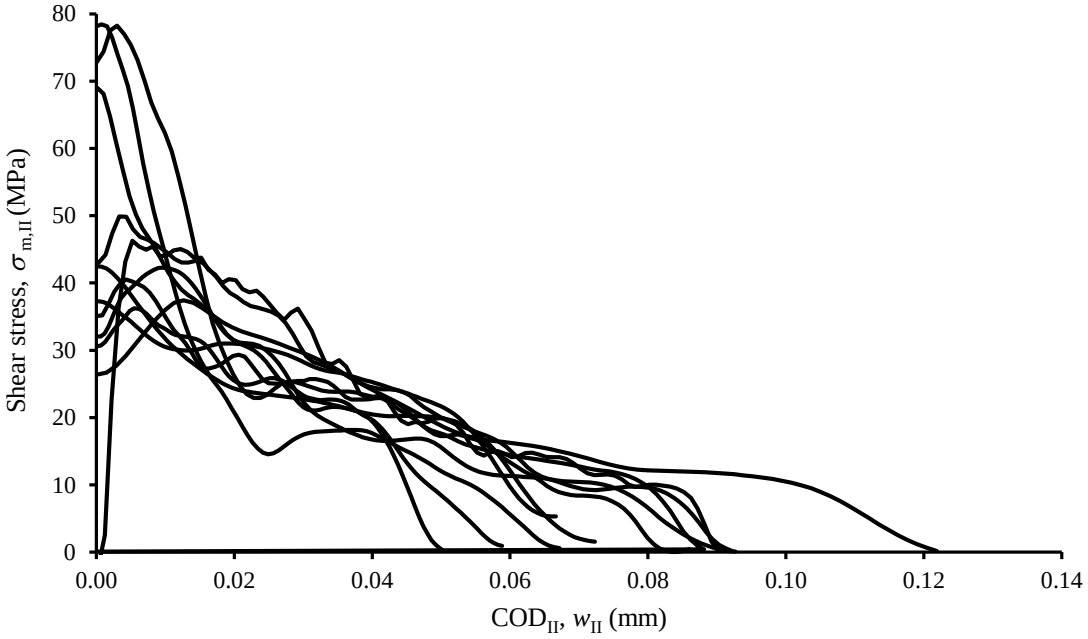

(a)

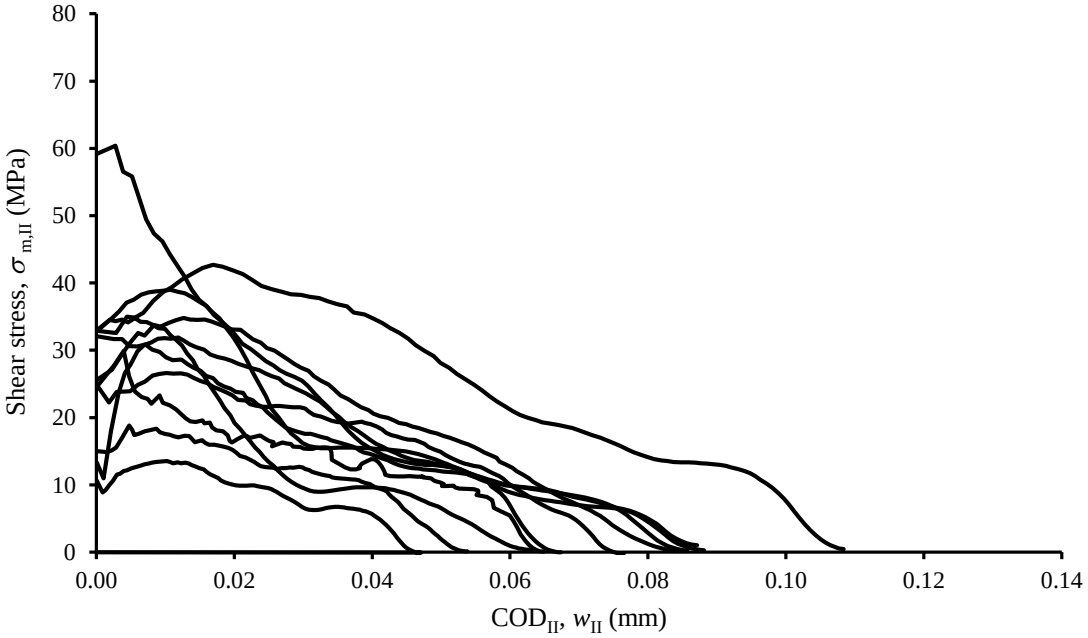

(b)

Fig. 5.17 – Mode II components of the cohesive laws for G_I/G_{II}=0.33: (a) uncoupled method; (b) Högberg.

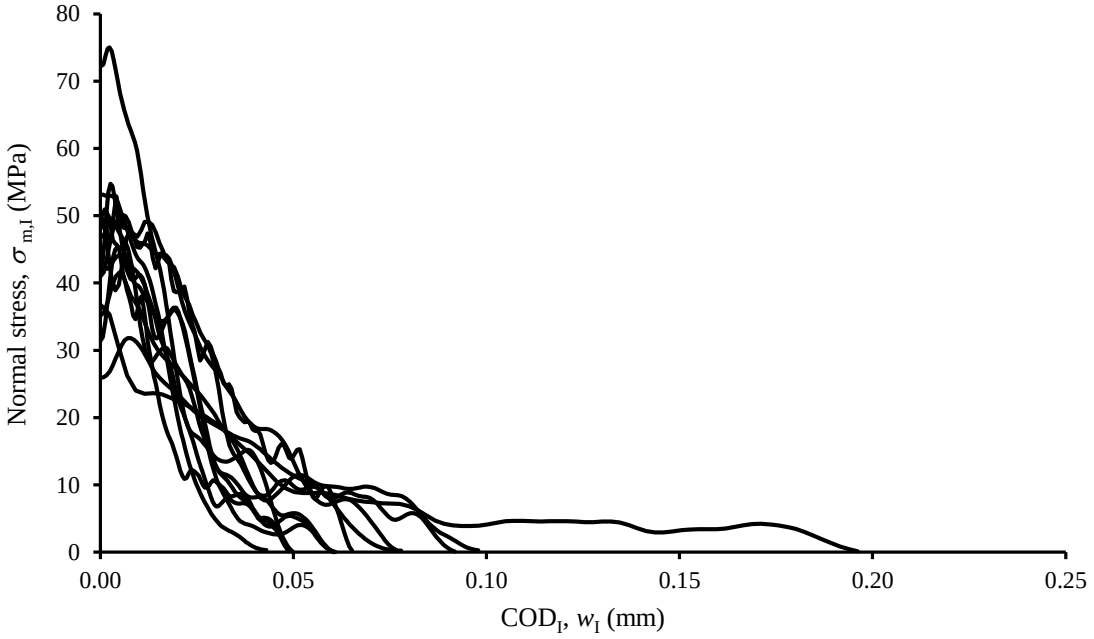

(a)

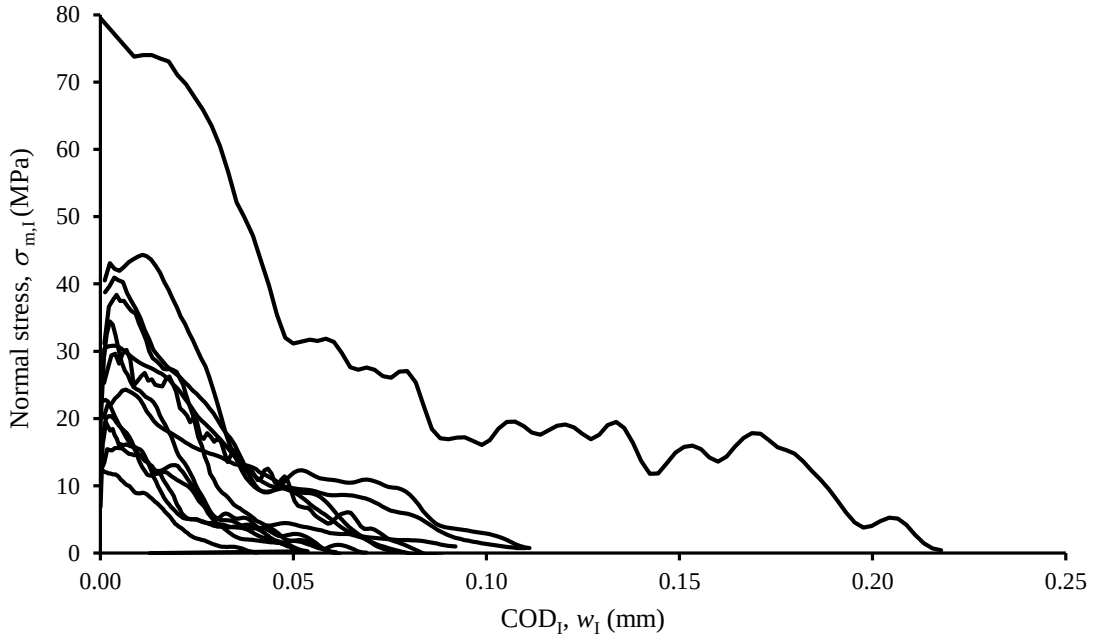

(b)

Fig. 5.18 – Mode I components of the cohesive laws for G_I/G_{II}=1.24: (a) uncoupled method; (b) Högberg.

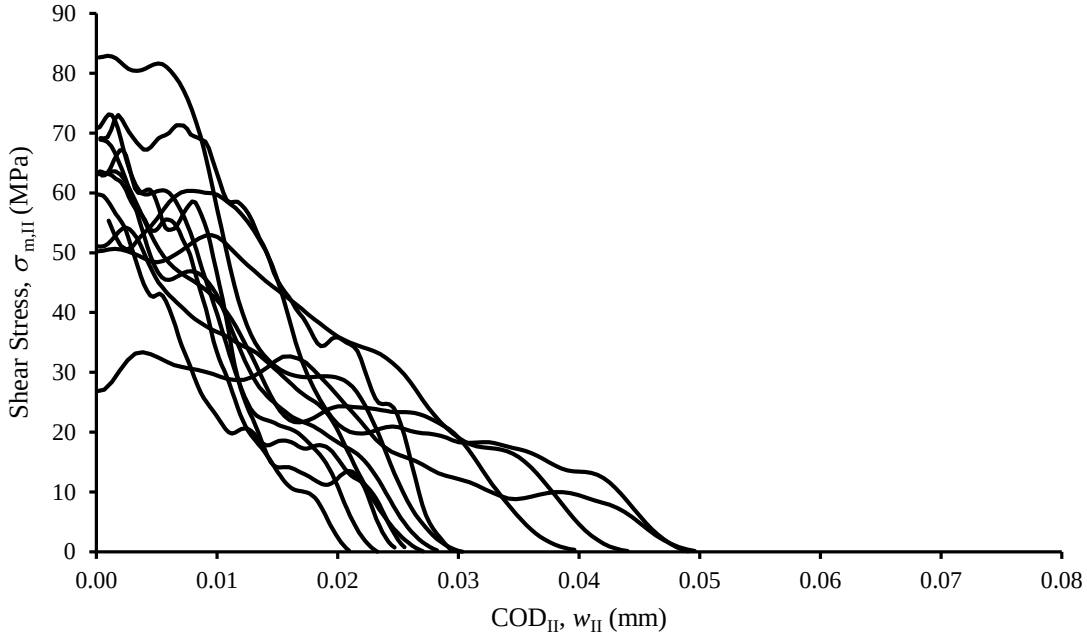

(a)

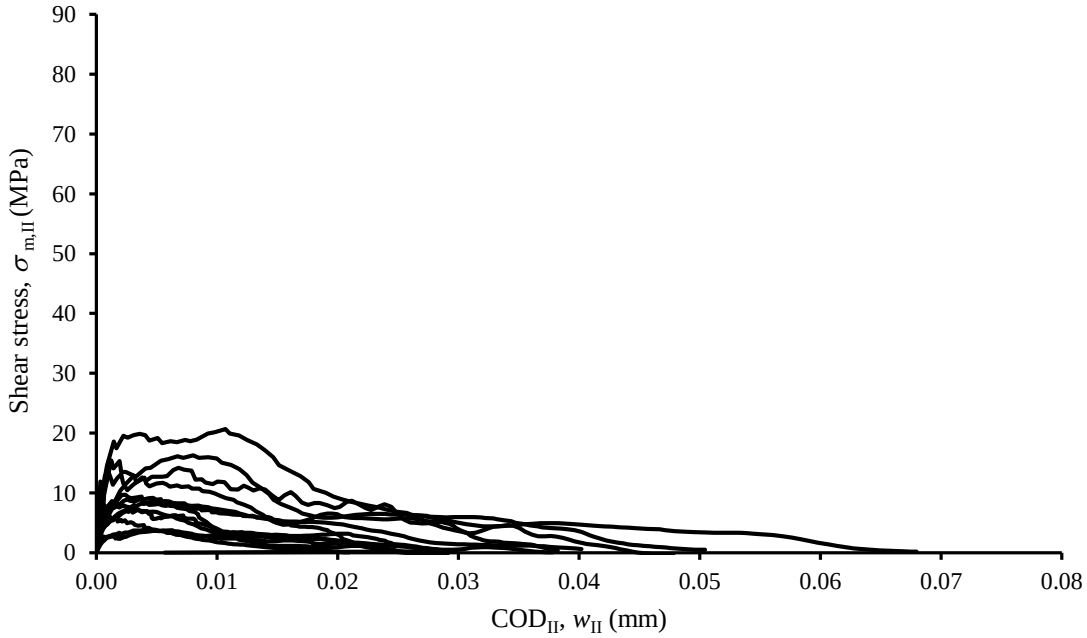

(b)

Fig. 5.19 – Mode II components of the cohesive laws for G_I/G_{II}=1.24: (a) uncoupled method; (b) Högberg.

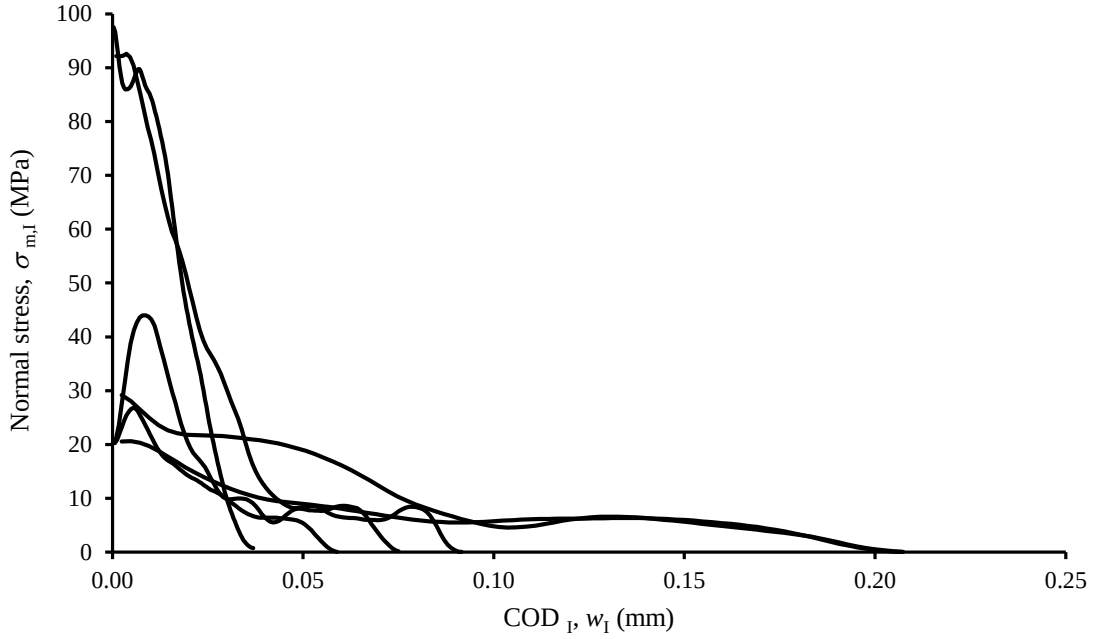

(a)

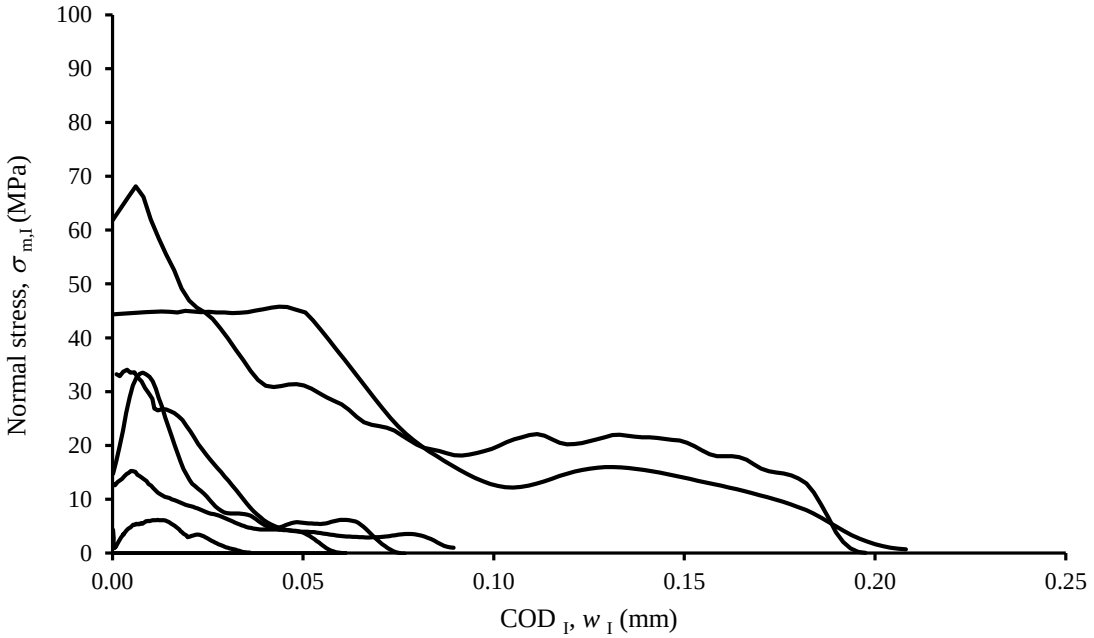

(b)

Fig. 5.20 – Mode I components of the cohesive laws for G_I/G_{II}=2.53: (a) uncoupled method; (b) Högberg.

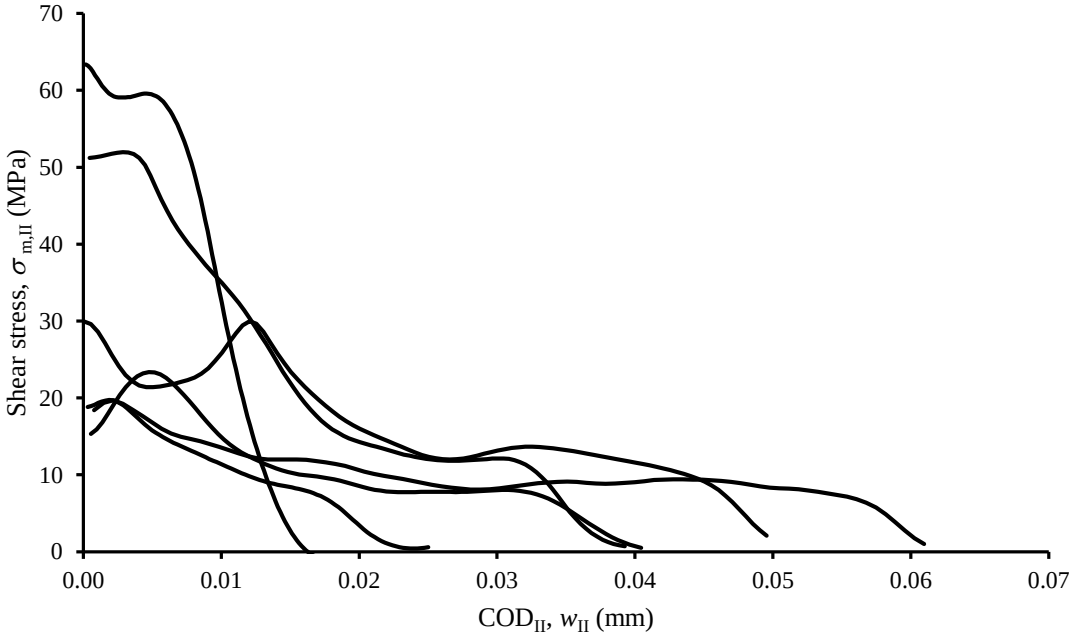

(a)

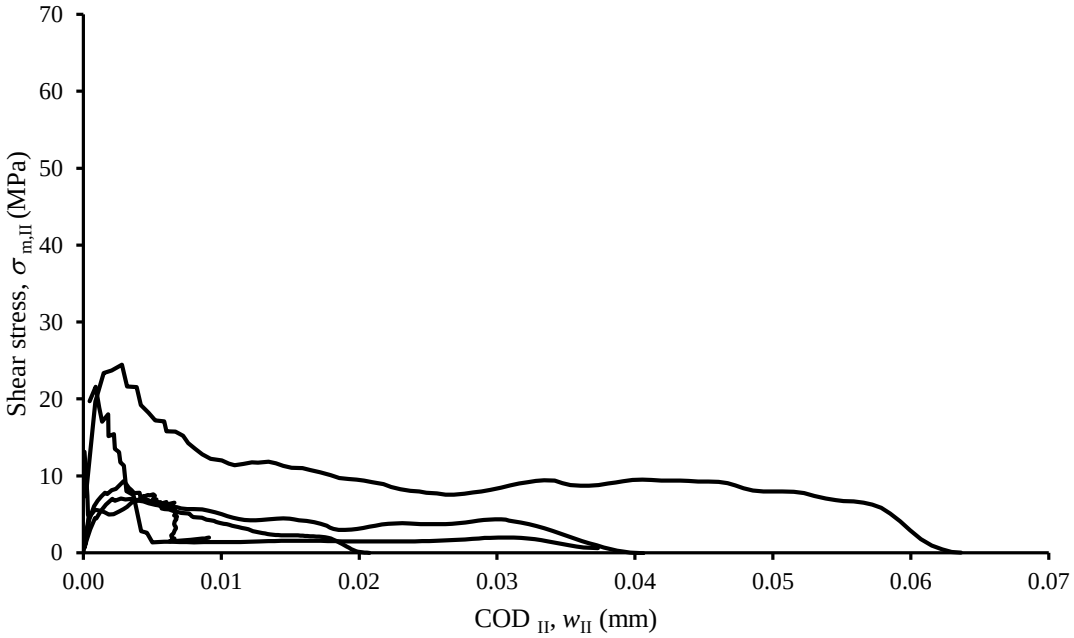

(b)

Fig. 5.21 – Mode II components of the cohesive laws for G_I/G_{II}=2.53: (a) uncoupled method; (b) Högberg.

Table 5.7 – Experimental components of cohesive laws for G_I/G_{II}=0.33.

			Uncoupled				Högberg			
Spec.	θ(º)	w_{mc} (mm)	$\sigma_{um,I}$ (MPa)	$\sigma_{um,II}$ (MPa)	$G_{law,I}$ (N/mm)	$G_{law,II}$ (N/mm)	$\sigma_{um,I}$ (MPa)	$\sigma_{um,II}$ (MPa)	$G_{law,I}$ (N/mm)	$G_{law,II}$ (N/mm)
1	46.94	0.15	14.29	46.26	0.75	2.13	37.15	36.24	2.33	1.46
2	46.12	0.08	13.63	42.29	0.52	1.36	13.26	13.52	0.59	0.41
3	52.43	0.14	11.35	42.48	0.60	1.54	17.99	32.09	1.73	1.18
4	38.31	0.11	16.34	40.53	0.65	1.72	14.3	26.63	0.85	1.28
5	50.66	0.17	16.07	69.00	0.72	1.94	45.43	60.42	2.58	1.8
6	39.01	0.09	32.00	78.42	0.56	1.58	14.38	35.95	0.5	0.96
7	54.85	0.13	9.80	37.28	0.62	1.65	18.66	29.89	1.77	0.94
8	37.60	0.13	21.04	49.88	0.80	2.14	18.38	34.78	1.03	1.65
9	47.20	0.1	11.19	36.23	0.50	1.29	14.91	18.83	0.83	0.63
10	31.80	0.11	41.49	78.23	0.78	2.29	13.03	38.97	0.51	1.52
11	43.23	0.18	13.52	37.44	0.79	2.29	29.49	42.71	2.58	2.69
Avg	44.38	0.13	18.25	50.73	0.66	1.81	21.54	33.64	1.39	1.32
CoV(%)	16.0	25.3	54.1	32.3	16.7	20.1	50.8	36.8	59.8	47.2

Table 5.8 – Experimental components of cohesive laws for G_I/G_{II}=1.24 (– non valid test).

			Uncoupled				Högberg			
Specimen	θ(º)	w_{mc} (mm)	$\sigma_{um,I}$ (MPa)	$\sigma_{um,II}$ (MPa)	$G_{law,I}$ (N/mm)	$G_{law,II}$ (N/mm)	$\sigma_{um,I}$ (MPa)	$\sigma_{um,II}$ (MPa)	$G_{law,I}$ (N/mm)	$G_{law,II}$ (N/mm)
1	42.30	0.07	45.38	33.35	1.19	0.93	38.37	20.67	1.00	0.52
2	53.27	0.05	75.03	82.94	1.47	1.25	19.39	9.14	0.39	0.12
3	53.67	0.08	50.12	52.95	1.80	1.38	30.18	14.19	1.09	0.32
4	64.95	0.08	31.83	54.16	1.22	0.84	24.30	15.27	0.94	0.14
5	60.53	0.20	36.77	49.27	1.70	1.44	76.38	38.85	5.95	1.25
6	55.03	0.04	53.11	63.59	0.96	0.69	12.20	3.89	0.20	0.04
7	59.09	0.05	54.75	73.14	1.04	0.84	34.45	7.73	0.68	0.10
8	62.49	0.10	41.56	63.6	1.51	1.11	40.94	15.42	1.59	0.25
9	59.39	0.06	49.59	68.9	1.16	0.88	20.34	26.44	0.47	0.06
10	-	-	-	-	-	-	-	-	-	-
11	60.11	0.07	52.87	73.01	1.75	1.35	30.82	34.43	1.15	0.17
12	54.85	0.10	50.28	60.35	1.77	1.42	44.34	27.17	1.67	0.36
13	60.81	0.06	44.09	67.15	1.11	0.80	15.66	8.17	0.42	0.08
14	55.03	0.05	50.95	59.74	0.9	0.66	22.78	7.09	0.39	0.07
Average	57.04	0.08	48.95	61.70	1.35	1.05	31.55	17.57	1.23	0.27
CoV(%)	10.0	53.1	21.2	20.4	24.2	27.7	52.9	63.5	121.8	122.3

Table 5.9 – Experimental components of cohesive laws for G_I/G_{II}=2.53 (– non valid test).

			Uncoupled				Högberg			
Specimen	$\bar{\theta}$(º)	w_{mc} (mm)	$\sigma_{um,I}$ (MPa)	$\sigma_{um,II}$ (MPa)	$G_{law,I}$ (N/mm)	$G_{law,II}$ (N/mm)	$\sigma_{um,I}$ (MPa)	$\sigma_{um,II}$ (MPa)	$G_{law,I}$ (N/mm)	$G_{law,II}$ (N/mm)
1	60.81	0.09	92.56	51.97	1.01	0.10	34.03	21.55	2.44	0.87
2	-	-	-	-	-	-	-	-	-	-
3	69.95	0.31	29.57	30.00	4.56	0.33	45.75	16.08	2.15	0.81
4	60.81	0.03	97.49	63.38	0.12	0.04	6.18	7.59	1.84	0.63
5	54.27	0.08	43.99	23.35	0.84	0.16	33.50	13.13	1.13	0.43
6	69.11	0.21	26.79	19.74	0.43	0.08	15.25	9.28	0.69	0.25
7	66.59	0.20	20.62	19.68	5.05	0.61	68.11	24.47	1.55	0.62
8	-	-	-	-	-	-	-	-	-	-
Average	63.59	0.15	51.84	34.69	2.00	0.22	33.80	15.35	1.63	0.60
CoV(%)	9.5	68.1	66.3	53.5	109.9	98.4	65.2	43.6	39.8	38.6

Using the results listed in Tables 5.7-5.9, the trends of the stresses in function of θ were evaluated (see Figs 5.22-5.23) for both methods. Even with a low coefficient of correlation, the normal stresses seem to increase with θ, although the shear stresses show an opposite trend. This is a logical result since the pure mode I occurs for θ equal to 90º and the pure mode II for θ equal to 0º.

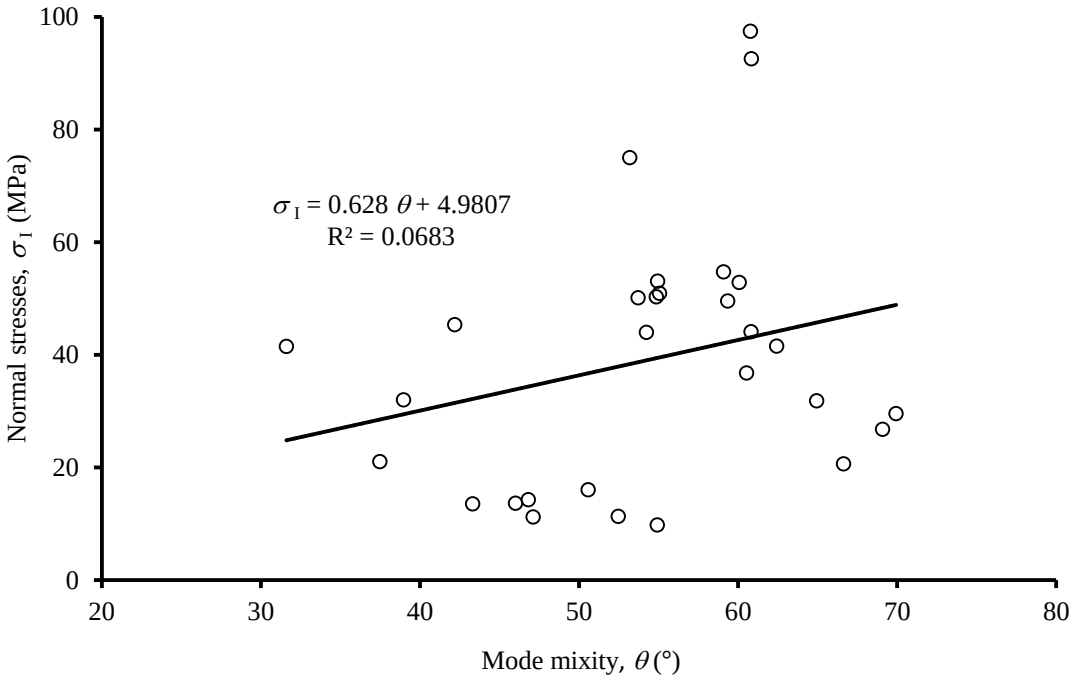

(a)

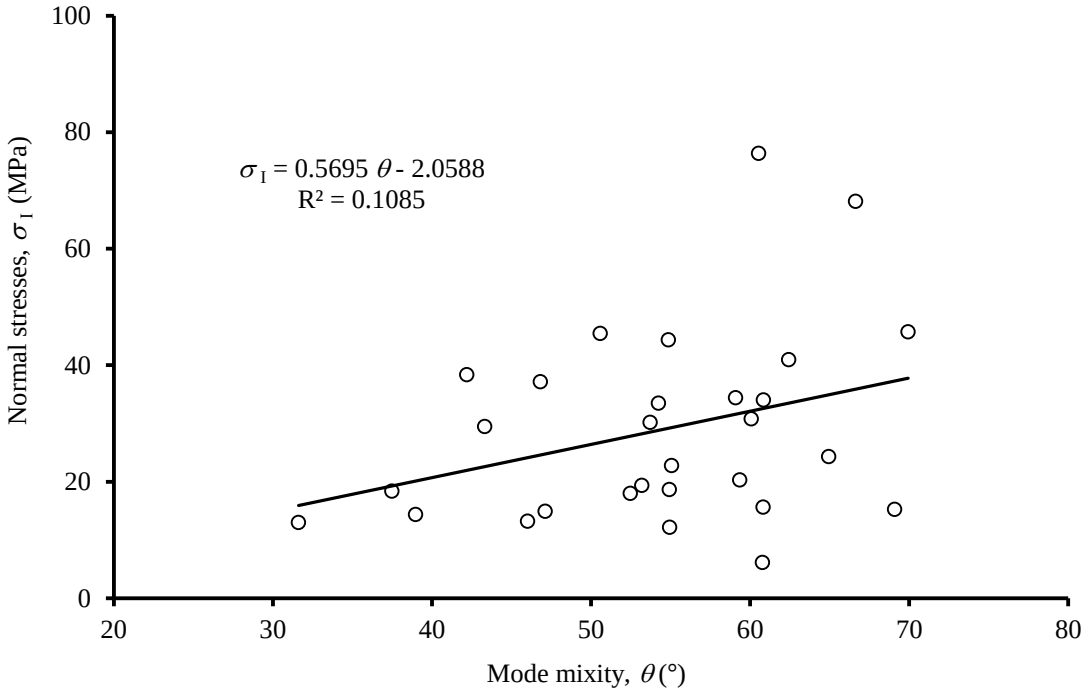

(b)

Fig. 5.22 – Normal stress variation as a function of mode mixity, θ: (a) uncoupled; (b) Högberg.

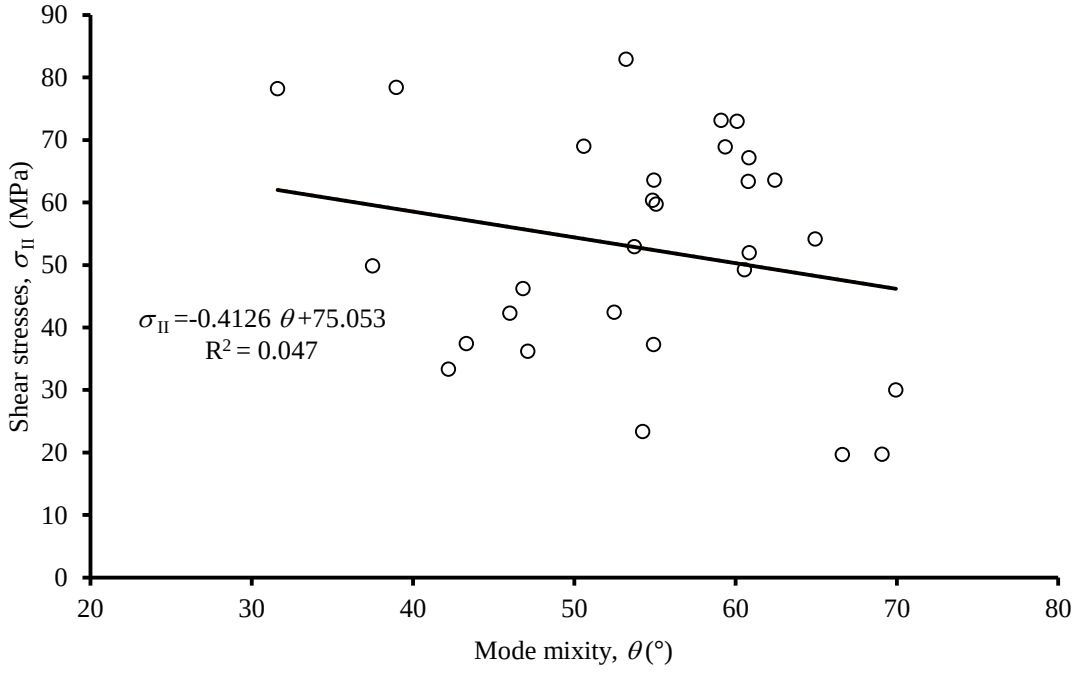

(a)

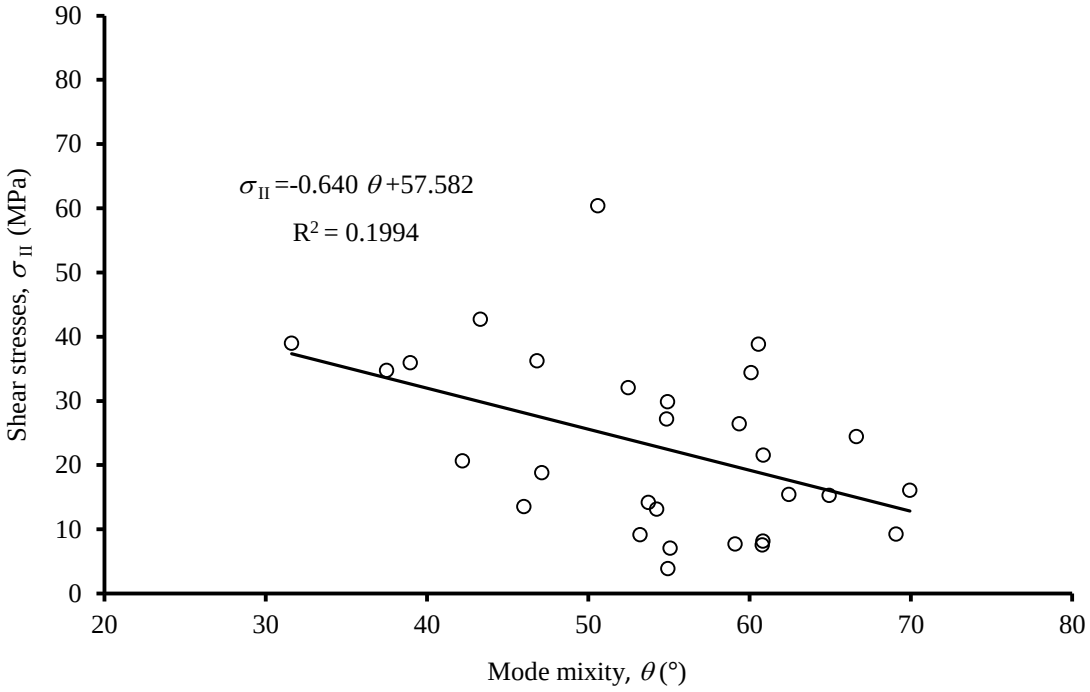

(b)

Fig. 5.23 – Shear stress variation as a function of mode mixity, θ: (a) uncoupled; (b) Högberg.

A linear function was adjusted to the plots in order to estimate the local strengths under pure modes (θ=0º, pure mode II and θ=90º pure mode I) by extrapolation. It was verified that the normal stresses are in the range $5.0<\sigma_I<61.3$ MPa for the uncoupled and $-2.1<\sigma_I<49.2$ MPa for the Högberg method. Similarly, the limits in the shear stresses are $38.0>\sigma_{II}>75.1$ MPa for uncoupled and $57.6>\sigma_{II}>0.0$ MPa for the Högberg method. It can be concluded that Högberg method behaves well on the estimation of the pure local strengths ($\sigma_{I,u}$=49.18 MPa and $\sigma_{II,u}$=51.01 MPa in the direct method and $\sigma_{I,u}$ =47.25 MPa and $\sigma_{II,u}$ =59.68 MPa by the inverse method), but the same did not occurred by the uncoupled one. A possible justification for this malfunction of the uncoupled method probably lies on the fact that the COD measurements were performed in points with some distance between them, thus making the uncoupling assumption somewhat inaccurate. Moreover, the difficulty to get a rigorous evaluation of the COD_{II} by DIC analysis also contributes to this noticed differences, namely on the prediction of normal (acceptable estimation) and shear stresses (imprecise prediction).

Another important parameter is the critical COD_{I+II}. In this case the equivalent crack opening seems to be greater in mode I than in mode II (Fig. 5.24), which agrees with the results obtained from pure modes. In the present analysis the extrapolated value for pure

mode I points to 0.16 mm (θ=90º in Fig. 5.24), which compares well with the one issuing from DCB test using the direct method (0.17 mm). However, under pure mode II a significant difference was found. In fact, for pure mode II a value of 0.032 mm is achieved by extrapolation (Fig. 5.24) although the pure mode value pointed to 0.13 mm. In conclusion it can be affirmed that even if the linear evolutions between the mode I and mode II presented above could eventually be considered physically not sound owing to low correlations, the results seem to confirm that these linear trends are not totally incorrect. It can be affirmed that the Högberg method with the adaptation implemented in this work seems to be able to identify the cohesive laws components.

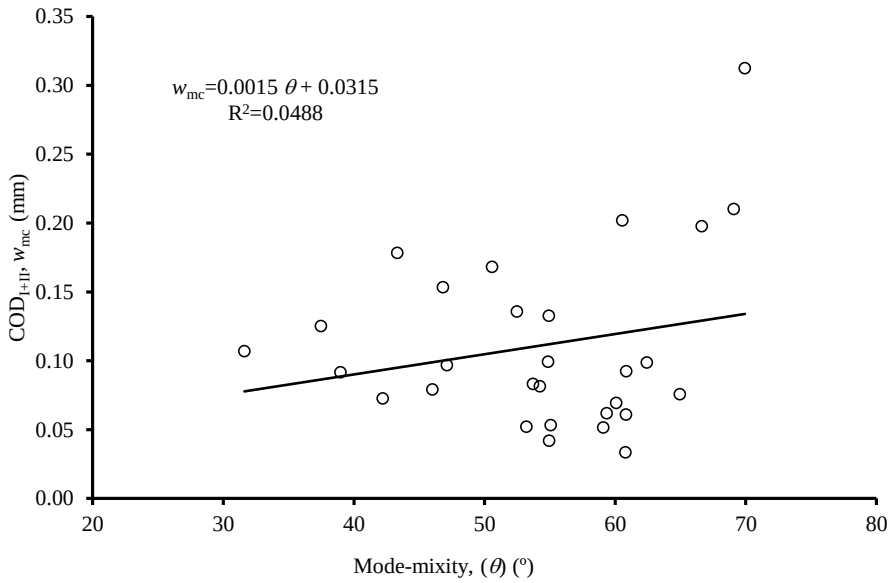

Fig. 5.24 – Critical equivalent crack opening displacements as a function of mode mixity, θ.

Högberg proposes the following expression to estimate the total fracture energy (G_{Tc}) for each mode mixity (θ) from the critical pure mode fracture energies (Högberg et al., 2007),

$$G_{c,t} = G_{Ic} \sin^2 \theta + G_{IIc} \cos^2 \theta \tag{5.37}$$

Also, an analytical expression has been proposed to predict the critical total displacement (λ_{Tc}) dependent of the mode mixity and the critical pure crack opening displacements (Högberg et al., 2007),

$$\lambda_{Tc} = \sqrt{(w_{Ic} \sin\theta)^2 + (w_{IIc} \cos\theta)^2} \tag{5.38}$$

Using the presented expressions the prediction curves were compared with the experimental results (Figs. 5.25-5.26). It was verified that mean values of G_{Tc} issuing from the experimental tests are in agreement (Fig. 5.25) with the trend defined by Eq. (5.37).

However Fig. 5.26 reveal an opposite trend, which can be explained by the assumption innerent to the Högberg method of a linear energetic criterion. As observed previously Fig. 5.15 this statement can be somewhat unrealistic thus explaining the noticed trend.

These results gives some additional indication about the suitability of Högberg method when applied to the identification of cortical bone fracture properties under mixed-mode I+II loading.

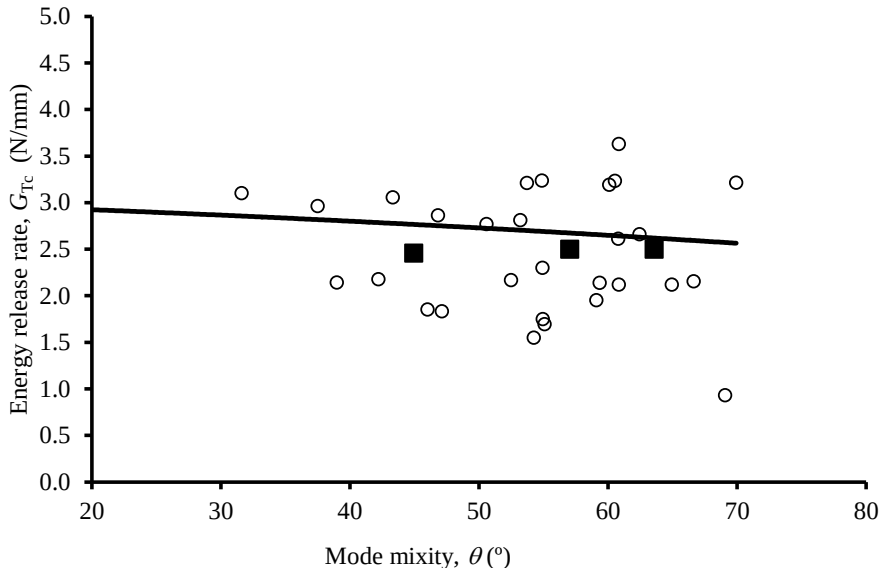

Fig. 5.25 – Total energy release rate variation as a function of mode mixity, θ (■ mean series values).

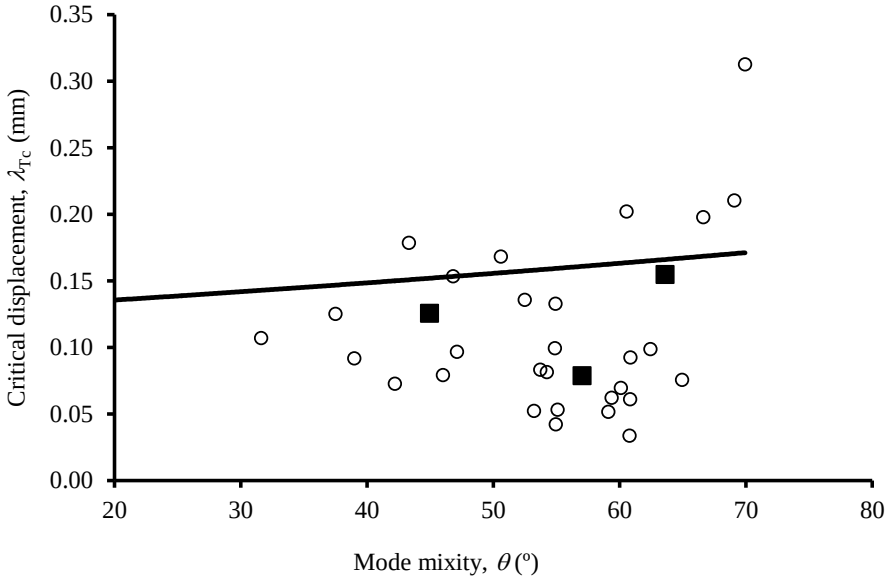

Fig. 5.26 – Critical opening displacement variation as a function mode mixity, θ (■ mean series values).

5.7 - Conclusions

The MMB apparatus was adapted to perform mixed-mode fracture tests in bovine cortical bone due to its ability to provide easy alteration of mixed-mode ratio. Three different mode ratios were evaluated: a predominant mode I, a predominant mode II and an equitable mode loading. The main goal is to cover a wide range of mode mixities propitiating the definition of a fracture envelop in the mode I versus mode II space. The MMB test can be viewed as a combination of the DCB and ENF tests used in this thesis for pure mode fracture characterization under pure mode I and pure mode II loading. Consequently, the CBBM was also used to evaluate the *R*-curves for mode I and mode II components of the mixed-mode loading, thus avoiding crack length monitoring during the fracture tests. Three methods were applied to the experimental identification of cohesive law components under mixed-mode I+II loading: Sørensen's method, uncoupled and Högberg's method.

The main conclusions issuing from this Chapter can be summarized as follows:

- in general, at least small plateaus were obtained from *R*-curves of both loading modes (I and II), revealing that crack propagation occurred in a self-similar way; this result proved that the corresponding fracture energy components were measured accurately;
- a numerical analysis considering CZM was performed on the MMB test; it was verified that the issued fracture energies are in agreement with the fracture criterion used as input for the three mode ratios considered; this lead to the conclusion that MMB test with the proposed specimen dimensions is appropriated for bone fracture characterization under mixed-mode I+II loading;
- overall, all of the methods used to get the cohesive laws proved to be satisfactory in terms of the revealed trends;
- due to probable insufficient datasets used in the Sørensen method the results were not fully acceptable in the entire domain of the fracture envelop, namely on the pure mode II region;
- the Högberg method proved to be effective in the identification of cohesive law components of the mixed-mode I+II loading; the only limitation lies on the fact that pure mode data is required and in materials with non-negligible scatter the use of critical values from different samples can be a problem;

- the uncoupled method is simple and straightforward to apply, though it does not consider the combined effects between stresses and crack opening displacements, which may be pointed as a limitation;

CHAPTER VI

Conclusions

The objective of this work is to perform fracture characterization of cortical bone under mode I, mode II and mixed-mode I+II loading including the evaluation of the corresponding cohesive laws that allow simulating bone fracture behaviour. The interest of this study is to assess how bone fragility is affected by several features and also to provide guidelines that must be analysed in orthopaedic complications. These are crucial aspects, owing to problems affecting bone toughness, as is the case of diseases, daily accidents, reaction to medical therapies and ageing.

Four different tests were performed to deal with different loading modes: Double Cantilever Beam (DCB) in mode I, End-Notched Flexure (ENF) in mode II and, Single-Leg Bending (SLB) and Mixed-Mode Bending (MMB) in mixed-mode I+II loading. The following procedure including five main steps was applied in these tests:

- experimental measurement of the load-displacement curves and crack opening displacements using Digital Image Correlation (DIC) technique;
- evaluation of *Resistance*-curves (*R*-curves), from which the corresponding critical values of fracture energy were obtained;
- numerical validation of the proposed tests using cohesive zone modelling;
- determination of the cohesive law by the direct method, which consists in differentiating the strain energy release rate versus crack opening displacement relation;
- only for the pure modes, application of an inverse method based on an optimization technique using the *Bissection* and *Nelder-Mead* algorithms.

In general, the digital image correlation technique (DIC) proved to be adequate to perform rigorous measurements of crack opening displacements (COD) in bone, presenting limitations only in the measurement of COD_{II} in MMB tests. However, these limitations were restricted to the early stages of the test, whose COD_{II} values were below the resolution of the technique. The *R*-curves were obtained using an equivalent crack length based procedure based on specimen compliance and Timoshenko beam theory (Compliance Based Beam Method - CBBM). The application of the CBBM avoids crack length monitoring in the course of the fracture tests which was verified to be an almost impossible task to be accomplished with the required accuracy. In all tests it was verified that small plateaus were obtained, which means that self-similar crack growth took place for a given crack extent. This is a very interesting result proving that the proposed specimen geometries are able to propitiate accurate measurements of fracture energies, despite the natural size limitations of bone specimens.

The application of the CBBM to experimental results was validated numerically by means of cohesive zone modelling (CZM). With this aim, the values of fracture energy issuing from the CBBM using the numerical data were compared with the ones used as input. Additionally, the numerical load-displacement curves were compared with the experimental ones. In general, excellent agreement was obtained, thus validating the proposed procedure and selected fracture tests in the context of bone fracture characterization.

The mixed-mode I+II fracture studies were performed using the SLB and MMB tests. The SLB test only provides a constant mixed-mode ratio. To overcome this limitation a miniaturized version of the MMB test rig was conceived, since this test allows an easy variation of the mode mixity. Three mixed-mode ratios were analysed in this work. The mode I and mode II components of the fracture energy determined in the SLB and MMB tests were plotted in the $G_I - G_{II}$ space. It was observed that the evolution of the fracture energy envelop under mixed-mode I+II loading can be estimated by a power law criterion. The numerical analysis using CZM demonstrated the reliability of these results.

Cohesive laws were subsequently determined through direct and inverse procedures. The direct one is based on the differentiation of the function fitted to the experimental relation between strain energy release rate and crack opening displacement. In general, coherent results were obtained, especially in the case of pure modes. Under mixed-mode I+II loading some adaptations were required to get the mode I and mode II components of the cohesive law. Following the experimental work these components were identified by three methods:

uncoupled, Sørensen and Högberg, all of them revealing reliable trends. The uncoupled method is the simplest one, but it does not account for eventual cross effects between stresses and crack opening displacements. The Sørensen method revealed unreliable results in the vicinity of the pure mode II loading, probably due to insufficient used datasets. The method developed by Högberg proved to be efficient, although it requires the combination of mixed-mode values with pure mode ones, which inevitably derive from another group of samples. This can constitute a difficulty owing to scatter typical of natural materials like bone.

The inverse procedure combines numerical simulations with a developed optimization algorithm to determine the cohesive law that minimizes the difference between the numerical and the experimental load-displacement curves. The main characteristic of the proposed inverse methodology is the identification of the cohesive law without imposing its shape a priori, as occurs in the classical inverse procedures. In the present model the cohesive law is defined considering several branches in the softening region without assuming any constraint in the shape of the law. The inverse method was successfully applied to pure modes loading cases.

Although the described work was performed considering bovine bone, the proposed processes and procedures can also be applied and extended to human bone. Consequently, the proposed methodologies can be viewed as a novel valuable tool to be used in parametric and methodical clinical studies regarding features influencing bone fracture (e.g., age, diseases, drugs) under analised loading modes

The evaluation of fatigue and impact behaviour of cortical bone tissue constitute important topics of research that can be exploited in the nearly future. These types of loading are commom in humans' daily activities, thus becoming relevant subjects of investigation. The mastery of specific experimental techniques developed in this thesis provides the required prerequisites to conduct these studies with success. These aspects allied to the developed fracture characterization will enlarge the spectrum of knowledge of bone mechanical behaviour.

References

Akkus, O., Jepsen, K.J., and Rimnac, C.M. (2000). Microstructural aspects of the fracture process in human cortical bone. J. Mater. Sci. 35, 6065–6074.

Andersson, T., and Biel, A. (2006). On the effective constitutive properties of a thin adhesive layer loaded in peel. Int. J. Fract. 141, 227–246.

Barenblatt, G.. (1959). Concerning equilibrium cracks forming during brittle fracture. The stability of isolated cracks. Relationships with energetic theories. Journal of Applied Mathematics and Mechanics 23, 1273–1282.

Barenblatt, G.I. (1962). The Mathematical Theory of Equilibrium Cracks in Brittle Fracture. In Advances in Applied Mechanics, T. von K. G. Kuerti, F. H. van den Dungen and L. Howarth H.L. Dryden, ed. (Elsevier), pp. 55–129.

Bažant, Z.P. (2002). Concrete fracture models: testing and practice. Eng Fract Mech 69: 165-205. Eng. Fract. Mech. 69, 165–205.

Behiri, J.C., and Bonfield, W. (1984). Fracture mechanics of bone--the effects of density, specimen thickness and crack velocity on longitudinal fracture. J. Biomech. 17, 25–34.

Bonfield, W., Grynpas, M.D., and Young, R.J. (1978). Crack velocity and the fracture of bone. J. Biomech. 11, 473–479.

Brown, C.U., Yeni, Y.N., and Norman, T.L. (2000). Fracture toughness is dependent on bone location--a study of the femoral neck, femoral shaft, and the tibial shaft. J. Biomed. Mater. Res. 49, 380–389.

Burstein, A.H., Currey, J.D., Frankel, V.H., and Reilly, D.T. (1972). The ultimate properties of bone tissue: The effects of yielding. J. Biomech. 5, 35–44.

Chapra, S.C., and Canale, R.P. (1985). Numerical methods for engineers: with personal computer applications (McGraw-Hill).

Clifford, J., Rosen, Bouillon, R., and Compston, J.E. (2013). Wiley: Primer on the Metabolic Bone Diseases and Disorders of Mineral Metabolism, 8th Edition.

Cox, B.N., and Yang, Q. (2007). Cohesive zone models of localization and fracture in bone. Eng. Fract. Mech. 74, 1079–1092.

Currey, J.D., Brear, K., Zioupos, P., and Reilly, G.C. (1995). Effect of formaldehyde fixation on some mechanical properties of bovine bone. Biomaterials 16, 1267–1271.

de Moura, M.F.S.F., Morais, J.J.L., and Dourado, N. (2008). A new data reduction scheme for mode I wood fracture characterization using the double cantilever beam test. Eng. Fract. Mech. 75, 3852–3865.

de Moura, M.F.S.F., Oliveira, J.M.Q., Morais, J.J.L., and Xavier, J. (2010). Mixed-mode I/II wood fracture characterization using the mixed-mode bending test. Eng. Fract. Mech. 77, 144–152.

de Moura, M.F.S.F., Silva, M.A.L., de Morais, A.B., and Morais, J.J.L. (2006). Equivalent crack based mode II fracture characterization of wood. Eng. Fract. Mech. 73, 978–993.

de Moura, M.F.S.F., Dourado, N., Morais, J.J.L., and Pereira, F. a. M. (2011). Numerical analysis of the ENF and ELS tests applied to mode II fracture characterization of cortical bone tissue. Fatigue Fract. Eng. Mater. Struct. 34, 149–158.

de Moura, M.F.S.F., Gonçalves, J.P.M., and Magalhães, A.G. (2012). A straightforward method to obtain the cohesive laws of bonded joints under mode I loading. Int. J. Adhes. Adhes. 39, 54–59.

De Santis, R., Anderson, P., Tanner, K.E., Ambrosio, L., Nicolais, L., Bonfield, W., and Davis, G.R. (2000). Bone fracture analysis on the short rod chevron-notch specimens using the X-ray computer micro-tomography. J. Mater. Sci. Mater. Med. 11, 629–636.

Dias, M.I.R., Costa, L., Viegas, C., Alves, H., and Pires, M. (2005). O Tecido Ósseo Biologia da Cicatrização (Vila Real: Universidade de Trás-os-Montes e Alto Douro).

Doblaré, M., García, J.M., and Gómez, M.J. (2004). Modelling bone tissue fracture and healing: a review. Eng. Fract. Mech. 71, 1809–1840.

Dong, X.N., Luo, Q., and Wang, X. (2013). Progressive post-yield behavior of human cortical bone in shear. Bone 53, 1–5.

Dourado, N., Pereira, F.A.M., de Moura, M.F.S.F., Morais, J.J.L., and Dias, M.I.R. (2013). Bone fracture characterization using the end notched flexure test. Mater. Sci. Eng. C 33, 405–410.

Dugdale, D.S. (1960). Yielding of steel sheets containing slits. J. Mech. Phys. Solids 8, 100–104.

Feng, Z., Rho, J., Han, S., and Ziv, I. (2000). Orientation and loading condition dependence of fracture toughness in cortical bone. Mater. Sci. Eng. C 11, 41–46.

Fratzl, P., and Weinkamer, R. (2007). Nature's hierarchical materials. Prog. Mater. Sci. 52, 1263–1334.

George, W.T., and Vashishth, D. (2006). Susceptibility of aging human bone to mixed-mode fracture increases bone fragility. Bone 38, 105–111.

GOM mbH (2007). ARAMIS DIC 2D/3D. Commercial software.

Gross, D., and Seelig, T. (2007). Fracture Mechanics: With an Introduction to Micromechanics (Springer Science & Business Media).

Hashemi, S., Kinloch, A.J., and Williams, J.G. (1990). The Analysis of Interlaminar Fracture in Uniaxial Fibre-Polymer Composites. Proc. R. Soc. Lond. Ser. Math. Phys. Sci. 427, 173–199.

Hillerborg, A., Modéer, M., and Petersson, P.-E. (1976). Analysis of crack formation and crack growth in concrete by means of fracture mechanics and finite elements. Cem. Concr. Res. 6, 773–781.

Högberg, J.L. (2006). Mixed mode cohesive law. Int. J. Fract. 141, 549–559.

Högberg, J.L., Sørensen, B.F., and Stigh, U. (2007). Constitutive behaviour of mixed mode loaded adhesive layer. Int. J. Solids Struct. *44*, 8335–8354.

Juntti, M., Asp, L.E., and Olsson, R. (1999). Assessment of Evaluation Methods for the Mixed-Mode Bending Test. J. Compos. Technol. Res. 21, 34–48.

Kafkalidis, M.S., and Thouless, M.D. (2002). The effects of geometry and material properties on the fracture of single lap-shear joints. Int. J. Solids Struct. 39, 4367–4383.

Koester, K.J., Barth, H.D., and Ritchie, R.O. (2011). Effect of aging on the transverse toughness of human cortical bone: evaluation by R-curves. J. Mech. Behav. Biomed. Mater. 4, 1504–1513.

Li, S., Demirci, E., and Silberschmidt, V.V. (2013). Variability and anisotropy of mechanical behavior of cortical bone in tension and compression. J. Mech. Behav. Biomed. Mater. 21, 109–120.

Lucksanasombool, P., Higgs, W.A., Higgs, R.J., and Swain, M.V. (2001). Fracture toughness of bovine bone: influence of orientation and storage media. Biomaterials 22, 3127–3132.

Malik, C.L., Stover, S.M., Martin, R.B., and Gibeling, J.C. (2003). Equine cortical bone exhibits rising R-curve fracture mechanics. J. Biomech. 36, 191–198.

Melvin, J.W., and Evans, F.G. (1973). Crack propagation in bone. Biomater. Symp. Am. Soc. Mech. Eng.

Mohammed, I., and Liechti, K.M. (2000). Cohesive zone modeling of crack nucleation at bimaterial corners. J. Mech. Phys. Solids 48, 735–764.

Morais, J.J.L., de Moura, M.F.S.F., Pereira, F.A.M., Xavier, J., Dourado, N., Dias, M.I.R., and Azevedo, J.M.T. (2010). The double cantilever beam test applied to mode I fracture characterization of cortical bone tissue. J. Mech. Behav. Biomed. Mater. 3, 446–453.

Nalla, R.K., Kinney, J.H., and Ritchie, R.O. (2003). Mechanistic fracture criteria for the failure of human cortical bone. Nat. Mater. 2, 164–168.

Nalla, R.K., Kruzic, J.J., Kinney, J.H., and Ritchie, R.O. (2004). Effect of aging on the toughness of human cortical bone: evaluation by R-curves. Bone 35, 1240–1246.

Needleman, A. (1987). A Continuum Model for Void Nucleation by Inclusion Debonding. J. Appl. Mech.-Trans. Asme - J APPL MECH 54.

Needleman, A. (1990). An analysis of decohesion along an imperfect interface. Int. J. Fract. 42, 21–40.

Norman, T.L., Vashishth, D., and Burr, D.B. (1992). Effect of groove on bone fracture toughness. J. Biomech. 25, 1489–1492.

Norman, T.L., Vashishth, D., and Burr, D.B. (1995). Fracture toughness of human bone under tension. J. Biomech. 28, 309–320.

Norman, T.L., Nivargikar, S.V., and Burr, D.B. (1996). Resistance to crack growth in human cortical bone is greater in shear than in tension. J. Biomech. 29, 1023–1031.

Norris, M., and Siegfried, D. (2011). Anatomy and Physiology For Dummies (Hoboken, NJ: For Dummies).

Oliveira, J.M.Q., de Moura, M.F.S.F., and Morais, J.J.L. (2009). Application of the end loaded split and single-leg bending tests to the mixed-mode fracture characterization of wood. Holzforschung 63.

Olvera, D., Zimmermann, E.A., and Ritchie, R.O. (2012). Mixed-mode toughness of human cortical bone containing a longitudinal crack in far-field compression. Bone 50, 331–336.

Pereira, F.A.M. (2009). Comportamento à fractura em modo I do tecido ósseo cortical. Dissertação de mestrado. Universidade de Trás-os-montes e Alto Douro.

Pereira, F.A.M., Morais, J.J.L., Dourado, N., de Moura, M.F.S.F., and Dias, M.I.R. (2011). Fracture characterization of bone under mode II loading using the end loaded split test. J. Mech. Behav. Biomed. Mater. 4, 1764–1773.

Pereira, F.A.M., Morais, J.J.L., de Moura, M.F.S.F., Dourado, N., and Dias, M.I.R. (2012). Evaluation of bone cohesive laws using an inverse method applied to the DCB test. Eng. Fract. Mech. 96, 724–736.

Pereira, F. a. M., de Moura, M.F.S.F., Dourado, N., Morais, J.J.L., and Dias, M.I.R. (2014). Bone fracture characterization under mixed-mode I+II loading using the single leg bending test. Biomech. Model. Mechanobiol. 13, 1331–1339.

Phelps, J.B., Hubbard, G.B., Wang, X., and Agrawal, C.M. (2000). Microstructural heterogeneity and the fracture toughness of bone. J. Biomed. Mater. Res. 51, 735–741.

Reeder, J.J.C. (1989). Mixed-Mode Bending Method for Delamination Testing. AIAA J. 28.

Reeder, J.R. (2003). Refinements to the Mixed-Mode Bending Test for Delamination Toughness. J. Compos. Technol. Res. 25, 191–195.

Rho, J.Y., Kuhn-Spearing, L., and Zioupos, P. (1998). Mechanical properties and the hierarchical structure of bone. Med. Eng. Phys. 20, 92–102.

Rice, J.R. (1968). A Path Independent Integral and the Approximate Analysis of Strain Concentration by Notches and Cracks. J. Appl. Mech. 35, 379–386.

Salgado, A.J., Coutinho, O.P., and Reis, R.L. (2004). Bone tissue engineering: state of the art and future trends. Macromol. Biosci. 4, 743–765.

Scheider, I., and Brocks, W. (2003). Simulation of cup–cone fracture using the cohesive model. Eng. Fract. Mech. 70, 1943–1961.

Schwalbe, K.-H., Scheider, I., and Cornec, A. (2012). Guidelines for Applying Cohesive Models to the Damage Behaviour of Engineering Materials and Structures (Springer Science & Business Media).

Sheskin, D.J. (2003). Handbook of Parametric and Nonparametric Statistical Procedures: Third Edition (CRC Press).

Sikavitsas, V.I., Temenoff, J.S., and Mikos, A.G. (2001). Biomaterials and bone mechanotransduction. Biomaterials 22, 2581–2593.

Silva, F.G.A., Xavier, J., Pereira, F.A.M., Morais, J.J.L., Dourado, N., and Moura, M.F.S.F. (2013). Determination of cohesive laws in wood bonded joints under mode I loading using the DCB test. Holzforschung 67.

Sobelman, O.S., Gibeling, J.C., Stover, S.M., Hazelwood, S.J., Yeh, O.C., Shelton, D.R., and Martin, R.B. (2004). Do microcracks decrease or increase fatigue resistance in cortical bone? J. Biomech. 37, 1295–1303.

Sørensen, B.F. (2002). Cohesive law and notch sensitivity of adhesive joints. Acta Mater. 50, 1053–1061.

Sørensen, B.F., and Kirkegaard, P. (2006). Determination of mixed mode cohesive laws. Eng. Fract. Mech. 73, 2642–2661.

Sousa, A.M.R., Xavier, J., Morais, J.J.L., Filipe, V.M.J., and Vaz, M. (2011b). Processing discontinuous displacement fields by a spatio-temporal derivative technique. Opt. Lasers Eng. 49, 1402–1412.

Sousa, A.M.R., Xavier, J., Vaz, M., Morais, J.J.L., and Filipe, V.M.J. (2011a). Cross-Correlation and Differential Technique Combination to Determine Displacement Fields. Strain 47, 87–98.

Szekrényes, A., and Uj, J. (2004). Beam and finite element analysis of quasi-unidirectional composite SLB and ELS specimens. Compos. Sci. Technol. 64, 2393–2406.

Tang, T., Ebacher, V., Cripton, P., Guy, P., McKay, H., and Wang, R. (2015). Shear deformation and fracture of human cortical bone. Bone 71, 25–35.

Termine, J., and Robey, P. (1996). Bone matrix proteins and the mineralization process. In Primer on the Metabolic Bone Diseases and Disorders of Mineral Metabolism., M.Favus, ed. (Official Publication of the American Society for Bone and Mineral Research, Lippincott-Raven Publishers).

Turner, C.H., Wang, T., and Burr, D.B. (2001). Shear Strength and Fatigue Properties of Human Cortical Bone Determined from Pure Shear Tests. Calcif. Tissue Int. 69, 373–378.

Tvergaard, V., and Hutchinson, J.W. (1992). The relation between crack growth resistance and fracture process parameters in elastic-plastic solids. J. Mech. Phys. Solids 40, 1377–1397.

Ural, A., and Vashishth, D. (2006). Cohesive finite element modeling of age-related toughness loss in human cortical bone. J. Biomech. 39, 2974–2982.

Vashishth, D., Behiri, J.C., and Bonfield, W. (1997). Crack growth resistance in cortical bone: Concept of microcrack toughening. J. Biomech. 30, 763–769.

Vashishth, D., Tanner, K.E., and Bonfield, W. (2000). Contribution, development and morphology of microcracking in cortical bone during crack propagation. J. Biomech. 33, 1169–1174.

Vashishth, D. (2004). Rising crack-growth-resistance behavior in cortical bone:: implications for toughness measurements. J. Biomech. 37, 943–946.

Wang, X., and Agrawal, C.M. (1996). Fracture toughness of bone using a compact sandwich specimen: effects of sampling sites and crack orientations. J. Biomed. Mater. Res. 33, 13–21.

Walters, F.H. (1991). Sequential simplex optimization: a technique for improving quality and productivity in research, development, and manufacturing (CRC Press).

Wang, X.D., Masilamani, N.S., Mabrey, J.D., Alder, M.E., and Agrawal, C.M. (1998). Changes in the fracture toughness of bone may not be reflected in its mineral density, porosity, and tensile properties. Bone 23, 67–72.

Wang, X., and Puram, S. (2004). The Toughness of Cortical Bone and Its Relationship with Age. Ann. Biomed. Eng. 32, 123–135.

Wang, Y., and Williams, J.G. (1992). Corrections for mode II fracture toughness specimens of composites materials. Compos. Sci. Technol. 43, 251–256.

Williams, J.G. (1988). On the calculation of energy release rates for cracked laminates. Int. J. Fract. 36, 101–119.

Williams, J.G. (1989). End corrections for orthotropic DCB specimens. Compos. Sci. Technol. 35, 367–376.

Wright, T.M., and Hayes, W.C. (1977). Fracture mechanics parameters for compact bone--effects of density and specimen thickness. J. Biomech. 10, 419–430.

Xavier, J., de Jesus, A.M.P., Morais, J.J.L., and Pinto, J.M.T. (2012). Stereovision measurements on evaluating the modulus of elasticity of wood by compression tests parallel to the grain. Constr. Build. Mater. 26, 207–215.

Yan, J., Clifton, K.B., Mecholsky, J.J., Jr, and Reep, R.L. (2006). Fracture toughness of manatee rib and bovine femur using a chevron-notched beam test. J. Biomech. 39, 1066–1074.

Yan, J., Mecholsky Jr., J.J., and Clifton, K.B. (2007). How tough is bone? Application of elastic–plastic fracture mechanics to bone. Bone 40, 479–484.

Yan, J., Daga, A., Kumar, R., and Mecholsky, J.J. (2008). Fracture toughness and work of fracture of hydrated, dehydrated, and ashed bovine bone. J. Biomech. 41, 1929–1936.

Yang, Q.D., and Thouless, M.D. (2001). Mixed-mode fracture analyses of plastically-deforming adhesive joints. Int. J. Fract. 110, 175–187.

Yang, Q.D., Cox, B.N., Nalla, R.K., and Ritchie, R.O. (2006). Re-evaluating the toughness of human cortical bone. Bone 38, 878–887.

Yeni, Y.., Brown, C.., and Norman, T.. (1998). Influence of Bone Composition and Apparent Density on Fracture Toughness of the Human Femur and Tibia. Bone 22, 79–84.

Yeni, Y.N., and Norman, T.L. (2000). Calculation of porosity and osteonal cement line effects on the effective fracture toughness of cortical bone in longitudinal crack growth. J. Biomed. Mater. Res. 51, 504–509.

Zimmermann, E.A., Launey, M.E., and Ritchie, R.O. (2010). The significance of crack-resistance curves to the mixed-mode fracture toughness of human cortical bone. Biomaterials 31, 5297–5305.

Zimmermann, E.A., Launey, M.E., Barth, H.D., and Ritchie, R.O. (2009). Mixed-mode fracture of human cortical bone. Biomaterials 30, 5877–5884.

Zioupos, P., and Currey, J.D. (1998). Changes in the Stiffness, Strength, and Toughness of Human Cortical Bone With Age. Bone 22, 57–66.